Spring 2022

Light-Matter Interactions in Thin-Film Materials and their Optoelectronic Applications

Chen Chen
Yale University Graduate School of Arts and Sciences, chen.chen.cc2483@yale.edu

Abstract

Light-Matter Interactions in Thin-Film Materials and their Optoelectronic Applications

Chen Chen

2022

Thin-film layered and traditional materials exhibit distinctive physics properties from their bulk counterparts. Thin-film materials bridge the gap between monolayer two-dimensional (2D) materials and bulk materials and possess the advantages of both, e.g., large tunability and high stability. However, recent research efforts focus on physical properties of monolayer 2D materials while state-of-art commercialized device applications are dominated by conventional bulk materials. Therefore, great potentials remain unexplored in thin-film materials, which host novel physics phenomenon and are promising for advanced device applications. In this thesis, we investigate the fundamental light-matter interaction properties of the thin-film materials and further demonstrate thin film devices for optoelectronic applications.

The light-matter interactions in thin-film materials exhibit many fascinating physical properties. We first report symmetry-controlled electron-phonon interactions in strong-coupled thin-film layered materials/silicon dioxide (SiO_2) vdWs heterostructures. Two optically silent Raman modes in amorphous SiO_2 are activated by coupling with electronic transitions in thin-film layered materials, where the chirality and anisotropy are controlled by intrinsic electronic band properties of layered materials. In addition, Raman mode in honeycomb lattice can acquire unique chirality due to its pseudoangular momentum (PAM). We discuss a reduced chirality of Raman G mode with increasing layer number of the honeycomb graphene and hBN, suggesting

that the interlayer interaction can significantly influence the symmetry of lattice vibration. Finally, we report a novel valley-selective linear dichroism in thin-film Tin Sulfide (SnS) with orthorhombic lattice. We observe two photoluminescence (PL) peaks, arising from band-edge optical interband transitions from two inequivalent valleys in SnS. The PL emission from Γ-X (Y) valley is completely x (y)-polarized.

Thin-film materials also exhibit great potential for mid-infrared light generation, modulation and detection applications. We first report the PL properties of thin-film black phosphorus (BP), whose brightness is comparable to that of an indium arsenide multiple quantum well (MQW) structure. Remarkably, with a moderate displacement field up to 0.48 V/nm, the PL emission from a ~20-layer BP flake is continuously tuned from 3.7 to 7.7 µm, spanning 4 µm in mid-infrared spectral range. Our work provides a comprehensive understanding of mid-infrared light emission properties of thin-film BP, suggesting its promising future in mid-infrared tunable light emitting and lasing applications. In addition, we demonstrate an ultrafast microbolometer for mid-infrared light detection based on ultrathin silicon nanomembrane. In this device, a small heat capacity of approximately $1.9 \times 10^{-11} \, J/K$ is achieved, which allows for its operation at a speed of over 10 kHz, around 100 times faster than commercial bolometers. Moreover, a compact diabolo antenna is leveraged for efficient mid-infrared light absorption, enabling the downscaling of the active area size to 6.2 µm by 6.2 µm. Due to its CMOS compatible fabrication processes, our demonstration may lead to the future high-resolution and high-speed LWIR imaging solution.

Light-Matter Interactions in Thin-Film Materials and their Optoelectronic Applications

A Dissertation

Presented to the Faculty of the Graduate School

of

Yale University

in Candidacy for the Degree of

Doctor of Philosophy

by

Chen Chen

Dissertation Director: Prof. Fengnian Xia

May 2022

Contents

Acknowledgements

First and foremost, I would like to express my deepest gratitude to my advisor, Professor Fengnian Xia for his exceptional support, guidance and mentorship of six years. He led me to the fantastic world of emerging materials and devices research and also taught me how to become a qualified scientists and develop my own research interest. His research philosophy and profound insight influences me significantly. Throughout six years, Professor Xia has always been very accessible and I benefit greatly from our fruitful discussions and relaxing communications. Especially when I meet challenges and failures, he is always there with encouragement, support and helpful guidance. There is no chance I can accomplish what I have achieved today without him, and it is my great honor to work with him.

My sincere appreciation also goes to my thesis committee members, Professor Hong X. Tang and Professor Jiang Liang for their supervision and valuable feedback on my research progress. I was deeply impressed by their insightful perspective and helpful advice on my research from each committing meeting. Their dedication to research has also inspired me during my study here.

It is a fantastic experience that I can work with so many brilliant lab members. My thank you first goes to Dr. Xiaolong Chen for our close cooperation and discussions. I learnt not only the experimental techniques but also his deep understanding of the physics. My beginning of the PhD study cannot be so smooth without his help. I would also like to thank Dr. Bingchen Deng who accommodated me and helped me get familiar with the lab and the university the first time I arrived here. I would like to thank Dr. Ibrahim Sarpkaya, Dr. Yuchuan Shao, Dr. Qiushi Guo, Dr

Cheng Li, Dr. Matthieu Fortin-Deschênes, Shaofan Yuan and Chao Ma for their useful suggestions and generous help during my research.

It is also an extraordinary opportunity to collaborate with many amazing groups all over the world. I would like to express my gratitude to Prof. Li Yang and Xiaobo Lu from Washington University in St. Louis, Professor Zhengqiang Ma, Dr. ZhengYang Xia and Seunghwan Min from University of Wisconsin-Madison, Professor Wang Yao and Dr. Hongyi Yu from Hong Kong University, Professor Je-Geun Park and Sungmin Lee from Seoul National University, Professor Minjoo L. Lee, Brendan Eng and Daehwan Jung from University of Illinois Urbana-Champaign, Professor Shengxi Huang from Pennsylvania State University and Professor Xiaodong Xu from University of Washington-Seattle for their productive collaborations and significant contributions to our research projects.

I would like to thank Dr. Michael Rooks at YINQE and all the staffs at Yale SEAS cleanroom for their assistance on the nanofabrication. I cannot accomplish my research projects so efficiently without their maintenance of the equipment and guidance of usage. Their professionality deeply influenced me. I would also like to thank all the staffs at Yale Graduate School of SEAS for their help out of the research.

It was fortunate for me to have the chance to meet so many nice fellows and friends here. I would like to thank Naijia Liu first. We always had dinner together as we began our life here.

We shared everything about our study and life and I got plenty of valuable advice from you. I would also like to thank Sisi Zhou, Peiqi Li, Xiruo Li, Jun Zhao, Zhang Chao, Zheng Chen. We spent many happy Friday tonight together on board games. Thanks for your company.

Finally, my deepest gratitude goes to my parents for their unconditional love and support to me. Throughout the six years, they provide me with endless motivations and passions to my life and study and they are always there with me whatever, wherever and whenever. This thesis is dedicated to my beloved parents.

To my parents

List of Publications

Publications discussed in this thesis

1. **Chen, C.**, Li, C., Min, S., Xia, Z., Guo, Q., Ma, Z. and Xia, F. Ultrafast silicon microbolometer for long-wavelength infrared detection. *Nano Letters* 21.19 (2021): 8385-8392.

The section 3.2 is mainly adopted from this paper

2. Chen, C., Chen, X., Deng, B., Watanabe, K., Taniguchi, T., Huang, S., and Xia, F. Probing interlayer interaction via chiral phonons in layered honeycomb materials. *Physical Review B,* 103(3), 035405 (2021).

The section 2.2 is mainly adopted from this paper

3. **Chen, C.**, Lu, X., Deng, B., Chen, X., Guo, Q., Li, C., Ma, C., Yuan, S., Sung, E., Watanabe, K., Taniguchi, T., Yang, L., and Xia, F. Widely tunable mid-infrared light emission in thin-film black phosphorus. *Science advances*, 6(7), p.eaay6134 (2020).

4. **Chen, C.**, Chen, F., Chen, X., Deng, B., Eng, B., Jung, D., Guo, Q., Yuan, S., Watanabe, K., Taniguchi, T., Lee, M. L. and Xia, F. Bright Mid-Infrared Photoluminescence from Thin-Film Black Phosphorus. *Nano letters*, *19*(3), pp.1488-1493 (2019).

The section 3.1 is mainly adopted from these two papers

5. **Chen, C.**, Chen, X., Yu, H., Shao, Y., Guo, Q., Deng, B., Lee, S., Ma, C., Watanabe, K., Taniguchi, T., Park, J.G. and Xia, F. Symmetry-Controlled Electron–Phonon Interactions in van der Waals Heterostructures. *ACS nano*, *13*(1), pp.552-559 (2018).

The section 2.1 is mainly adopted from this paper

6. **Chen, C.**, Chen, X., Shao, Y., Deng, B., Guo, Q., Ma, C. and Xia, F. Valley-Selective Linear Dichroism in Layered Tin Sulfide. *ACS Photonics*, *5*(9), pp.3814-3819 (2018).

The section 2.3 is mainly adopted from this paper

Other Publications

1. Yuan, S., Yu, R., Ma, C., Deng, B., Guo, Q., Chen, X., Li, C., **Chen, C.**, Watanabe, K., Taniguchi, T., García de Abajo, F.J. and Xia, F. Room temperature graphene mid-infrared bolometer with a broad operational wavelength range. *ACS Photonics*, *7*(5), pp.1206-1215 (2020).

2. Yuan, S., **Chen, C.**, Guo, Q. and Xia, F. Enhancing infrared emission of mercury telluride (HgTe) quantum dots by plasmonic structures. *Light, Science & Applications*, *9*, 37 (2020). (news & views)

3. Chen, X., **Chen, C.**, Levi, A., Houben, L., Deng, B., Yuan, S., Ma, C., Watanabe, K., Taniguchi, T., Naveh, D., Du, X. and Xia, F. Large-velocity saturation in thin-film black phosphorus transistors. *ACS nano*, *12*(5), pp.5003-5010 (2018).

4. Shao, Y., Liu, Y., Chen, X., **Chen, C.**, Sarpkaya, I., Chen, Z., Fang, Y., Kong, J., Watanabe, K., Taniguchi, T., Taylor, A., Huang, J., and Xia, F. Stable graphene-two-dimensional multiphase perovskite heterostructure phototransistors with high gain. *Nano letters*, *17*(12), pp.7330-7338 (2017).

5. Guo, Q., Guinea, F., Deng, B., Sarpkaya, I., Li, C., **Chen, C.**, Ling, X., Kong, J. and Xia, F. Electrothermal control of graphene plasmon–phonon polaritons. *Advanced Materials*, *29*(31), p.1700566 (2017).

List of Figures

1. Introduction

1.1 Light-matter interactions in layered two-dimensional (2D) materials

The emergence of two-dimensional (2D) materials (*1-7*) provides an exceptional platform for investigating fundamental physics (*8-17*) and device applications (*18-28*). Due to the strong quantum confinement perpendicular to the 2D plane (*29*), 2D materials exhibit distinctively different physics properties from their bulk counterparts (*30-33*). Moreover, 2D materials can cover almost the entire electromagnetic spectrum from ultraviolet to radiowaves, as shown in **Fig 1.1** (*19*). Due to the diversity of electronic band properties, different 2D materials can interact with photons of different photon energy, enabling their optoelectronic and photonic applications in different spectrum regions.
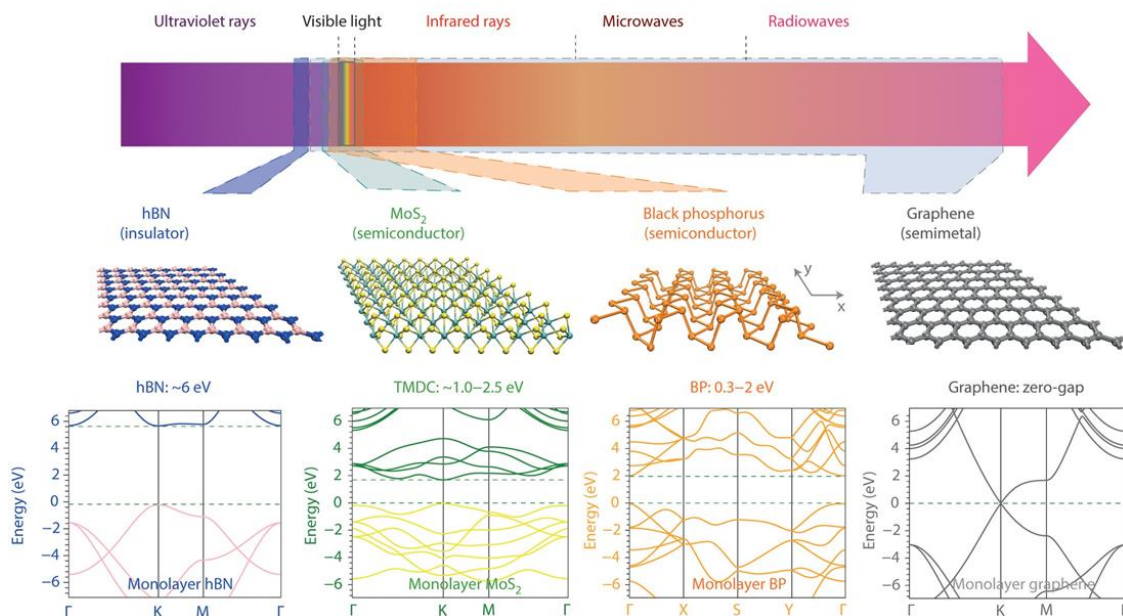
Fig 1.1 Electromagnetic spectrum from ultraviolet rays to radiowaves covered by representative 2D materials (hBN, TMDs, BP and graphene) with their atomic structure, bandgap and band structure. Adapted with permission from ref. *(19)* Copyright 2014, Springer Nature.

The light-matter interactions in 2D material are dominated by its bandgap, since it intrinsically determines the spectrum region that can interact with the 2D material. **Fig 1.1** exhibits the band structure and the bandgap of some representative 2D materials (*19*). For example, hexagonal boron nitride (hBN) is an insulator with a large bandgap of ~ 6 eV (*34, 35*), making it a good dielectric material (*36*). Due to its wide bandgap, the light emitting applications mainly arise from the single photon emission leveraging defect levels (*37-39*). The transition metal dichalcogenides (TMDs), in contrast, exhibits significantly smaller bandgap ranging from 1.0 eV to 2.5 eV (*40, 41*). Therefore, TMDs-based photodetectors (*42, 43*) and light emitting diodes (LEDs) (*44, 45*) have been demonstrated in visible and near-infrared spectrum region (*46, 47*). In addition, the black phosphorus (BP) exhibits a moderate bandgap of ~ 0.3 eV in its bulk form (>10 layers) (*48*). The bandgap of BP can be widely tunable by varying its layer number (*31, 49, 50*) or applying an external displacement field (*51-53*), making BP an appropriate candidate for mid-infrared applications (*54-56*). Finally, graphene is a zero bandgap Dirac semimetal (*30*), providing great possibility for light harvesting in longer wavelength region from terahertz to radiowaves (*57, 58*).

Besides the bandgap, many other factors can have a profound impact on light-matter interactions in 2D materials, giving rise to novel physics phenomena. One exceptional example is the lattice structure and corresponding lattice symmetry. For example, bilayer graphene (*30*), TMDs (*59*) and hBN (*60*) have 2D honeycomb lattice structure as shown in **Fig 1.1**, which exhibits an in-plane C_3 symmetry (*61*). There are two energy degenerate but inequivalent valleys at K+ and K-point in electronic band structure of honeycomb lattice, as illustrated in **Fig 1.2a** (*62, 63*). The K+ (K-) valley can be selectively pumped by right (left)-circularly polarized photons, giving rise to novel physics phenomena such as valley-selective circular dichroism (**Fig 1.2b**) (*64-66*),

topological valley transport (**Fig 1.2c**) (*67-69*) and valley hall effect (**Fig 1.2d**) (*70, 71*). In contrast, BP has orthorhombic lattice structure with reduced lattice symmetry as shown in **Fig 1.1**, leading to the strong in-plane anisotropy (*72*). Therefore, BP exhibits distinctively different light-matter interaction properties when excited by photons of different linear polarization, giving rise to highly anisotropic Raman modes (**Fig 1.3a**) (*73, 74*), optical absorption (**Fig 1.3b**) (*75, 76*), excitons (**Fig 1.3c**) (*31, 77*) and photodetectivity (**Fig 1.3d**) (*55, 78*).
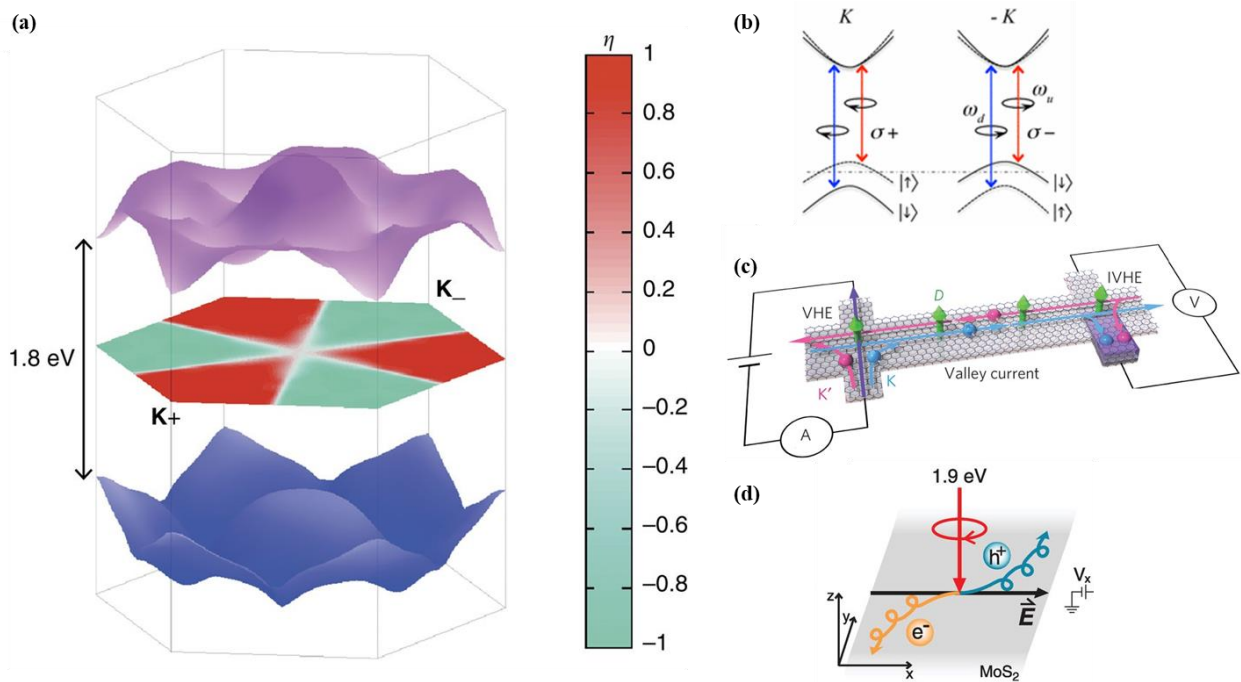
Fig 1.2 (a) The electronic band structure of MoS_2. K- and K+ represent the two degenerate but inequivalent valleys. Adapted with permission from ref. *(146)* Copyright 2012, Springer Nature. The schematical illustration of **(b)** valley selective circular dichroism in MoS_2. Adapted with permission from ref. *(62)* Copyright 2012, American Physical Society. **(c)** topological valley transport in graphene. Adapted with permission from ref. *(69)* Copyright 2015, Springer Nature. **(d)** valley hall effect in MoS_2. Adapted with permission from ref. *(70)* Copyright 2014, American Association for the Advancement of Science.
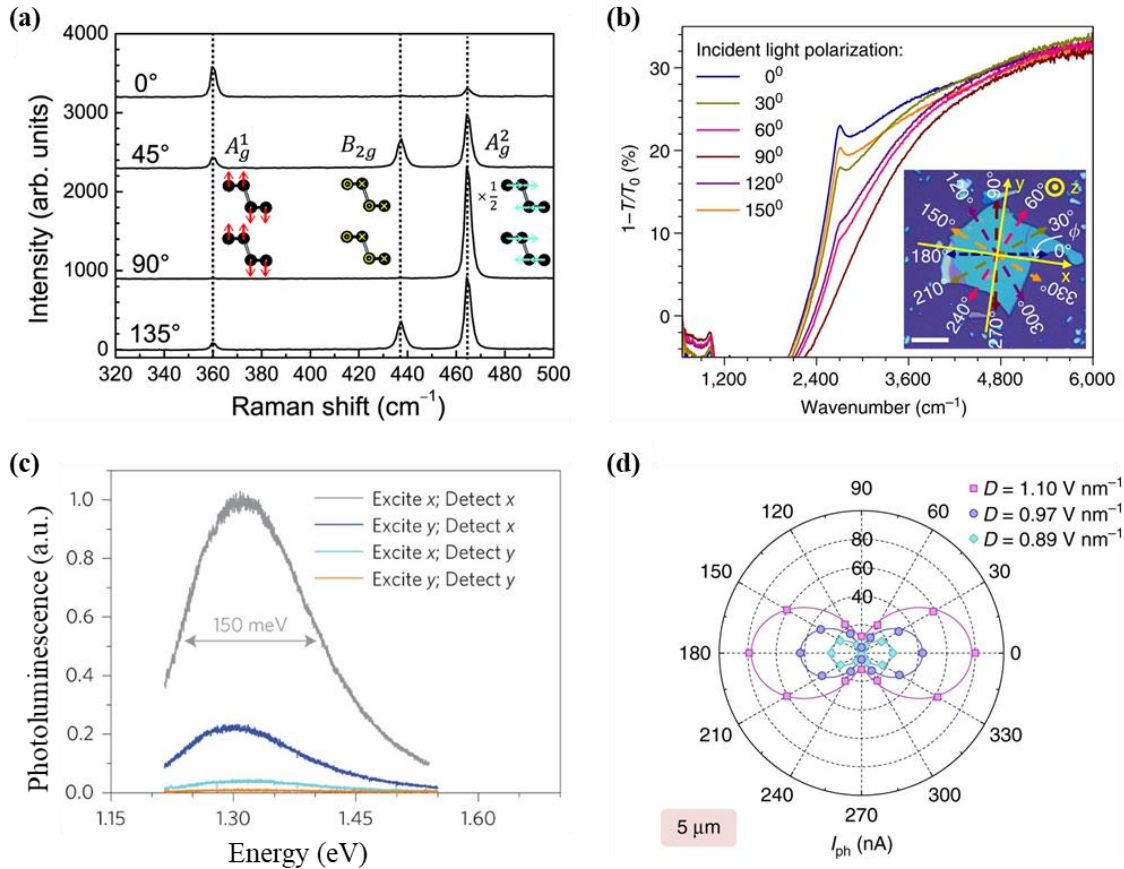
Fig 1.3 (a) The anisotropic Raman spectrum of BP. Adapted with permission from ref. *(73)* Copyright 2015, The Royal Society of Chemistry. **(b)** The anisotropic infrared extinction spectrum of BP. Adapted with permission from ref. *(75)* Copyright 2010, American Chemical Society. **(c)** The anisotropic PL spectrum of monolayer BP. Adapted with permission from ref. *(77)* Copyright 2015, Springer Nature. **(d)** The anisotropic photocurrent in dual hBN/BP/hBN device under different displacement field at incident wavelength of 5 µm. Adapted with permission from ref. *(55)* Copyright 2017, Springer Nature.

The light-matter interactions in 2D materials can also be significantly influenced by interlayer interaction and electron-phonon coupling. The interlayer interaction can modify the electronic band structure of layered 2D materials, and accordingly affect the light-matter interaction properties *(30-33)*. For example, a direct-to-indirect bandgap transition is demonstrated from monolayer Molybdenum disulfide (MoS_2) to its multilayer counterpart due to the interlayer

interaction, as illustrated in **Fig 1.4a** (*32, 33*). Therefore, the photoluminescence (PL) emissions from few-layer and bulk MoS_2 are significantly quenched compared with its monolayer counterpart, as exhibited in **Fig 1.4b** (*32, 33*). In addition, the photon excited electrons in 2D materials can strongly interact with phonons, leading to many intriguing optical phenomena (*79-81*). For example, the optically silent ZO phonon mode in hBN can be activated by the electronic resonance in Tungsten diselenide (WSe_2) in hBN/WSe_2 heterostructure as illustrated in **Fig 1.4c** (*82*). In consequence, emerging Raman peaks are observed in resonant emission spectrum of the heterostructure, as shown in **Fig 1.4d** (*82*).
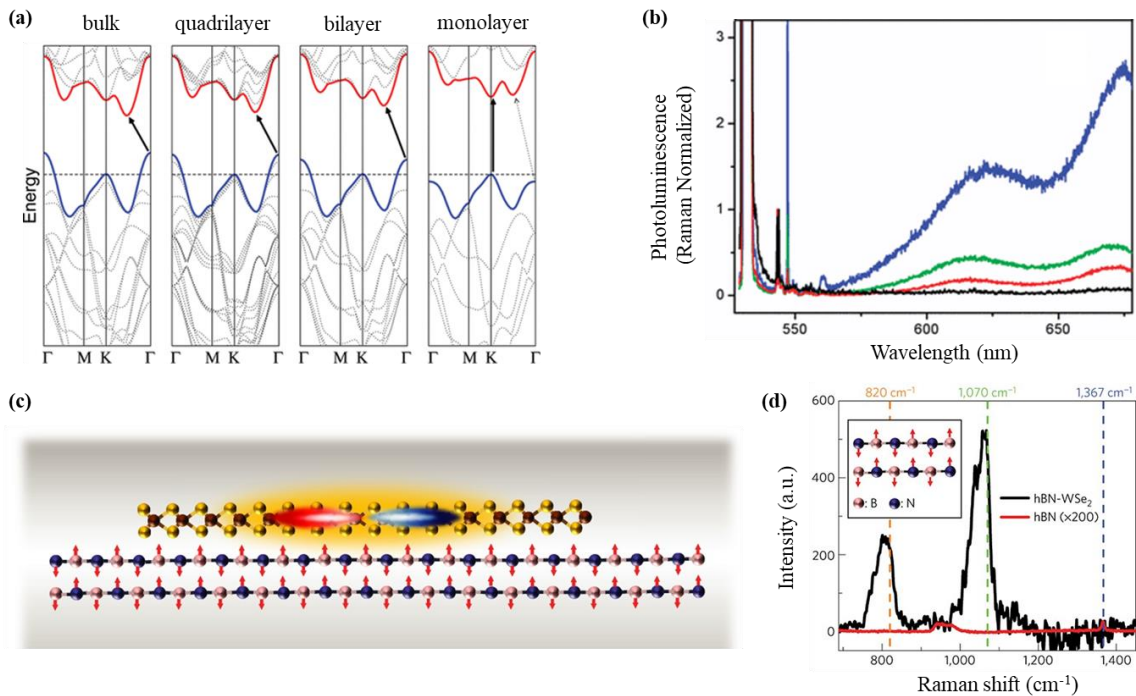
Fig 1.4 (a) The electronic band structure of bulk, quadrilayer, bilayer and monolayer MoS_2. Adapted with permission from ref. *(32)* Copyright 2010, American Chemical Society. **(b)** The PL spectrum of bulk, quadrilayer, bilayer and monolayer MoS_2 normalized to Raman intensity. Adapted with permission from ref. *(32)* Copyright 2010, American Chemical Society. **(c)** The schematic illustration of the electron-phonon coupling in WSe_2/hBN heterostructure. Adapted with permission from ref. *(82)* Copyright 2016, Springer Nature. **(d)** Resonant Raman spectrum of WSe_2/hBN heterostructure. Adapted with permission from ref. *(82)* Copyright 2016, Springer Nature.

1.2 Mid-infrared optoelectronic applications of layered 2D materials

The distinguished light-matter interaction properties in various 2D materials give rise to their unique optoelectronic applications. The investigations on 2D material based optoelectronic devices have been more extensively focused on visible and near-infrared spectrum region due to more appropriate candidates, e.g., TMDs (*46, 47*), monolayer and few-layer BP (*83, 84*) and Group-IV monochalcogenide (*85, 86*). For example, so far 2D material-based LEDs and lasers have only been demonstrated in visible and near-infrared by TMDs-based p-n junctions (*44, 45*) and by TMDs (*87*) and BP (*88*) embedded in photonic crystal cavity, respectively.

However, mid-infrared technology is important since this spectral region hosts many important applications such as thermal imaging (*89-92*) and molecular sensing (*93, 94*). The thin-film BP has a moderate bandgap of ~0.3 eV in its multilayer form (>10 layers) (*48*), making it an appropriate candidate for mid-infrared optoelectronic applications (*54-56*). Accordingly, a BP-based mid-infrared photodetector is demonstrated at 3.39 µm with a high external responsivity of 82 A/W and a moderate operational bandwidth up to kHz, as shown in **Fig 1.5a** and **Fig 1.5b** (*78*). In addition, the bandgap of thin-film BP (~20 layers) can be efficiently tuned by an external electric field, which extends its operational spectral wavelength (*51-53*). On this basis, a widely tunable mid-infrared photodetector is realized in a dual-gate hBN/BP/hBN device, as shown in **Fig 1.5c** (*55*). The detection limit is extended up to 7.7 µm, far above the intrinsic capacity of pristine BP (**Fig 1.5d**) (*55*). However, BP suffers from poor air stability (*95, 96*) and therefore, well-established passivation technology is compulsory for its practical applications (*97, 98*).
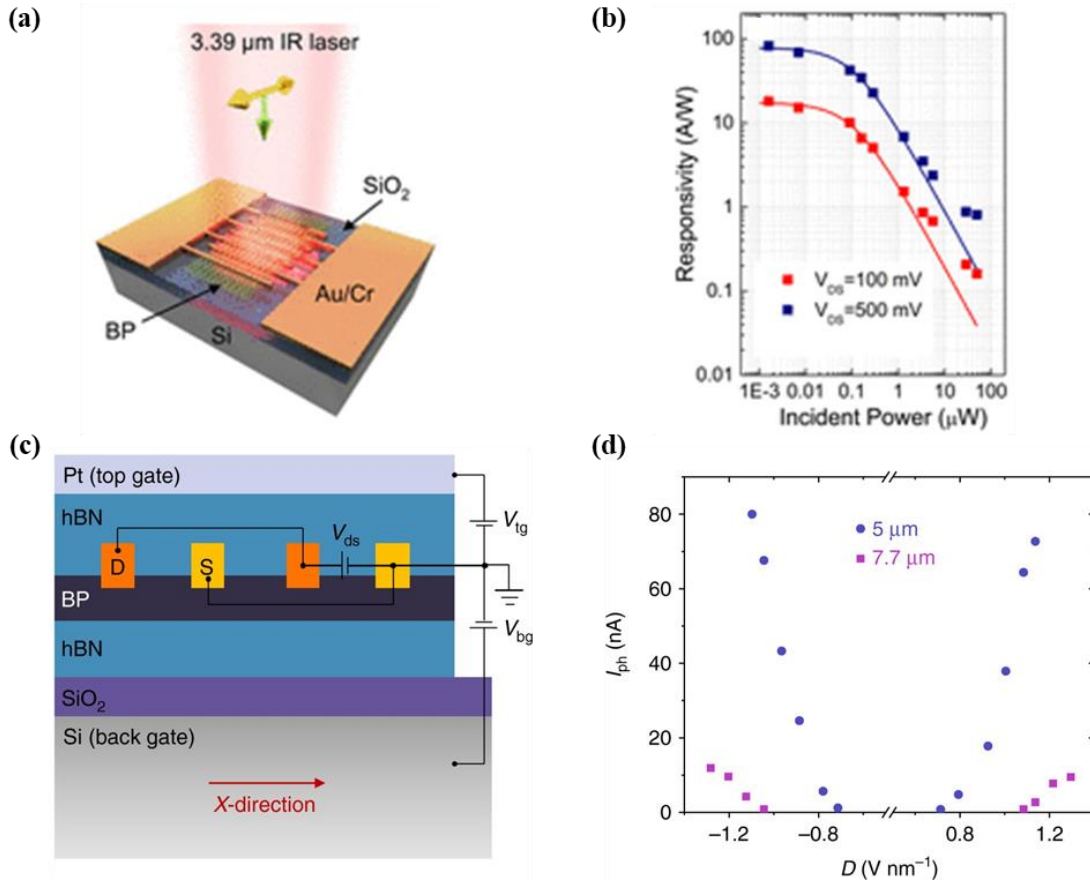
Fig 1.5 (a) The schematic image of the BP-based mid-infrared photodetector device. Adapted with permission from ref. *(78)* Copyright 2016, American Chemical Society. **(b)** Incident power dependence of responsivity at source-drain bias voltage of 100 and 500 mV. Adapted with permission from ref. *(78)* Copyright 2016, American Chemical Society. **(c)** The schematic image of the dual-gate hBN/BP/hBN heterostructure device. Adapted with permission from ref. *(55)* Copyright 2017, Springer Nature. **(d)** Photocurrents versus displacements fields at the incident wavelength of 5 and 7.7 µm. Adapted with permission from ref. *(55)* Copyright 2017, Springer Nature.

Meanwhile, the zero bandgap makes graphene intrinsically possible to interact with photons over the entire spectrum, giving rise to its potential for mid-infrared device applications (*99-102*). However, the light-matter interactions in mid-infrared is extremely weak in monolayer graphene due to the Pauli blocking (*103, 104*). Extensive efforts have been devoted to enhancing the mid-
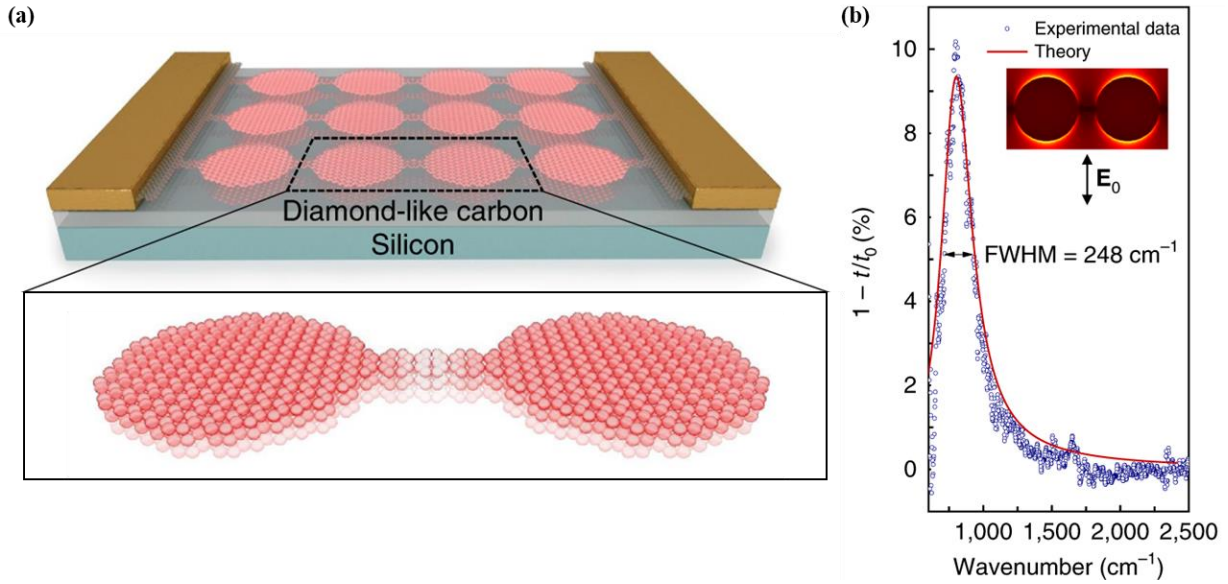
Fig 1.6 (a) The schematic image of the graphene-disk plasmonic resonator device. The graphene nanodisks are connected by quasi-1D graphene nanoribbons. Adapted with permission from ref. *(99)* Copyright 2018, Springer Nature. **(b)** Infrared extinction spectrum of the graphene-disk plasmonic resonator with excitation polarization perpendicular to nanoribbons. Adapted with permission from ref. *(99)* Copyright 2018, Springer Nature.

infrared light-matter interactions in graphene and much research progress has been achieved in engineered graphene plasmonic nanostructures (*105-107*). By tuning the width and Fermi level of graphene nanoribbon arrays, significant enhancement of mid-infrared optical absorption has been realized. On this basis, mid-infrared light detection have been demonstrated in graphene plasmonic devices. **Fig 1.6a** and **Fig 1.6b** show the schematic and infrared extinction spectra of an established graphene microbolometer, respectively (*99*). The optical absorption has been prominently improved to ~10% compared to ~ 1% in unpatterned monolayer graphene (*108*). Remarkably, the graphene microbolometer exhibits a high operational bandwidth up to GHz (*99*). However, graphene based mid-infrared detectors are still at early stage of fundamental research

and their sensitivity are not competitive with state-of-art commercialized photon and thermal detectors. Therefore, more investigations are required before 2D material based mid-infrared optoelectronic devices can be employed for future commercial applications.
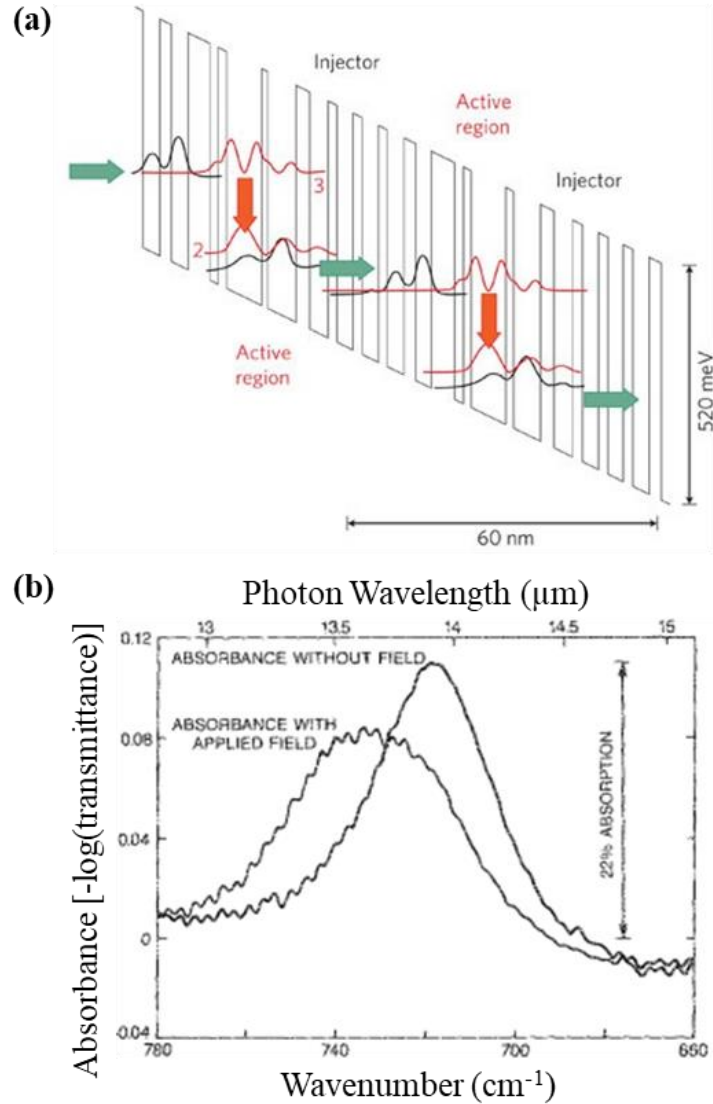
Fig 1.7 (a) The schematic image of intersubband laser transition in the conduction band of a typical MQW structure. Adapted with permission from ref. *(111)* Copyright 2012, Springer Nature. **(b)** Infrared absorbance spectrum of a GaAs QW structure with/without an external electric field of 36 kV/cm. Adapted with permission from ref. *(115)* Copyright 1987, AIP Publishing.

1.3 Mid-infrared optoelectronic applications of conventional semiconductors

The commercialized mid-infrared optoelectronic applications are still dominant by conventional semiconducting materials (e.g., III-V compounds) based devices due to their high efficiency and sensitivity. Moreover, the well-developed fabrication technology gives rise to their advantages of high yield, large-scale production and low cost.

On the one hand, mid-infrared light generation mostly arises from the intersubband transitions in multiple-quantum-well (MQW) structures (*109, 110*). **Fig 1.7a** exhibits the schematic illustration of intersubband laser transition in the conduction band of a typical MQW structure (*111*). On this basis, quantum cascade lasers (QCL) have been demonstrated and widely applied for commercialized mid-infrared light generation and pumping applications (*111-113*). In addition, the intersubband transitions from MQW structure can be slightly modulated by an external electric field due to optical stark effect (*114*), demonstrated by infrared absorption spectra shown in **Fig 1.7b** (*115*). However, the wavelength modulation is mostly less than 1 µm since the maximum applied electric field in MQW structure is limited.

On the other hand, mid-infrared light detection has mainly been realized by photon detectors and thermal detectors based on conventional bulk materials (*116-118*). The light sensing of photon detectors are achieved by direct collection of photon-excited photocarrier and its conversion to photocurrent, as exhibited in **Fig 1.8a** (*116*). Commercialized mid-infrared photon detectors are based on mercury cadmium telluride (MCT) detectors due to its narrow bandgap (*119*) and quantum well infrared photodetectors (QWIP) by its intersubband transitions (*120*). These detectors enjoy high sensitivity and high speed but suffer from high dark current at room temperature, which can only operate at cryogenic temperature. Moreover, photon detectors exhibit great challenges in integration with the commonly used complementary metal-oxide-
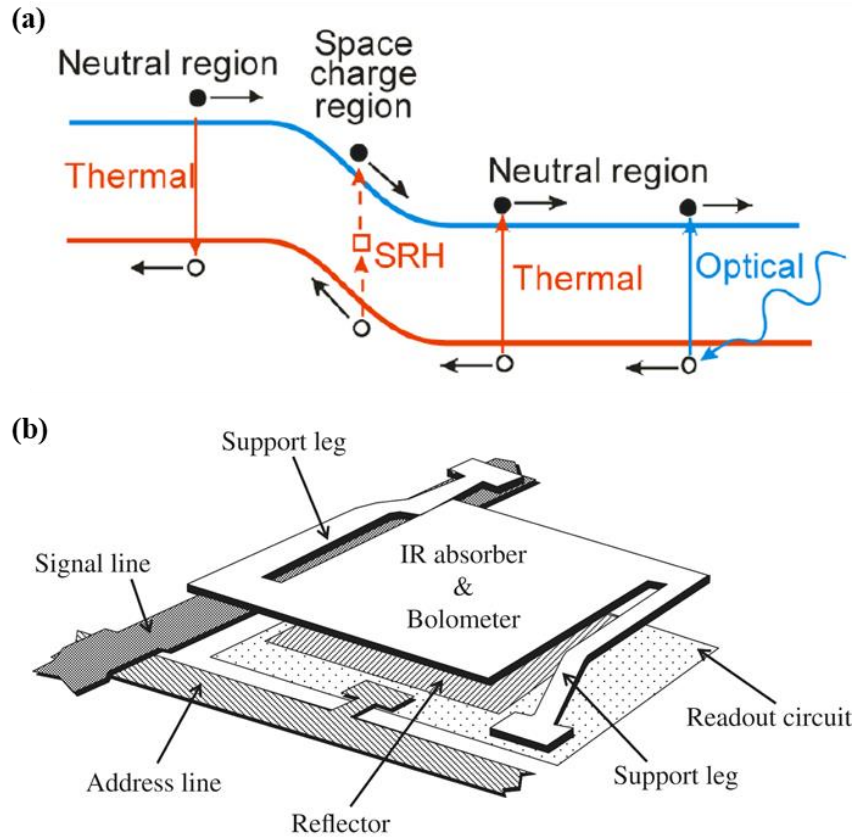
Fig 1.8 (a) The schematic illustration of the working mechanism of a p-n photodiode. Adapted with permission from ref. *(116)* Copyright 2016, IOP Publishing Ltd. **(b)** The schematic image of a typical microbolometer structure. Adapted with permission from ref. *(123)* Copyright 2017, Institute of Electrical Engineers of Japan. Published by John Wiley & Sons, Inc.

semiconductor (CMOS) technology and MCT is even toxic. Therefore, photon detectors are not economic for large-scale applications, which are mostly used in precise instruments and scientific equipment such as infrared spectrometers (*121*) and research-level infrared cameras (*122*). In contrast, thermal detectors, dominated by microbolometers, can operate at room temperature with reasonably high sensitivity (*123-125*). A microbolometer consists of an infrared light absorber and a temperature sensitive thermistor, as shown in **Fig 1.8b** (*123*). The light detection is realized by probing the resistance variation due to light-induced temperature

11

elevation in thermistor. The state-of-art microbolometers exhibit high responsivity with a low noise equivalent temperature difference (NETD) of ~50 mK, which are widely employed in thermal imaging applications (*123-125*). However, further improvement of the microbolometer performance has been hindered by challenges in decreasing its high thermal constant time (~10 ms) and downscaling of the pixel size (~10 µm) (*123-125*). Therefore, exploring new technology to overcome these challenges is highly desired for future microbolometer applications.

1.4 The outline of the thesis

In this thesis, we study the light-matter interactions in thin-film materials including both thin-film layered materials (graphene, hBN, TMDs, BP) and ultrathin conventional materials (silicon) and investigate their optoelectronic applications in mid-infrared. The light-matter interaction properties in thin-film layered materials are significantly influenced by the electronic band properties, lattice symmetry, electron-phonon coupling and van der Waals (vdWs) interlayer interactions. We uncover many intriguing physics phenomena and provide new insight into microscopic mechanisms of light-matter interactions in this material system. Moreover, due to the moderate thickness, thin-film materials can combine the desirable properties of strong light-matter interactions, high tunability and low thermal capacity. By engineering these features, we realize device applications for mid-infrared light generation, modulation and detection.

In Chapter 2, we study the light-matter interaction properties in thin-film 2D materials, which is divided into three sub-chapters. The electron-phonon interaction can have a profound influence on the light-matter interaction properties in thin-film 2D materials. In Chapter 2.1, we discover symmetry-controlled electron-phonon interactions in strong coupled 2D material/silicon dioxide

(SiO$_2$) vdWs heterostructures. We show that two optically silent Raman modes from amorphous SiO$_2$, can be activated through coupling with the electronic transitions in 2D materials. We find the Raman emissions indicate distinctively different polarization characteristics for coupled 2D materials with different lattice symmetry. By tuning the coupling strength in strongly coupled TMDs/SiO$_2$, we reveal that phonons from SiO$_2$ can effectively participate in excitonic intervalley scattering and valley depolarization process in TMDs. We demonstrate that the Raman modes activated by electron-phonon coupling can reflect the physical properties of electronic transitions in 2D materials. Our discovery provides a universal scheme of investigating the electronic band properties and optical selectivity in atomically thin materials. Part of Chapter 2.1 is adapted with the permission from the ref. (*126*), Chen, Chen, *et al*. "Symmetry-Controlled Electron–Phonon Interactions in van der Waals Heterostructures." *ACS nano* **13**.1 (2018): 552-559. Copyright 2019, American Chemical Society. In addition, the interlayer interaction can also significantly influence the light-matter interactions in thin-film 2D materials, which exhibits distinguished characteristics from their monolayer counterpart. In Chapter 2.2, we report a new strategy for probing the interlayer interaction via chiral phonons in layered honeycomb materials. We show that the Raman G mode in graphene and hBN exhibits reduced phonon chirality with increasing layer number, evidenced by the decreasing polarization degree of the Raman signal in helicity-resolved measurements. We introduce interlayer coupling terms to the fundamental Raman tensor to account for the effect of coupling and simulate the evolution of the phonon chirality by Raman tensor calculation. Our observation reveals that the interlayer interaction plays a crucial role in the lattice symmetry in thin-film 2D honeycomb lattice. Part of Chapter 2.2 is adapted with the permission from the ref. (*127*), Chen, Chen, *et al*. "Probing interlayer interaction via chiral phonons in layered honeycomb materials." *Physical Review B* **103**.3 (2021): 035405.

Copyright 2021, American Physical Society. Finally, the light-matter interaction properties in thin-film 2D materials are dominated by its lattice symmetry and electronic band properties, e.g., the valley physics. So far, explorations on valley physics have been extensively advanced but limited to 2D honeycomb lattice. In Chapter 2.3, we report the valley-selective linear dichroism of PL in layered thin-film Tin Sulfide (SnS) with reduced lattice symmetry and uncover its unique valley-related optical transition rules. We observe two emission peaks in its PL spectrum, which show a perfect but orthogonal linear dichroism, subject to the corresponding optical transition rules in two valleys. We further confirm the valley-selective linear dichroism by polarization-dependent optical absorption spectra. Our work opens up a new material system for valleytronic applications. Part of Chapter 2.3 is adapted with the permission from the ref. (*128*), Chen, Chen, *et al*. "Valley-selective linear dichroism in layered tin sulfide." *ACS Photonics* **5**.9 (2018): 3814-3819. Copyright 2018, American Chemical Society.

In Chapter 3, we investigate the mid-infrared optoelectronic applications of thin-film materials, which is divided into two sub-chapters. Though thin-film BP shows various intriguing properties, the investigation on its mid-infrared light emission properties is rare. In fact, its moderate band gap of 0.3 eV and wide tunablity under external displacement field make it ideal for mid-infrared light generation and modulation applications. We leverage these properties to explore its possible applications in widely tunable mid-infrared light emitting diodes and lasers. In Chapter 3.1, we demonstrate the bright and widely tunable PL emissions from thin-film BP. We observe a bright PL at 2485 cm^{-1} in ~46-nm thick BP at 80 K, indicating a bandgap of 0.308 eV. We reveal that such PL emission is quite strong, which is only seven times less bright than that of an InAs MQW sample. We also study the temperature and layer number dependence of PL emission, which provides a comprehensive understanding of the band properties in thin-film BP. Moreover,

we realize the widely tunable mid-infrared PL emissions from dual-gate hBN/BP/hBN devices. The emission peak from a ~10.5-nm thick BP flake can be continuously tuned from 3.7 to 7.7 µm with a moderate displacement field up to 0.48 V/nm, covering a broad spectral range in mid-infrared. Together with theoretical analysis we show that the radiative decay probably dominates over other nonradiative decay channels in thin-film BP. Part of Chapter 3.1 is adapted with the permission from the ref. (*129, 130*), Chen, Chen, *et al*. "Bright mid-infrared photoluminescence from thin-film black phosphorus." *Nano letters* **19**.3 (2019): 1488-1493. Copyright 2019, American Chemical Society, and from Chen, Chen, *et al*. "Widely tunable mid-infrared light emission in thin-film black phosphorus." *Science advances* **6**.7 (2020): eaay6134, Copyright 2020, the authors, some rights reserved; exclusive licensee American Association for the Advancement of Science. Meanwhile, the commercialized mid-infrared light detection at room temperature mainly relies on microbolometers. The development of state-of-art microbolometers is limited by its low operational speed and difficulty in downscaling the pixel size. In Chapter 3.2, we demonstrate an ultrafast microbolometer based on a 220 nm-thick single-crystalline silicon nanomembrane with a subwavelength pixel size for mid-infrared light detection. We utilize the ultra-thinness of the silicon nanomembrane to achieve an ultra-small C_{th}, based on which the τ_{th} of the bolometer has been reduced by over 500 times compared to that of commercialized ones. We design an ultracompact cross diabolo antenna as an infrared absorber, which allows for the realization of the subwavelength bolometer with active area pixel size of only 6.2 µm by 6.2 µm. Moreover, we implement a titanium (Ti)-Si-Ti structure on the silicon nanomembrane as the temperature sensitive resistor of the bolometer, which exhibits a high TCR of ~5%/K and a resistance of ~100 kΩ. We achieve an extrinsic responsivity of 114 mA/W at the wavelength of 12.2 µm, resulting in a calculated NETD value of 518 mK in demonstrated microbolometer. Part

of Chapter 3.2 is adapted with the permission from the ref. (*131*) Chen, Chen, *et al*. "Ultrafast Silicon Nanomembrane Microbolometer for Long-Wavelength Infrared Light Detection." *Nano Letters* **21**.19 (2021): 8385-8392. Copyright 2021, American Chemical Society.

In Chapter 4, we provide our outlook on future development of mid-infrared technology based on thin-film materials and discuss some possible future works that worth exploration. In Chapter 4.1, we discuss the advantages of thin-film materials for mid-infrared optoelectronic applications in reference to our works presented in Chapter 3. In Chapter 4.2, we discuss some possible future works for mid-infrared applications of thin-film materials and present some preliminary results. The Chapter 4.2 is divided into two sub-chapters. In Chapter 4.2.1, we investigate the potential of thin-film graphite based plasmonic device for mid-infrared light detection. We show that both the mid-infrared optical absorption and the TCR take advantages over its monolayer or few-layer CVD graphene counterpart. In Chapter 4.2.2. we explore the possibility of thin-film Tellurene (Te) as an appropriate substitute of BP for mid-infrared light emitting applications due to its outstanding air stability.

In Chapter 5, we provide a summary of the thesis.

2. Light-matter interaction in layered 2D materials

2.1 Probing the lattice symmetry of layered 2D materials via electron-phonon coupling in 2D materials/SiO₂ heterostructures

2.1.1 Motivation

The rise of the 2D materials provides an extraordinary platform for investigating the light-matter interactions since their bandgaps can cover the entire spectrum region from ultraviolet rays to radiowaves (*19*). Besides the bandgap, the band structure, determined by the lattice structure and lattice symmetry of 2D materials, can also significantly influence light-matter interactions and bring about many intriguing physics phenomena (*30, 59, 60, 72*). The band properties arising from the lattice geometry can be investigated by PL spectroscopy. For example, the PL from BP (*49, 77*) and Germanium Sulfide (GeS) (*132*) with orthorhombic lattice exhibits strong in-plane anisotropy. In contrast, the PL from TMDs and hBN with honeycomb lattice shows circular polarization (*64-66, 133*). The distinct PL properties arise from the optical transition rule (*31, 62, 63, 77*), subjective to the momentum and angular momentum conservation rule of photons and photon-excited electron-hole pairs at the band edge of 2D materials. However, most 2D materials do not exhibit observable PL emissions due to their indirect bandgap and prevalent non-radiative recombination channels (*134*). Therefore, a more universal scheme is highly desired to probe the lattice structure and corresponding band properties in 2D materials.

Notably, the electron-phonon interaction can significantly influence the light-matter interaction properties in vdWs heterostructures (*79-81*). Recently, control of electron-phonon coupling was realized in WSe₂/hBN heterostructures (*82*), in which Raman-silent phonon modes in hBN were activated through coupling with resonant electronic transitions in WSe₂. Due to the crystalline

17

structure of hBN, the geometry of activated Raman modes was still subjected to its intrinsic lattice symmetry. However, this work provides a new perspective that the electron-phonon interaction can be applied to probe light excited electron-hole pairs and therefore, reveal the band properties of the 2D materials. Here, we observed strong electron-phonon interactions in engineered 2D material/SiO_2 vdWs heterostructures. Two emerging Raman modes from amorphous SiO_2, which are originally Raman silent, are activated through the coupling between phonon modes of SiO_2 and the electronic transitions in 2D materials. Since the Raman modes arise from amorphous SiO_2, they do not inherit intrinsic lattice symmetry property. Therefore, it is possible that the Raman modes can inherit the properties of electronic transitions in 2D materials and reveal their band properties and lattice symmetry.

2.1.2 Fabrication of the strong-coupled 2D materials/SiO_2 heterostructures

Three classes of 2D materials were chosen for constructing the 2D material/SiO_2 heterostructures, including the TMDs with honeycomb lattice structure (monolayer and bilayer Tungsten disulfide (WS_2)), few-layer metal phosphorus trichalcogenides (MPTs) with honeycomb lattice structure (less than five layers manganese phosphorus triselenide ($MnPSe_3$) and iron phosphorus trisulfide ($FePS_3$)) (*135, 136*), and few-layer (less than five layers) BP (*75, 76*) and Tin Selenide (SnSe) with orthorhombic lattice structure (*137, 138*).

The SiO_2 on Si substrate was purchased from University Wafer where 285 nm SiO_2 was grown on one side of the Si wafer through the dry oxidation. Before the deposition of the 2D materials, the SiO_2/Si substrate was first cleaned by Acetone and followed by Isopropanol both for ten minutes under sonication to remove the possible organic residue and air-adsorbate. After

cleaning process, the SiO$_2$/Si substrate was immediately transferred into the argon-filled glove box to avoid further contamination from the ambient environment. Then, the atomically thin (mono- or few-layer) WS$_2$, FePS$_3$, MnPSe$_3$, BP and SnSe were mechanically exfoliated onto the SiO$_2$/Si substrate. The exfoliation of WS$_2$ was performed in ambient condition, while FePS$_3$, MnPSe$_3$, BP and SnSe were prepared in glove box to minimize the possible oxidation.
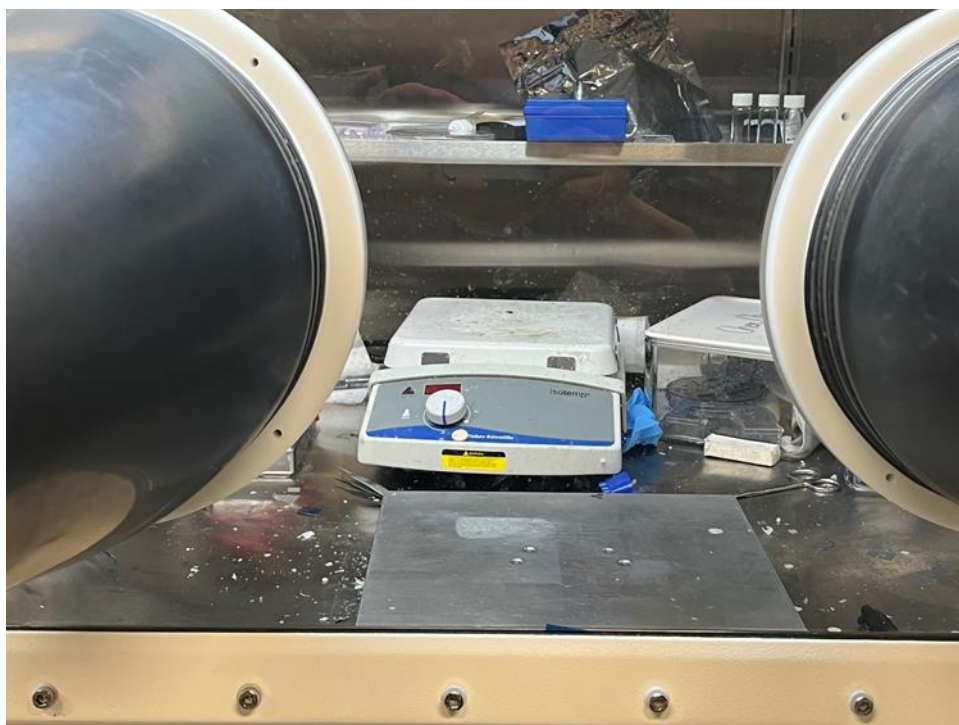
Fig 2.1.1 A photo of the hotplate in the glove box for sample annealing.

To achieve a strong coupling between 2D materials and SiO$_2$ substrates, we annealed samples (WS$_2$, FePS$_3$, MnPSe$_3$ and SnSe) at 500 ^{o}C for 5 to 30 mins on a hotplate in an argon-filled glove box (with H$_2$O and O$_2$ concentration below 0.1 ppm), as shown in **Fig 2.1.1**. Thin BP samples were annealed at 300 ^{o}C in the glove box for 20 mins to prevent degradation due to its instability at higher temperature. This annealing process has been widely used to realize an enhanced

19

coupling strength in vdWs heterostructures (*139, 140*). **Fig 2.1.2** shows the optical microscope images of the 2D material/SiO_2 heterostructures. Then all samples were immediately transferred to an optical stage and pumped down to 10^{-6} Torr for Raman and PL measurements.
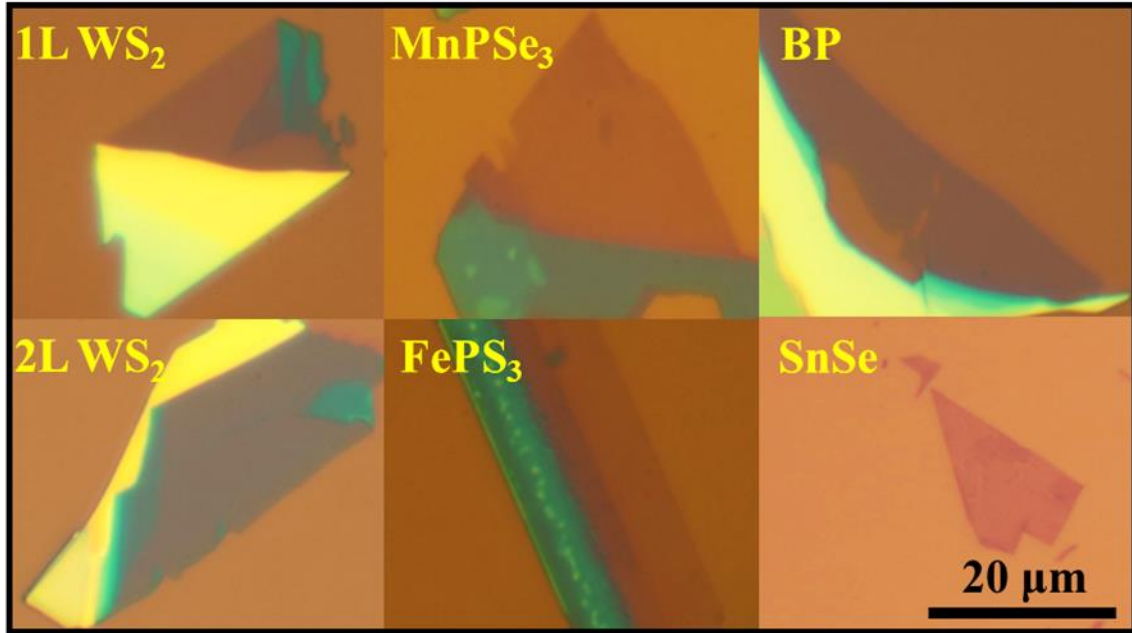
Fig 2.1.2 Optical images of strong-coupled 2D materials/SiO_2 heterostructures. Monolayer WS_2, bilayer WS_2, few-layer $MnPSe_3$, $FePS_3$, BP and SnSe were used to construct heterostructures. All panels: from ref. *(126)*.

2.1.3 The measurement scheme of the Raman spectroscopy

We established a home-made low-temperature micro-Raman/PL measurement system, as shown in **Fig 2.1.3**. **Fig 2.1.4** exhibits the schematic illustration of the optical system. A 532 nm and 640 nm solid state laser was used as the excitation source, which was focused onto the sample with a 40x microscope objective. The backscattering emission signal was collected with the same objective, followed by a notch filter to eliminate the reflected laser lines. The signal was detected by an Andor Sharmock SR750 Spectrometer equipped with an iDus 420 series CCD camera. To

20
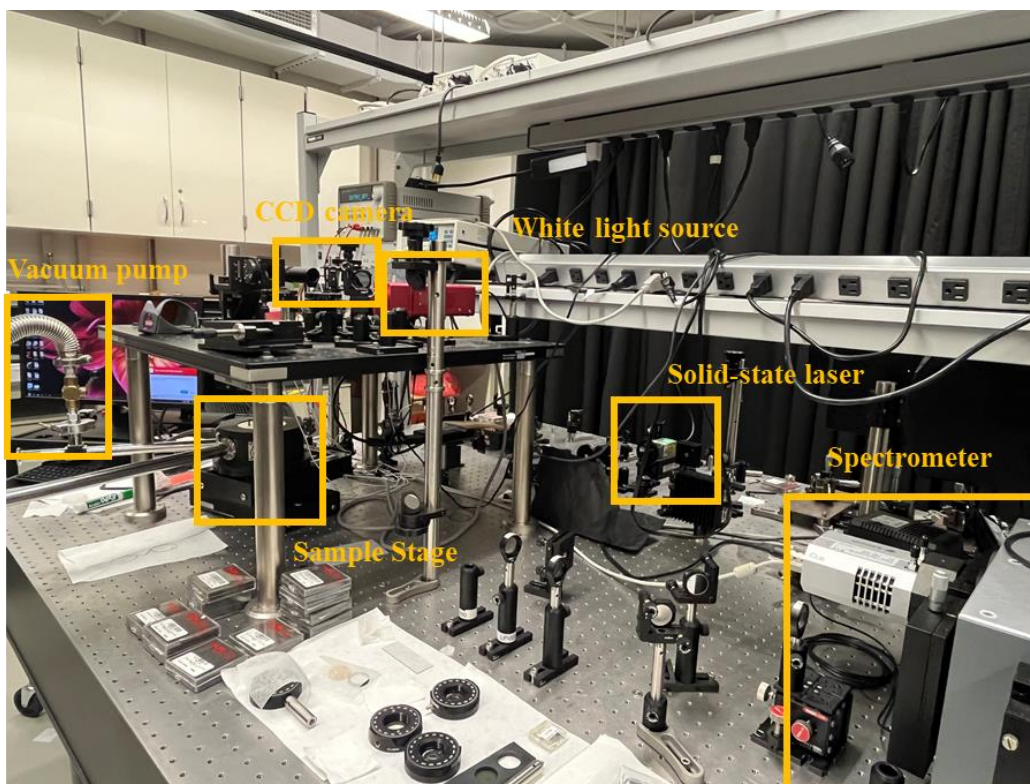
Fig 2.1.3 A photo of the home-made low-temperature micro-Raman/PL measurement system.
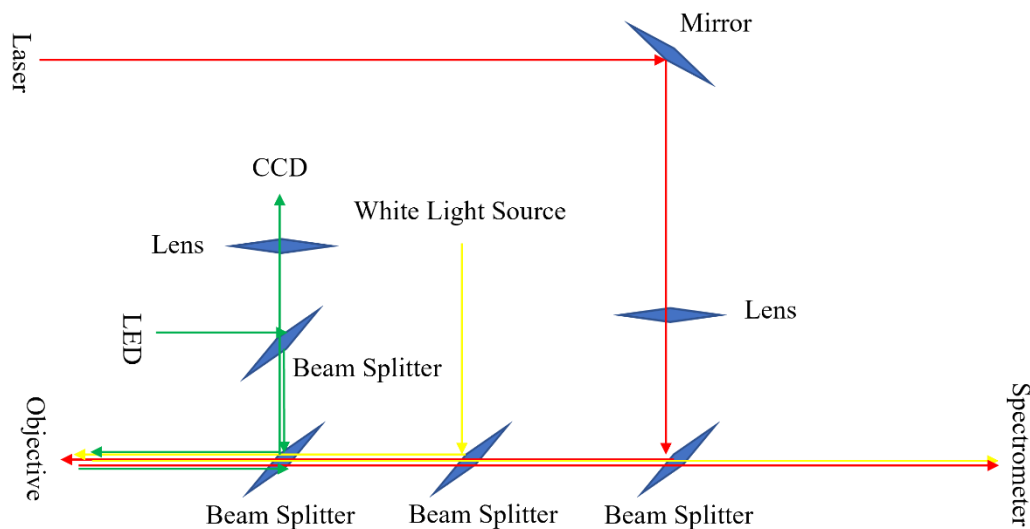
Fig 2.1.4 Schematic illustration of the optical measurement system. Red line: Optical path for Raman and PL measurement. Yellow line: Optical path for absorption measurement. Green line: Optical path for sample illumination and imaging.

locate the sample position under the microscope, a Thorlabs MEWHL5 light emitting diode (LED) powered by Agilent E3634A DC Power Supply was used to illuminate the sample. The sample image was detected and exhibited by Thorlabs Zelux™ Compact Scientific Cameras.

Fig 2.1.5 A photo of broadband wave-plates and linear polarizers for polarization-resolved optical measurements.

The polarization-resolved optical measurements were realized by a combination of broadband wave-plates and linear polarizers (**Fig 2.1.5**). **Fig 2.1.6a (b)** exhibits the schematic illustration of the circularly (linearly) polarized Raman measurements, respectively. For circularly polarized helicity-resolved Raman measurements, a combination of linear polarizer and broadband quarter-wave plate was used to generate σ+/σ- excitation. The backscattering emission signal went

through the same quarter-wave plate, and the different circularly polarized components were analyzed by a combination of broadband half-wave plate and linear polarizer. For linearly-polarized angular-resolved Raman measurements, a half-wave plate was used to tune the polarization of the excitation laser. The polarization of emissions was analyzed by a combination of broadband half-wave plate and a linear polarizer.
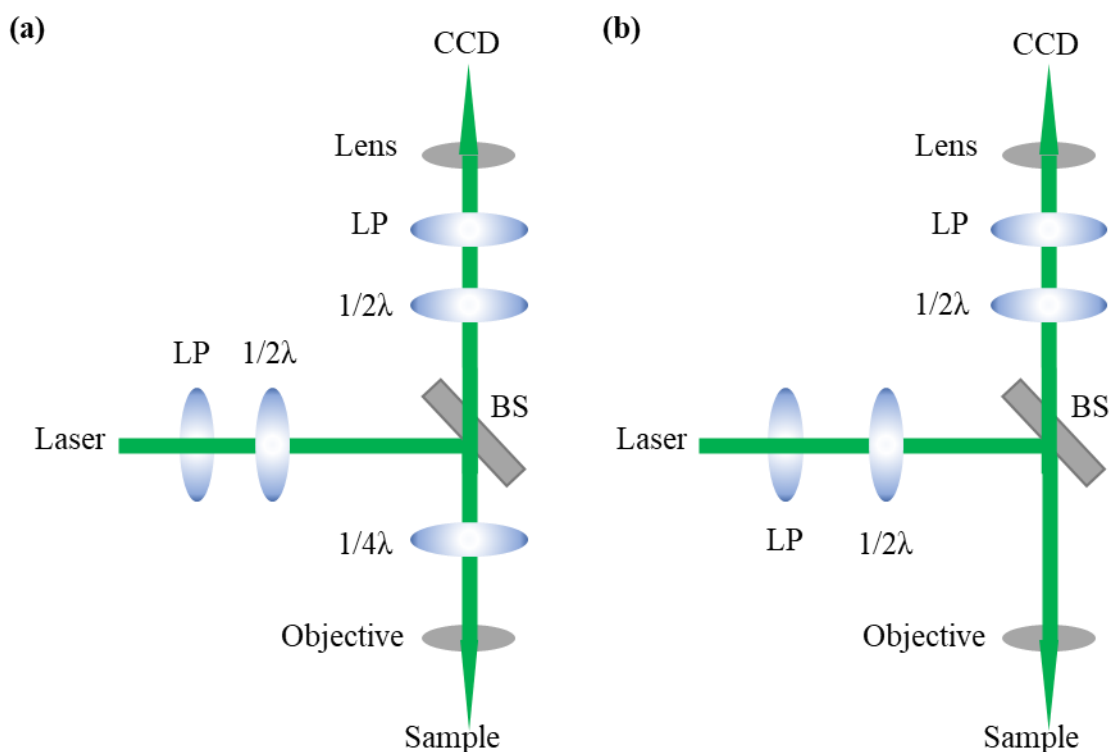
Fig 2.1.6 Schematic illustration of the (**a**) circularly and (**b**) linearly polarized optical measurements.

The sample was mounted in Janis ST-500 Microscopy Cryostat (**Fig 2.1.7**), which is monitored by a Lakeshore 335 temperature controller for temperature-dependent optical measurements. This measurement scheme was also applied to the Raman and PL spectroscopy in **Section 2.2** and **2.3** without specification.
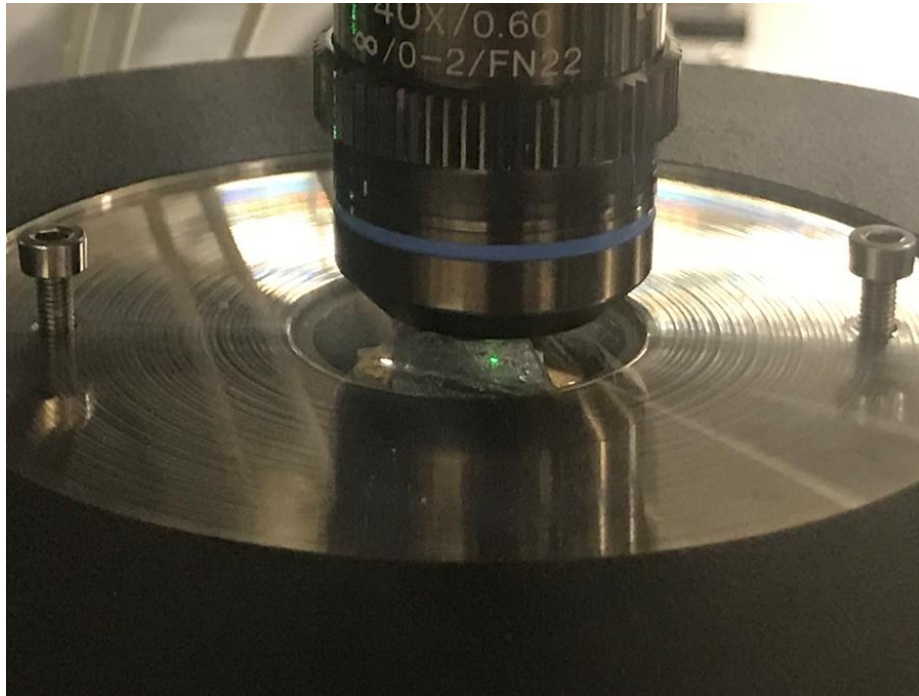
Fig 2.1.7 A photo of the sample mounted in Janis ST-500 Microscopy Cryostat.

2.1.4 Emerging Raman modes from 2D materials/SiO₂ heterostructures

We performed the unpolarized Raman spectroscopy measurements on representative samples of each class under the excitation photon energy of 2.33 eV and the excitation power of 500 μW at 77K. As shown in **Fig 2.1.8a**, two prominent Raman peaks were observed in all samples with the same Raman shifts at 1290 and 1540 cm^{-1}, respectively. The nature of the Raman modes was further confirmed by the observation of the same Raman shift under different excitation photon energy of 1.94 eV (**Fig 2.1.8b**). The Raman modes from various 2D material/SiO₂ heterostructures have the same peak positions, which suggests that the Raman emissions are determined by the intrinsic phonon properties of SiO₂.
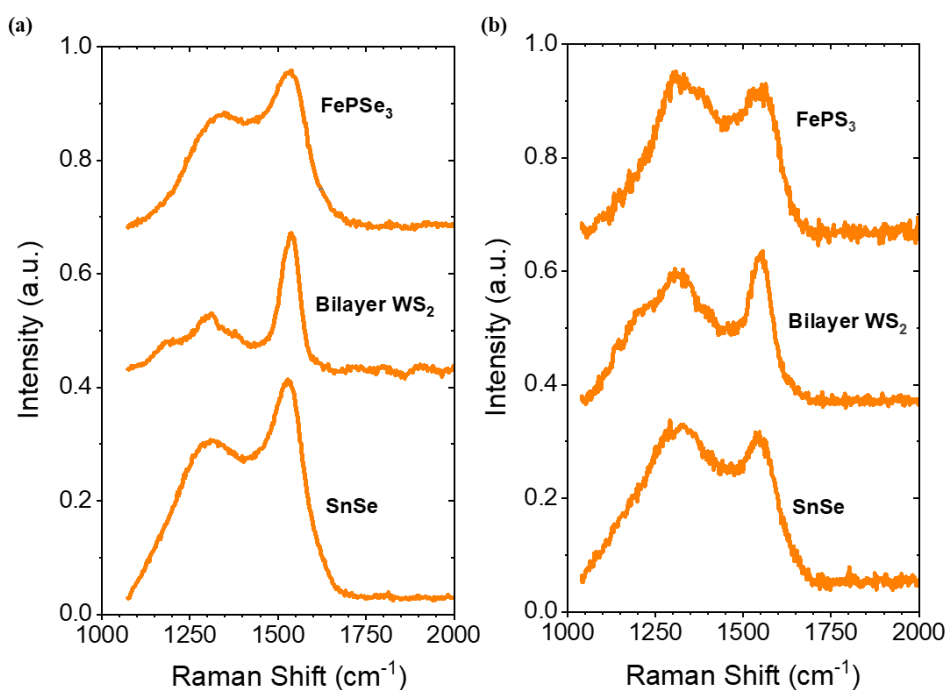
Fig 2.1.8 Unpolarized Raman spectra of strong-coupled 2D material/SiO_2 heterostructures with $FePS_3$, bilayer WS_2 and SnSe as the 2D materials in heterostructures under excitation photon energy of **(a)** 2.33 and **(b)** 1.94 eV, respectively. All panels: from ref. *(126).*
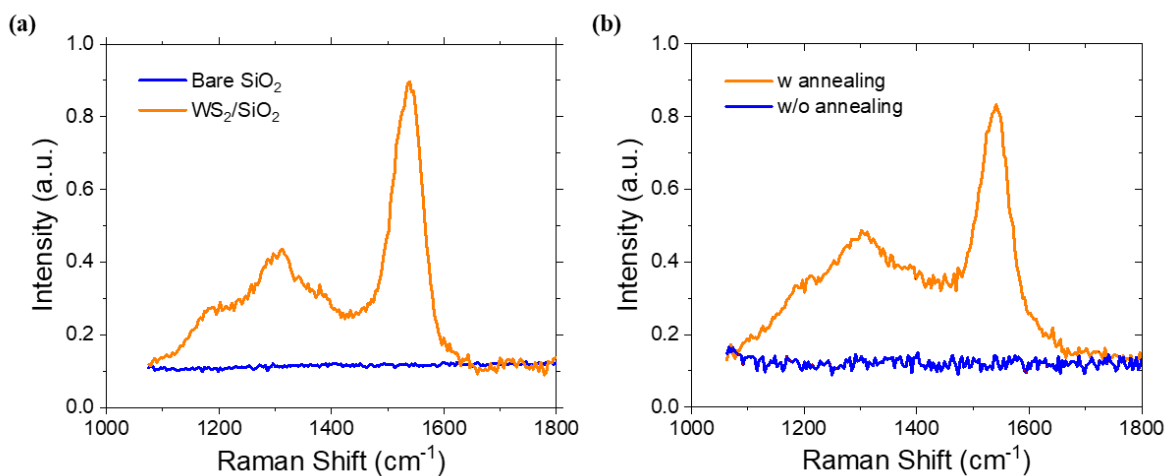
Fig 2.1.9 (a) Unpolarized Raman spectrum of isolated SiO_2/Si substrate and monolayer WS_2/SiO_2/Si heterostructure after annealing. **(b)** Unpolarized Raman spectrum of bilayer WS_2/SiO_2 heterostructure before and after thermal annealing process. All panels: from ref. *(126).*
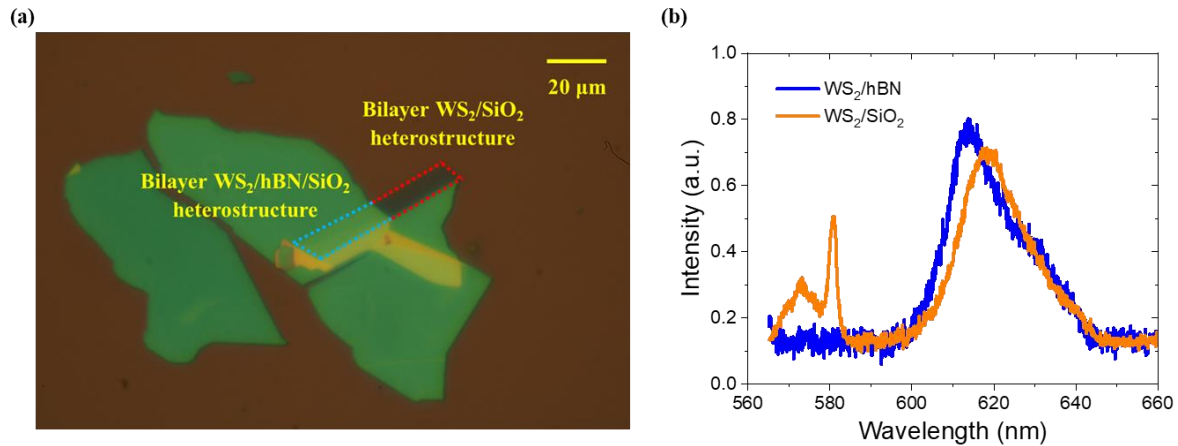
Fig 2.1.10 (a) Optical micrograph of monolayer WS_2/hBN/SiO_2 heterostructure. **(b)** Unpolarized emission spectra of bilayer WS_2/hBN/SiO_2 heterostructure and bilayer WS_2/SiO_2 heterostructure after 30 minutes annealing. All panels: from ref. *(126).*

The Raman spectra of isolated SiO_2 and 2D material/SiO_2 heterostructures without annealing process were then measured, as shown in **Fig 2.1.9a** and **Fig 2.1.9b** respectively. The emerging Raman modes vanished due to the absence of the 2D materials and the weak coupling strength at vdWs interface. These phenomena suggested that such Raman modes are optically silent in isolated SiO_2, while activated due to the presence of the strongly coupled 2D materials. This argument was further confirmed by performing Raman measurement on an annealed bilayer-WS_2/hBN/SiO_2 structure. The hBN flake was first exfoliated onto the SiO_2/Si substrate and the monolayer WS_2 was then transfer onto the hBN flake using the dry transfer approach. As shown in **Fig 2.1.10a**, the area of bilayer WS_2/hBN/SiO_2 heterostructure and bilayer WS_2/SiO_2 structure is respectively marked by blue and red. The Raman peaks completely vanished due to the minimal coupling between WS_2 and SiO_2 with the hBN separation layer, as shown in **Fig 2.1.10b**. The slightly different peak positions of PL from monolayer WS_2 can be attribute to different dielectric environment due to different substrates. Our complementary experiments discussed

26

above indicate that the Raman modes are intrinsic to the strongly coupled 2D material/SiO$_2$ heterostructures. They do not arise from the defects or other chemical bonds and organic impurities since they are robust and consistent for all strongly coupled heterostructures and vanish in all heterostructures with weak coupling between 2D materials and SiO$_2$.
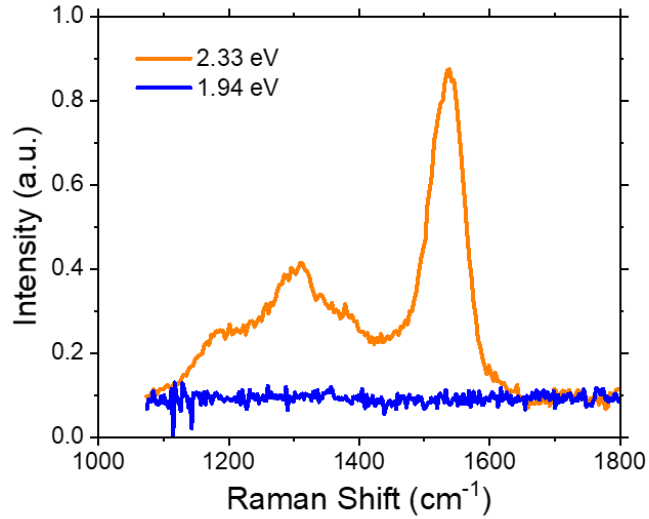
Fig 2.1.11 Unpolarized Raman spectra of monolayer WS$_2$/SiO$_2$ heterostructure under excitation photon energy of 2.33 eV and 1.94 eV. All panels: from ref. *(126)*.

To explore the role of electronic transitions in 2D materials in activating Raman-silent phonon modes, we further performed Raman measurements in monolayer-WS$_2$/SiO$_2$ heterostructure with excitation photon energies of 1.94 eV and 2.33 eV, respectively. The excitation power was 500 μW for both excitation photon energies. The Raman modes were only observed with 2.33 eV excitation, which is larger than the bandgap of monolayer-WS$_2$ (~2.05 eV) (*141, 142*), while completely vanished with 1.94 eV excitation, as shown in **Fig 2.1.11**. This observation demonstrates that the electronic transition in such 2D materials/SiO$_2$ heterostructures is essential for activating Raman-silent phonon modes in SiO$_2$. Our Raman measurement on the annealed

bilayer-WS$_2$/hBN/SiO$_2$ structure discussed above also provides strong evidence for the significance of the electronic transitions. The hBN is an insulator with a bandgap of approximately 6 eV, significantly larger than the excitation photon energy of around 2 eV. Therefore, these is no photoexcited electronic transitions in hBN, leading to the vanishing Raman emissions from the hBN/SiO$_2$ heterostructure.
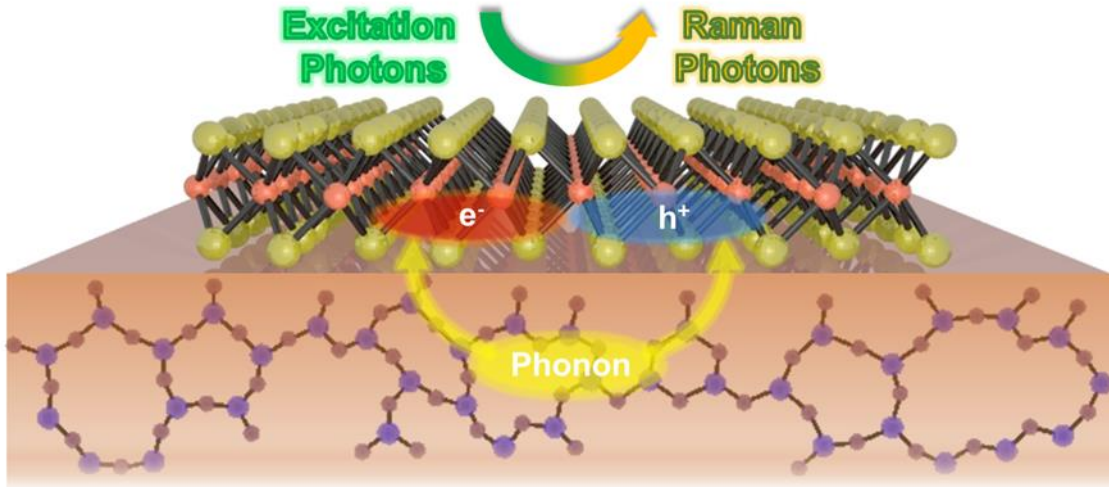
Fig 2.1.12 Schematic of electron-phonon interaction and activation of optically-silent Raman modes in the 2D material/SiO$_2$ heterostructures. All panels: from ref. *(126)*.

Due to the strong electron-phonon interaction between SiO$_2$ and the 2D materials, the phonon modes in SiO$_2$ can couple with the excited electrons in 2D materials, resulting in the Raman emissions, as illustrated in **Fig 2.1.12**. In contrast, for 2D material/SiO$_2$ heterostructures without annealing, the lattice vibration from SiO$_2$ cannot couple with transition electrons in 2D materials efficiently due to the weak coupling strength at vdWs interface. Hence, the electronic Raman scattering process cannot occur, leading to the vanished Raman modes.
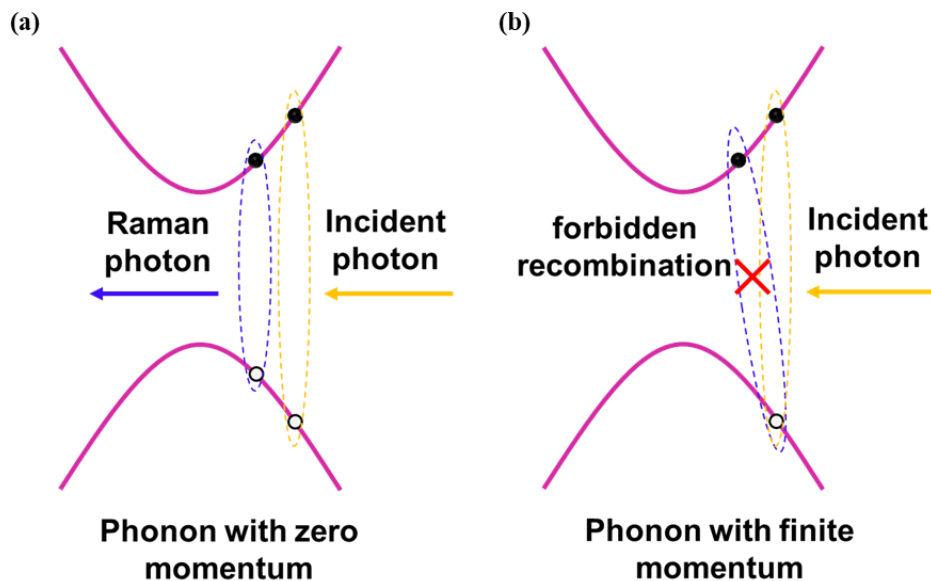
Fig 2.1.13 Schematic of **(a)** allowed and **(b)** forbidden pathways for recombination of phonon coupled electron-hole pair. All panels: from ref. *(126)*.

The energies of the two Raman modes do not match previous theoretical calculations and infrared absorption measurements of individual phonon modes in amorphous SiO_2. However, they do match the phonon energies of a two-phonon scattering process in combination of the rocking (R) mode (446 cm^{-1} ~ 505 cm^{-1}), the symmetric stretching (SS) mode (810 cm^{-1} ~ 819 cm^{-1}) and the asymmetric stretching (AS) modes (1063 cm^{-1}) *(143, 144)*. Our measurements indicate that the two-phonon scattering process is much more prominent than single-phonon scattering process. Here we provide an explanation for two-phonon scattering dominated electronic Raman scattering from the perspective of momentum conservation. The emission of the Raman photons arises from the recombination of the phonon-coupled electron-hole pairs. Therefore, the net momentum of the phonons coupled with the electron-hole pair must be zero, due to the requirement of the momentum conservation. **Fig 2.1.13**. exhibits the schematic of **(a)** allowed and **(b)** forbidden pathways for recombination of phonon coupled electron-hole pair. In

Fig 2.1.13a, the momentum of the phonons that coupled with the excited electron-hole pair is zero ($k_{phonon}=0$). Since the required momentum match is satisfied, the recombination of the phonon coupled electron-hole pair is allowed, leading to the emission of the Raman photons. In **Fig 2.1.13b**, the phonons that coupled with the excited electron-hole pair have finite momentum ($k_{phonon} \neq 0$), leading to the momentum mismatch of the scattered electron-hole pair. In that case, the recombination of such phonon coupled electron-hole pair is forbidden. Therefore, only phonons with zero momentum can become Raman active through the electron-phonon coupling, while the phonons with finite momentum cannot contribute to Raman emissions we observed. In single-phonon scattering process, only phonons with zero momentum ($k=0$) can be involved, whose population is very limited. In contrast, for two-phonon scattering process, not only the phonons with zero momentum ($k_1=0, k_2=0$) can participate in the Raman emission, but the two phonons with opposite momentum ($k_1+k_2=0$). Here k_1 and k_2 are defined as the momentum of the two phonons, respectively. Therefore, most likely two-phonon scattering process dominates the electronic Raman scattering in this work. This phenomenon has been reported previously in hBN/WSe$_2$/hBN heterostructures where the optically silent A$_{2u}$ mode of hBN is activated through electron-phonon coupling with electron transition in WSe$_2$ (*81, 82*). The amplitude of the second-order Raman mode arising from the two-phonon scattering process (A$_{2u}$ mode in hBN combined with A$_1$ mode in WSe$_2$) can be one-order of magnitude stronger than that of the A$_{2u}$ Raman mode in hBN. This result supports our observations here while the detailed mechanism involved still remains an interesting topic for future investigation. Moreover, the shape of the Raman peaks varies for different classes of 2D materials/SiO$_2$ heterostructures while the two main peak positions remain unchanged, as shown in **Fig 2.1.8**. The electronic Raman scattering strongly depends on the electronic band structures of the 2D materials, which limits the phonon

modes in SiO_2 that can be involved in the electronic Raman scattering due to the requirements of energy and momentum conservation. Therefore, for different 2D materials/SiO_2 heterostructures, phonons that can participate in the electronic Raman scattering can be slightly different, leading to different peak shapes in the Raman spectra.

2.1.5 The chirality and anisotropy of the Raman modes

Since the phonons in SiO_2 strongly couple with electronic transitions in 2D materials, the band properties, determined by the lattice structure of the 2D materials can significantly influence the geometry (chirality and anisotropy) of the emerging Raman modes. We performed polarization-resolved Raman measurements on heterostructures with 2D materials of different lattice structure to investigate the corresponding geometry of the Raman modes.

The helicity-resolved Raman measurement was first performed to investigate the chiral properties of the Raman modes. The engineered heterostructures with 2D materials of different crystalline symmetries were excited with right circularly polarized (σ+) photons with photon energy of 2.33 eV at 77K. We used the same measurement scheme for helicity-resolved Raman measurements discussed below if there is no specific notification. Both left (σ-) and right (σ+) circularly polarized components of the Raman emission were collected, respectively. In honeycomb TMDs/SiO_2 heterostructures the dominant helicity of the Raman emission was opposite to that of the incident photons. As shown in **Fig 2.1.14a**, under the σ+ excitation, the σ-component of the Raman emission exhibits stronger intensity than the σ+ component. This phenomenon is opposite to the valley effect in TMDs where the helicity of PL follows that of

31

incident photons (*64, 66, 145*). Here, we define the degree of polarization for Raman modes as (*146*)

$$P = \left| \frac{I_+ - I_-}{I_+ + I_-} \right| \tag{1}$$

where I_+ and I_- represent the peak intensity of the σ+ and σ- component of Raman scattering signal, respectively. The polarization degree was calculated to be 23% and 22% at monolayer-WS_2/SiO_2 and bilayer-WS_2/SiO_2 heterostructures, respectively. For honeycomb MPTs with predicted spin-valley degree of freedom (*147*), similar chiral Raman emissions were observed in corresponding MPTs/SiO_2 heterostructures (**Fig 2.1.14b**). The *P* was calculated to be 24% and 19% in $MnPSe_3$/SiO_2 and $FePS_3$/SiO_2, respectively. In contrast, for BP and SnSe with orthorhombic lattice, the chirality of the Raman emissions completely vanished (**Fig 2.1.14c**).
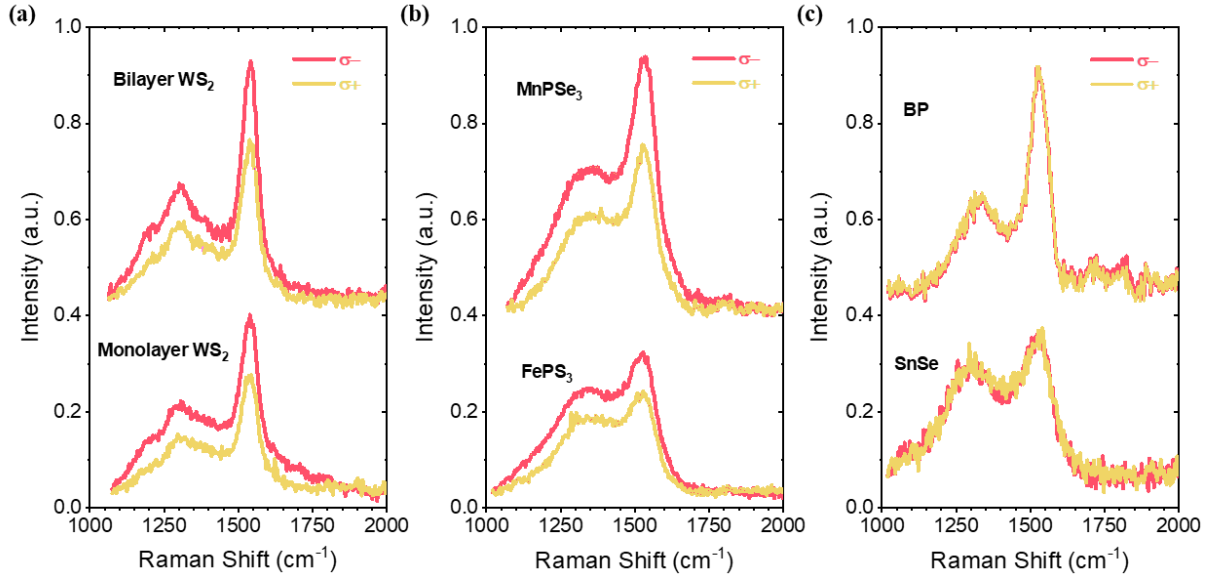
Fig 2.1.14 Helicity-resolved Raman spectra of strong-coupled **(a)** monolayer WS_2/SiO_2 and bilayer WS_2/SiO_2 heterostructures, **(b)** $FePS_3$/SiO_2 and $MnPSe_3$/SiO_2 heterostructures, and **(c)** SnSe/SiO_2 and BP/SiO_2 heterostructures under σ+ excitation with photon energy of 2.33 eV. All panels: from ref. (*126*).
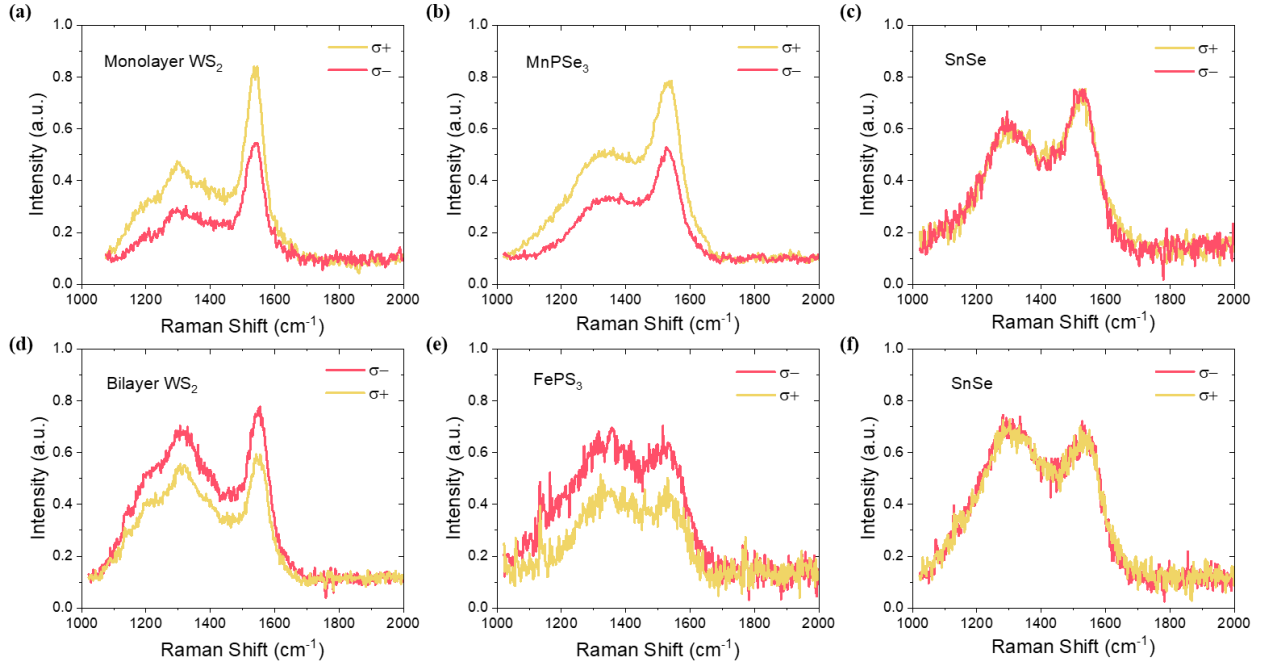
Fig 2.1.15 Upper panel: Helicity-resolved Raman spectra of 2D material/SiO$_2$ heterostructures with **(a)** monolayer WS$_2$, **(b)** MnPSe$_3$ and **(c)** SnSe as the 2D materials under left-circularly polarized (σ-) excitation. **Lower Panel:** Helicity-resolved Raman spectra of 2D material/SiO$_2$ heterostructures with **(d)** bilayer WS$_2$, **(e)** FePS$_3$ and **(f)** SnSe as the 2D materials under excitation photon energy of 1.94 eV. All panels: from ref. *(126)*.

To confirm our observation, we repeated the helicity-resolved Raman measurement on these three types of heterostructures under both σ- excitation and excitation photon energy of 1.94 eV. In both cases, the chirality of Raman emissions was only observed in honeycomb material/SiO$_2$ heterostructures, as shown in **Fig 2.1.15 a-c and d-f** respectively. Our observations indicate that the chirality of the Raman mode is dominated by the lattice structure of 2D materials.

The anisotropy of the emerging Raman modes was investigated in materials system with reduced lattice symmetry. As materials with non-honeycomb orthorhombic lattice structure, BP and SnSe exhibit highly anisotropic optical and electronic properties *(77, 148, 149)*, which are distinctly

33

different from TMDs and MPTs. To further explore the correlations between Raman modes and electronic transitions, we performed the linearly polarized Raman measurements. The BP/SiO$_2$ and SnSe/SiO$_2$ heterostructures were excited with linearly polarized laser along either x-(armchair) or y-(zigzag) direction and both x- and y-polarized components of the Raman emissions were detected, respectively.
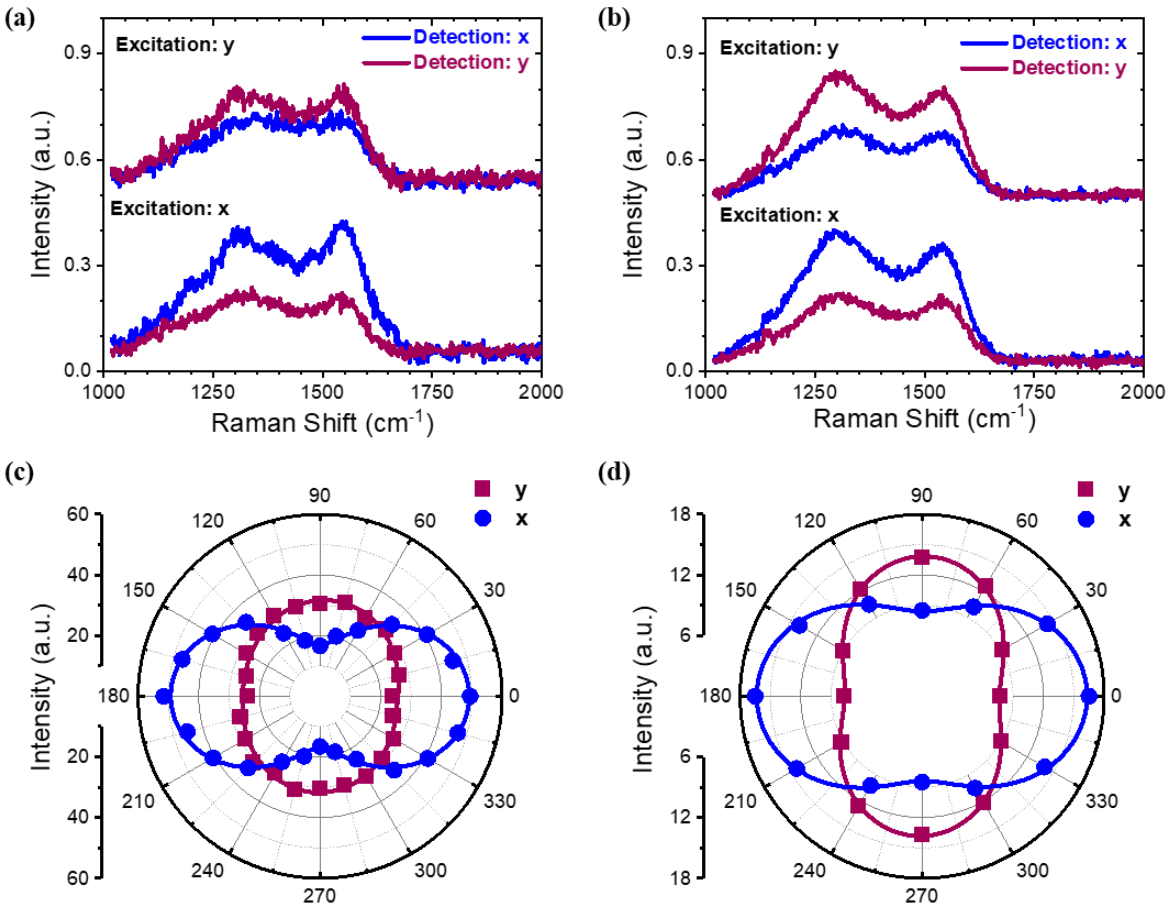
Fig 2.1.16 Upper Panel: The linearly polarized Raman spectra of strong-coupled **(a)** BP/SiO$_2$ and **(b)** SnSe/SiO$_2$ heterostructures under x-polarized and y-polarized excitation. **Lower Panel:** The angular resolved Raman intensity of strong-coupled **(c)** BP/SiO$_2$ and **(d)** SnSe/SiO$_2$ heterostructures under x-polarized and y-polarized excitations. All panels: from ref. *(126)*.

Fig 2.1.16a and b show the linearly polarized Raman spectra at the BP/SiO$_2$ and SnSe/SiO$_2$ heterostructure under both x-polarized and y-polarized excitation, respectively. Generally, the polarization of Raman modes followed the excitation polarization. Under the x- (y-) polarized excitation, the x- (y-) polarized component of the Raman emission was more prominent. However, if we calculated the polarization degree of Raman modes under different excitation polarization, the in-plane anisotropy exhibited quite different characteristics from these two heterostructures. For BP/SiO$_2$ heterostructure, the polarization degree reached 44% with x-polarized excitation while it dropped to 16% under y-polarized excitation. In comparison, the polarization degree of Raman modes for SnSe/SiO$_2$ heterostructure was calculated to be 31% and 29% under x- and y-polarized excitation, respectively. We further performed the angular-resolved Raman measurement for both heterostructures, where the extracted Raman intensity were plotted in **Fig 2.1.16c, d**. The Raman modes of SnSe/SiO$_2$ heterostructure show almost the same emission anisotropy with different excitation polarizations. In contrast, at BP/SiO$_2$ heterostructure, much higher anisotropic emission was observed with x-polarized excitation.

The difference in BP and SnSe is due to the optical selection rules for electronic transitions. For BP, the interband optical transition is significantly more preferable along the x-direction than along the y-direction at high excitation photon energy due to the single valley at the Γ point in electronic band structure, as illustrated in **Fig 2.1.17a** (*31, 49, 52, 74*). In that case, the excited electron-hole pairs will be strongly confined in Γ valley under x-polarized excitation. Therefore, the recombination of the phonon-coupled electron-hole pair in Γ valley will dominate the emission of the Raman photons, which leads to highly x-polarized Raman emissions. On the contrary, the excited electron-hole pair will be significantly less confined with y-polarized excitation due to the lack of the flat band structure along Γ-Y direction in the momentum space.

The excited electron-hole pairs can be easily relaxed to other points of the momentum space, where the emission of Raman photons arising from the recombination of the phonon-coupled electron-hole pair is significantly depolarized. Therefore, the in-plane anisotropy of Raman emissions is much smaller when excitation laser is polarized along y-direction. In contrast, the electronic band structure of SnSe has two nearly degenerate valleys along both Γ-X and Γ-Y directions, and the optical interband transition can occur under both x- and y-polarized excitations, as illustrated in **Fig 2.1.17b** (*128, 150, 151*). Hence, the anisotropy of the Raman emissions is expected to be similar under x- and y-polarized excitations, consistent with our experimental observations. Our observations suggest that the geometry of the Raman modes is strongly correlated to the band structure and the corresponding optical selectivity of the electronic transitions in 2D materials.
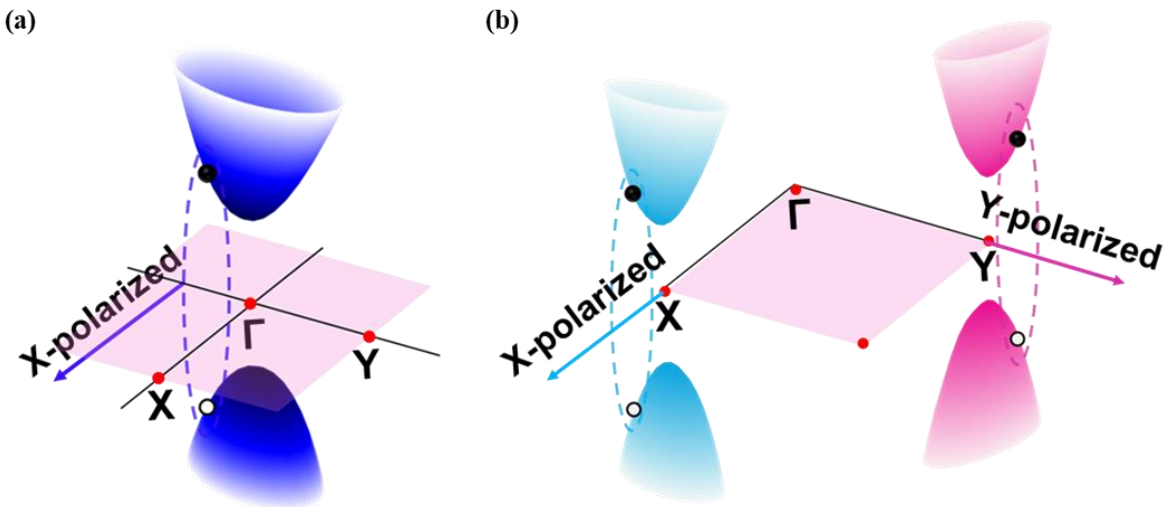
Fig 2.1.17 Schematic illustration of band structure and corresponding optical selection rule in **(a)** BP and **(b)** SnSe. All panels: from ref. *(126).*

2.1.6 Phonon-assisted intervalley scattering process
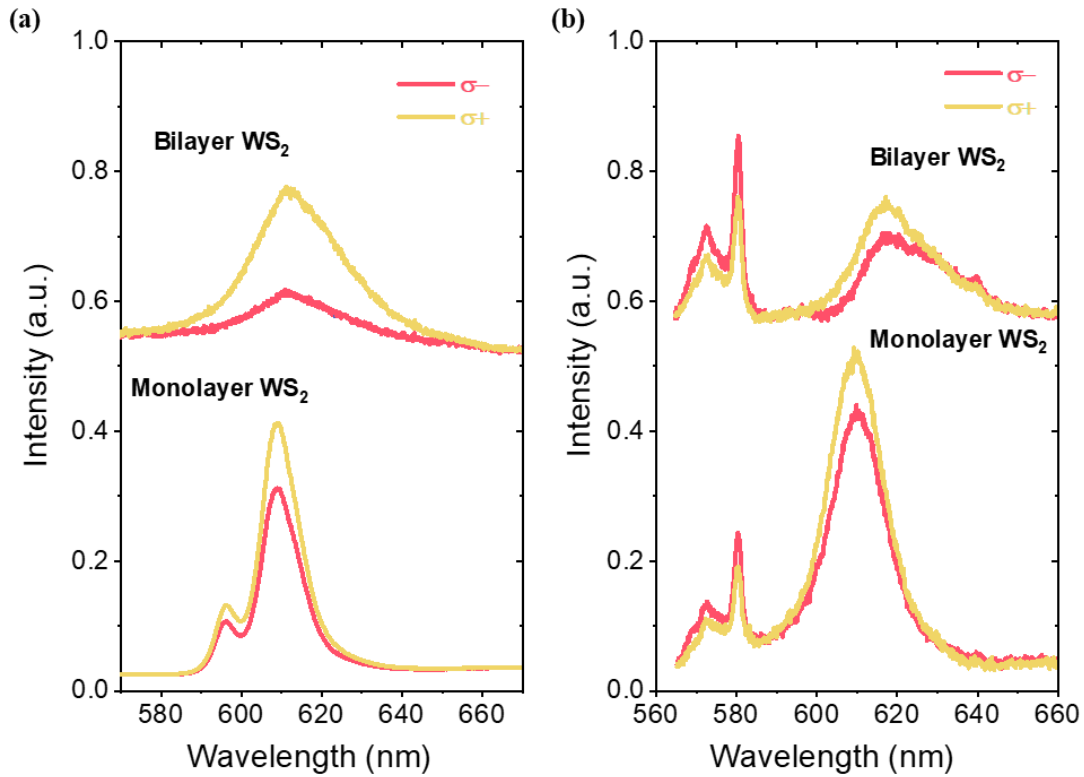
Fig 2.1.18 The helicity-resolved emission spectra from monolayer WS_2/SiO_2 and bilayer WS_2/SiO_2 heterostructures **(a)** before and **(b)** after 30 min annealing process under σ+ excitation with photon energy of 2.33 eV. All panels: from ref. *(126)*.

To further investigate the coupling between the photoexcited electron-hole pairs in 2D materials and the phonons in amorphous SiO_2, we focused on TMDs/SiO_2 heterostructures where the PL emissions from intrinsic TMDs and Raman emissions from the electron-phonon coupling can be measured spontaneously. Monolayer- and bilayer- WS_2 were exfoliated onto SiO_2 directly and the helicity-resolved PL measurements were performed. The well-known optical valley effect was observed in both monolayer and bilayer WS_2, with polarization degree of 15% and 56% respectively (**Fig 2.1.18a**), consistent with previous study (*66*). As discussed before, there was no

signature of Raman signals at 1290 and 1540 cm^{-1} due to the weak coupling between SiO_2 and WS_2 before annealing. After annealing the samples at 500 $^{\circ}$C in argon for 30 minutes, the typical helicity-resolved emission spectra of monolayer and bilayer WS_2/SiO_2 stacking structures were observed as shown in **Fig 2.1.18b**. In both samples, the Raman modes emerged at 1290 and 1540 cm^{-1} and they exhibited opposite helicity compared with the PL signals, in which the valley polarization was preserved and significantly suppressed.
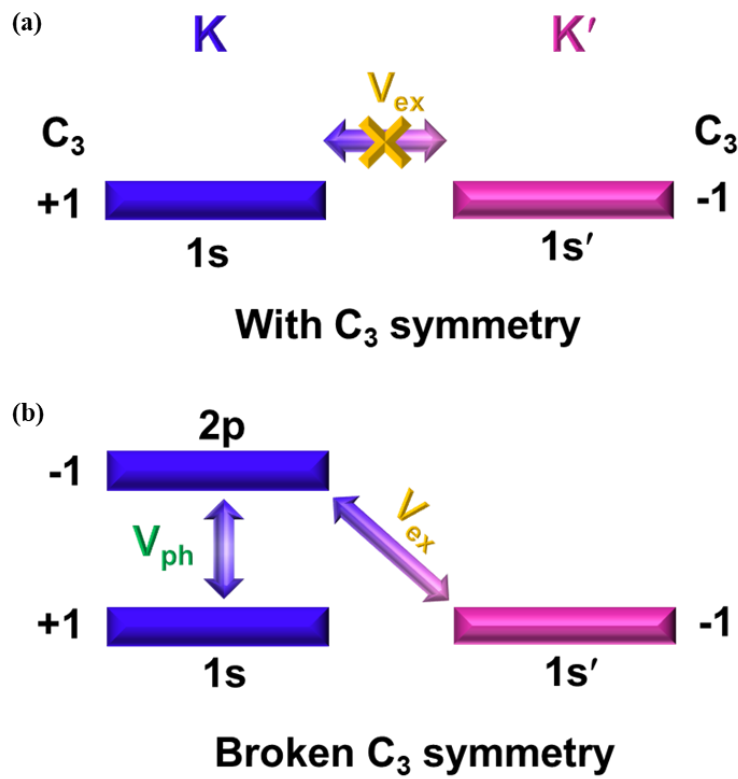
Fig 2.1.19 **(a)** The schematic illustration of the forbidden excitonic intervalley scattering under electron-hole exchange interaction with preserved C_3 symmetry. **(b)** A possible configuration for Phonon-assisted excitonic intervalley scattering process due to electron-hole exchange interaction under broken C_3 symmetry. All panels: from ref. *(126)*.

This phenomenon indicates that the phonons in SiO_2 can contribute to the intervalley scattering process in 2D honeycomb lattice. Typically, in 2D materials with honeycomb lattice, such as

TMDs and MPTs, the high symmetry points K(K′) is invariant under C_3 operation, which is referred as C_3 symmetry (*61*). With preserved C_3 symmetry, the electron-hole exchange interaction can only couple two exciton states with the same C_3 quantum number of either +1 or -1 (*152*). Since the two ground states of excitons (1s and 1s') corresponding to K and K' valleys acquire opposite C_3 quantum number of +1 for 1s state and -1 for 1s' state, the electron-hole exchange interaction cannot couple these two exciton states. Therefore, the intrinsic C_3 quantum number preserves the valley polarization and the excitonic intervalley scattering process caused by electron-hole exchange interaction is forbidden, as illustrated in **Fig 2.1.19a** (*153*). Meanwhile, the excitonic valley scattering at finite momentum can only quench the valley polarization, while the reversed polarization must arise from the scattering process that flips the valley polarization. Due to strong coupling between SiO_2 and 2D materials, the in-plane electric field induced by phonon modes in amorphous SiO_2 can break the C_3 symmetry in TMDs and MPTs. Under broken C_3 symmetry, the excitonic intervalley scattering due to the strong electron-hole exchange interaction is allowed (*65, 153, 154*). We provide a possible configuration for phonon-assisted excitonic intervalley scattering process, which can flip the valley index of excitons and reverse its helicity, as illustrated in **Fig 2.1.19b**. The in-plane electric field from the phonons can couple the ground state and the excited state with opposite C_3 quantum number in the same valley, *e.g.,* the 1s state with C_3 quantum number of +1 and 2p state with C_3 quantum number of -1 in K valley. Meanwhile, the in-plane electric field induced by phonons can lead to a finite value of the short-range term of electron-hole exchange interaction at zero momentum. The electron-hole exchange interaction can couple the excited 2p state of the excitons to the ground 1s' state with the same C_3 quantum number of -1. Therefore, the excitonic intervalley scattering process can be induced by in-plane electric field arising from phonons

39

together with the Coulomb interaction arising from the electron-hole exchange interaction. The entire photoexcited electronic transition and electronic Raman emission process can be described as follows. The incident σ+ (σ-) photon can excite an exciton in K (K′) valley, which is subsequently scattered to K′ (K) valley assisted by phonons in SiO_2 due to electron-hole exchange interaction, followed by the emission of an σ- (σ+) photon, leading to the reversed helicity of the Raman photons as shown in **Fig 2.1.20**. In the figure, V_{ex} represents the Coulomb interaction from electron-hole exchange interaction while V_{ph} denotes the in-plane electric field induced by phonons. On the contrary, BP and SnSe with orthorhombic lattice lack such valley degeneracies in their electronic band structures (*49, 52, 137, 138*). Therefore, the chirality of the Raman emissions in BP/SiO_2 and SnSe/SiO_2 heterostructures cannot be observed.
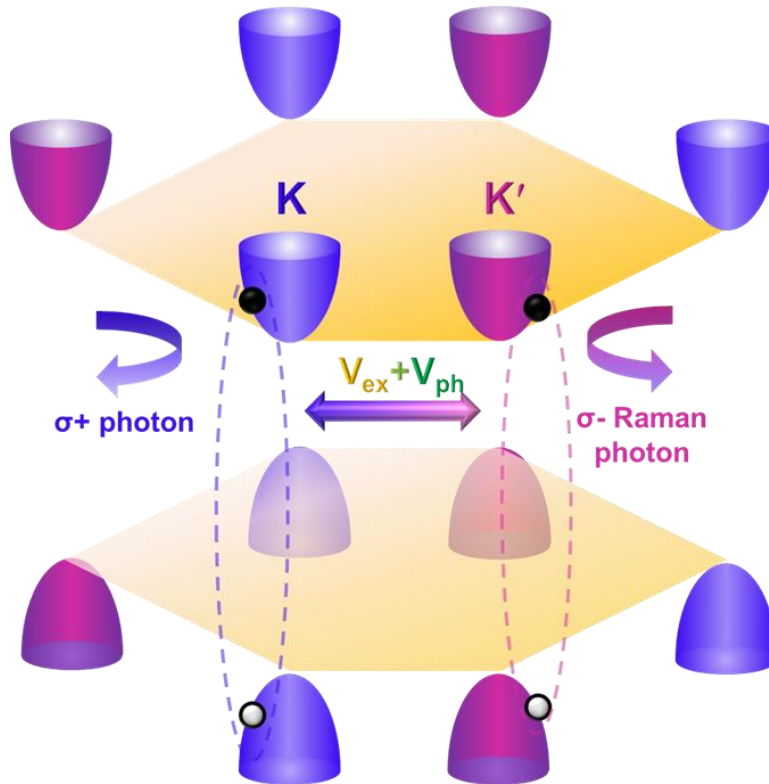
Fig 2.1.20 Schematic of optical transition process for phonon-assisted excitonic intervalley scattering and the reversed helicity of Raman photons under broken C_3 symmetry. All panels: from ref. *(126)*.

40
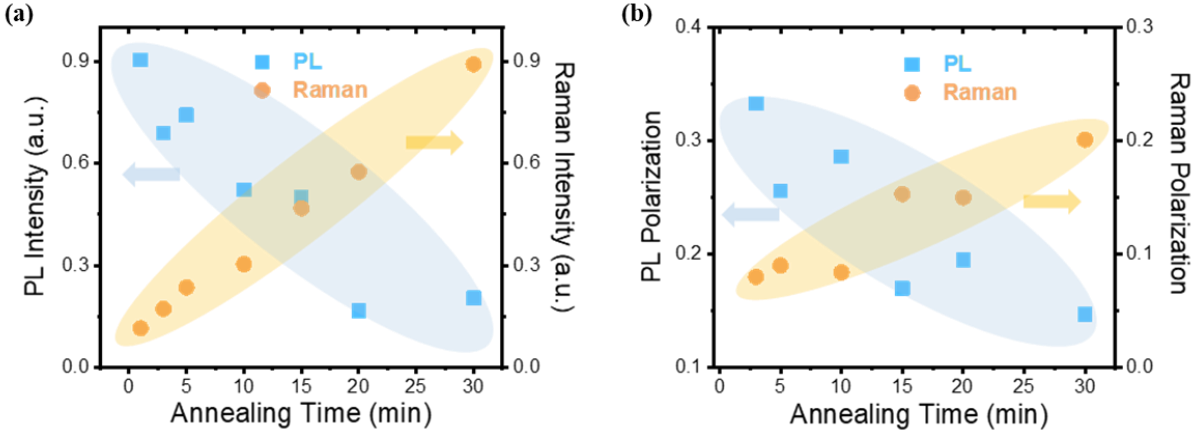
Fig 2.1.21 The **(a)** intensity and **(b)** polarization degree of the Raman modes and the PL in bilayer WS$_2$/SiO$_2$ heterostructures versus the annealing time. All panels: from ref. *(126)*.

By controlling the annealing time, we further tuned the coupling strength between 2D materials and SiO$_2$. As shown in **Fig 2.1.21a**, the intensity of Raman emissions increased monotonically with the annealing time, in contrast to the suppression of the PL intensity, indicating an enhancement of coupling strength in bilayer-WS$_2$/SiO$_2$ heterostructure. Fig **2.1.21b** further shows the polarization degree for both Raman modes and PL as a function of the annealing time. The polarization degree for Raman modes increased with increasing annealing time, opposite to that of PL. This strong correlation indicates that with stronger coupling strength, the in-plane electric field arising from lattice vibration in amorphous SiO$_2$ can break the C$_3$ symmetry of bilayer WS$_2$ more efficiently. Therefore, the phonon-assisted excitonic intervalley scattering can significantly facilitate the valley depolarization and flip the polarization of incident photons, leading to the decreasing (increasing) polarization degree of PL (Raman). To further confirm our observation, we repeated the experiment in monolayer-WS$_2$/SiO$_2$ heterostructures, where similar evolution trend of polarization degree for PL and Raman modes was observed (**Fig 2.1.22**).
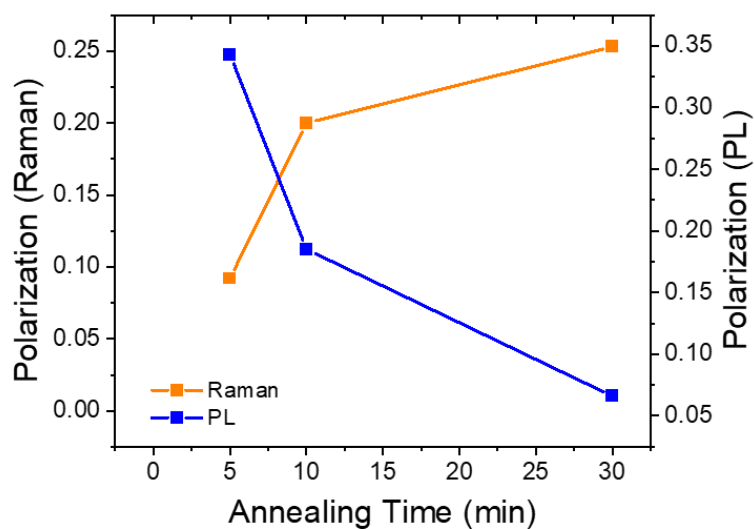
Fig 2.1.22 The polarization degree of Raman modes and PL in monolayer WS_2/SiO_2 heterostructure versus the annealing time. All panels: from ref. *(126)*.
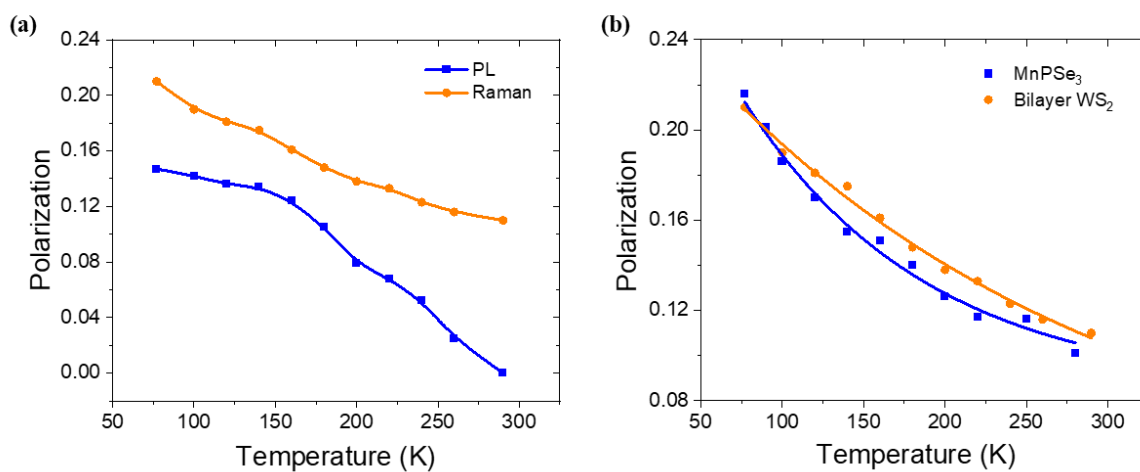
Fig 2.1.23 (a) The temperature dependence of the polarization degree of both Raman modes and PL in bilayer WS_2/SiO_2 heterostructure. **(b)** The temperature dependence of polarization degree of Raman modes in $MnPSe_3/SiO_2$ heterostructures compared with bilayer WS_2/SiO_2 heterostructures. All panels: from ref. *(126)*.

In addition, we measured the temperature dependence of the polarization degree for both Raman modes and PL, as exhibited in **Fig 2.1.23a**. In both cases, the polarization degree decreased with increasing temperature, indicating an enhanced role of acoustic phonons of 2D materials in intervalley scattering at higher temperature (*145*). Therefore, the excitonic intervalley scattering assisted by phonon modes in SiO_2 will be suppressed. The temperature dependence of the polarization degree for Raman modes was also measured in $MnPSe_3/SiO_2$ structures, which shows similar results with that in $TMDs/SiO_2$ structures (**Fig 2.1.23b**).

2.1.7 Discussion and summary

In conclusion, we report emerging Raman modes at strongly coupled vdWs heterostructures. We observe chiral Raman emissions at honeycomb-2D material/SiO_2 heterostructures and in-plane anisotropic Raman emissions at BP family/SiO_2 heterostructures. Through systematic Raman and PL measurements, we reveal that the originally Raman-silent phonon modes in SiO_2 can efficiently couple with the excited electrons in 2D materials and become Raman active. Due to efficient electron-phonon interactions, the Raman emissions from vdWs heterostructures can exhibit controlled symmetry, which inherits the band properties of the 2D materials. The chiral Raman response from honeycomb-2D material/SiO_2 heterostructures further provide strong experimental evidence for the phonon-assisted excitonic intervalley scattering process. Our study reveals the microscopic mechanism of electron-phonon coupling in heterostructures. Raman photons arise from the recombination of the substrate phonon-coupled electron-hole pair in 2D materials, and hence can reflect the intrinsic properties of electronic transitions. Our observations provide a new perspective of investigating the electronic band properties and optical selectivity in atomically thin materials, especially in materials whose photoluminescence is difficult to

measure. Our study also opens up new ways to manipulate electrons and phonons in vdWs heterostructures, which offers new opportunities for realizing phononic devices. One possible application is to realize the valley phonon Hall device (*155*) utilizing a device scheme similar to the exciton Hall effect (*156*). Under temperature or chemical potential gradients, the excited excitons in K and K' valley of TMDs will acquire a drift velocity opposite to the gradients. Under the circularly polarized excitation (*e.g.,* σ+ excitation), the excitons in K valley will be selected and diffuse, generating a spatial difference of the exciton intensity on the sample, which can be probed by 2D PL mapping (*156*). Since the phonons in SiO_2 can efficiently couple with the excitons in K (K') valley of the TMDs, the phonons in SiO_2 can diffuse with the selected excitons in corresponding valleys of the TMDs and accumulate on one edge of the sample. As a result, the valley phonon hall effect can be detected by the 2D mapping of the Raman spectra.

2.2 Probing the interlayer interaction in 2D honeycomb lattice via chiral phonons

2.2.1 Motivation

As we demonstrated in Section 2.1, phonons in amorphous material can couple with electronic transitions and exhibit non-trivial chirality and anisotropy, therefore reflect the lattice geometry of the 2D materials. On the other hand, phonons in crystalline 2D materials can exhibit specific geometry as well, subjected to the crystal symmetry of 2D materials. One distinguished example is that Raman modes in materials with reduced lattice symmetry such as BP (*157, 158*), Rhenium diselenide (ReSe$_2$) (*159, 160*), Zirconium Pentatelluride (ZrTe$_5$) (*161, 162*) and Group IV monochalcogenides (*148, 163-165*) exhibit strong in-plane anisotropy. Therefore, the polarization-resolved Raman measurements have been widely applied to determine the crystal orientation of these materials. On the contrary, the chirality of phonons in crystalline 2D materials was less investigated. Recently, a theoretical study showed that the phonons at high-symmetry points in monolayer honeycomb lattices can acquire a quantized pseudoangular momentum (PAM) (*155*). Therefore, the corresponding Raman modes can exhibit unique chirality, which has been experimentally demonstrated in monolayer TMDCs (*166-168*).

However, the chiral property of phonons in 2D honeycomb lattice with increasing layer numbers remains unexplored. Due to the presence of the van der Waals (vdWs) interlayer interaction, the layered materials can exhibit distinct physics properties from their monolayer counterpart (*9, 14, 169, 170*). For example, the band structure of the MoS$_2$ experiences a direct-to-indirect bandgap transition from monolayer MoS$_2$ to its multilayer counterpart due to the interlayer interaction (*32, 171*). Moreover, the bandgap of BP can be tuned from around 2.0 eV in monolayer BP to 0.3 eV in its bulk limit (*31, 50*), leading to PL emission from visible to mid-infrared (*49, 77, 129*).

45

Therefore, it is also intriguing to investigate the influence of the interlayer interaction on the lattice symmetry.

Meanwhile, the strength of the interlayer interaction can be estimated by theoretical calculations utilizing the density functional theory (DFT) (*172*), which has been demonstrated in many layered materials, e.g., graphene (*173, 174*), TMDs (*175, 176*) and hBN (*177*). Experimentally the direct probe of interlayer interaction has been demonstrated through the low-frequency Raman spectroscopy (*178-180*). Quantum capacitance measurements has also been applied to investigate the interlayer coupling strength, which is limited to few-layer graphene (*181, 182*). Therefore, it is desirable to develop other complementary approaches to experimentally characterize the strength of interlayer interactions. And the evolution of the phonon chirality against the layer number can provide a new perspective for probing the interlayer interaction in 2D honeycomb lattice.

2.2.2 Preparation of 2D honeycomb lattice with different layers

Graphene flakes with different layer numbers were directly deposited onto 90 nm SiO_2/Si substrate using the mechanical exfoliation method. **Fig. 2.2.1a** shows the optical micrograph of graphene flakes used for Raman spectrum measurements. The layer numbers of the monolayer and few-layer graphene were first identified by the optical contrast (*183, 184*). The optical contrast shows a monochromatically linear increase with layer numbers, as shown in **Fig 2.2.1b**. The unpolarized Raman spectra further confirmed the layer numbers (**Fig 2.2.1c**), which agreed with previous Raman studies well (*185, 186*). To investigate the Raman D mode arising from the defects which was absent in the pristine graphene, we introduced defects into monolayer

graphene through oxygen plasma etching. The defects in graphene was introduced through gentle oxygen plasma (plasma power: 10W, oxygen flow: 10 sccm, duration: 1s). The unpolarized Raman spectrum of the etched monolayer graphene exhibits prominent Raman D mode emission (**Fig 2.2.1d**), which is absent in pristine graphene (*187, 188*).
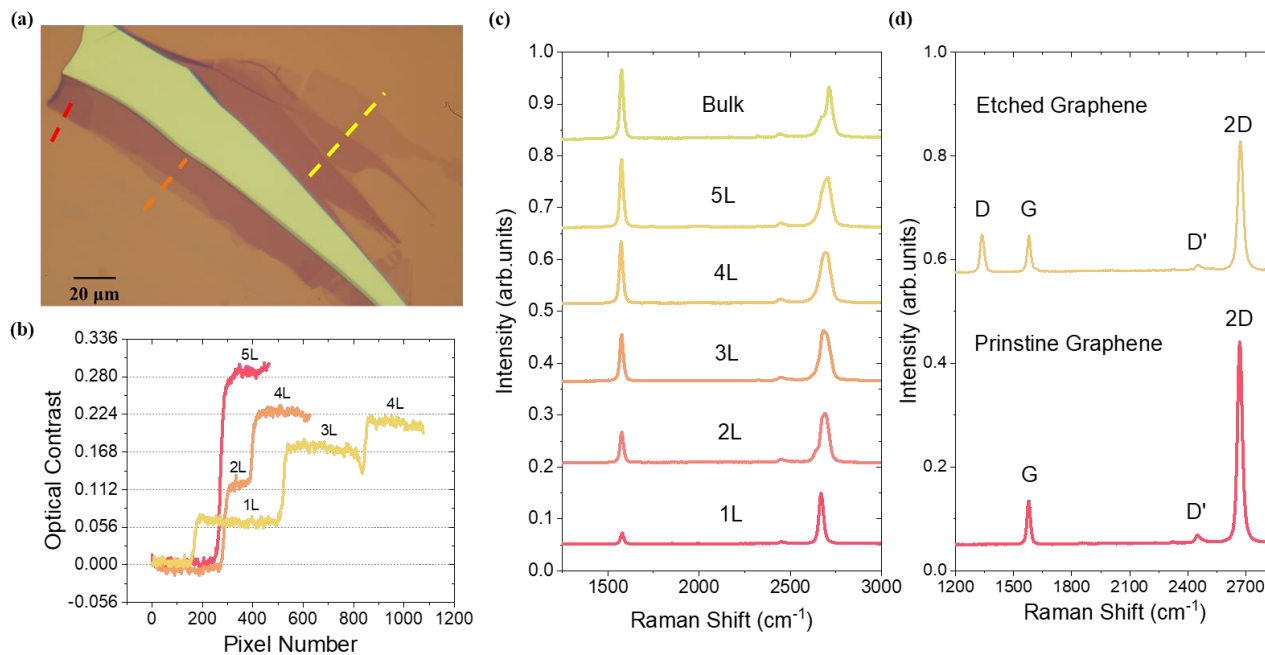
Fig 2.2.1 (a) Optical micrograph of graphene flakes. **(b)** Optical contrast of graphene flakes measured along the lines in (a). **(c)** Unpolarized Raman spectra of few-layer (1L to 5L) and thin-film (>100L) graphite. **(d)** Unpolarized Raman spectra of etched monolayer graphene and pristine monolayer graphene. All panels: from ref. *(127)*.

We also prepared monolayer and bulk hBN flakes. Monolayer hBN on SiO_2/Si substrate was transferred from hBN on copper grown by chemical vapor deposition (CVD). Large area CVD monolayer hBN on copper (2x2 inches) was purchased from HQ graphene. Firstly, a 400 nm-thick polymethyl methacrylate (PMMA) layer was spin-coated onto the hBN/copper surface. Secondly, the PMMA/hBN/copper was floated on the Iron chloride ($FeCl_3$) solvent with copper

layer downside for 30 mins to etch off the copper substrate. Then the PMMA/hBN layer was washed with DI water and was picked up by the 90 nm SiO$_2$/Si substrate. Finally, the PMMA layer was washed out by acetone. We also prepared thin-film hBN (> 100L) by mechanical exfoliation from bulk crystal. **Fig 2.2.2** shows the unpolarized Raman E$_{2g}$ mode measurements. The Raman E$_{2g}$ mode peaks at 1368.5 cm^{-1} and 1366 cm^{-1} for monolayer and bulk hBN, respectively, consistent with previous reports (*37, 189*).
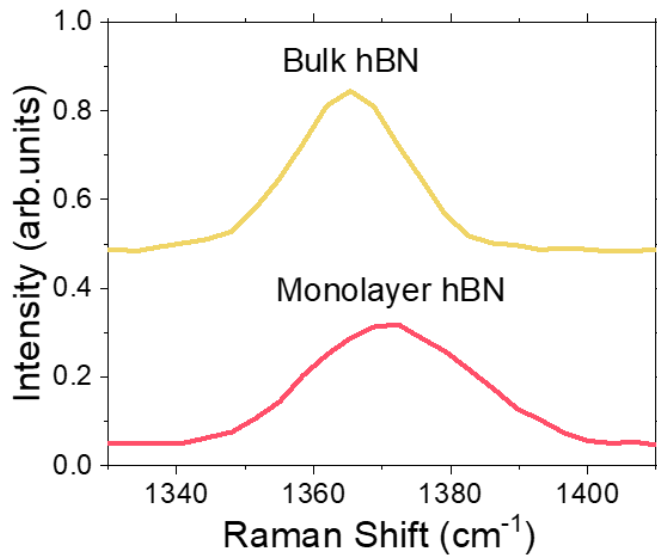
Fig 2.2.2 Unpolarized Raman spectra of monolayer and bulk hBN. All panels: from ref. *(127)*.

2.2.3 Chiral phonons in monolayer and multilayer graphene

The helicity-resolved Raman measurement was performed in a home-made optical measurement system as illustrated in **Section 2.1.3**. The graphene flakes with different layer numbers were excited with either σ- or σ+ laser and σ- and σ+ component of Raman emissions were detected respectively. We first investigated the chirality of the Raman modes in monolayer graphene at

room temperature. Under σ+ excitation with photon energy of 2.33 eV, only σ- emissions of Raman G mode were detected while σ+ emissions completely vanished, indicating that the Raman G mode perfectly switched the helicity of the incident photons (**Fig 2.2.3a**), which is consistent with previous observation (*167, 168*). This perfect Raman chirality was also preserved under the excitation photon energy of 1.94 eV (**Fig 2.2.**) or σ- excitation polarization (**Fig 2.2.3c**).
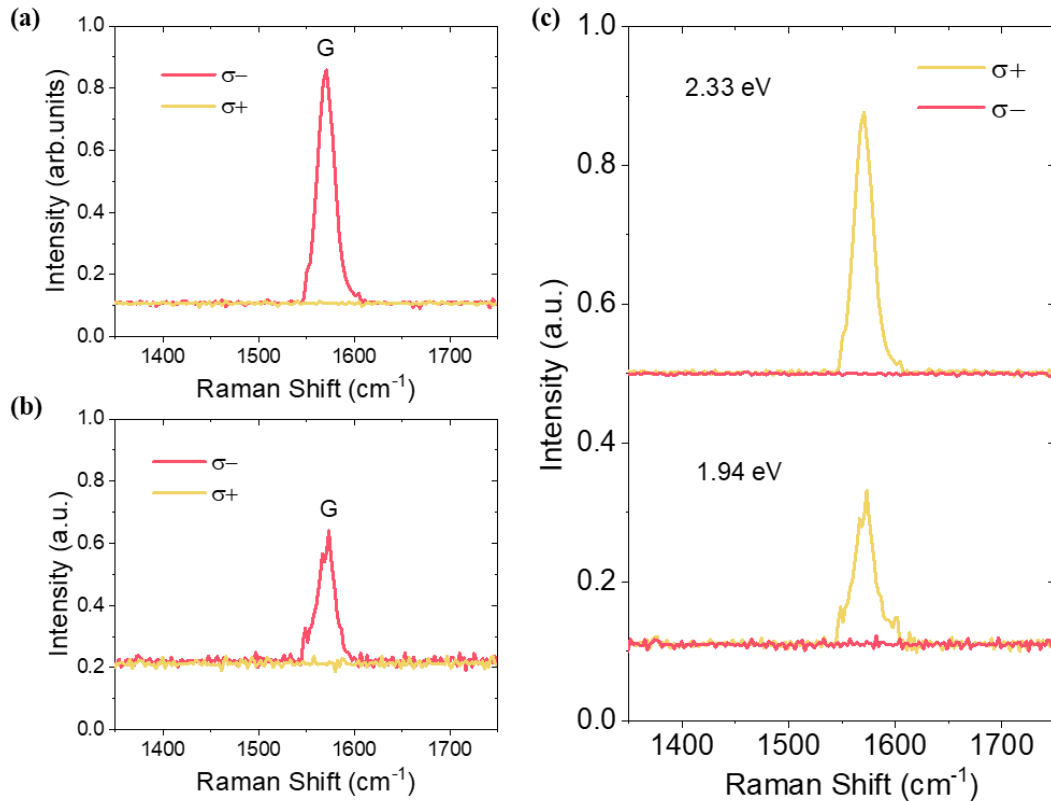
Fig 2.2.3 Helicity-resolved Raman spectra of Raman G mode in monolayer graphene under **(a)** σ+ excitation with photon energy of 2.33 eV **(b)** σ+ excitation with photon energy of 1.94 eV **(c)** σ- excitation. All panels: from ref. *(127).*

In contrast, as shown in **Fig 2.2.4a** and **Fig 2.2.4b**, the Raman D and 2D modes in monolayer graphene showed no such chirality, evidenced by the insignificant difference between σ+ and σ- component of the Raman signal under σ+ excitation.
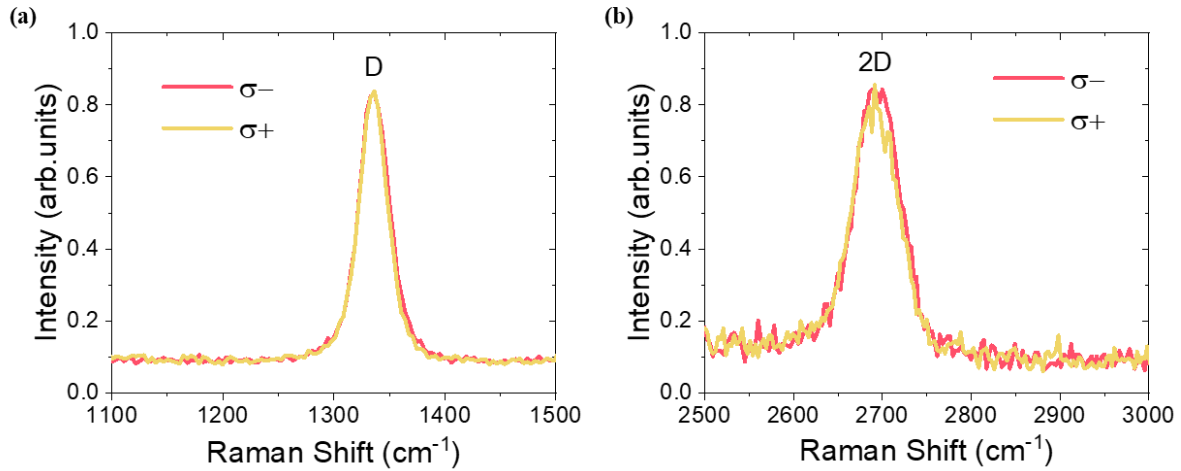
Fig 2.2.4 Helicity-resolved Raman spectra of Raman **(a)** D and **(b)** 2D modes in monolayer graphene under σ+ excitation with photon energy of 2.33 eV. All panels: from ref. *(127)*.

The distinct chiral properties between graphene Raman G, D and 2D modes can be attributed to their unique phonon scattering processes subject to the conservation of PAM between graphene valleys. The Raman G mode arises from the intravalley scattering of excitation photons by a doubly degenerate phonon mode at highly symmetric Brillouin zone center (Γ point) *(190)*, where the phonon mode acquires a PAM of ± 1 *(155)*. Since the intravalley scattering process requires the conservation of PAM, the variation of the PAM between the excitation photons and the emitting Raman photons should be equal to the PAM of the involved phonons. Therefore, the σ- (σ+) incident photons can only emit a σ+ (σ-) phonons, leading to the switching of the helicity of the Raman photons as illustrated in **Fig. 2.2.5a** *(155)*. On the contrary, the Raman 2D mode arises from the second order Raman process in the vicinity of the K and K′ points where intervalley scattering is involved. The excited electrons in K valley are first scattered to K′ valley and then scattered back to K valley by emitting a phonon in both scattering processes, as illustrated by **Fig 2.2.5b** *(190)*. Since the phonons involved in these two processes have the

50

opposite chirality, the emitted Raman photons will exhibit the same helicity as the incident photons, leading to the non-chirality of the Raman 2D mode. The Raman D mode involves the similar electron-phonon scattering processes to the 2D mode, while one of the scattering processes between K and K′ valleys is enabled by defects instead of the phonons, as shown in **Fig 2.2.5b** (*190*). In equilibrium, the phonon-involved scattering processes can occur either from K to K' valley or K' to K valley. Since the phonons involved in these two processes acquire the opposite PAM, the Raman D modes exhibit no chirality.
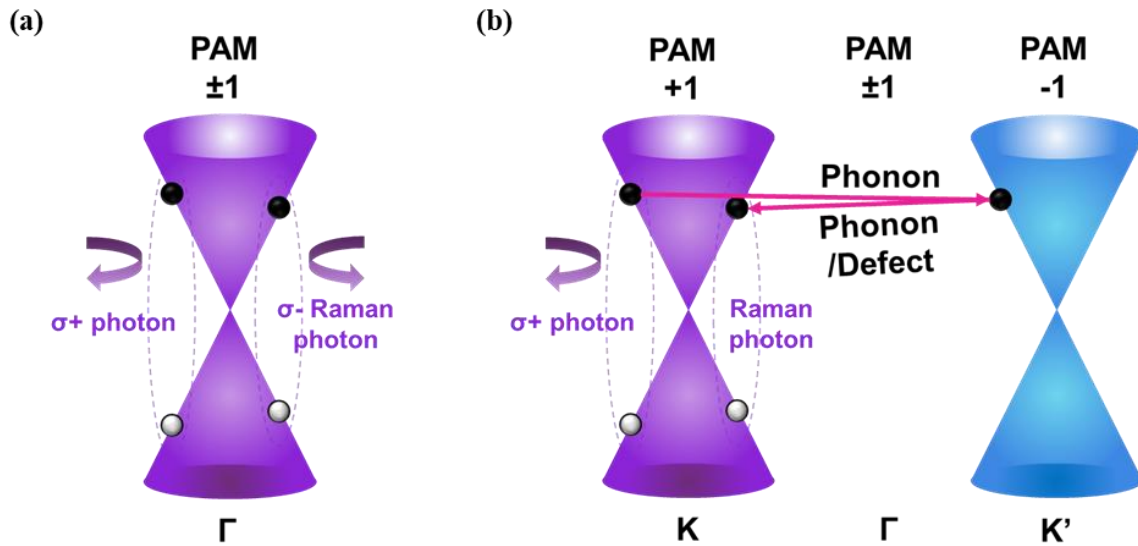
Fig 2.2.5 Schematic illustration of the valley phonon scattering processes and corresponding variation of PAM for Raman **(a)** G, **(b)** D and 2D modes in monolayer graphene. All panels: from ref. *(127)*.

We then performed helicity-resolved Raman spectrum measurements on pristine 2-5L graphene and thin-film graphite (> 100L) under the excitation photon energy of 2.33 eV. The Raman 2D mode exhibits no chirality regardless of the layer number, as shown in **Fig 2.2.6a**. **Fig 2.2.6b** shows the polarization resolved Raman G mode spectra for graphene thicker than monolayer. In monolayer graphene, under σ+ excitation, the σ+ component of Raman G mode emission is

completely absent. Here, a minor σ+ is observed starting from 2L graphene and the intensity increases as graphene becomes thicker. We extracted the Raman intensities of σ+ (I_{min}) and σ-component (I_{max}) respectively and calculated the polarization degree (P) of the Raman G mode using $P=(I_{max}-I_{min})/(I_{max}+I_{min})$.
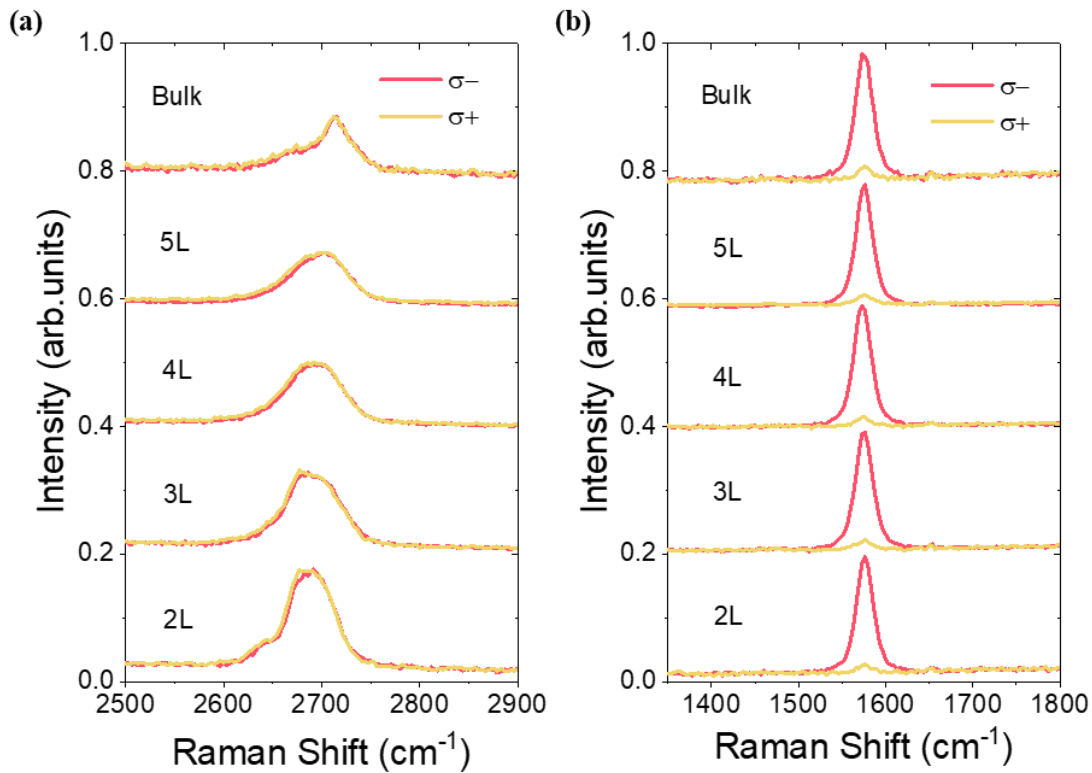
Fig 2.2.6 Helicity-resolved Raman spectra of Raman **(a)** 2D and **(b)** G modes in 2L-5L graphene and thin-film (>100L) graphite under σ+ excitation with photon energy of 2.33 eV. All panels: from ref. *(127)*.

As shown in **Fig 2.2.7**, the polarization degree is plotted against the layer number of graphene, which decreases sharply from 100% in monolayer graphene to 87.1% in bilayer graphene. It further decreases monotonously and approaches its bulk limit of 80.8%. Similar phenomenon was observed when the excitation photon energy was 1.94 eV (**Fig 2.2.7**). The layer dependence

of the polarization degree suggests that interlayer interaction among graphene layers significantly influences the phonon chirality.
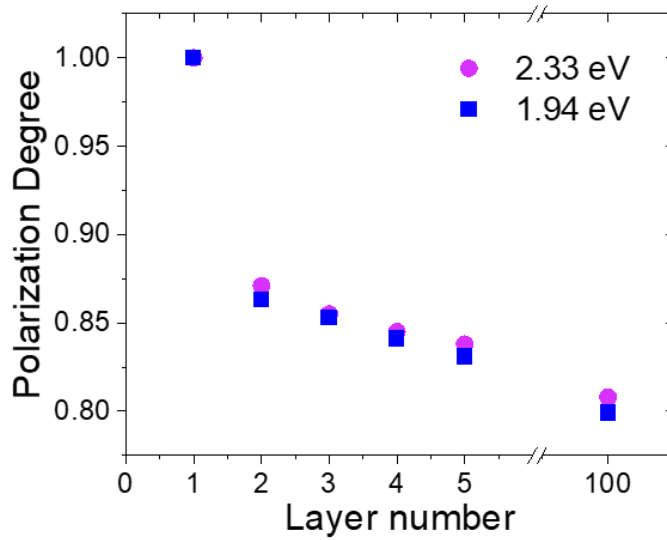
Fig 2.2.7 Layer number dependence of polarization degree of Raman G mode in graphene flakes at excitation photon energy of 2.33 eV and 1.94 eV. All panels: from ref. *(127)*.

We further investigated the temperature dependence of the polarization degree in graphene Raman G mode. In monolayer graphene, the perfect phonon chirality was preserved at all temperatures, as illustrated in **Fig 2.2.8**. Moreover, **Fig 2.2.8** also shows the degree of polarization as a function of the temperature for multilayer graphene. In general, the degree of polarization decreases as the temperature increases. The temperature dependence of the polarization degree indicates the role of interlayer phonon-phonon interaction, which suppresses the degree of phonon polarization. Reduced temperature can freeze the lattice vibration and therefore, suppress the interlayer phonon-phonon interaction in multilayer graphene and facilitates the preservation of the phonon chirality.
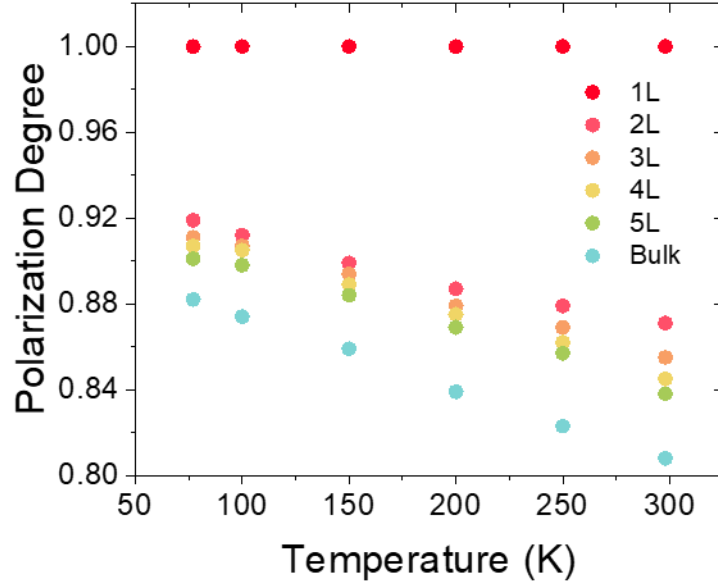
Fig 2.2.8 Temperature dependence of polarization degree for Raman G mode in 1L-5L graphene and thin-film graphite. All panels: from ref. *(127)*.

2.2.4 Establishment of the Raman tensor for multilayer graphene

To further understand the mechanism of the layer number dependent phonon chirality induced by interlayer interaction, we calculated the polarization degree in multilayer graphene based on symmetry analysis using Raman tensors. Here we first discuss the Raman G modes of monolayer graphene. At Γ point, the monolayer graphene belongs to the D_{6h} point group where the Raman G mode can be described as E_{2g} representations according to the symmetry analysis, corresponding to the Raman tensor A (*166*), where

$$A = \begin{vmatrix} a_{11} & a_{12} & a_{11} \\ a_{21} & a_{22} & a_{23} \\ a_{31} & a_{32} & a_{33} \end{vmatrix} = \begin{vmatrix} 0 & d & 0 \\ d & 0 & 0 \\ 0 & 0 & 0 \end{vmatrix} \text{ or } A = \begin{vmatrix} a_{11} & a_{12} & a_{11} \\ a_{21} & a_{22} & a_{23} \\ a_{31} & a_{32} & a_{33} \end{vmatrix} = \begin{vmatrix} d & 0 & 0 \\ 0 & -d & 0 \\ 0 & 0 & 0 \end{vmatrix} \quad (2)$$

The left ($|\sigma_-\rangle$) and right ($|\sigma_+\rangle$) circularly polarized wave-vectors are defined as

$$|\sigma_-\rangle = \frac{1}{\sqrt{2}} \begin{pmatrix} 1 & i & 0 \end{pmatrix}^T \text{ and}$$

$$|\sigma_+\rangle = \frac{1}{\sqrt{2}} \begin{pmatrix} 1 & -i & 0 \end{pmatrix}^T, \text{ respectively.} \tag{3}$$

The normalized Raman intensity for different excitation/detection configuration can be calculated as $\left|\sigma_i^\dagger A \sigma_j\right|^2$, where both i and j can be "-" or "+". For excitation/detection configuration with the same polarization ($i = j$), the Raman signal completely vanishes as $I_{min} = \left|\sigma_i^\dagger A \sigma_j\right|^2 = 0$. In contrast, for excitation/detection configuration with the opposite polarization where $i \neq j$, the Raman intensity reaches its maximum as $I_{max} = \left|\sigma_i^\dagger A \sigma_j\right|^2 = d^2$.

Furthermore, we established the Raman tensor for Raman G mode in bilayer graphene by adding an additional interlayer hopping term (*191, 192*), which can be represented by a 6×6 matrix R.

$$R = \begin{vmatrix} A & B \\ B & A \end{vmatrix} \tag{4}$$

Here A matrix is the same as that in monolayer graphene and B is the matrix representation of the interlayer coupling term, which is defined as

$$B = \begin{vmatrix} t_{11} & t_{12} & t_{13} \\ t_{21} & t_{22} & t_{23} \\ t_{31} & t_{32} & t_{33} \end{vmatrix} \tag{5}$$

The matrix element t_{ij} ($i, j = 1, 2, 3$) is defined as the interlayer coupling coefficient between the adjacent graphene layers where $t_{ji} = t_{ij}$ due to the symmetry. The left and right circularly polarized wave-vectors are also extended to be compatible with the Raman tensor, which are defined as

$$|\sigma_-\rangle = \frac{1}{\sqrt{2}} \begin{pmatrix} 1 & i & 0 & 1 & i & 0 \end{pmatrix}^T \text{ and}$$

$$|\sigma_+\rangle = \frac{1}{\sqrt{2}} \begin{pmatrix} 1 & -i & 0 & 1 & -i & 0 \end{pmatrix}^T, \text{respectively.} \tag{6}$$

Similarly, $\left| \sigma_i^\dagger A \sigma_j \right|$ is used to calculate the Raman intensity under the different excitation/detection polarization configurations. For excitation/detection configuration with the same polarization, the Raman intensity is

$$I_{min} = \left| \sigma_+^\dagger A \sigma_+ \right|^2 = \left| \sigma_-^\dagger A \sigma_- \right|^2 = (t_{11} + t_{22})^2 \tag{7}$$

which is non-vanishing in contrast to that in monolayer graphene. While for excitation/detection configuration with the opposite polarization, the Raman intensity is

$$I_{max} = \left| \sigma_+^\dagger A \sigma_- \right|^2 = \left| \sigma_-^\dagger A \sigma_+ \right|^2 \approx 4d^2 \tag{8}$$

Therefore, the polarization degree of Raman G mode in bilayer graphene is

$$P_2 = \frac{I_{max} - I_{min}}{I_{max} + I_{min}} = \frac{4d^2 - (t_{11} + t_{22})^2}{4d^2 + (t_{11} + t_{22})^2} \tag{9}$$

According to the Raman tensor calculation, the polarization degree in bilayer graphene will not be perfect (100%) due to the existence of the interlayer interaction coefficient. However, since the interlayer coupling coefficient t_{ij} should be significantly smaller than the fundamental Raman tensor term d, the polarization degree will not decrease significantly, evidenced by the low intensity Raman signal under excitation/detection configuration with the same polarization.

The method to establish the Raman G mode tensor in bilayer graphene can be applied to trilayer graphene as well. The tensor can be represented by a 9×9 matrix R

$$R = \begin{vmatrix} A & B_{12} & B_{13} \\ B_{21} & A & B_{23} \\ B_{31} & B_{32} & A \end{vmatrix} \tag{10}$$

Here A is the fundamental Raman tensor for E_{2g} mode, $B_{12} = B_{21} = B_{23} = B_{32}$ is the matrix representation of the interlayer coupling terms for two adjacent layers, while $B_{13} = B_{31}$ is the matrix representation of the interlayer coupling terms for two non-adjacent layers. These Raman tensors can be defined as

$$B_{12}{=}B_{21}{=}B_{23}{=}B_{32} = \begin{vmatrix} t_{11} & t_{12} & t_{11} \\ t_{21} & t_{22} & t_{23} \\ t_{31} & t_{32} & t_{33} \end{vmatrix}; \ B_{13}{=}B_{31} = \begin{vmatrix} t_{44} & t_{45} & t_{46} \\ t_{54} & t_{55} & t_{56} \\ t_{64} & t_{65} & t_{66} \end{vmatrix} \tag{11}$$

Similarly, the matrix element t_{ij} is defined as the interlayer coupling coefficient where $t_{ji} = t_{ij}$ due to the symmetry consideration. Then, $|\sigma_-\rangle$ and $|\sigma_+\rangle$ are extended in the same configuration to accommodate the Raman tensor, which can be represented as

$$|\sigma_-\rangle = \frac{1}{\sqrt{2}} (1 \quad i \quad 0 \quad 1 \quad i \quad 0 \quad 1 \quad i \quad 0)^T$$

$$|\sigma_+\rangle = \frac{1}{\sqrt{2}} (1 \quad -i \quad 0 \quad 1 \quad -i \quad 0 \quad 1 \quad -i \quad 0)^T \tag{12}$$

Then the Raman intensity for the same excitation/detection polarization configuration

$$I_{min} = \left| \sigma_+^\dagger A \sigma_+ \right|^2 = \left| \sigma_-^\dagger A \sigma_- \right|^2 = \frac{9}{4} (t_{11} + t_{22} + t_{44} + t_{55})^2 \tag{13}$$

While the Raman intensity for the opposite excitation/detection polarization configuration

$$I_{max} = \left| \sigma_+^\dagger A \sigma_- \right|^2 = \left| \sigma_-^\dagger A \sigma_+ \right|^2 \approx 9d^2 \tag{14}$$

Hence, the polarization degree of Raman G mode in trilayer layer graphene can be represented as

$$P = \frac{I_{max} - I_{min}}{I_{max} + I_{min}} = \frac{4d^2 - (t_{11} + t_{22} + t_{44} + t_{55})^2}{4d^2 + (t_{11} + t_{22} + t_{44} + t_{55})^2} \tag{15}$$

Compared with the polarization degree formula in bilayer graphene, there is an additional term $t_{44} + t_{55}$ representing the interlayer interaction between two non-adjacent layers, which leads to the lower polarization degree experimentally observed in trilayer graphene (85.5%) if compared with that in bilayer graphene (87.1%). Moreover, since the interlayer interaction between the non-adjacent layers can be regarded as a second-order effect compared with that between adjacent layers, the interlayer coupling coefficient t_{44} and t_{55} should be significantly smaller than t_{11} and t_{22}. As a result, the decreasing of the polarization degree from bilayer to trilayer is much less prominent compared with that from monolayer to bilayer. Our model can be further applied to multilayer graphene, where the polarization degree of the Raman G mode in n layer graphene can be denoted as

$$P = \frac{4d^2 - (t_{11} + t_{22} + t_{44} + t_{55} + t_{44} + t_{55} + \cdots + t_{3n-5,3n-5} + t_{3n-4,3n-4})^2}{4d^2 - (t_{11} + t_{22} + t_{44} + t_{55} + t_{44} + t_{55} + \cdots + t_{3n-5,3n-5} + t_{3n-4,3n-4})^2} \tag{16}$$

Here, t_{3n-5} and t_{3n-4} represents the interlayer coupling coefficient between the adjacent n layers, which decays significantly with the increasing n. Therefore, in multilayer graphene, the polarization degree of the Raman G mode will decrease with increasing layer numbers, which is consistent with our measurements.

2.2.5 Numerical calculation of the polarization degree

To further verify the established model, we calculated the polarization degree by deducting the value of interlayer coupling coefficient t_{ii}. The value of the $(t_{11} + t_{22})^2$ was directly extracted from the helicity-resolved Raman spectrum in bilayer graphene at room temperature, which exhibits a polarization degree of 87.1%. Therefore, the value of interlayer coupling coefficient in the adjacent graphene layers was determined as $(t_{11} + t_{22})^2 = 0.3d^2$. Since we assume that the interlayer interaction in graphene layers is contributed by dipole-dipole interaction which decays with the distance by $1/r^3$ (*193*), the interlayer coupling coefficient in adjacent three layers can be estimated as

$$(t_{44} + t_{55})^2 = \frac{1}{8}(t_{11} + t_{22})^2 = 0.0375d^2 \tag{17}$$

Therefore, the calculated polarization degree of the Raman G mode in trilayer graphene is 84.4%, which agrees well with our experimental result (85.5%). Similarly, we can further deduct the interlayer coupling coefficient in adjacent n layers, which gives

$$(t_{3n-5,3n-5} + t_{3n-4,3n-4})^2 = \frac{1}{(n-1)^3}(t_{11} + t_{22})^2 \tag{18}$$

Then when n is very large, we have

$$(t_{11} + t_{22} + t_{44} + t_{55} + t_{44} + t_{55} + \cdots + t_{3n-5,3n-5} + t_{3n-4,3n-4})^2 = 0.36d^2 \tag{19}$$

Therefore, the calculated polarization degree of the Raman G mode in thin-film graphite should be 83.0%, which also agrees well with the experimental results (80.8%). The evolution of the polarization degree against the layer number at room temperature from Raman tensor calculation is also plotted in **Fig 2.2.9a** together with the experimental results. It is clear that our model captures the impact of interlayer coupling on the phonon chirality.
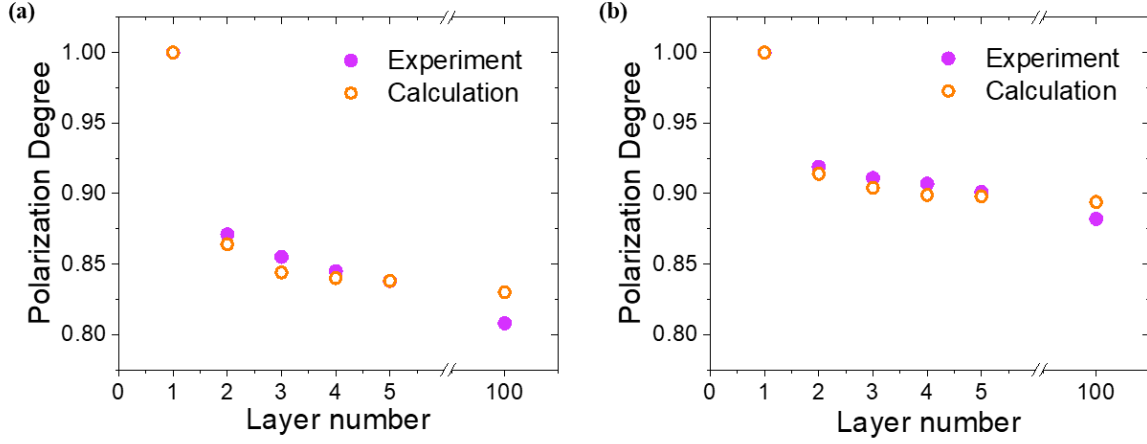
Fig 2.2.9 The layer number dependent polarization degree of graphene Raman G mode from Raman tensor calculation compared with the experimental results **(a)** at room temperature and **(b)** at 77K. All panels: from ref. *(127)*.

We applied the same model to simulate the evolution of the polarization degree against the layer number at 77K. The value of $(t_{11} + t_{22})^2$ at 77K was directly extracted from the measured polarization degree of 91.9%, from which we get $(t_{11} + t_{22})^2 = 0.18d^2$. According to our discussion in main text, we have

$$(t_{44} + t_{55})^2 = \frac{1}{8}(t_{11} + t_{22})^2 = 0.0225d^2 \tag{19}$$

The higher order coupling coefficients can also be calculated accordingly. For thin-film graphite (n>10), we have

$$(t_{11} + t_{22} + t_{44} + t_{55} + t_{44} + t_{55} + \cdots + t_{3n-5,3n-5} + t_{3n-4,3n-4})^2 = 0.22d^2 \tag{20}$$

The polarization degree for trilayer graphene also be calculated. Therefore, the calculated polarization degree of Raman G mode in trilayer graphene (thin-film graphite) at 77K is 90.4% (89.4%), which also agrees well with the experiment results of 91.1% (88.2%). The calculated

polarization degrees at different layer numbers are plotted in **Fig 2.2.9b**, which also agrees with the experimental results well .

2.2.6 Chiral phonons in monolayer and multilayer hBN
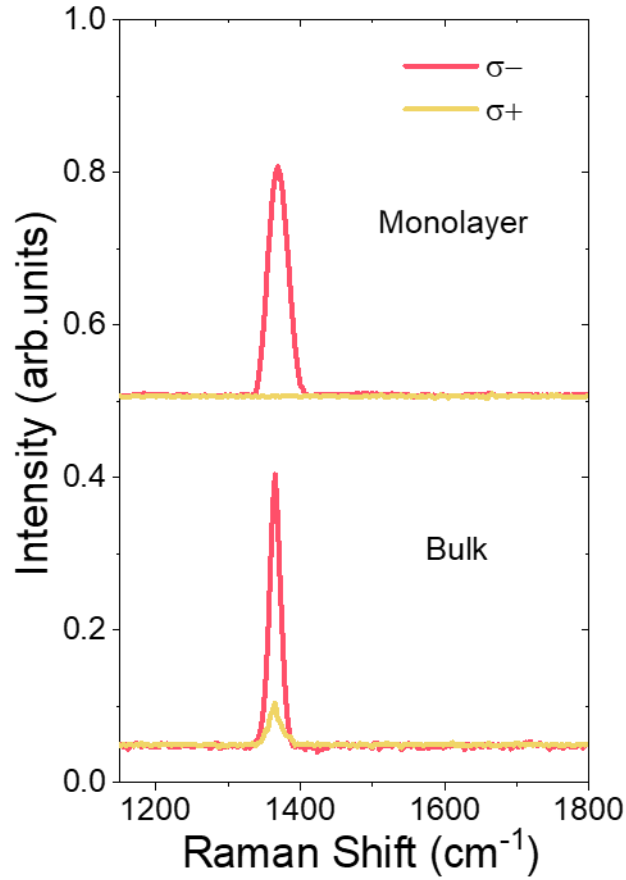
Fig 2.2.10 Helicity-resolved Raman spectra of monolayer and bulk hBN under σ+ excitation with photon energy of 2.33 eV. All panels: from ref. *(127)*.

We further explored the phonon chirality in 2D honeycomb hBN to verify our observations. The helicity-resolved Raman measurements were performed in both monolayer and thin-film hBN under 2.33 eV σ+ excitation at room temperature. The perfect phonon chirality was only

preserved in monolayer hBN. For thin-film hBN, a clear σ+ peak was observed, as shown in **Fig 2.2.10**. The temperature dependence of the polarization degree in hBN Raman E_{2g} modes for both monolayer and thin-film hBN is plotted in **Fig 2.2.11**. The phonon chirality remains perfect at all temperatures in monolayer hBN, while the degree of polarization decreases at elevated temperature in thin-film hBN. The layer number and temperature dependent chiral Raman modes in hBN further illustrate the role of the interlayer phonon-phonon interactions, which can affect the lattice vibration in 2D honeycomb lattice.
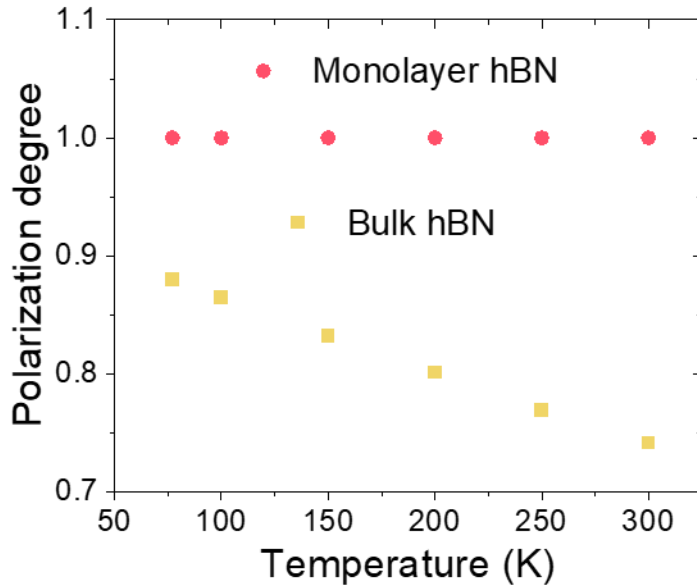
Fig 2.2.11 Temperature dependence of polarization degree of Raman E_{2g} mode in monolayer and bulk hBN. All panels: from ref. *(127)*.

2.2.7 Discussion and summary

Previously, the circular polarization of the Raman emission has also been investigated in monolayer and few-layer TMDs *(166)*. The Raman emission due to out-of-plane relative motion

of only chalcogen atoms (OC) mode has the same polarization state of the excitation photons. In contrast, the Raman emission due to in-plane relative motion of transition metal and chalcogen atoms (IMC) mode exhibits opposite circular polarization if compared with the circular polarization of the excitation photons. Remarkably, the circular polarization of Raman emission due to the OC modes remains perfect regardless of the layer number, while it becomes imperfect for Raman emission due to the IMC modes in multilayers. This observation suggests that the in-plane vibration modes are less robust to interlayer interactions compared with the out-of-plane vibration modes in TMDs. In graphene and hBN, the Raman active G mode is only contributed by the in-plane lattice vibrations, while the out-of-plane lattice vibration modes are Raman inactive (*189, 194*). Although it is not feasible to investigate the impact of interlayer coupling on out-of-plane modes in graphene and hBN using Raman scattering, our observation of the imperfect and layer-dependent phonon chirality of the Raman G mode is consistent with the previously reported results on the IMC modes in TMDs.

In conclusion, we performed a comprehensive investigation on the vdWs interlayer interactions in honeycomb lattice via chiral phonons. The interlayer interaction plays an important role in lattice vibrations of the honeycomb lattice and therefore, affects the phonon chirality, evidenced by the decreasing polarization degree of Raman G modes with increasing layer number and temperature. We further established a new method to construct the tensor for Raman G modes in multilayer 2D honeycomb lattice by introducing the interlayer coupling coefficients, which characterizes the strength of the interlayer interaction. The layer dependent phonon chirality extracted from Raman tensor calculation agrees with the helicity-resolved Raman measurement results well. Our observations provide a new perspective to probe the interlayer interaction in vdWs materials and heterostructures with unique honeycomb lattice symmetry.

2.3 Valley-selective linear dichroism in 2D non-honeycomb Tin Sulfide

2.3.1 Motivation

As we mentioned above, the extensive exploration of valley physics has been limited to 2D honeycomb lattice such as graphene (*68, 195*), TMDs (*65, 66, 145*) and hBN (*133*). Since its first demonstration in monolayer MoS_2 (*64, 145, 146*), valley has been intensively investigated as an emerging degree of freedom and is referred as pseudospin in analogy to the electron spin (*14, 63*). There are two energy degenerate but inequivalent valleys (K and K') in the band structure of 2D honeycomb lattice (*62*). Due to the optical selective rule, the K(K') valley can be pumped with σ+(σ-) photons followed by a photon emission of the same helicity, giving rise to the valley-selective circular dichroism (*62*). This valley-related optical selectivity also leads to the observation of valley Hall effect, providing great opportunity for the realization of valleytronic device (*70, 71*).

Therefore, it is highly desired to expand material system and find new candidates for exploring both fundamental valley physics and valleytronic application. According to our discussion above, three fundamental factors must be satisfied to make a 2D material appropriate for probing valley effect. First, there are two or more valleys with nearly degenerate energy gaps in the band structure. Moreover, each valley can be selectively excited with photons of different polarization properties (either linear or circular polarization). Finally, the energy gap at these valleys must be significantly smaller than that at other points of the band structure to dominate photon-excited electronic transitions.

Recently the linear dichroism was demonstrated in BP with a low lattice symmetry (*49, 50, 52, 196*). However, BP only possesses one-fold linear dichroism property due to its single valley at Γ

point, which limits its potential for the exploration of the valley-related degree of freedom (*31, 76*). On the other hand, in monolayer (*150, 197*) and bulk (*198*) group-IV monochalcogenides, theorists predict that two pair of valleys along Γ-X and Γ-Y directions can be selectively pumped with linearly polarized light with different polarization, respectively. The linear dichroism has also been studied in one of the group-IV monochalcogenides, GeS (*132, 199*). However, only single-fold linear dichroism was observed in GeS. This is because the band gap at Γ point in GeS is much smaller than that at Γ-X and Γ-Y valleys, hence more preferred for optical transition. As a result, the linear dichroism of GeS is determined by the optical transition rule at Γ point, lack of freedom for valley manipulation. In contrast, the band gap of Γ-X and Γ-Y valley is significantly smaller than that at Γ point in SnS, making it an extraordinary platform for investigating valley-related linear dichroism and corresponding optical transition rule (*197, 198*).

2.3.2 Sample preparation and crystal orientation determination

The SnS has a layered orthorhombic crystal structure, subjective to the D_{2h}^{16} space group, similar to that of black phosphorus and other group-IV monochalcogenides, as shown in **Fig 2.3.1** *(148, 163, 199)*. The armchair and zigzag chains of SnS are defined as x and y direction, respectively, and z direction is defined as the direction perpendicular to the layers. Due to its highly asymmetric crystal structure, SnS exhibits strong in-plane anisotropic physical properties (*200, 201*). The layered SnS samples for optical characterization were first deposited onto 285nm SiO2/Si substrate using standard exfoliation approach. **Fig 2.3.2** shows the optical microscope image of a typical SnS flake used for optical characterization. The thickness of this particular SnS flake is 109 nm-thick, determined by the Atomic Force Microscopy (AFM) measurement, as shown in inset of **Fig 2.3.2**. We performed optical characterization on samples of different

thickness ranging from 50 to 500 nm, which show similar results and can be considered as bulk SnS.
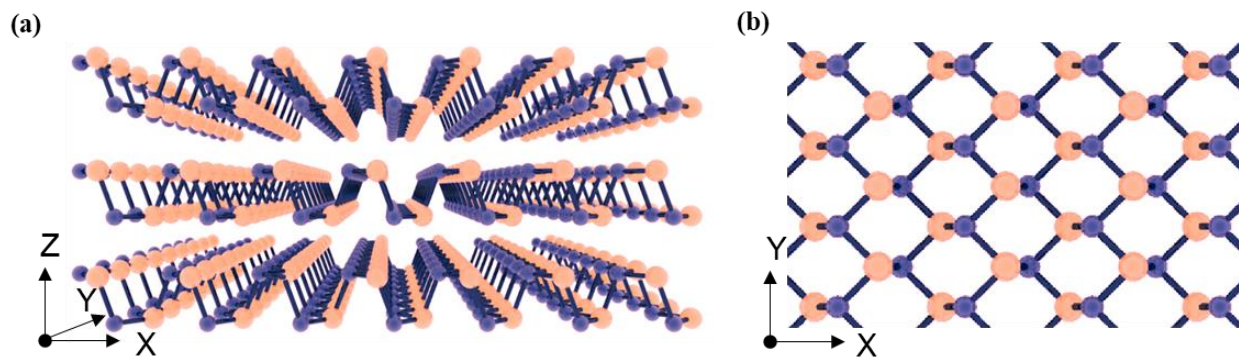
Fig 2.3.1 Schematic illustration of the crystal structure of layered SnS. (left panel: front view of the x-z plane; right panel: top view of the x-y plane). All panels: from ref. *(128)*.
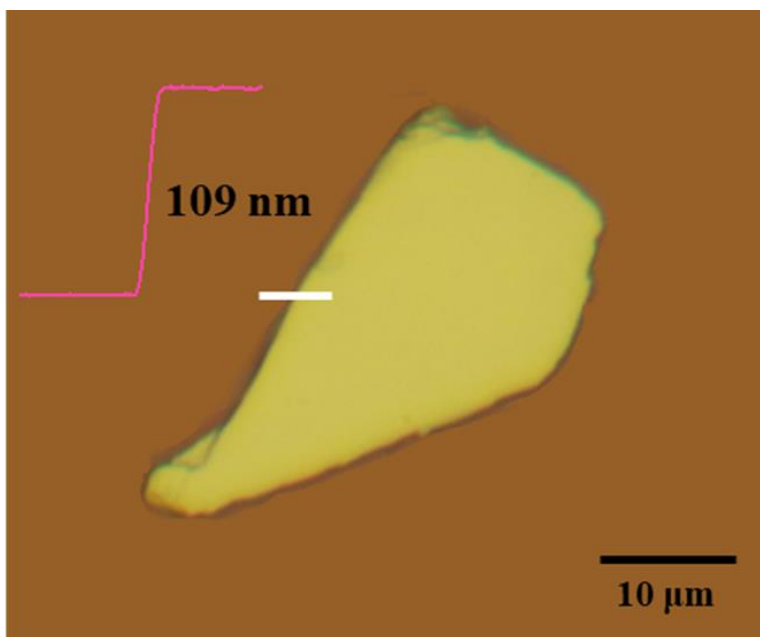
Fig 2.3.2 Optical micrograph of a typical SnS flake on 285 nm SiO_2/Si. Insert: The atomic force microscopy scan performed on the SnS flake. Its thickness is determined to be 109 nm. All panels: from ref. *(128)*.
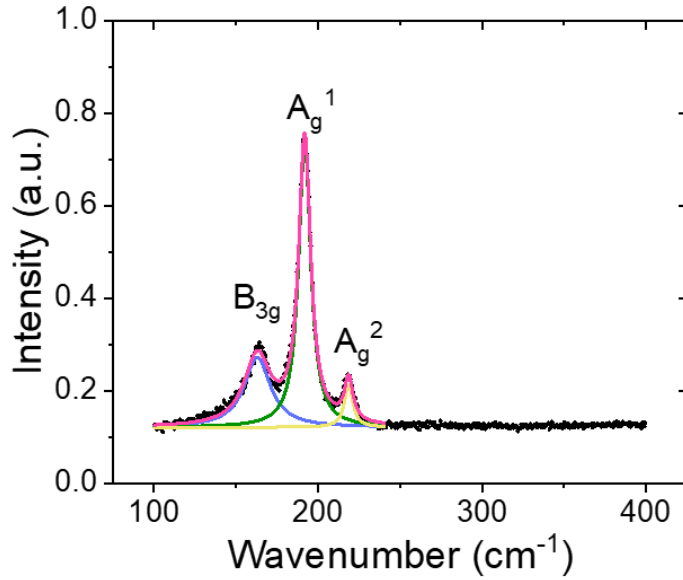
Fig 2.3.3 Raman scattering spectra of the SnS sample. The Lorentz fitting curves of B_{3g}, A_{g1} and A_{g2} mode are shown by blue, green and yellow lines, respectively. All panels: from ref. *(128)*.

The SnS flake was further characterized by Raman scattering spectroscopy. The Raman scattering spectroscopy was performed with Horiba LabRAM HR Evolution Raman Microscope with excitation photon energy of 2.33eV. Three prominent Raman modes were resolved, corresponding to the B_{3g}, A_g^1 and A_g^2 mode, as reported previously *(202)*. All these Raman modes show the typical Lorentz shape and they are positioned at 161 cm^{-1}, 191 cm^{-1} and 217 cm^{-1}, respectively, as illustrated in **Fig 2.3.3**. The polarization dependence of Raman spectrum is a convenient way to determine the crystal orientation *(157, 159)*. We measured the angular resolved Raman spectrum by rotating the sample with respect to the laser polarization, as exhibited in **Fig 2.3.4a**. The **Fig 2.3.4b** shows the angular resolved Raman intensity of A_g^1 mode, where 0 degree is determined as the x-direction of the SnS crystal. The rotation angle θ is referred to the intersect angle between the laser polarization direction and x direction. The B_{3g} mode intensity shows a good agreement with the dependence of $asin^2 2\theta + b$, while the intensity

of two A_g modes were well fitted with the dependence of $a\cos^2\theta + b$ (**Fig 2.3.4c,d**), where a and b are fitting parameters. This observation agrees well with previous Raman studies in SnS (*165, 203*). The distinct behavior of B_{3g} mode and the A_g modes can be attributed to the different Raman tensors governing them. With angular-resolved Raman scattering measurements, we can determine the armchair (x) and zigzag (y) direction of the SnS flake, which set a reference for the crystal orientation for the following polarization-resolved PL and absorption measurements.
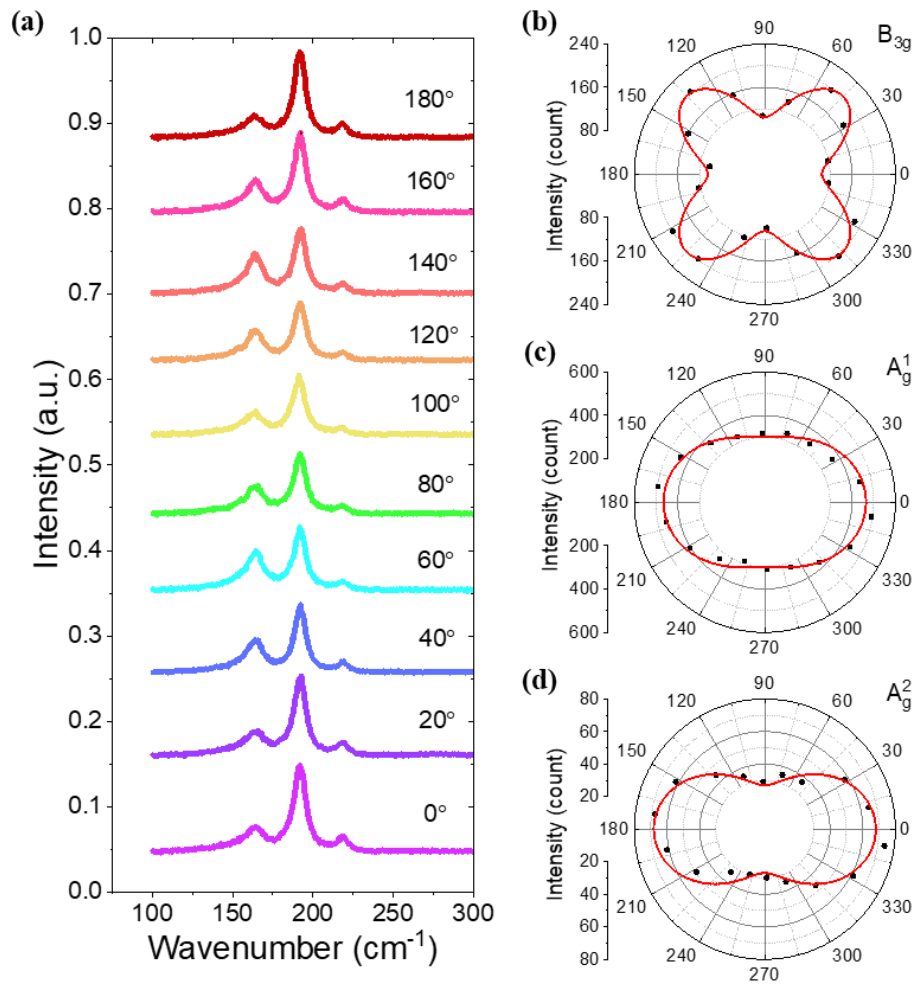
Fig 2.3.4 (a) Angular-resolved Raman spectra in SnS. **(b-d)** Angular-resolved Raman intensity of **(b)** B_{3g}, **(c)** A_{g1} and **(d)** A_{g2} mode. All panels: from ref. *(128)*.

2.3.3 Unpolarized Photoluminescence (PL) spectroscopy at 77K

The PL measurements were performed in a homemade optical micro-PL system, as illustrated in **Section 2.1.3**. The unpolarized PL spectrum was measured with an excitation photon energy of 2.33 eV and excitation power of 500 μW. Since the PL emission was significantly quenched at room temperature, all the PL measurements were performed under 77K (*204*). Two photon emission peaks were resolved from the PL spectrum, locating at 1.160 eV and 1.204 eV, as exhibited **in Fig 2.3.5a**. Here, we use I^Y and I^X to denote the intensity of these two peaks, respectively. To exclude the possible PL emission from the substrate, we measured emission spectrum directly from the SiO_2/Si substrate. As expected, a much weaker emission peak was observed at 1.130 eV, which can be attributed to the indirect band gap of the silicon (*205*). Since the excitation light will be significantly attenuated by the SnS flake (~100 nm), the emission from the SiO_2/Si substrate can be ignored when the SnS PL is measured. The PL intensity increases linearly with the excitation laser power, as shown in **Fig 2.3.5b**.
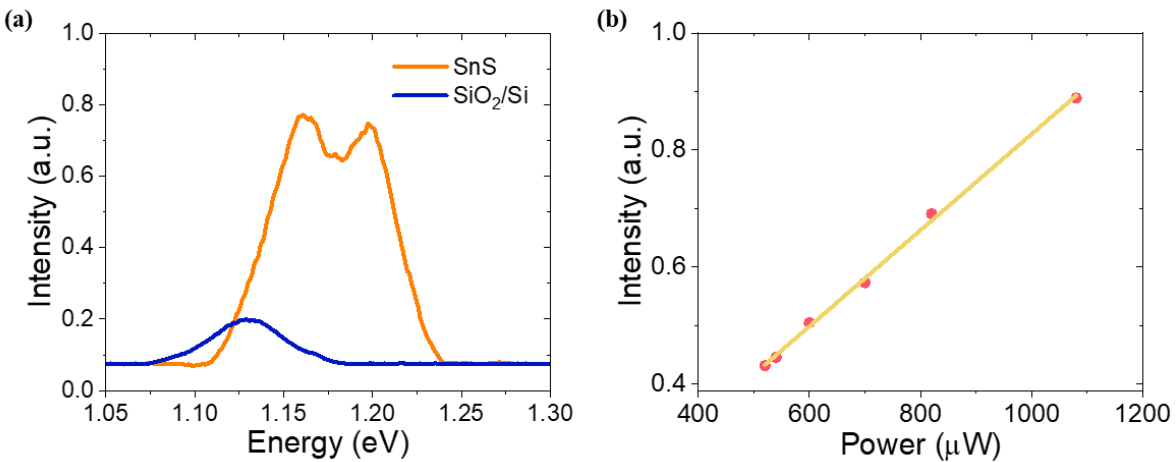
Fig 2.3.5 **(a)** PL spectra from the SnS sample and SiO_2/Si substrate. **(b)** Excitation power dependence of the SnS PL intensity. All panels: from ref. *(128)*.

According to the theoretical calculation results reported previously, SnS exhibits two valleys with close energy gaps along Γ-X and Γ-Y directions in momentum space (*138, 198, 206*). If the energies of the conduction band minimum (CBM) and the valence band maximum (VBM) of the Γ-X valley and Γ-Y valley are defined as E_I^J $(I = C, V; J = X, Y)$, respectively, previous calculations indicate $E_C^Y - E_V^X < E_C^Y - E_V^Y < E_C^X - E_V^X$, as illustrated in **Fig 2.3.6**. Since previous first-principle calculation has already provided a comprehensive understanding of the electronic band structure of SnS, here we show a schematic diagram in reference to those works (*138, 198, 206*). Hence, the I^X (1.204 eV) peak probably arises from the band edge transition between E_C^X and E_V^X and I^Y (1.160 eV) PL peak is due to the band edge transition between E_C^Y and E_V^Y. Such assignments are further confirmed by the polarization-resolved PL and absorption spectrum measurement, which will be discussed below.
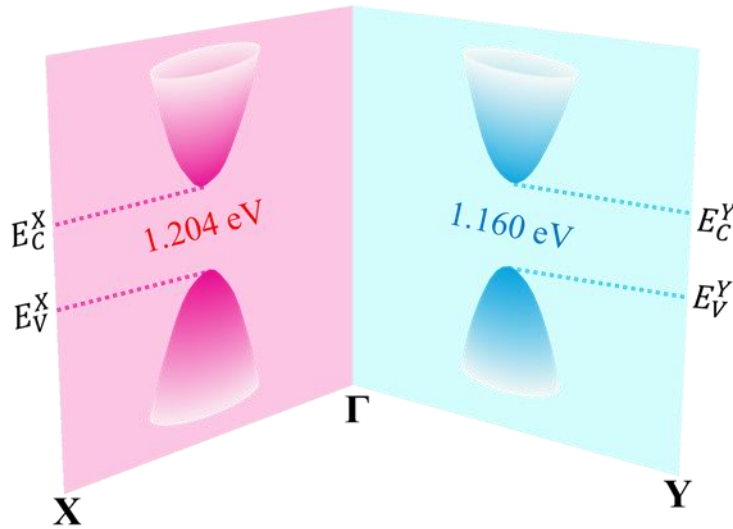
Fig 2.3.6 Schematic illustration of the band structure of layered SnS. All panels: from ref. *(128)*.

2.3.4 Excitation anisotropy of PL spectroscopy

To further reveal the anisotropic properties of the band edge emissions, we performed PL measurements under different laser excitation polarization. In this measurement, the polarization direction of the laser was tuned while there is no polarization control in the detection path. **Fig 2.3.7a** shows the PL spectrum where θ represents the intersect angle between the excitation laser polarization and the x-direction of SnS. We fitted the measured PL spectrum with Gaussian Formula and extracted the intensity of I^X (1.204 eV) and I^Y (1.160 eV) emission peaks. The extracted PL intensity of I^X and I^Y peaks were correspondingly plotted in **Fig 2.3.7b**, and they showed the $cos^2\theta$ - and $sin^2\theta$ - dependent shapes respectively. To highlight the excitation anisotropy, the angular resolved PL intensity is plotted from 0.8 to 1. For band edge emission along Γ-X valley, I^X reached its maximum with excitation polarization parallel to x direction. In contrast, I^Y from Γ-Y valley reached its maximum when excitation polarization is along the y-direction. Our observation suggests that for each valley in the momentum space, the emission dominates when the excitation polarization is parallel to its corresponding crystal orientation in the real space. We further calculated the degree of polarization for anisotropic emissions from Γ-X and Γ-Y valleys, which is defined as

$$P^X = \frac{I_x^X - I_y^X}{I_x^X + I_y^X}; \qquad P^Y = \frac{I_y^Y - I_x^Y}{I_y^Y + I_x^Y} \tag{21}$$

respectively. Here I_i^J ($i = x, y; J = X, Y$) represents the emission from J valley under i-polarized excitation. The emission from X (Y) valley indicates a degree of polarization P^X =8.5% (P^Y=3.4%).
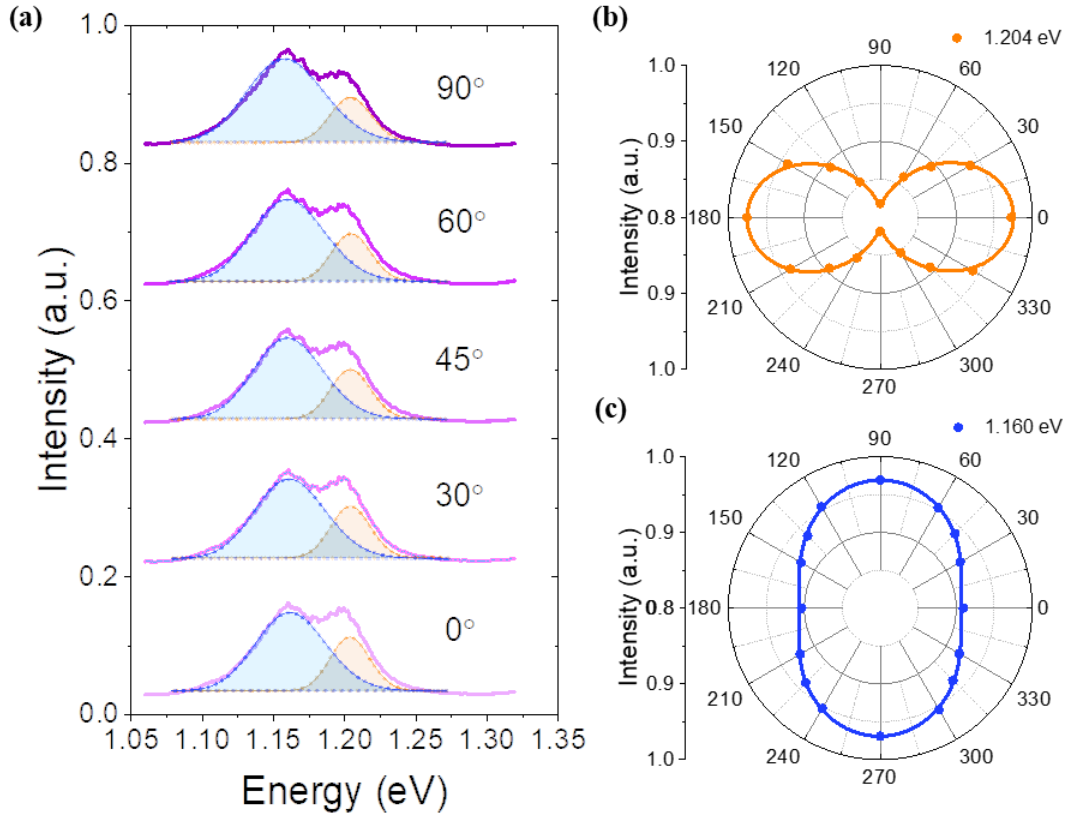
Fig 2.3.7 (a) PL spectra of SnS under different excitation polarization. **(b)** Angular-resolved PL intensity of the 1.204 eV (yellow) and 1.160 eV (blue) emission peaks under different excitation polarization. The fitting curves for PL emissions from Γ-X and Γ-Y valley are indicated by yellow and blue lines, respectively. All panels: from ref. *(128)*.

Despite of the low degree of polarization, the distinct excitation anisotropic behavior of the two PL peaks was a result of the valley-related optical selective rules. According to the symmetry analysis based on group theory, the interband transition probability for both valleys under different excitation polarization has been calculated (*198*). Under linearly polarized excitation, the electrons in Γ-X valley can be only excited with x-polarized photons while the Γ-Y valley can be only pumped with y-polarized excitation. However, due to the off-resonant excitation photon energy (2.33 eV) in our PL measurements, the valley electrons selected by corresponding

excitation polarization acquire significantly higher energy in the conduction band. Though the valley-related optical selection rule is still preserved, the excited electron is easily relaxed to the other valley (*207*). Hence the intervalley scattering of the excited electrons is significantly enhanced, which leads to suppressed degree of polarization. The slight difference between P^X and P^Y can be attribute to the detailed characteristics of the different band structures of Γ-X and Γ-Y valley, which may lead to the different rate of intervalley scattering and relaxation of the excited electrons.

2.3.5 Emission anisotropy of PL spectroscopy
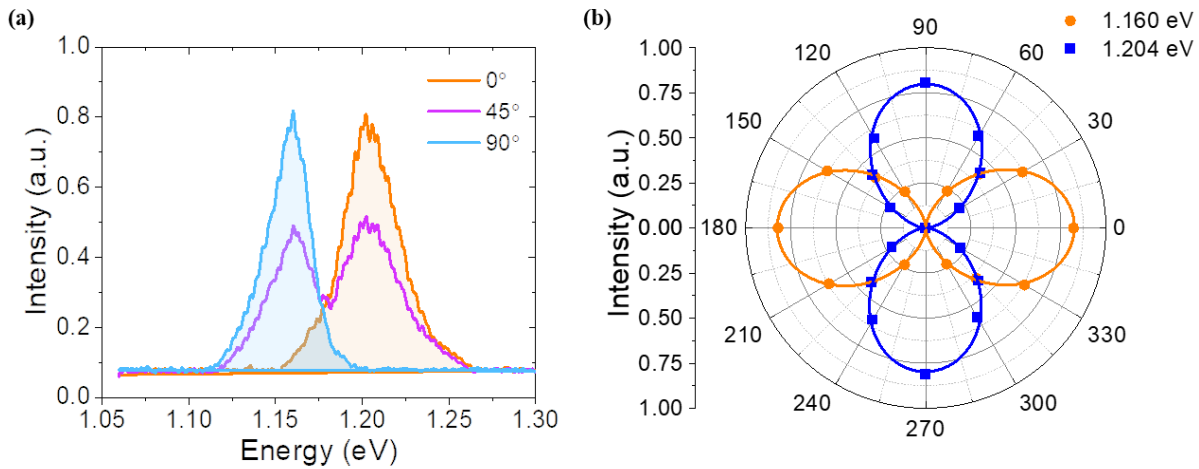
Fig 2.3.8 (a) PL spectra of SnS under different detection polarization. **(b)** Angular-resolved PL intensity of the 1.204 eV (yellow) and 1.160 eV (blue) emission peaks under different detection polarization. The fitting curves for PL emissions from Γ-X and Γ-Y valley are indicated by yellow and blue lines, respectively. All panels: from ref. *(128)*.

To further clarify the optical transition rules in SnS, we also performed PL measurements under different detection polarization. The excitation polarization was kept parallel to the y-direction of

SnS while PL signal of different emission polarization was detected. **Fig 2.3.8a** shows the PL spectrum under different detection polarization. Here, θ represents the angle between the detection polarization and x-direction. We observed a novel valley-selective linear dichroism phenomenon for the emission peaks. The emission from Γ-X valley reached the highest intensity under x-polarized detection while vanished under y-polarized detection, indicating a completely x-polarized emission from Γ-X valley. In contrast, the emission from Γ-Y valley was completely y-polarized. Both emissions from Γ-X and Γ-Y valley emerged under the detection polarization $\theta = 45°$. We extracted the angular resolved PL intensity of both peaks, which was plotted in the polar coordinate (**Fig 2.3.8b**). The emission from Γ-X valley and Γ-Y valley show the pattern of $cos^2\theta$ and $sin^2\theta$, respectively. The results demonstrate the perfect and orthogonal linear dichroism in Γ-X and Γ-Y valleys of SnS in PL. Compared with BP where single-fold linear dichroism is observed, our results represent the first observation of the valley-selective linear dichroism in PL arising from its inequivalent valleys in energy band of SnS, as illustrated in **Fig 2.3.9**. Meanwhile, the PL emissions from both valleys have different peak positions and are well resolved and perfectly polarized, which may be useful for future valleytronic applications.

The valley-selective linear dichroism arises from the optical transition rule at Γ-X and Γ-Y valley of the SnS. The optical transition rule of the PL emission is subject to interband transitional probability of the electron-hole pair, which is determined by $\left|\langle\varphi_i|p_n|\varphi_f\rangle\right|^2$ (*150, 197*). Here φ_i and φ_f represent the wave function of the initial and final states of the transition electron, respectively, while p_n $(n = x, y)$ is defined as the momentum operator where *n* is the direction of photon polarization. The optical transition is allowed only if the moment matrix elements $\langle\varphi_i|p_n|\varphi_f\rangle$ have non-vanishing values. Meanwhile, we define the initial state and the final state in Γ-X and Γ-Y valleys as φ_i^j and φ_f^j $(j = x, y)$ respectively. For the valley in Γ-X direction,

group theory analysis gives a vanishing moment matrix element along the y-direction $\langle \varphi_i^x | p_y | \varphi_f^x \rangle = 0$ (*198*). Hence, the photon transition along y-direction in Γ-X valley is forbidden. In contrast, electron transition is allowed along the x-direction in Γ-X valley due to the non-vanishing value of $\langle \varphi_i^x | p_x | \varphi_f^x \rangle$ (*198*). The strongly x-polarized photon emission from Γ-X valley in SnS is similar to that observed in BP (*49, 77*). However, different from BP, there is a nearly degenerate valley along Γ-Y direction in the energy band of SnS, where group theory analysis gives non-vanishing value of $\langle \varphi_i^y | p_y | \varphi_f^y \rangle$ and vanishing value of $\langle \varphi_i^y | p_x | \varphi_f^y \rangle$ (*198*). Hence, y-polarized photon transition is allowed while x-polarized photon transition is forbidden, leading to a completely y-polarized PL emission from the Γ-Y valley.
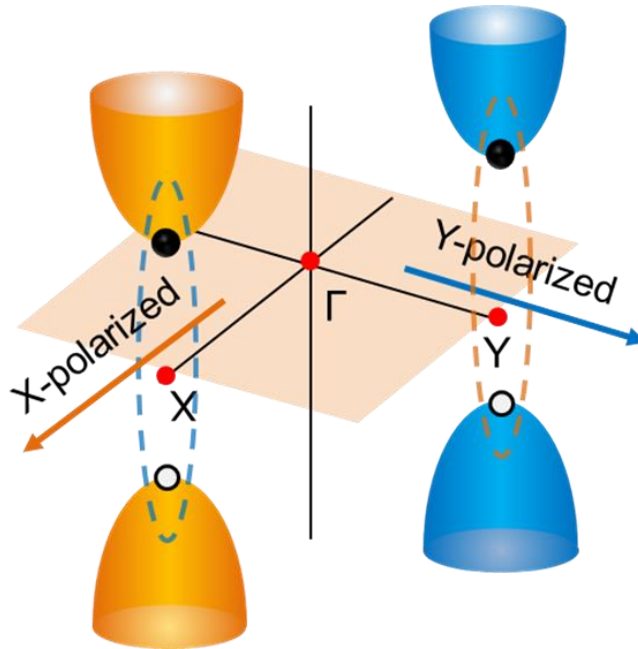
Fig 2.3.9 Schematic illustration of the optical selective rule of the band edge emission. All panels: from ref. *(128)*.

2.3.6 Linearly-polarized absorption spectroscopy

We further performed the linear polarization-resolved absorption spectrum measurement on SnS flakes to validate our observations (*208*). In this experiment, the SnS flakes were exfoliated directly onto the gold film deposited by thermal evaporation on SiO$_2$/Si substrate to achieve a strong reflection of the broadband white light, as shown in **Fig 2.3.10**. A stabilized Tungsten-Halogen light source was used to generate a broadband white light for absorption measurements. The reflection spectrum of both SnS/gold film and gold film was measured at 77 K respectively, illuminated by an incident beam with tunable polarization in the x-y plane, which is defined as R and R_0. Then the absorption spectrum of the SnS flakes was estimated as $1 - R/R_0$. This configuration has been widely used to study the absorption spectrum of the BP in previous study (*49, 76*). Here, we improved the configuration by using the gold film in substitution of the SiO$_2$/Si substrate to exclude the possible absorption and transmission by SiO$_2$/Si considering the nearly perfect reflection in measured wavelength region (*209*).
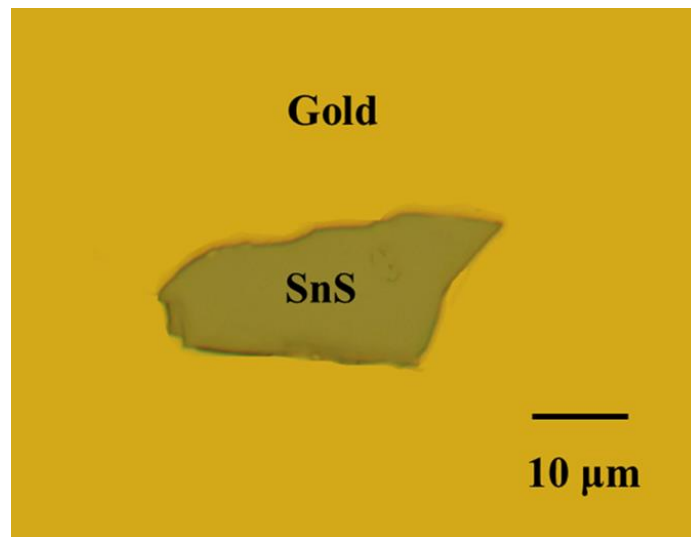
Fig 2.3.10 Optical micrograph of SnS flake exfoliated on gold film/SiO$_2$/Si substrate. All panels: from ref. *(128)*.

Fig 2.3.11 shows the anisotropic absorption spectrum under the illumination of x- and y-polarizations (solid line), together with previous PL spectrum (dots). We extracted the band gap of SnS from the onset of absorption spectrum. The band gap along Γ-X (Y) direction was 1.173 (1.147) eV. These values agreed quite well with the values 1.204 (1.160) eV along Γ-X (Y) direction obtained from the PL measurements. The consistence between the absorption and PL results further confirmed that the two PL peaks originate from the unique band edge transitions along Γ-X and Γ-Y directions.
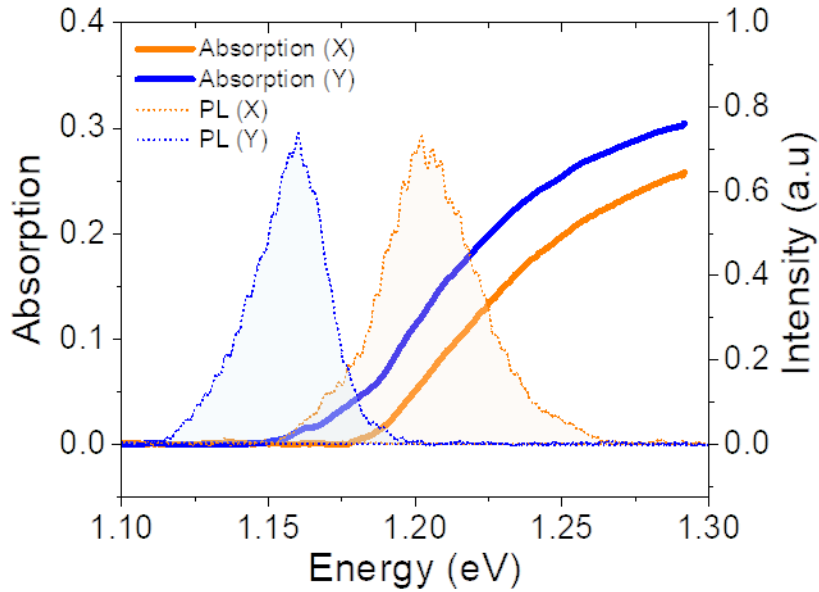
Fig 2.3.11 Anisotropic absorption spectra of SnS along x- and y-polarized illumination at 77K and its comparison with PL spectra. All panels: from ref. *(128)*.

The angular resolved absorption spectra under different illumination polarization are plotted in **Fig 2.3.12a**. The absorption edge of SnS shows a clear redshift when the incident light polarization was rotated from x- to y-direction. We further extracted the band gap of SnS along different crystal directions from the absorption spectrum measurement, as shown in **Fig 2.3.12b**. The extracted angular resolved band gap was well fitted with the function of $a cos^2\theta + b$, where

a and *b* are fitting parameters. Here, a=1.148 eV represents the energy gap along Γ-Y direction and b=0.030 eV represents the energy difference between Γ-X and Γ-Y valley, consistent with the value directly extracted from the absorption spectra.
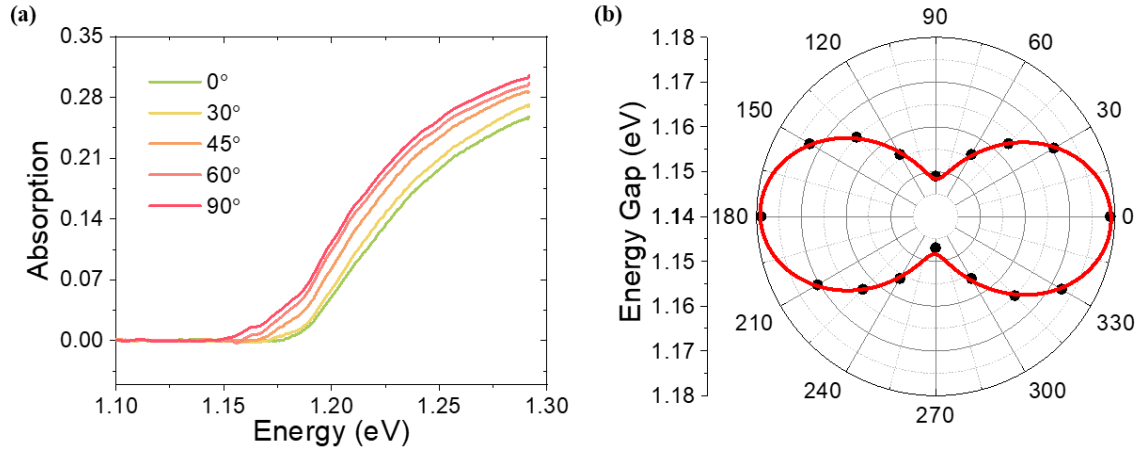
Fig 2.3.12 (a) Absorption spectra of SnS at 77K under different illumination polarization. **(b)** Angular-resolved energy gap extracted from the absorption spectra. All panels: from ref. *(128)*.

We further measured the linearly-polarized absorption spectrum of SnS under 298K, as shown in **Fig 2.3.13**. The absorption edge exhibits an overall redshift compared with the low temperature results, a typical semiconductor property indicating that our observations are band gap transitions (*210*). Moreover, the redshift of the absorption edge along y-direction compared with that along x-direction is similar to that observed at 77 K. This observation confirmed that the band gap along Γ-X direction is larger than that along Γ-Y direction, consistent with our previous measurement. More importantly, it provided strong evidence for the optical selective rule since the absorption of x-polarized photon was forbidden in the valley along Γ-Y direction. In that case, the Γ-Y valley can be pumped only with y-polarized photon, demonstrated by the redshift of the absorption edge under y-polarized illumination.
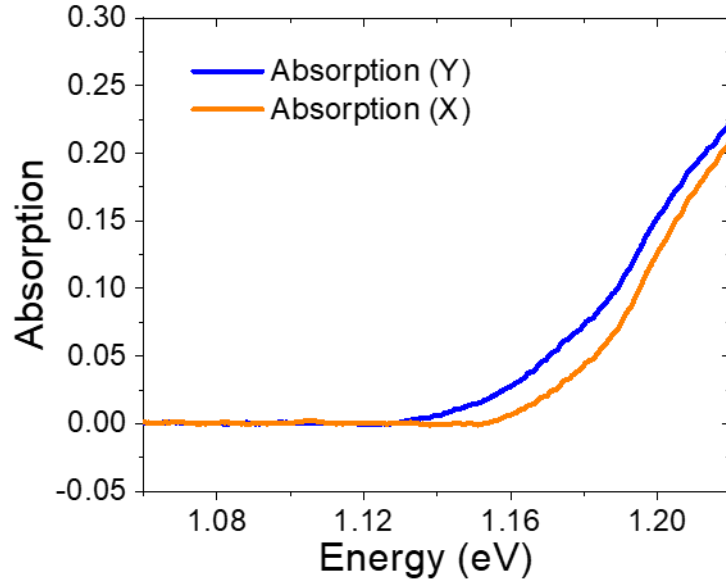
Fig 2.3.13 Anisotropic absorption spectra of SnS along x- and y-polarization at room temperature. All panels: from ref. *(128)*.

2.3.7 Discussion and summary

In conclusion, we observe the novel valley-selective linear dichroism of PL in layered thin-film SnS. Two photon emission peaks, arising from Γ-X and Γ-Y valley transitions respectively, are purely linearly polarized along x- and y-directions, respectively, regardless of the excitation laser polarization. This valley-selective linear dichroism and the highly anisotropic band structure of SnS were further elaborated by angular-resolved optical absorption spectroscopy. Our observations reveal the highly anisotropic electronic band structure and the unique optical transition rules in a low-symmetry group IV monochalcogenide SnS, further establishing it as a promising material for valley-related applications.

3. Mid-infrared optoelectronic applications in thin-film materials

3.1 Bright and widely-tunable mid-infrared light emissions in thin-film BP

3.1.1 Motivation

Mid-infrared, referring to the spectrum region from 2 µm to 20 µm, hosts many important applications. For example, the typical temperature of our environment is approximately 300K, corresponding to the thermal radiation wavelength of 10 µm. Therefore, thermal imaging mainly applied mid-infrared detection, which has been widely used in night vision (*89, 90*) and medical imaging (*91, 92*). In addition, the vibration frequency of the molecule atoms typically ranges from 10 THz to 100 THz, corresponding to wavelength range from 3 µm to 30 µm (*211*). Therefore, mid infrared spectrum region is also fundamental to molecular sensing, which has been applied in chemical analysis (*93, 94*) and gas sensing (*212, 213*). Besides that, mid-infrared technologies are also critical for space exploration (*214, 215*) and radiative cooling (*216*). Therefore, it is highly desired to develop novel mid-infrared light generation, modulation and detection technologies.

The conventional mid-infrared light generation mainly leverages the intersubband transitions in MQW structures (*109, 110*). Today, mid-infrared QCL are widely used in many optical applications (*111, 112*). However, the light emissions from multiple-quantum-well structures are lack of large tunablity and therefore, difficult to for optical modulation covering a wide spectral range. The emerging 2D materials provide great opportunities to break this limitation since their atomically thin nature makes them intrinsically sensitive to external modulations like electric field (*217, 218*). However, investigations on their light emission properties and applications in

mid-infrared spectral range were rare due to less appropriate candidates and more challenging detection scheme.

Layered BP (*75, 76, 149, 219-222*) has been recently rediscovered as an attractive 2D and thin-film material, providing rich opportunities for investigating both fundamental physics (*49, 77, 223-228*) and device applications (*56, 78, 83, 84, 229-234*). Thin-film BP (> 10 layers) has a moderate bandgap of around 0.33 eV (*31, 50*), suitable for mid-infrared applications (*56, 84, 231, 232*). Moreover, the bandgap of BP can be widely tuned by a moderate external electric field (*51-53, 235-237*), thus extending the operational spectral range beyond the cut-off wavelength of pristine thin-film BP (~ 3.7 μm). Recently, a widely tunable mid-infrared photodetector with a detection limit up to 7.7 μm has been demonstrated in a dual-gate hBN/BP/hBN device (*55*). Meanwhile, the broadband photodetection in infrared spectral region has been successfully demonstrated in various heterostructures consisting of BP (*54, 238, 239*). In contrast, the light emitting properties of BP have not been investigated extensively. For example, only PL spectra of 1-5 layers have been explored, which is limited to visible and near-infrared region (*49, 240*). Interestingly, the mid-infrared light emission properties of thin-film BP with thickness greater than 6 layers have rarely been reported, probably due to the challenges in PL measurements in mid-infrared wavelength range. In addition, the impact of the external electrical field on light emission properties of BP remains unexplored, which significantly limits its potential for tunable mid-infrared light emitting applications.

3.1.2 Establishment of a mid-infrared PL measurement system

81
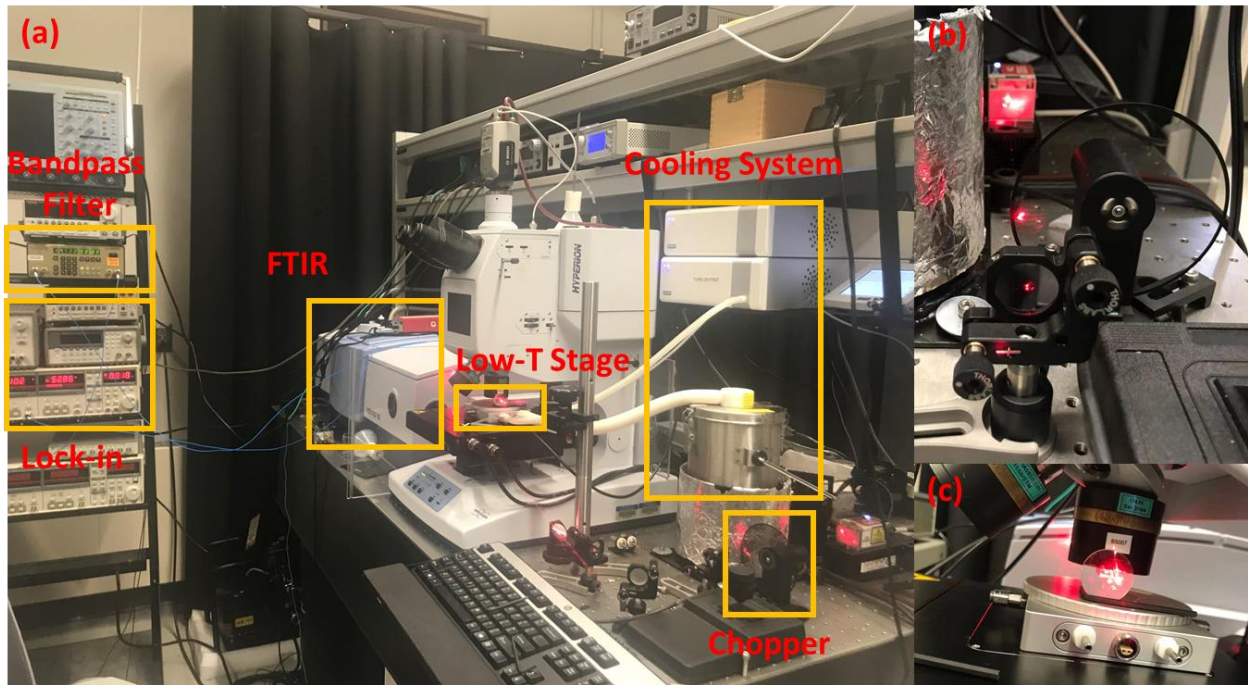
Fig 3.1.1 (a) An overall photo of the low-temperature mid-infrared PL measurement setup. **(b)** A close-up of the set-up at the mechanical chopper side. **(c)** A close-up of the set-up at the low-temperature sample stage side.
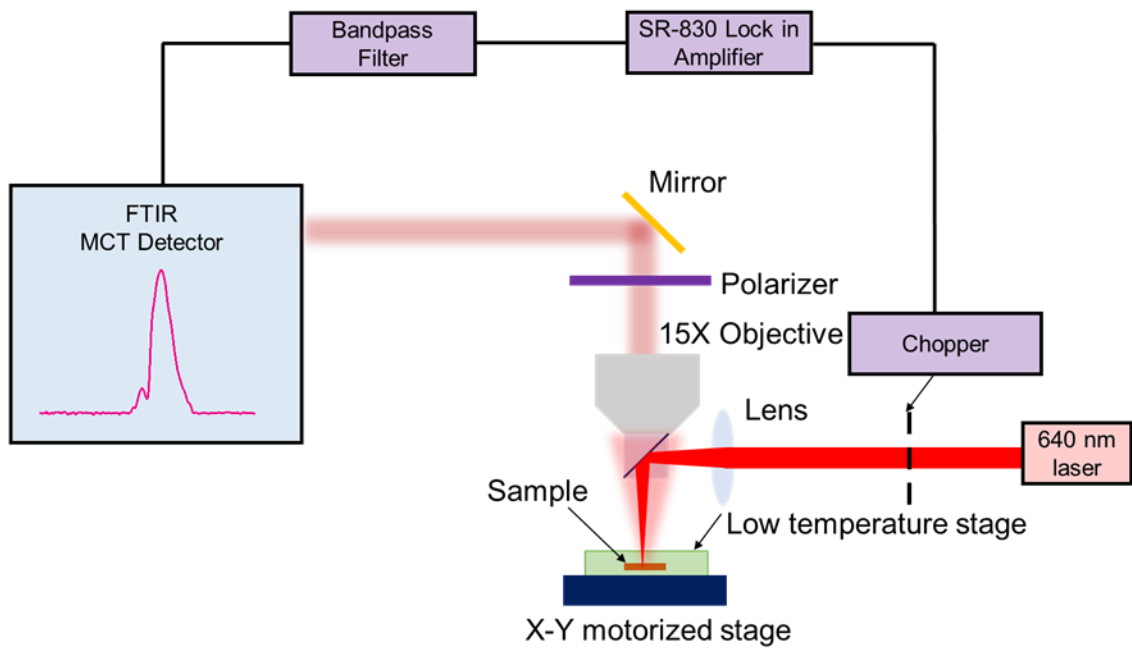
Fig 3.1.2 Schematic illustration of the mid-infrared PL measurement setup. All panels: from ref. *(129)*.
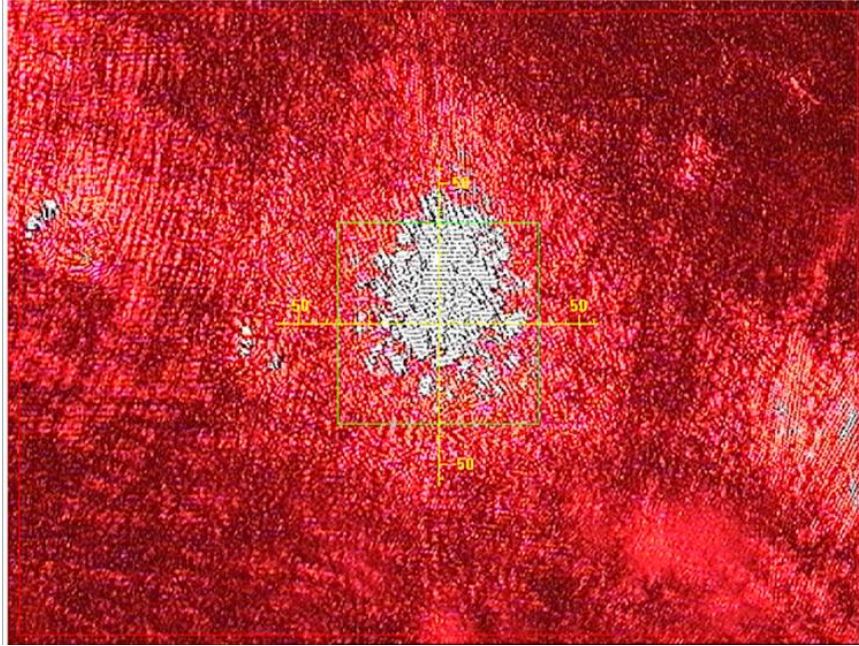
Fig 3.1.3 Optical image of the focused laser spot under the microscope.

Here, we established a home-made mid-infrared micro-PL measurement system to resolve the detection challenge, as shown in **Fig 3.1.1a-c**. The schematic illustration of the system is shown in **Fig 3.1.2**. A chopped 640 nm solid-state laser was used as an excitation source, which was focused on the sample by optical lenses and a prism attached to 15× mid-infrared objective lens in a Hyperion 2000 microscope. The radius of the laser spot focused onto the sample was optimized to be around 20 µm, which is smaller than the sample size, as shown in **Fig 3.1.3**. The PL signal was collected by this 15× objective and was further analyzed using a Brucker Fourier transform infrared spectrometer (FTIR). An external lock-in scheme similar to that reported in previous works (*241, 242*) was used to suppress the noise arising from the background thermal emission. The Stanford Research SR830 lock-in amplifier was in reference to the mechanical chopper at a chopping frequency of 10 kHz. Each spectrum is smoothed by averaging 512 measurements in FTIR to lower the noise level. The resolution of the directly measured spectra is

8 cm^{-1}. The polarization-resolved PL measurements of emission anisotropy were performed by rotating an infrared polarizer in the detection path. The sample was placed in a HFS600E-PB4 low-temperature stage from Linkam Scientific Instruments for temperature dependent PL measurements. For gate tunable PL measurements, the device was first wire-bonded to a chip carrier and the external displacement field was applied by a Keithley 2612 source meter.

3.1.3 Sample Preparation and Device Fabrication

The BP crystals with purity over 99.995% was purchased from HQ Graphene. BP flakes for optical characterizations were directly deposited onto the 285-nm SiO$_2$/Si substrate in an argon-filled glove box using the standard mechanical exfoliation method. Then, BP flakes were covered with hexagonal boron nitride (hBN) flakes using the polymer-free dry transfer method (*243*) to prevent BP from oxidation. **Fig 3.1.4a** shows the optical image of a typical hBN-covered BP flake. Its thickness is about 46-nm, determined by the atomic force microscopy (AFM) measurements. The crystal orientation of BP flake was identified by the polarization-resolved Raman measurements, as reported previously (*157, 158*). The Raman spectroscopy was performed in Horiba LabRAM HR Evolution Raman Microscope with an excitation photon energy of 2.33 eV. We performed the polarization-resolved Raman measurement by rotating the sample with respect to the excitation laser polarization. **Fig 3.1.4b** exhibits the Raman spectrum of the BP. The intensity ratio of A_g^2 and A_g^1 mode reaches the maximum when the excitation laser polarization was aligned along the armchair (x) direction of BP flakes (*73*), as shown in **Fig 3.1.4c**.
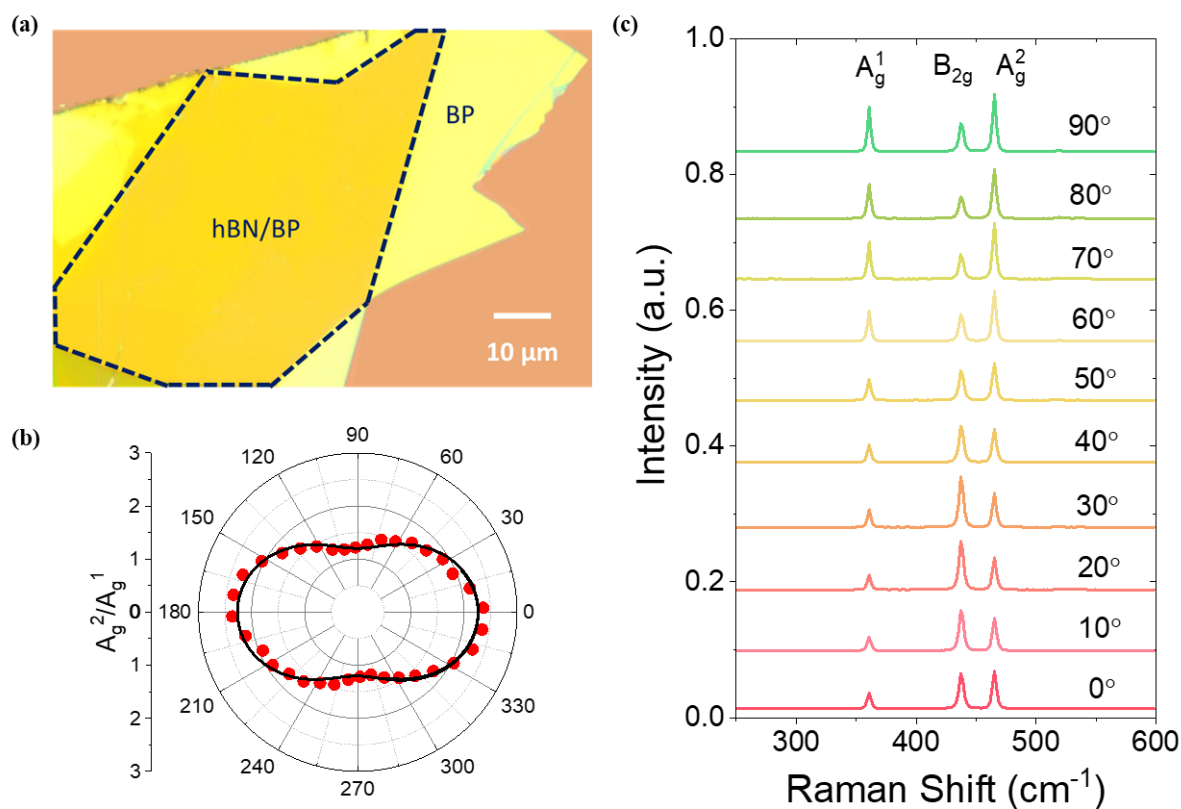
Fig 3.1.4 (a) Optical image of the hBN covered 46-nm thick BP flake on a 285-nm SiO$_2$/Si substrate. **(b)** Polarization-resolved Raman spectrum of the 46-nm thick BP. **(c)** The measured (dotes) and fitted (line) angular-resolved Raman intensity ratio of A$_g^2$ and A$_g^1$ mode. All panels: from ref. *(129)*.

Dual-gate hBN/BP/hBN heterostructure device was fabricated for gate tunable PL measurements, where a vertical electric field can be applied through the BP sample. The schematic image of the dual-gate hBN/BP/hBN heterostructure is shown in **Fig 3.1.5**. The hBN encapsulation has been demonstrated to prevent the BP from oxidation, and the stability of the hBN/BP/hBN devices can last for months without noticeable degradation (*98, 244*). Moreover, the hBN encapsulation can minimize the doping effect induced by the environment, leading to intrinsic BP (*55, 244*). The hBN-encapsulated BP heterostructures were fabricated using the polymer-free dry transfer
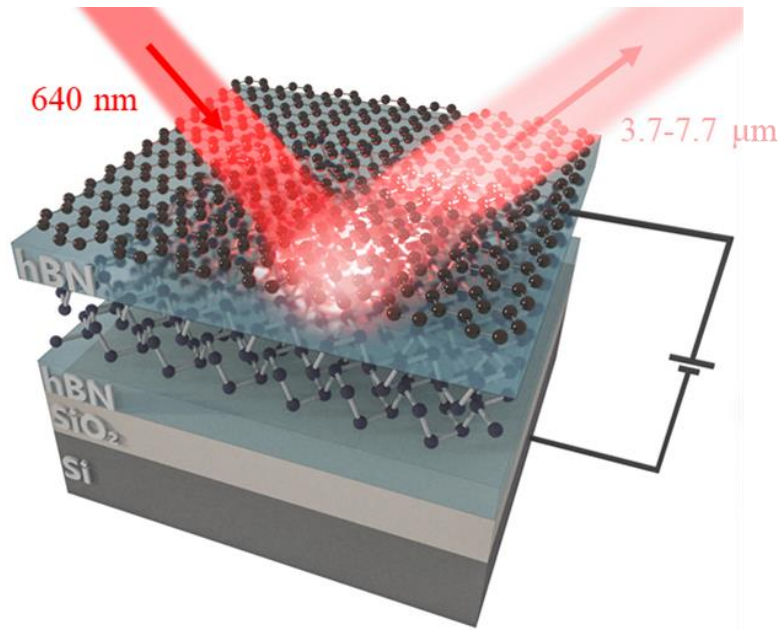
Fig 3.1.5 The schematic illustration of the dual-gate hBN/BP/hBN device. All panels: from ref. *(130)*.

method (*243*) and both hBN and BP layers were directly deposited onto the 285-nm SiO$_2$/Si substrate in sequence. All the exfoliation and transfer process were performed in an argon-filled glove box. As an electrode material, the monolayer CVD graphene was then transferred onto the hBN-encapsulated BP devices, which functions as top gate electrode (*245, 246*). Due to its extraordinary transparency with the transmittance over 98% in the mid-infrared spectrum region (*108*), CVD graphene electrode introduces negligible loss, which facilitates the measurement of the PL spectra. The Vistec 100 kV electron-beam lithography system and the Oxford Plasmalab 100 Reactive Ion Etching System were used to pattern the graphene top-gate. The metal electrode was formed by thermally evaporating chromium/gold (3/27 nm) films. The Si was used as the back gate. **Fig 3.1.6a** exhibits the optical image of the dual-gate hBN/BP/hBN device for optical measurements. The thicknesses of the BP, the bottom and top hBN flakes were 10.5 (~20 layers), 9 and 22 nm, respectively, determined by AFM measurements. The crystal orientation of

the BP flakes was also identified by the polarization-resolved Raman measurements, as shown in **Fig 3.1.6b**. **Fig 3.1.6c** shows the angular-resolved Raman intensity ratio of the A_g^1 mode and A_g^2 mode. Similarly, the armchair (x) and zigzag (y) directions are determined when intensity ratio reaches its maximum and minimum, respectively.
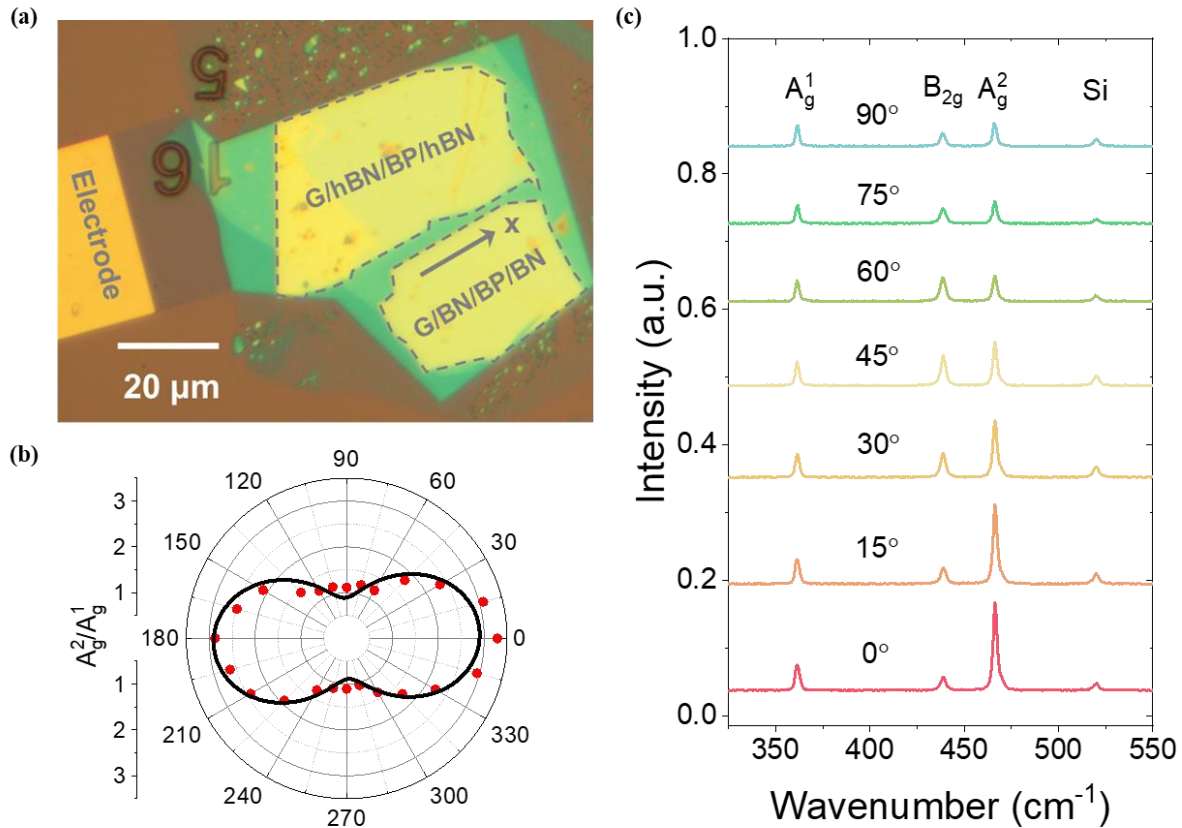
Fig 3.1.6 (a) Optical micrograph of the dual-gate hBN/BP/hBN device with CVD graphene as the top-gate. **(b)** Polarization-resolved Raman spectrum of the 10.5-nm thick BP. **(c)** The measured (dots) and fitted (line) angular-resolved Raman intensity ratio of A_g^2 and A_g^1 mode. All panels: from ref. *(130)*.

3.1.4 Bright PL emissions from thin-film BP
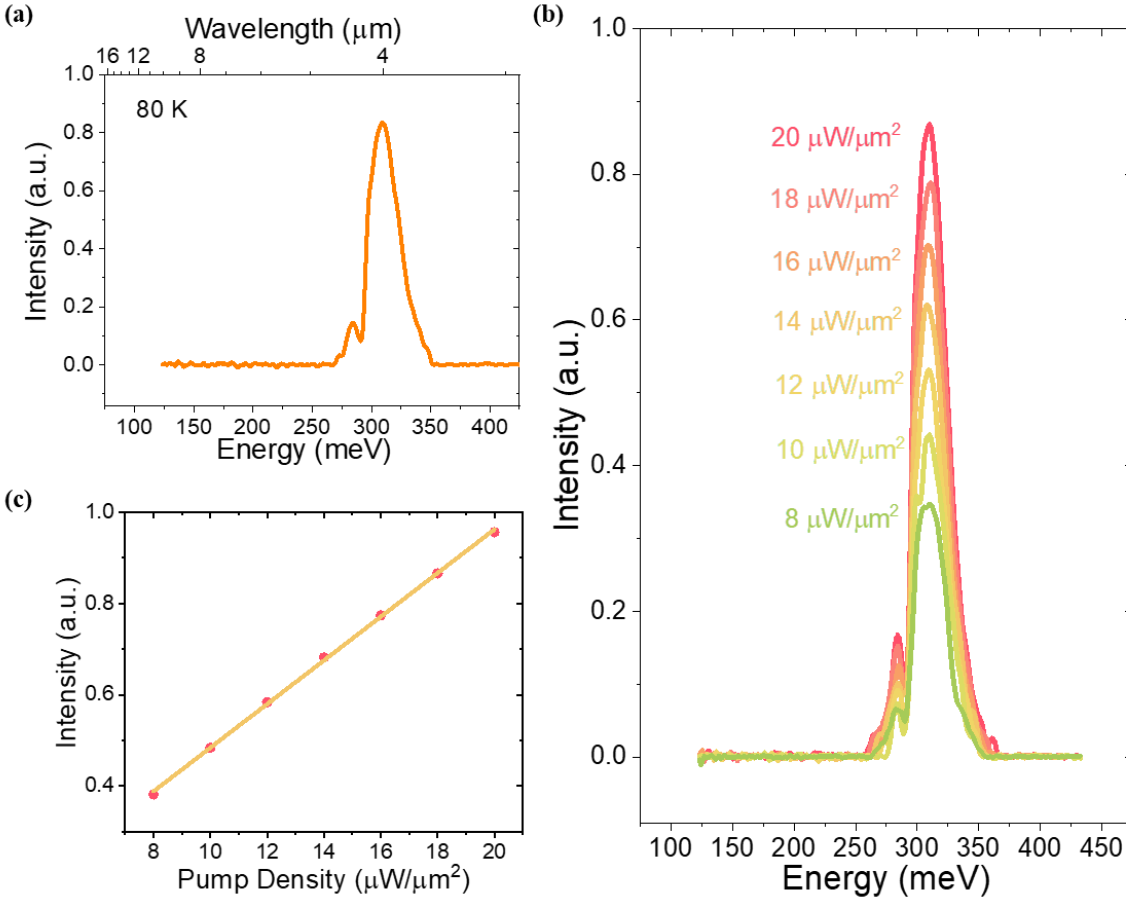
Fig 3.1.7 (a) Mid-infrared PL spectrum of the 46-nm thick BP at 80 K. **(b)** Excitation power dependence of the PL spectrum of the 46-nm thick BP. **(c)** The measured (dots) and fitted (line) power dependence of the BP PL peak intensity. All panels: from ref. *(129)*.

We first performed the PL measurements on the 46-nm thin-film BP flake at 80K with excitation power of 10 $\mu W/\mu m^2$. As shown in **Fig 3.1.7a**, the PL spectrum exhibits a peak position at 0.308 eV, corresponding to the bandgap of the bulk BP since the excitonic effect is negligible in thin-film BP thicker than 8 layers. The insignificant excitonic effect can be attribute to the reduced screening effect and relatively large dielectric constant in multilayer BP *(31)*. In fact, in bulk BP, the exciton binding energy is only around 10 meV *(48)*. The bandgap of the thin-film BP extracted from PL spectrum also agrees with the previous theoretical calculations *(31)* and the

infrared absorption measurements (*50*). To ensure the PL spectroscopy is in the linear response regime, we measured the PL spectrum of BP under different excitation power densities (**Fig 3.1.7b**). As exhibited in **Fig 3.1.7c**, the PL peak intensity shows a linear relationship with the power intensity ranging from 8 to 20 $\mu W/\mu m^2$.
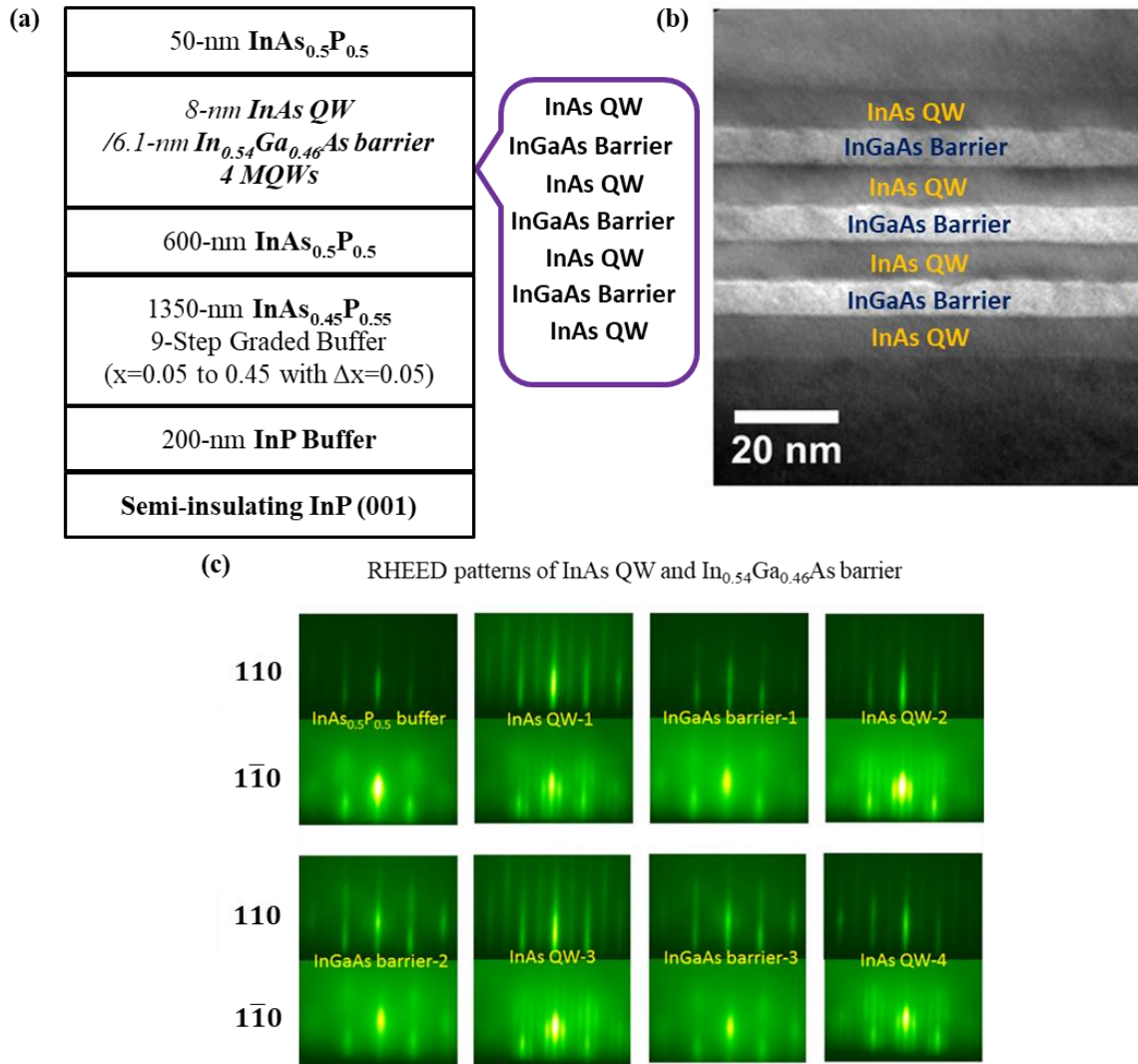
Fig 3.1.8 (a) Schematic structure of InAs MQW grown on indium phosphide (InP) substrate. **(b)** Cross-sectional transmission electron microscopy (X-TEM) of InAs QW/$In_{0.54}Ga_{0.46}$As barriers. **(c)** The Reflection high-energy electron diffraction (RHEED) patterns taken during the growth process. All panels: from ref. *(129)*.

Since it is difficult to accurately quantify the mid-infrared loss spectrum of various optical components in the collection pathway of the home-made PL system and the Fourier transform infrared spectrometer, we do not report the absolute quantum efficiency directly in this work. Instead, we evaluated the relative PL emission intensity of thin-film BP by comparing its PL with an InAs MQW sample grown by molecular beam epitaxy (MBE) with peak emission at 2.45 μm. The schematic structure of InAs MQW is shown in **Fig 3.1.8a**. Cross-sectional transmission electron microscopy (X-TEM) showed a coherently strained MQW active region and also revealed clear QW/barrier interfaces (**Fig 3.1.8b**). Reflection high-energy electron diffraction (RHEED) patterns were observed during growth showed streaky 2×4 patterns for the $InAs_xP_{1-x}$ graded buffer and the InAs QWs along with a streaky 1×3 pattern for the tensile strained $In_{0.54}Ga_{0.46}As$, as shown in **Fig 3.1.8c**, both indicating good crystal quality (*247-250*).

Fig 3.1.9 plots the PL spectra of both BP and InAs MQW measured at the same excitation power density of 10 µW/µm^2 and 80 K. The absolute PL intensity of black phosphorus is only seven times weaker than that of the InAs MQW, demonstrating that the PL emission from the thin-film BP is quite bright. Here we want to emphasize that our measurement results do not directly indicate that the quantum efficiency of PL in BP is seven times smaller than that in the InAs MQW. The absorbed powers of the pumping light (640 nm) by BP and InAs can be different and the collection and detection efficiency at 2.45 and 4 µm can also be different. However, this comparison shows that the PL signal from BP is quite bright such that the BP PL spectrum can be plotted together with the InAs MQW sample; where similarly grown MQW samples can serve as the active region for electrically pulsed, room-temperature lasers (*251*). Therefore, the natural next step will be exploring the cavity controlled light emission and possible lasing based on BP, since the emission efficiency depends on the competition between the radiative and non-radiative

processes and the radiative decay time can be controlled by the local electromagnetic environment (*252*).
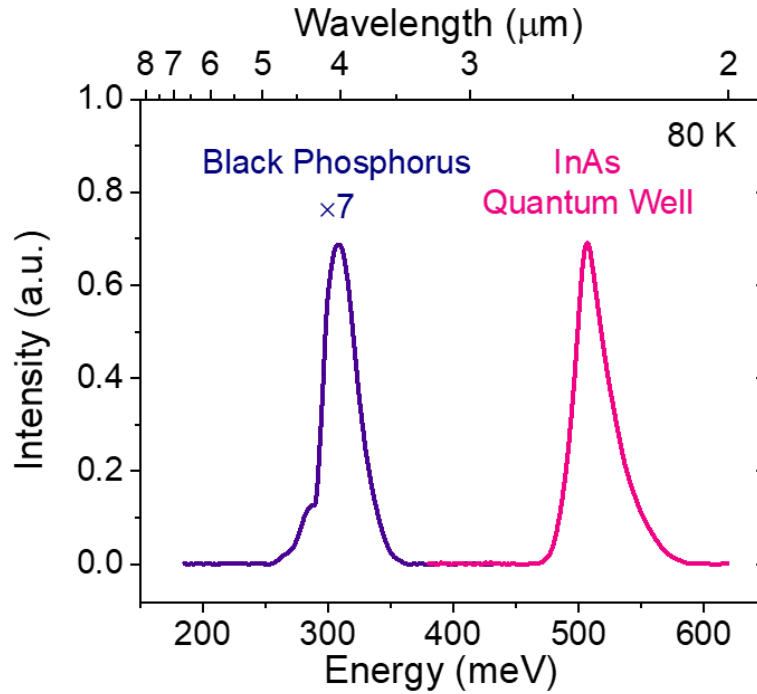
Fig 3.1.9 The PL emission spectra of thin-film BP and the InAs quantum well (The PL intensity of BP is multiplied by a factor of 7). All panels: from ref. *(129)*.

3.1.5 Band Properties of thin-film BP

The PL spectroscopy can be utilized to probe the band properties of thin-film BP. We first explored the anisotropy of the PL emission, where PL spectrum along armchair (x) and zigzag (y) directions were plotted in **Fig 3.1.10a**, respectively. The PL emission was almost perfectly polarized along the armchair (x) direction under the excitation photon energy of 1.94 eV. The angular resolved PL intensity of BP was well fitted with the function of $a cos^2\theta + b$ (**Fig 3.1.10b**), where θ is the angle between emission polarization direction and the armchair-direction of BP, and *a*, *b* are fitting parameters. This linear polarized PL emission from BP is because the

band-edge optical transition along the zigzag-direction was forbidden according to the symmetry analysis (*49, 50*). In fact, the similar PL emission anisotropy has been previously observed in its monolayer to trilayer counterparts (*49, 77*). The observation reported here also agrees with previously reported linearly polarized, band-edge infrared absorption in thin-film BP, since emission and absorption are two reciprocal processes (*50*). The anisotropy of PL emission in thin-film BP will be discussed in detail in **Section 3.1.8**.
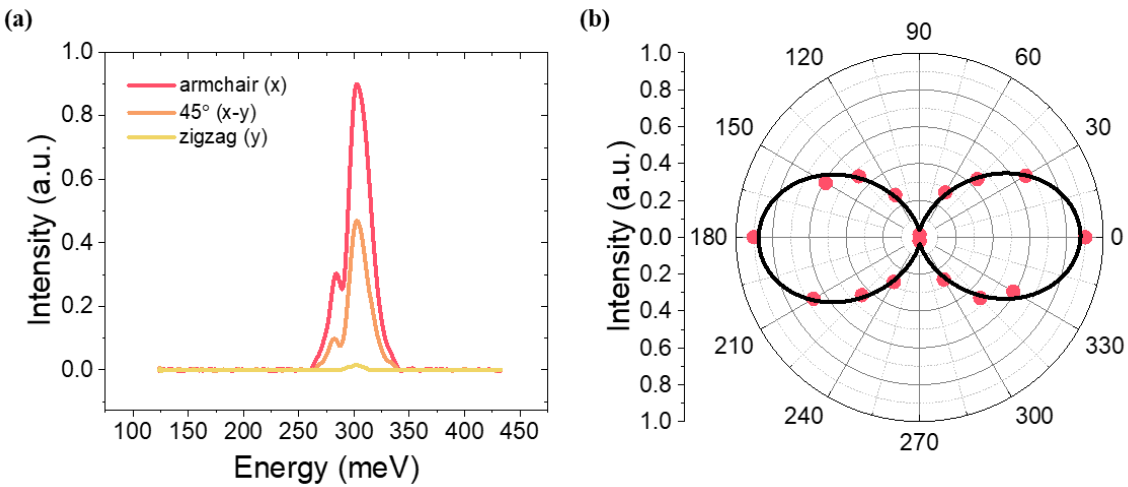
Fig 3.1.10 (a) Polarization-resolved PL spectra of 46-nm thick BP along x- (red), x-y (orange, 45 degrees to x and y) and y- (yellow) directions. **(b)** The measured (dots) and fitted (line) angular-resolved PL peak intensity of BP. All panels: from ref. *(129).*

The temperature dependence of the PL spectrum was then measured to investigate the temperature dependence of the 46-nm thin-film BP bandgap. **Fig 3.1.11a** shows the PL spectra at different temperatures ranging from 80 to 300 K at a step of 20 K. The PL intensity decreases as temperature increases, as plotted in **Fig 3.1.11b**. The decreasing PL intensity with increasing temperature probably arises from the thermal activation of the nonradiative recombination center at higher temperature (*253, 254*). At higher temperature, the probability of nonradiative recombination of the electron-hole pairs increases, which suppresses the PL emission.

92

Interestingly, the PL peak position of BP exhibits an anomalous blueshift with increasing temperature. This phenomenon reveals that the bandgap of thin-film BP increases monotonically with temperature, which is opposite to conventional semiconductors (*255-257*). Previously, such an anomalous temperature dependence of BP bandgap was explored both theoretically (*258*) and experimentally based on photoconductivity spectroscopy (*259*). **Fig 3.1.11c** shows the BP bandgap at different temperatures extracted from the PL spectra, which increases from 0.308 eV at 80 K to 0.334 eV at 300 K. The anomalous temperature-dependent PL position of BP can be attributed to the renormalization of bandgap from both electron-phonon coupling and lattice thermal expansion, which has been theoretically predicted (*258*) and also experimentally observed in monolayer BP (*253*). As shown in **Fig 3.1.11c**, the anomalous temperature-dependent trend can be divided into two temperature regions: 80-120 K and 160-300 K, giving different temperature coefficient (dE_g/dT) (*259*). Under low temperature (< 120 K), electron-phonon coupling and lattice thermal expansion play comparable role in the renormalization of the bandgap of BP. In contrast, at high temperature (> 160 K), the contributions from electron-phonon interaction become weaker while the lattice thermal expansion dominates. Our observation is also consistent with the recent studies on mechanical strain-induced bandgap renormalization in thin-film BP (*260-262*), since lattice thermal expansion can induce a similar strain effect. The linear fitting was performed to extract the temperature coefficient (dE_g/dT) of the optical bandgap in respective temperature ranges, which gives 1.53×10^{-4} eV/K and 1.04×10^{-4} eV/K within 80-120 K and 160-300 K, respectively. Interestingly, our measured temperature coefficient in both temperature ranges is about 40% smaller than previous theoretical prediction (*258*) and measurement results based on photoconductivity spectroscopy (*259*). As a result, the overall bandgap increases from 80 to 300 K measured in our experiment of 26 meV is also about

40% smaller than that reported (*240*). Such a difference could be due to the different methods used for the estimation of the BP bandgap. We also observe a side peak at around 283.5 meV in **Fig 3.1.11a**, whose position is almost independent of the temperature. This side peak may be attributed to a defect level. Since the bandgap renormalization is due to the anharmonic properties of phonons and defects experience different local lattice vibrations, it is not surprising that the defect level exhibits a different temperature behavior from that of the bandgap. On the other hand, it is also possible that the side peak is caused by the absorption of residue carbon dioxide in the detection optical pathway. Regardless of its origin, this side peak has minimal impact on our conclusion due to its low amplitude. The main PL properties are hardly affected by this side peak.

The anomalous temperature-dependent bandgap of BP can also be described based on a two-oscillator model, which contains two isolated Einstein oscillators governed by two discrete phonon energies (*263, 264*). The two-oscillator model has been leveraged to fit the temperature dependence of the bandgap of semiconductors including monolayer black phosphorus, where the bandgap E_g can be expressed as (*253, 265, 266*)

$$E_g = E_0 + E_1 \left(\frac{2}{e^{\frac{\hbar\omega_1}{k_B T}} - 1} + 1 \right) + E_2 \left(\frac{2}{e^{\frac{\hbar\omega_2}{k_B T}} - 1} + 1 \right) \tag{22}$$

Here, E_0 is bare bandgap representing the low-temperature bandgap without considering the zero-point motion energy, $\hbar\omega_1$ and $\hbar\omega_2$ denotes two oscillator energies, and E_1 and E_2 govern the renormalization energy strength of two oscillators. Here we choose $\hbar\omega_1 = 17.2$ meV and $\hbar\omega_2 = 52.8$ meV, extracted from the phonon densities of monolayer BP (*267*). Although the phonon densities may vary slightly with thickness, the changes are expected to be small such that

the fitting is hardly affected (*267, 268*). As shown in **Fig 3.1.11c**, the fitting results based on the two-oscillator model (dashed line) agree with the experiments well. The fitting results yield the fitting parameters E_0=339 meV, E_1=21 meV and E_2=-55 meV, respectively. The bandgap at low temperature (~308 meV at 80 K) is smaller than the bare bandgap (339 meV), indicating that the electron-phonon interactions can significantly renormalize the bandgap of the thin-film BP.
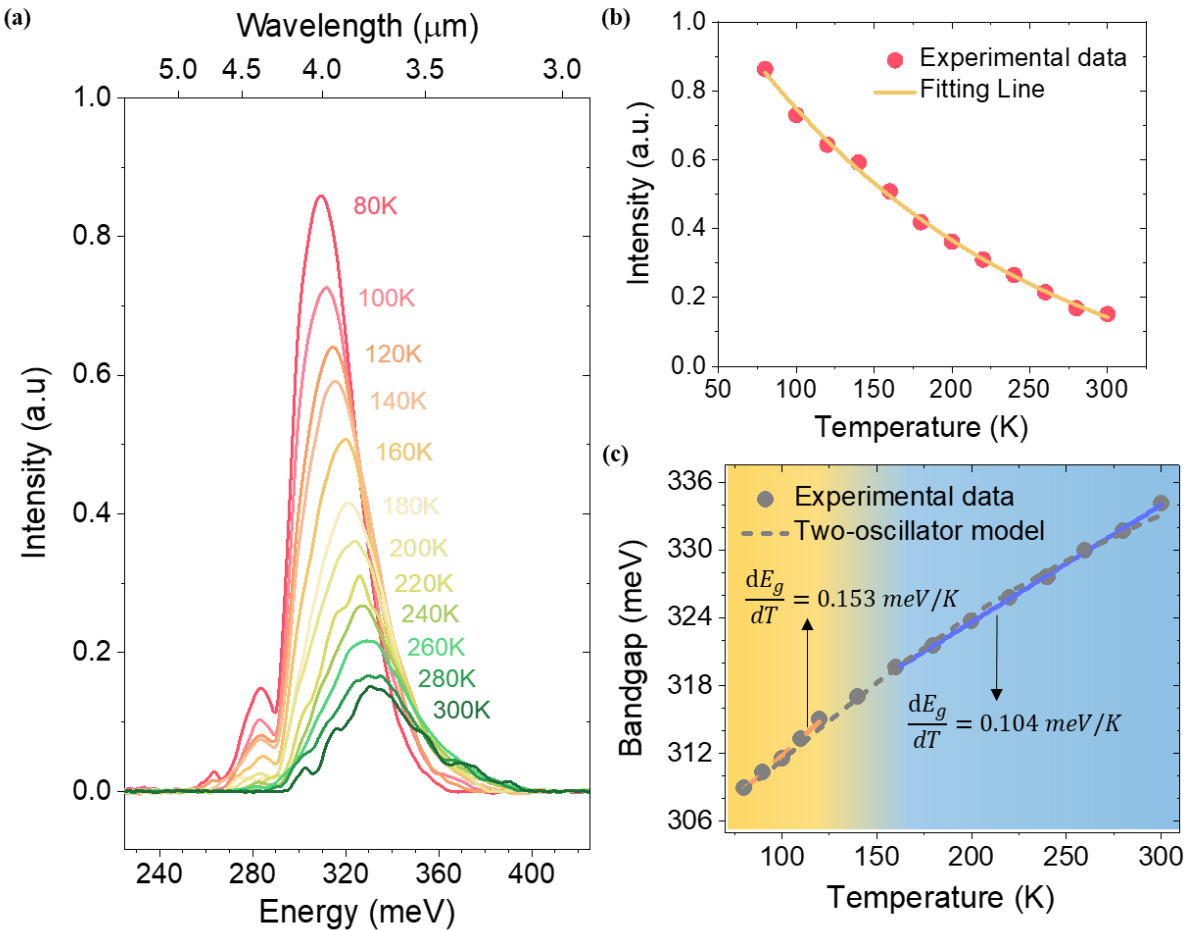
Fig 3.1.11 (a) Temperature dependence of the PL spectrum of the 46-nm thick BP. **(b)** Temperature dependence of the BP PL peak intensity. **(c)** Temperature-dependent bandgap of BP extracted from the PL peak position. All panels: from ref. *(129)*.
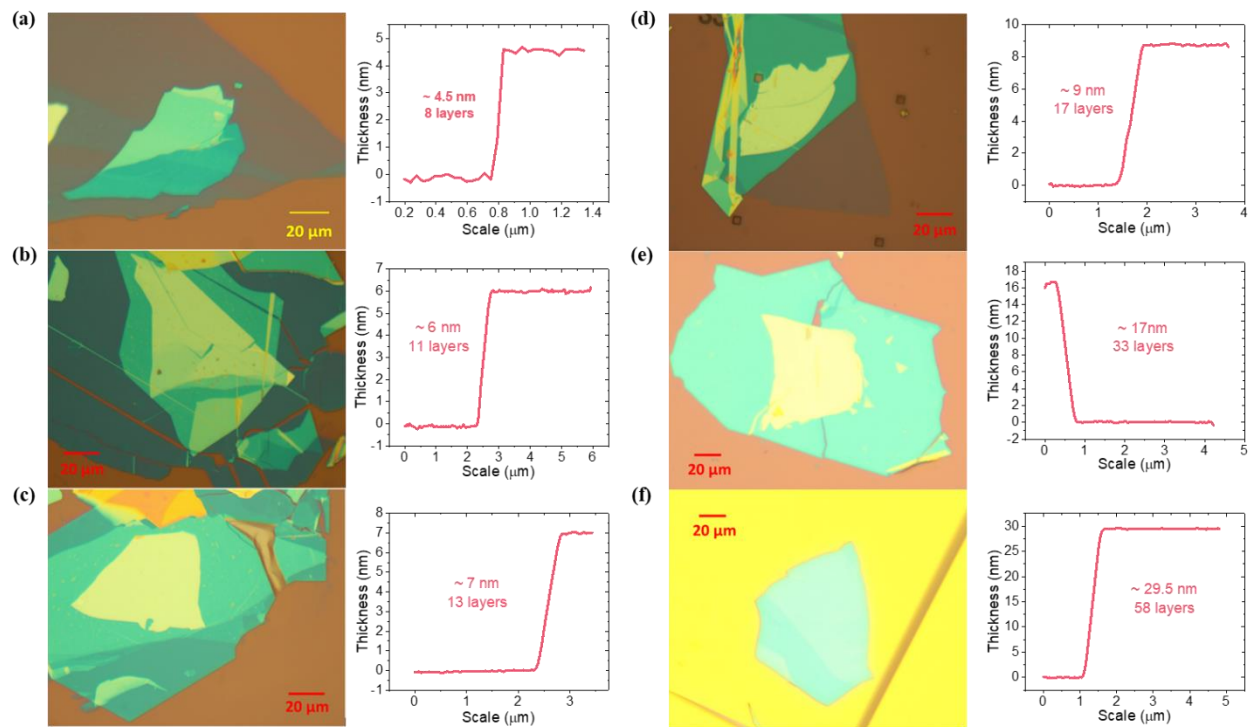
Fig 3.1.12 Optical image and detailed AFM analysis of BP with different layer number of **(a)** 8 layers, **(b)** 11 layers, **(c)** 13 layers, **(d)** 17 layers, **(e)** 33 layers, **(f)** 58 layers. All panels: from ref. *(129)*.

We further investigated the thickness-dependent bandgap through PL measurements on thin-film BP with thicknesses varying from 4.5- to 46-nm at 80 K. The optical image and detailed AFM analysis of these flakes are exhibited in **Fig 3.1.12 a-f**. **Fig 3.1.13a** exhibits the normalized PL spectra of thin-film BP at various thickness. With increasing layer numbers, the PL peak position shows a redshift, revealing the decreasing bandgap of BP. The layer-dependent bandgap of thin-film BP was summarized in Fig. 4b, which decreases monotonously from 0.441 eV at 4.5-nm (~8 layers), to 0.338 eV at 10-nm (~19 layers) and eventually to 0.308 eV in 46-nm thick BP (~91 layers). We added an error bar of ±1 layer as shown in Fig. 4b to take the possible errors in AFM measurements into account. As reported previously, the layer-dependent bandgap of BP can be well described by a one-dimensional tight-binding model, taking only the nearest-neighbor interlayer interaction into consideration *(49, 50)*. For an N-layer BP, both conduction

96

band and valence band will split into N subbands at the Γ point of the Brillouin zone due to the interlayer interactions. Then the energy gap between conduction band and valence band with the same subband index n $(n = 1, 2, 3, ..., N)$ E_N^n can be expressed as (49, 50)

$$E_N^n = E_g - 2(\gamma_c - \gamma_v)\cos\left(\frac{n\pi}{N+1}\right) \qquad (23)$$

Here, E_g represents the bandgap of monolayer BP, and γ_c and γ_v denote the nearest neighbor interlayer interactions of the conduction band and the valence band, respectively. The bandgap is determined by the energy difference between the conduction band minimum and the valence band maximum in subband $n = 1$. Using $E_g = 2.12$ eV and $\gamma_c - \gamma_v = 0.905$ eV, we fit the experimental data, as shown in **Fig 3.1.13b**. The fitted curve agrees with the measured thickness dependent bandgap very well.
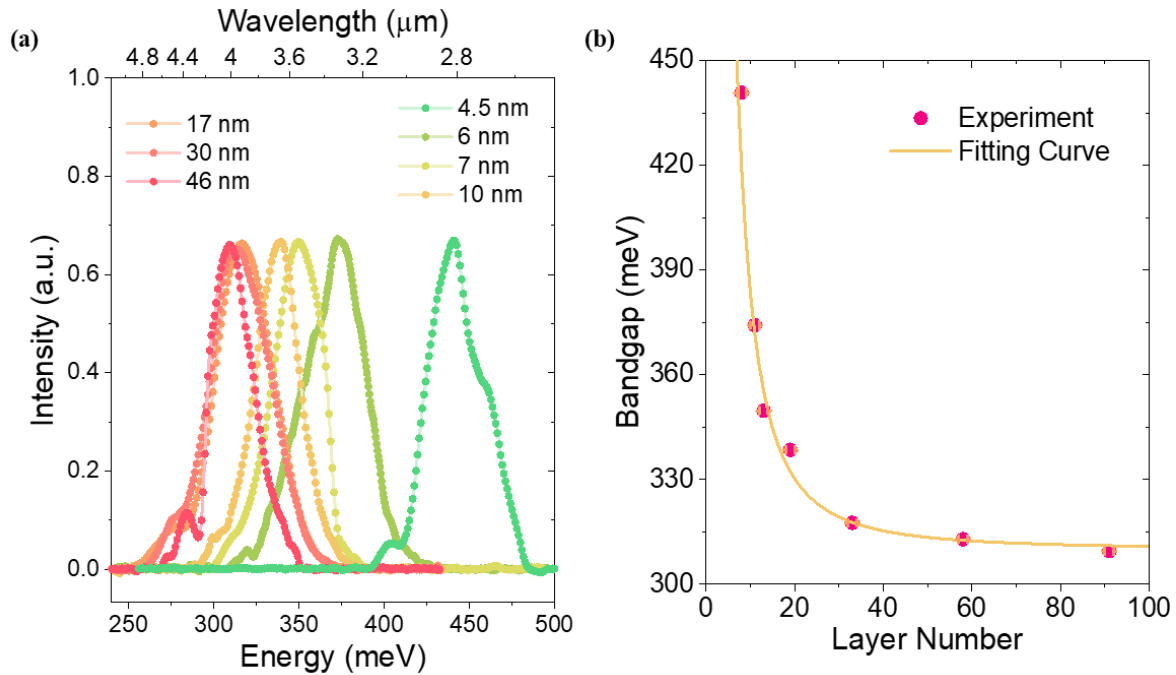
Fig 3.1.13 (a) Thickness dependence of the PL spectra of BP. **(b)** Thickness dependence of BP bandgap in mid-infrared. An error bar of ±1 layer is added to the layer number axis. All panels: from ref. *(129)*.

3.1.6 Widely tunable PL emissions from dual-gate BP devices

We then performed PL measurements on the hBN/BP/hBN heterostructure device to investigate its PL tunability. All PL measurements were performed at 83K with excitation photon energy of 1.94 eV and excitation power density of 20 µW/µm^2. The PL measurement under zero bias was first performed on the 10.5-nm BP flake. As shown in **Fig 3.1.14**, the PL spectrum of the 10.5-nm BP flake exhibits an emission peak position at 330 meV, corresponding to its bandgap.
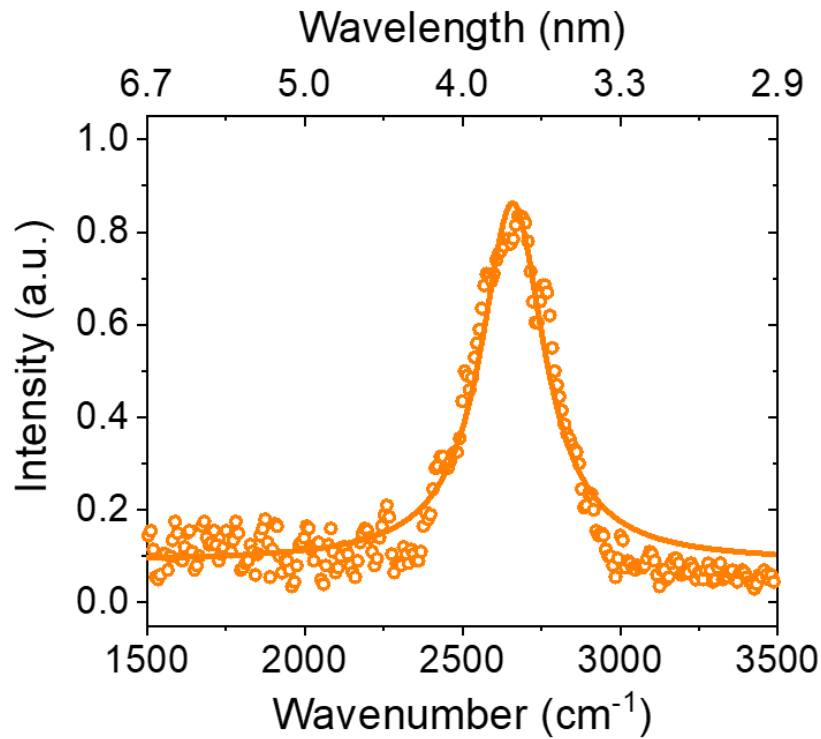
Fig 3.1.14 The measured (dotted) and fitted (solid) PL spectrum of the 20-layer BP device at 83 Kelvin. All panels: from ref. *(130)*.

We then performed the PL measurements under different bias voltage V_0 ranging from -40V to +40V. According to our previous experiments, the hBN encapsulated BP is very intrinsic and its unintentional doping is negligible (*55*). In the dual-gate hBN/BP/hBN device, the displacement

fields generated at the back and top gates can be represented as $D_b = \varepsilon_b V_b/d_b$ and $D_t = \varepsilon_t V_t/d_t$, respectively. Here, V_b and V_t are the bias voltage across the back and top gate dielectric layers, respectively. ε_b and d_b are the average relative permittivity and the thickness of the back-gate dielectric layer, which consists of 285-nm SiO$_2$ and 9-nm bottom hBN flake. ε_t and d_t represent the relative permittivity and the thickness of the top-gate hBN dielectric (22-nm). Using the reported parameters (*269, 270*), ε_b and ε_t are calculated to be 3.87 and 3.0, respectively. Since the thickness of the BP is much smaller than that of the total thickness of gate dielectric layers, the bias voltage over the BP can be ignored and we have $V_b + V_t = V_0$. Moreover, since the displacement field across the BP satisfies $D_0 = D_b = D_t$ (BP is charge-neutral), the quantitative relationship between the applied bias voltage V_0 and the displacement field across the BP D_0 can be determined as $D_0 = 0.012V_0$. Hence, the applied bias voltage ranging from -40 to 40V corresponds to an external displacement field from -0.48 V/nm to +0.48 V/nm.

Fig 3.1.15a shows the PL spectra of the 10.5-nm BP flake at different bias voltage ranging from 0 to +40 V. The PL peak exhibits a clear redshift with increasing bias voltage, indicating the shrinkage of its bandgap. The PL emission can be continuously tuned from 3.7 μm at zero bias voltage to 7.7 μm under a moderate external displacement filed of 0.48 V/nm, demonstrating the widely tunable, direct-bandgap light emission in mid-infrared. Further increasing the external bias is expected to shift the emission peak to wavelength longer than 7.7 μm. However, our measurement setup does not have the sensitivity required to capture those weak signals in longer wavelengths. The PL spectra at the bias voltage from 0 to -40V are shown in **Fig 3.1.15b**, exhibiting almost identical properties. The bandgap and emission wavelength in the 10.5-nm BP under different displacement fields were extracted from the PL measurements and plotted in **Fig 3.1.15c** (dots). The bandgap can be modulated from 330 meV in intrinsic BP to 160 meV

through a moderate displacement field of 0.48 V/nm, which agrees quite well with the previous report from the temperature-dependent four terminal conductance measurements (*51*).
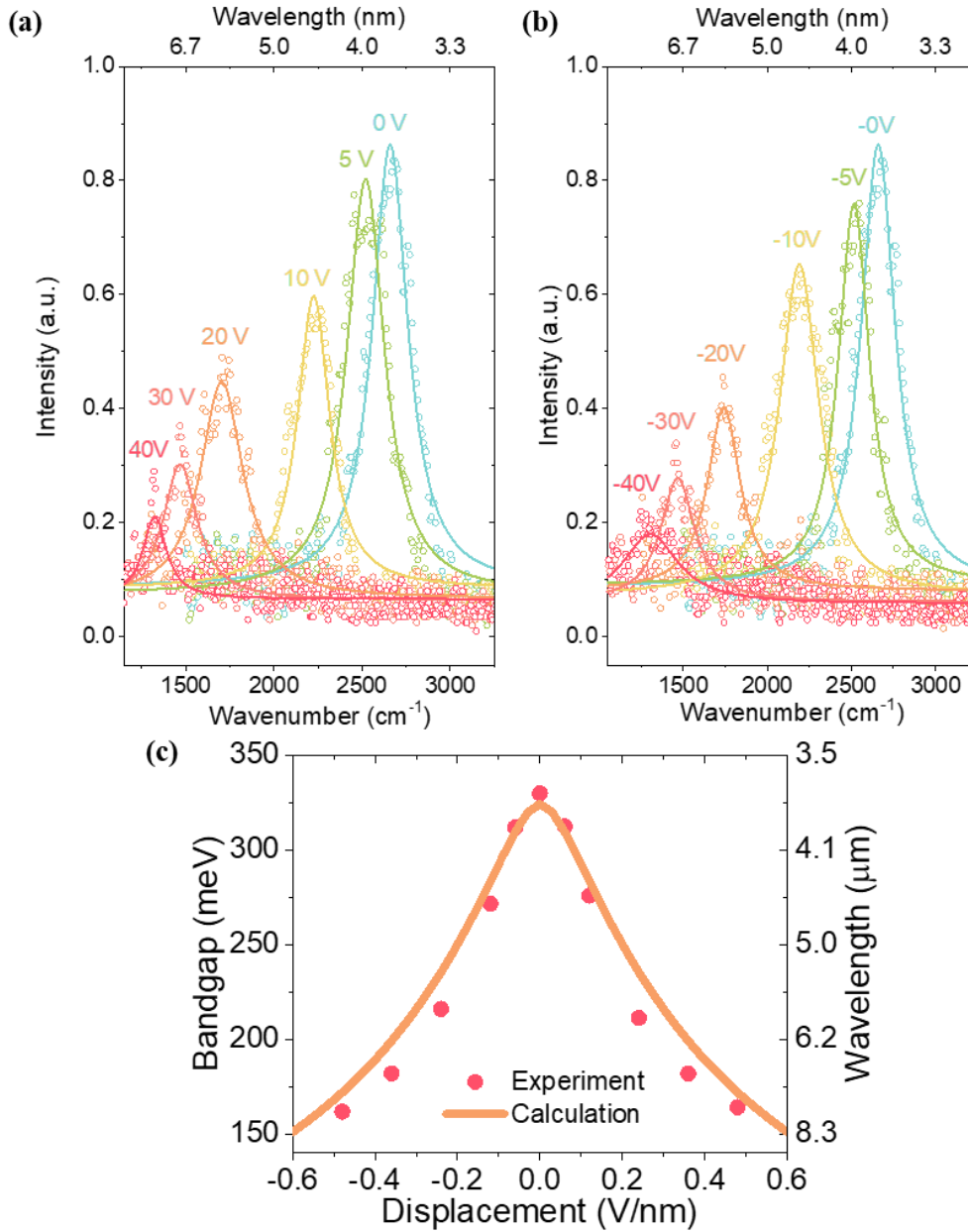
Fig 3.1.15 The measured (dots) and fitted (lines) tunable PL spectra of the 20-layer BP device under different displacement fields **(a)** from 0 to 0.48 V/nm **(b)** from 0 to 0.48 V/nm. **(c)** The bandgap/wavelength tuning of the 20-layer BP extracted from PL spectra (dots) and first-principle based model calculations (line). All panels: from ref. *(130)*.
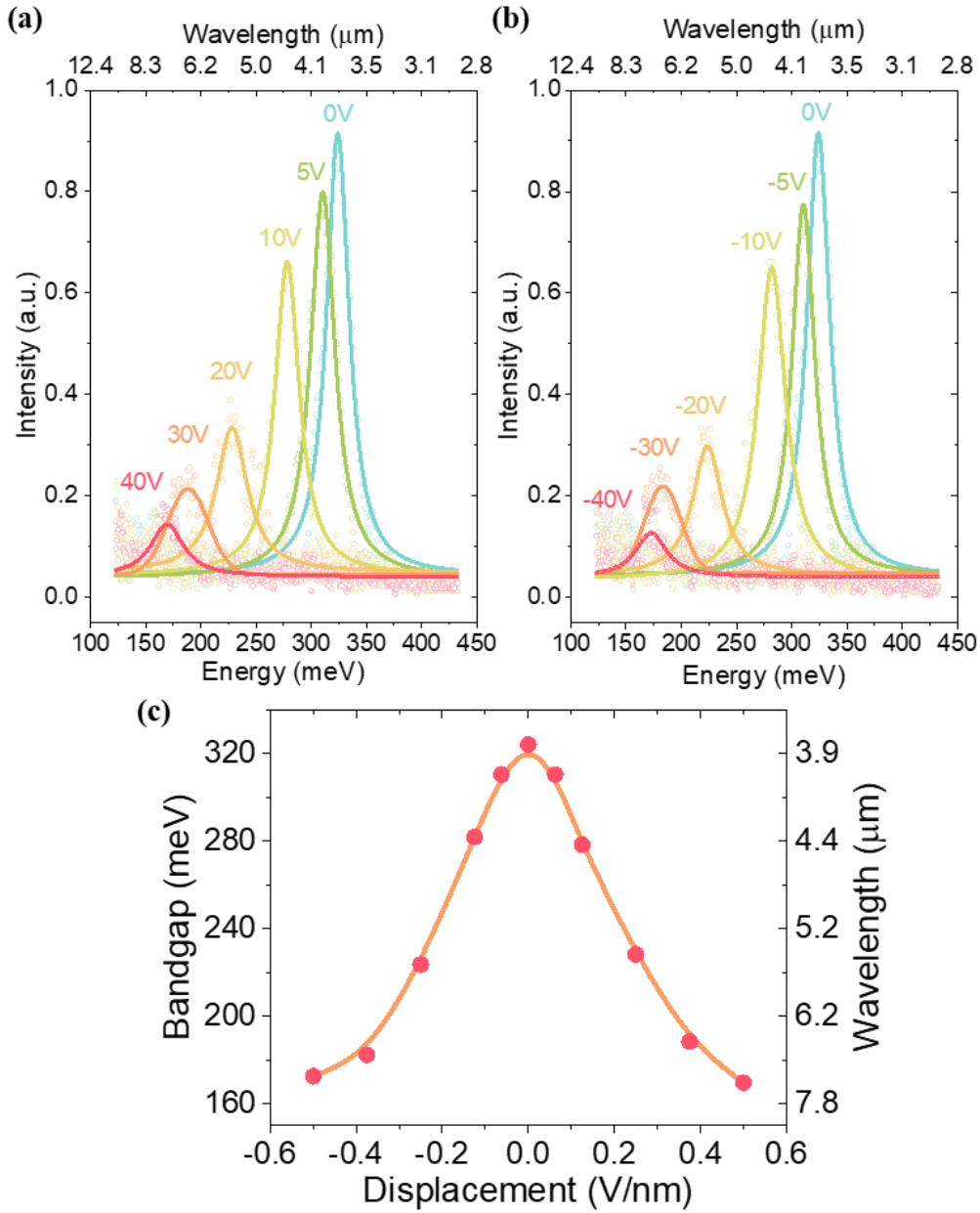
Fig 3.1.16 The measured (dots) and fitted (lines) tunable PL spectra of the 23-layer BP device under different displacement fields **(a)** from 0 to 0.48 V/nm **(b)** from 0 to 0.48 V/nm. **(c)** The bandgap/wavelength tuning of the 20-layer BP extracted from PL spectra.

Our observations have been repeated in several devices with similar thickness and such tunable emissions have been observed consistently. **Fig 3.1.16a** and **Fig 3.1.16b** exhibit the tunable PL

spectra of another 12-nm BP (23-layer) device under the different displacement fields from 0V/nm to 0.48V/nm and from 0V/nm to -0.48V/nm, respectively. Similarly, the bandgap tuning of the 23-layer BP device extracted from PL spectrum was shown in **Fig 3.1.16c**. The PL emission (bandgap) of the 12-nm BP can be continuously tuned from 3.8 μm (324 meV) in intrinsic BP to 7.4 μm (168 meV) at the displacement field of 0.48V/nm, which shows tunability slightly smaller than that of the 10.5-nm BP. This result demonstrated that the wide tunability of the PL emission can be robustly achieved in thin-film BP with thickness ranging from ~10-nm to ~12-nm. Moreover, it also implies that most likely due to free carrier screening, ~12-nm BP does not exhibit enhanced tuning range if compared with that of ~10-nm BP. For BP flake much thicker than 10 nm, it cannot be gated effectively by external electric field due to the strong free-carrier screening effect (*271*). For thinner BP flake of ~5 nm, previous conductance measurements revealed that it exhibits much weaker tunability due to the strong interlayer electronic coupling (*51*). Also, the PL emission will significantly reduce in thin-film BP due to decreased absorption. Therefore, we expect that the thickness of the best tunability should be around 10-nm.

We further investigated the band structure of the 10.5-nm (20-layer) BP under different displacement fields through a tight binding model, which has been discussed in detail in previous works (*51, 52, 55, 226*). Here, we briefly described the calculation process again for clarity and discussed the influence of the external electric field on the interlayer coupling strength and the wavefunction distributions of the electron and the hole states based on the calculation. To describe the band structures of BP thin film around the Γ point near the band edges. We carry out a tight-binding model based on DFT in conjunction with the $\vec{k} \cdot \vec{p}$ approximation. The low energy effective Hamiltonian of monolayer BP can be described by a two-band model:

$$H = \begin{pmatrix} E_c + \alpha k_x^2 + \beta k_y^2 & v_f k_y \\ v_f k_y & E_v - \lambda k_x^2 - \mu k_y^2 \end{pmatrix} \tag{24}$$

To further delineate multilayer BP thin film and the effect of external electric field, we introduce the interlayer couplings $t_i^{c,v}$ in the off-diagonal elements and static electric potential terms Δ_i in the diagonal elements under the tight-binding frameworks. Here in the calculations, the interlayer coupling coefficient remains constant under external displacement field, which is confirmed by our DFT calculations. Therefore, the low-energy effective Hamiltonian of N-layer BP can be written as (*50*):

$$
\begin{pmatrix}
E_c(k) & t_1^c & t_2^c & \cdots & 0 & v_f k_y + \theta k_x^2 & 0 & 0 & \cdots & 0 \\
t_1^c & E_c(k) + \Delta & t_1^c & & \vdots & 0 & v_f k_y + \theta k_x^2 & 0 & & 0 \\
t_2^c & t_1^c & E_c(k) + 2\Delta & & t_2^c & 0 & 0 & v_f k_y + \theta k_x^2 & & 0 \\
\vdots & & & \ddots & t_1^c & \vdots & & & \ddots & \vdots \\
0 & \cdots & t_2^c & t_1^c & E_c(k) + (n-1)\Delta & 0 & 0 & 0 & \cdots & v_f k_y + \theta k_x^2 \\
v_f k_y + \theta k_x^2 & 0 & 0 & \cdots & 0 & E_v(k) & t_1^v & 0 & \cdots & 0 \\
0 & v_f k_y + \theta k_x^2 & 0 & & 0 & t_1^v & E_v(k) + \Delta & t_1^v & & 0 \\
0 & 0 & v_f k_y + \theta k_x^2 & & 0 & 0 & t_1^v & E_v(k) + 2\Delta & & \vdots \\
\vdots & & & \ddots & \vdots & \vdots & & & \ddots & t_1^v \\
0 & 0 & 0 & \cdots & v_f k_y + \theta k_x^2 & 0 & 0 & \cdots & t_1^v & E_v(k) + (n-1)\Delta
\end{pmatrix}
$$

Here $E_c(k) = E_c + \alpha k_x^2 + \beta k_y^2$, $E_v(k) = E_v - \lambda k_x^2 - \mu k_y^2$. E_c and E_v are the conduction and valence band reference energies at the Γ point respectively. k_x and k_y are components of the crystal momentum along zigzag(x) and armchair(y) direction. The α, β, λ , μ and v_f are parameters related to effective masses in different directions and t_1^v, t_1^c, t_2^c are corresponding interlayer coupling constant. Δ is effective electrostatic potential induced by external field. All those parameters are inherited from previous work, which are fitted from first principle calculations.
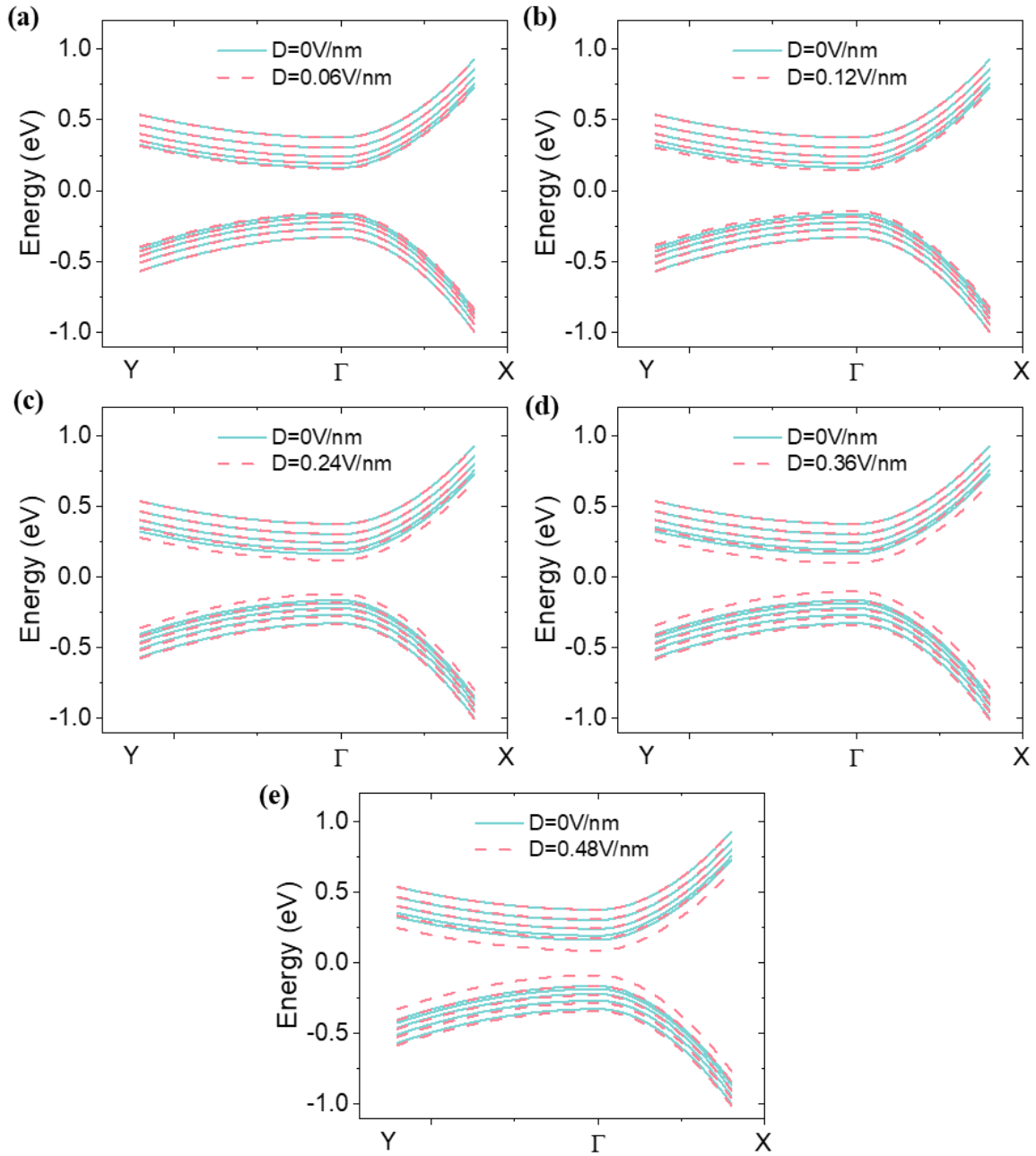
Fig 3.1.17 The bands of the 20-layer BP near the Γ point at displacement field of **(a)** 0.06V/nm, **(b)** 0.12 V/nm, **(c)** 0.24 V/nm, **(d)** 0.36 V/nm, **(e)** 0.48 V/nm, in comparison with those of the intrinsic 20-layer BP. Only 5 highest valance and 5 lowest conduction bands are plotted for simplicity. All panels: from ref. *(130)*.

At band edges Γ point ($\vec{k} = 0$), by solving this Hamiltonian we can get corresponding eigenvalues and eigenvectors which represent the energy levels and wavefunction compositions (square of eigenvector elements). Here we have assumed the band edge wavefunction under bias of BP film can be represented by a combination of separated monolayer BP top valance and bottom conduction wavefunction under tight binding framework. By interpolating this intrinsic normalized wavefunction composition coefficients we can get the band structure and further estimate the oscillator strength under bias. **Fig 3.1.17 a-e** exhibits the comparison between the band structure of the pristine BP and the BP under various displacement fields near the Γ point. Here, only 5 subbands at the top of the valence and bottom of conduction bands are plotted for clarity. As shown in the calculated band structures, the displacement field changes the bandgap but does not significantly vary the band shape. From the calculated band structure, we extracted the bandgap of the 20-layer BP under different displacement fields, as shown in **Fig 3.1.15c** (line). The calculated bandgap tuning properties agree with our experimental results from PL measurements very well.

3.1.7 Evolution of the PL intensity against the bias

Fig 3.1.18 shows the evolution of the peak PL intensity from the 20-layer BP versus the applied displacement field. The PL intensity decreases with increasing displacement field, which can be attribute to the decreasing of the oscillator strength under bias (*272*). Here, we calculated the oscillator by probing the wavefunction overlap of electronic states. For simplicity, we only consider the oscillator strength of single particle transition between band edges (valence band maximum and conduction band minimum) at Γ point.
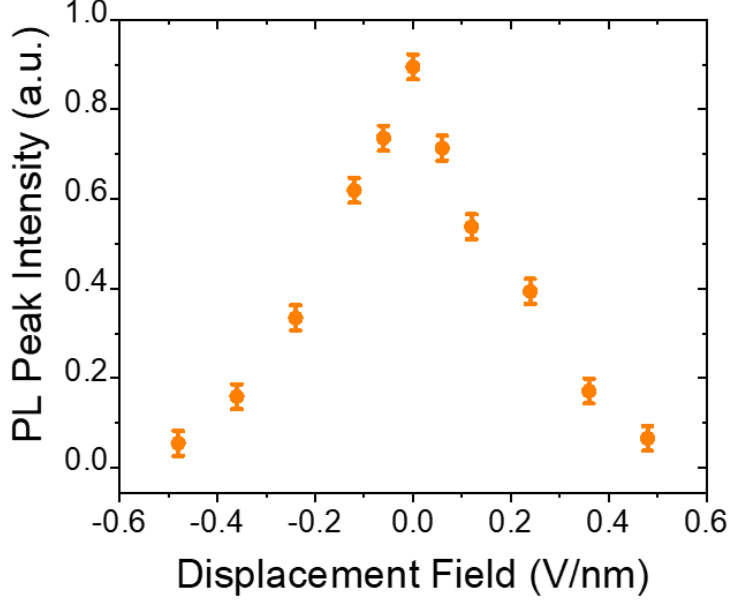
Fig 3.1.18 The PL intensity extracted from PL spectra as the function of displacement field. All panels: from ref. *(130)*.

Starting with the monolayer BP, the corresponding momentum matrix element (I_0) of such single particle optical transition can be written as (*273*):

$$I_0 = |< \phi_v^0| \vec{P} |\psi_c^0 >|^2 \tag{25}$$

Here, $|\phi_v^0 >$ and $|\psi_c^0 >$ represents the monolayer valence and conduction wavefunctions at the band edge of Γ point, respectively, and $\vec{P}$ is momentum operator.

Following the tight-binding framework, the multilayer BP top valence state and bottom conduction state could be described as the combination of identical monolayer valence and conduction wavefunctions:

$$|\Phi_v > = \sum_i a_i |\phi_v^i >$$

106

$$|\psi_c> = \sum_j b_j|\psi_c^j> \tag{26}$$

Here a_i and b_j are corresponding coefficients which satisfy the normalization condition. $|\phi_v^i>$ and $|\psi_c^j>$ are valence and conduction wavefunctions of the correspond layers.

Then the momentum matrix element (I) of the transition between band edges (at Γ point) of multilayer BP film can be simply expressed as:

$$I = |<\Phi_v|\vec{P}|\Psi_c>|^2 = \left|\sum_{i,j} <\phi_v^i|a_i^*\vec{P}b_j|\psi_c^j>\right|^2 \tag{27}$$

Assuming that the wavefunction of each layer BP doesn't have overlap with adjacent layers due to van der Waals interaction between layers. We simplify the expression to:

$$I = \left|\sum_i a_i^*b_i\right|^2 \times I_0 \tag{28}$$

Therefore, using this momentum matrix element expression, we can estimate the relative amplitude of oscillator strength f, which is proportional to the I under bias via the corresponding wavefunction coefficients under different external field. Those coefficients can be obtained from tight-binding model discussed in our previous publications.

The calculated wavefunctions of electronic states at the top of valence band (hole) and the bottom conduction band (electron) at Γ point in the 20-layer BP at different displacement fields are plotted in **Fig 3.1.19 a-f**. With increasing biasing field, the electron and hole wavefunctions shift in the opposite directions. Therefore, the overlap decreases, indicated by the increasing transparency of the background color in **Fig 3.1.19**, leading to reduced oscillator strength (*274*).
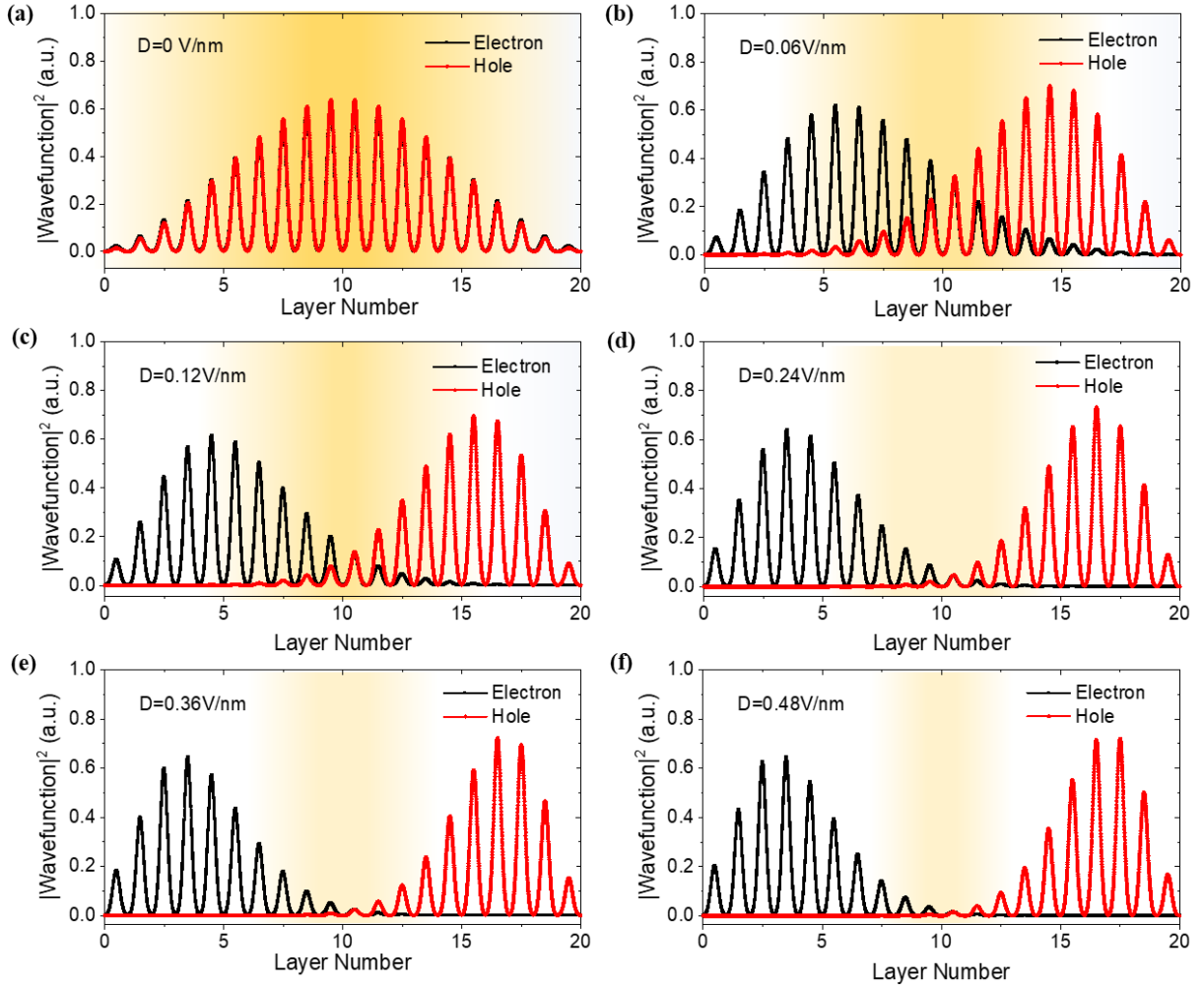
Fig 3.1.19 The wavefunction distributions of the electron and hole states at Γ point of the 20-layer BP at displacements field of **(a)** 0V/nm, **(b)** 0.06 V/nm, **(c)** 0.12 V/nm, **(d)** 0.24 V/nm, **(e)** 0.36 V/nm, **(f)** 0.48 V/nm. The wavefunction overlapping is illustrated by background color, whose transparency increases as the overlapping decreases. All panels: from ref. *(130)*.

We further estimated the oscillator strength from wavefunction overlap integral. As shown in **Fig 3.1.20**, the oscillator strength decreases as the displacement field increases, which leads to the reduced PL intensity. However, compared with the calculated oscillator strength, the experimentally measured peak PL intensity shows a much weaker dependence on the biasing

field. This is probably because the PL quantum efficiency depends on both the radiative and nonradiative lifetimes. The quantum efficiency η of the PL emission can be expressed as (*275*):

$$\eta = \frac{1/\tau_r}{1/\tau_r + 1/\tau_{nr}} = \frac{1}{1 + (\tau_r/\tau_{nr})} \tag{29}$$

Here, τ_r and τ_{nr} represents the radiative and the non-radiative lifetimes, respectively. The decreasing oscillator strength under bias field will directly suppress the radiative recombination probability, leading to longer radiative lifetime and reduced radiative rate $1/\tau_r$. However, the non-radiative recombination rate $1/\tau_{nr}$ is most likely much less dependent on the bias field. Moreover, in high quality BP, the nonradiative rate is expected to be small (or τ_{nr} is expected to be much larger than τ_r). Therefore, the quantum efficiency of PL emission is expected to have weaker dependence on radiative rate $1/\tau_r$.
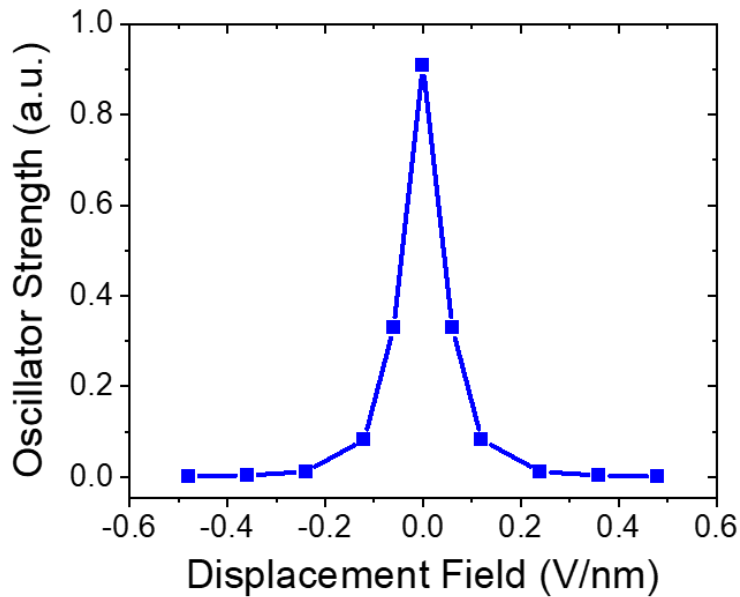
Fig 3.1.20 The oscillator strength as the function of the displacement field. All panels: from ref. *(130)*.

3.1.8 Linearly polarized PL emissions under bias
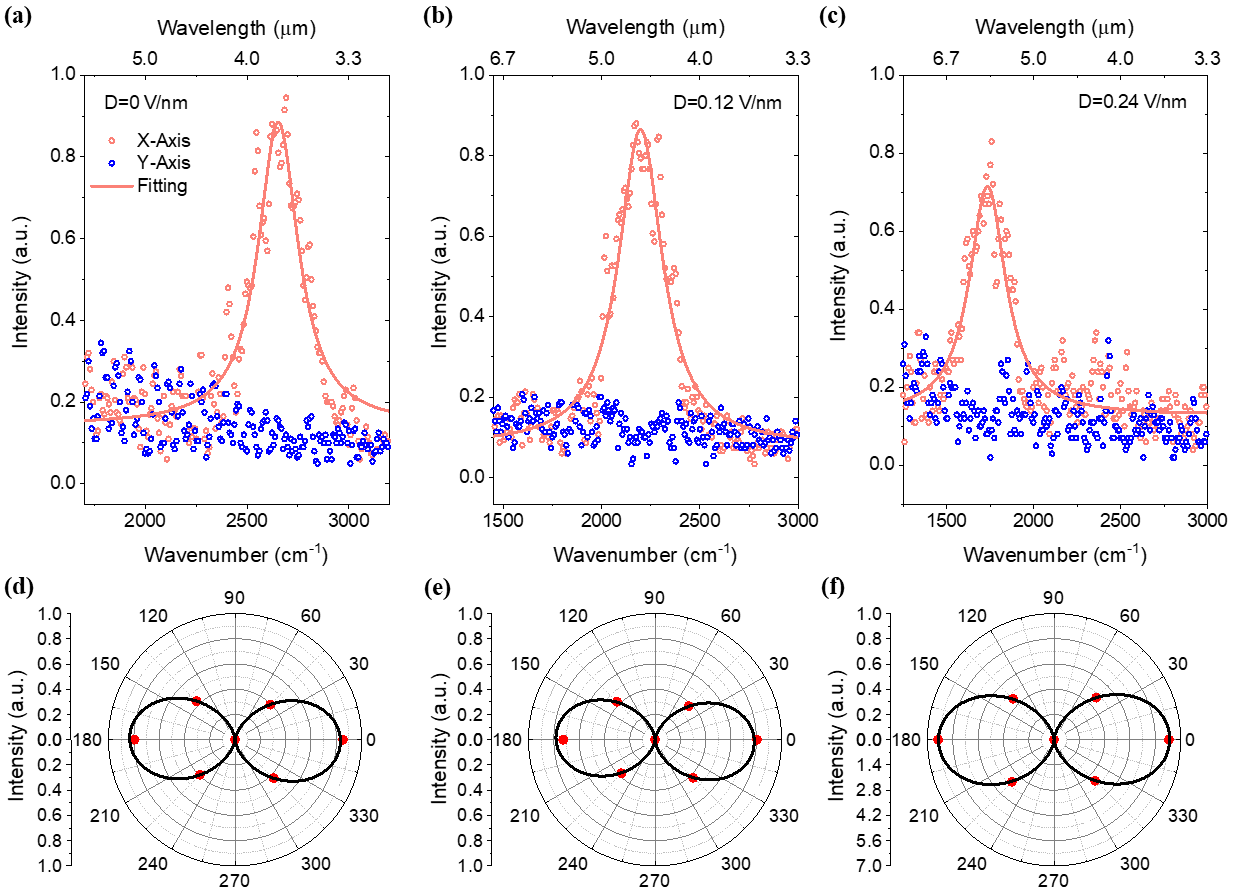
Fig 3.1.21 Upper panel: The PL spectra of the 20-layer BP measured along x- and y-directions of the crystal at the displacement field of **(a)** 0 V/nm, **(b)** 0.12 V/nm, **(c)** 0.24 V/nm. **Lower Panel:** The measured (dots) and fitted (line) angular-resolved PL intensity of the 20-layer BP at the displacement field of **(d)** 0 V/nm, **(e)** 0.12 V/nm, **(f)** 0.24 V/nm. All panels: from ref. *(130)*.

We further performed the polarization-resolved PL measurements under different displacement fields. The excitation polarization was aligned along the x-direction (armchair) of the BP flake while the PL signals of x- and y-polarized emissions were measured. **Fig 3.1.21a** shows the PL spectra along the x- and y-directions in intrinsic BP. The PL emission shows perfect linear polarization as reported previously (*49, 77, 129*). We further measured the PL spectra along x-

110

direction and y-direction under the displacement field of 0.12 and 0.24 V/nm, as shown in **Fig 3.1.21b** and **Fig 3.1.21c**, respectively. The bandgap of BP was tuned to 271 and 216 meV under displacement field of 0.12 and 0.24 V/nm, respectively. Regardless of the bias, the PL emission in BP preserves its perfect linear polarization. The angular-resolved PL intensity is plotted in **Fig 3.1.21d-f**, which can be fitted with the function of $acos^2\theta$, where θ represents the intersect angle between x-direction and the emission polarization. This observation agrees well with our band calculations where the vertical displacement field only rigidly shifts the subbands and the in-plane optical properties are largely unaltered. As a result, the symmetry analysis for pristine BP is still valid even under bias. Therefore, the optical interband transitions are forbidden along y-direction, leading to the x-polarized PL emissions even under external displacement fields.

The linearly polarized PL emission under different displacement fields can also be explained by anisotropic optical conductivity near the band edge of BP. **Fig 3.1.22 a-c** shows the anisotropic low-energy optical conductivity spectra calculated by Kubo formula and the corresponding angular-resolved optical conductivity at the first peak of the spectra under three displacement fields (*55*). The optical conductivity completely vanishes along y-direction near the band edge. This indicates that the optical interband transitions are only allowed along x-direction even under external bias, leading to the linearly-polarized PL emissions along x-direction (*31, 52*). The optical conductivity spectra consist of peaks due to the higher order optical transitions (E_{22}, E_{33}…), while the PL peaks characterize the band-edge transition energies (E_{11}) (*50, 276*). With increasing external electric field, the higher-order transitions such as E_{22} and E_{33} transition can also exhibit a redshift, but it is substantially smaller than that of the E_{11} transition. Because the E_{11} transition is from the top of the valence subbands to the bottom of the conduction subbands, the energy shift of the E_{11} transition is affected most significantly by the band splitting.
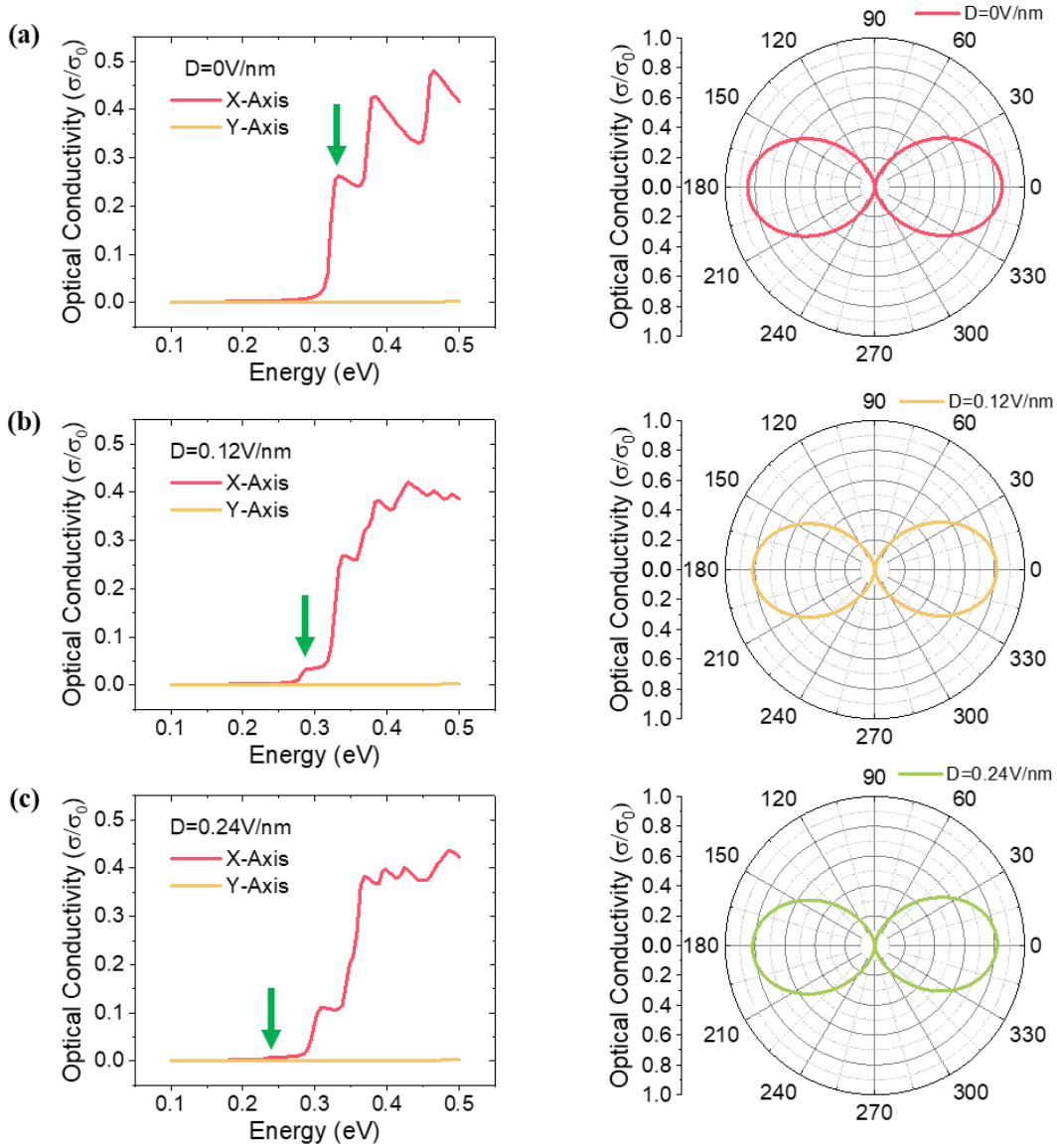
Fig 3.1.22 The anisotropic low-energy optical conductivity spectrum (left) and angular-resolved optical conductivity at the first peak (See the green arrows in the left panel) of the spectrum (right) of the 20-layer BP under the displacement field of **(a)** 0, **(b)** 0.12 and **(c)** 0.24 V/nm. All panels: from ref. *(130).*

3.1.9 Discussion and summary

Bandgap tuning in bilayer TMDs has been predicted theoretically (*277, 278*) and the PL tuning has also been reported experimentally (*279*). However, the tunable PL properties in thin-film BP

112

is distinctively different from that in bilayer MoS_2. Bilayer MoS_2 is an indirect bandgap material, where its PL emission, regardless of bias field, primarily arises from the inefficient direct bandgap optical transition within each individual layer itself (*279*). This primary emission peak hardly depends on the bias field. The bias field induces an additional weak and field-dependent emission peak due to the transitions between electronic states localized in two different layers (*279*). In contrast, BP is a direct bandgap material and it remains to be direct bandgap regardless of the bias field. As a result, the PL emission remains to be relatively strong and the transitions always occur between the top of the valence band and the bottom of the conduction band.

Moreover, previously in the mid-infrared wavelength spectral range, the optical stark effect has been demonstrated in MQW intersubband transitions within conduction band through the infrared absorption measurements (*114, 115*). Under the external bias field, the conduction band tilts, and the energy of lowest quantum state is more effectively modified compared with the higher energy states, leading to the blueshift of the absorption peaks. This phenomenon is opposite to the redshift of the direct bandgap PL emissions in thin-film BP reported in this work. Moreover, the tunability in MQW intersubband transitions is comparatively small (less than 1 μm) since the maximum bias electric field is limited to around 0.01 V/nm due to the moderate semiconducting bandgap of the epitaxially grown MQW structures. In contrast, due to the layered nature of BP, high quality dielectric hBN layers can be used to construct the heterostructures, which easily allows for the external displacement field of 0.5 V/nm in this work. In fact, the displacement field applied to the BP can even be much larger (at least 1 V/nm) (*55*), giving rise to the light emissions in longer wavelength region. Based on first-principle calculations, the bandgap of the 10.5-nm BP can be tuned to 60 meV at the displacement fields of 1 V/nm. Therefore, with further improvement of the BP sample quality and the excitation and

collection efficiency, the light emission of the hBN/BP/hBN devices could reach longer wavelength.

Our observation of the bright and widely tunable light emissions from thin-film BP has inspired many BP optoelectronic applications in mid-infrared. For example, a mid-infrared light-emitting diode has been demonstrated in BP/TMDs p-n junction. In addition, a mid-infrared laser has also been realized in thin-film BP nanosheets embedded in a distributed Bragg reflector (DBR) cavity. Considering its wide tunablity, future research will focus on the BP-based mid-infrared light emitting applications beyond the intrinsic spectral range of pristine BP. In conclusion, our results not only open up new possibilities for widely tunable BP-based mid-infrared light emitting applications, but also provide a comprehensive understanding of the optical and band properties in both pristine BP and BP under the external electric field.

3.2 Ultrafast long-wavelength infrared detection based on ultrathin silicon microbolometer

3.2.1 Motivation

Besides light generation and modulation, mid-infrared light detection is another important aspect of mid-infrared technology. Among mid-infrared (2-20 µm), long wavelength infrared (LWIR) provides an extraordinary platform for light detection technology due to the atmospheric window (9-14 µm) (*280, 281*). The absorption of radiation by atmospheric gases is significantly suppressed in this transmission band. Therefore, long wavelength infrared (LWIR) photodetectors and imagers are widely used in applications such as night vision (*89, 90*), medical imaging (*91, 92*), space exploration (*214, 215*), molecular sensing (*93, 94*), etc.

In general, conventional LWIR detectors can be classified into two categories: "photon" and "thermal" detectors (*117*). MCT detectors (*119*) and QWIP (*120*) are typical photon detectors, in which photocarriers excited by photons are directly collected and converted to electrical current. These detectors have high sensitivity and high speed but high dark current at room temperature, therefore requiring cryogenic cooling for operation with limited applications (*282, 283*). In contrast, microbolometers are thermal detectors that can operate at room temperature. A microbolometer consists of an infrared light absorber and a temperature sensitive resistor (*116, 123, 124*). The light sensing of the thermal detector is realized by the detection of the resistance variation that is caused by the light-induced temperature elevation. Due to the ease of operation, microbolometers are widely employed in thermal imaging applications (*284-286*).

In the state-of-art bolometers, weak LWIR light can induce significant temperature changes due to excellent thermal insulation design. The state-of-art bolometers have a high sensitivity with a NETD as small as 50 mK (*116, 123, 124*). However, such a high detection sensitivity achieved in

the state-of-art bolometers coming from a high photoresponsivity is achieved by maximizing the thermal resistance (R_{th}) of the device. A large R_{th} together with a high heat capacity (C_{th}) in the reported bolometers unavoidably leads to a large thermal time constant ($\tau_{th} = R_{th}C_{th}$) value of 10 mili-seconds (*116, 123, 124*). As a result, most existing bolometers have an operation frequency bandwidth well below one kilohertz. Simultaneous improvement of both the operation frequency and photoresponsivity in these bolometers thus encounters an impasse. Further improvement of the bolometer speed requires materials and structures a with low heat capacity (*125, 287*).

Moreover, the potential of the prevalently employed materials in the existing bolometers, e.g., amorphous silicon (α-Si) (*288*) and vanadium oxide (VO$_x$) (*289*), which have a temperature coefficient of resistance (TCR) of only 2-3%/K, for temperature sensitive resistors has been nearly depleted. Alternative materials with a higher TCR value than that can be achieved from these conventional ones are worthy of exploration. Finally, after decades of improvement, the bolometer pixel size was downscaled from around 50 µm (*290*) down to 10 µm (*291*). Although further reduction of the pixel size to below the wavelength scale has been attempted to improve the resolution of bolometer-based infrared imagers (*292, 293*), the pixel size reduction using the conventional bolometer design scheme would decrease the light absorption and impair the filling factor of a bolometer imaging array (*294-296*), leading to compromised photoresponsivity.

Recently, mid-infrared microbolometers have also been demonstrated in emerging 2D materials like graphene (*99-102*). The ultrathin 2D nature of graphene gives rise to its extremely small heat capacity. Therefore, ultrafast operational speed up to GHz has been realized in graphene microbolometers (*99*). Due to weak light absorption and low TCR at room temperature in monolayer or few-layer graphene, the responsivity of graphene bolometers is compromised compared with conventional bolometers, which hinders its pathway towards commercialized

116

applications at current stage (*99*). However, its ultra-small heat capacity sheds light on a promising strategy to improve bolometer speed. Therefore, it is highly enlightened to investigate whether ultrathin conventional materials such as ultrathin silicon can be applied for improving bolometer speed while preserving high sensitivity.

3.2.2 Overview of the microbolometer

An IR microbolometer usually consists of an infrared light absorber and a temperature sensitive resistor, of which the resistance variation caused by the light-induced temperature elevation quantifies the incident light power. **Fig 3.2.1** illustrates the schematic of the silicon nanomembrane-based microbolometer. The bolometer consists of a suspended square shaped silicon nanomembrane (220 nm thick) with two cantilevers (21.2 μm long and 0.5 μm wide) fabricated from a single piece of silicon on insulator (SOI) substrate. The ultra-thinness of the silicon nanomembrane results in an ultra-small heat capacity, giving rise to a much improved operational bandwidth. On top of the suspended silicon nanomembrane, a cross diabolo antenna located at the center of the silicon nanomembrane was designed to achieve a strong and polarization-independent broadband absorption centered at a wavelength of around 12.2 μm (*297-299*). Furthermore, the ultracompact antenna allows for the realization of the subwavelength bolometer pixel size. The absorbed LWIR light leads to a temperature elevation in the entire device, which is detected by the spiral-shaped Titanium (Ti)-Si-Ti resistor surrounding the cross-diabolo antenna. Herein, the resistance of the Ti-Si-Ti resistor is dominated by the Schottky barrier at the Ti-Si interfaces, in which the barrier height is analogous to the activation energy in traditional bolometers (*300, 301*). As a result, the TCR of the Schottky contact is negative, i.e., the resistance of the Ti-Si-Ti resistor decreases as the temperature

117

increases. The bottom Si, which is the handling substrate, is expected to reflect incident light partially. To maximize the device responsivity, the entire device is suspended in vacuum during operation/measurements to minimize its thermal conductance, and hence maximize the temperature elevation under LWIR light illumination.
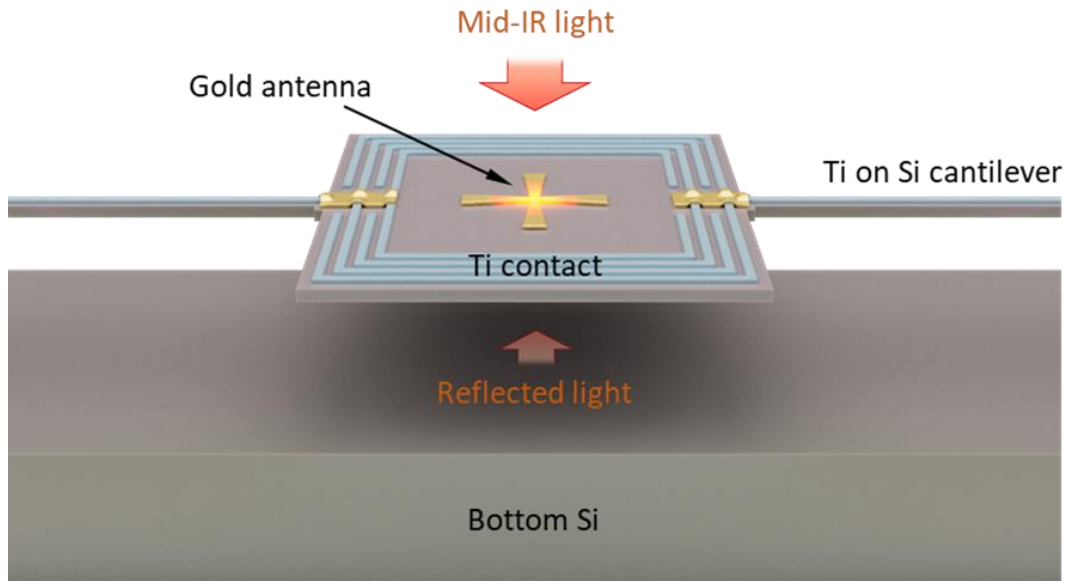
Fig 3.2.1 The schematic of the silicon nanomembrane microbolometer device. All panels: from ref. *(131).*

3.2.3 Design of the diabolo antenna for optical absorption

We first performed optical simulations to optimize the device performance. The optical absorption of the designed bolometer device was calculated using the commercial Lumerical FDTD software. The absorption by the antenna was obtained by comparing the volumetric integral of transmitted electromagnetic wave power and the total incident light power. The difference in incident and transmitted power is the absorbed power. The mesh size of our simulation was set to be 10 nm and we verified that further decreasing the mesh size did not

affect the simulated absorption spectrum. The simulation was performed under a periodic boundary condition with the periodicity of 6.2 µm. The diabolo plasmonic nanoantenna has previously been investigated (*297*). In this work, we optimized the antenna parameters to maximize the absorption and to tune its resonance wavelength to 12.2 µm. A cross design was utilized to realize polarization-independent light absorption (*298, 299*). **Fig 3.2.2a** shows the schematic of the antenna in which the length (L), width (W), and the metal gap (G) of the gold antenna were optimized to be 1900 nm, 600 nm, and 40 nm, respectively. **Fig 3.2.2b** plots the simulated optical absorption spectra of the antenna under the excitation of linearly polarized light at three different polarization directions, which reaches 50% of light absorption at the wavelength of 12.2 µm and shows insignificant polarization dependence due to the high geometric symmetry of the antenna. In this simulation, the reflection of silicon substrate has been taken into account.
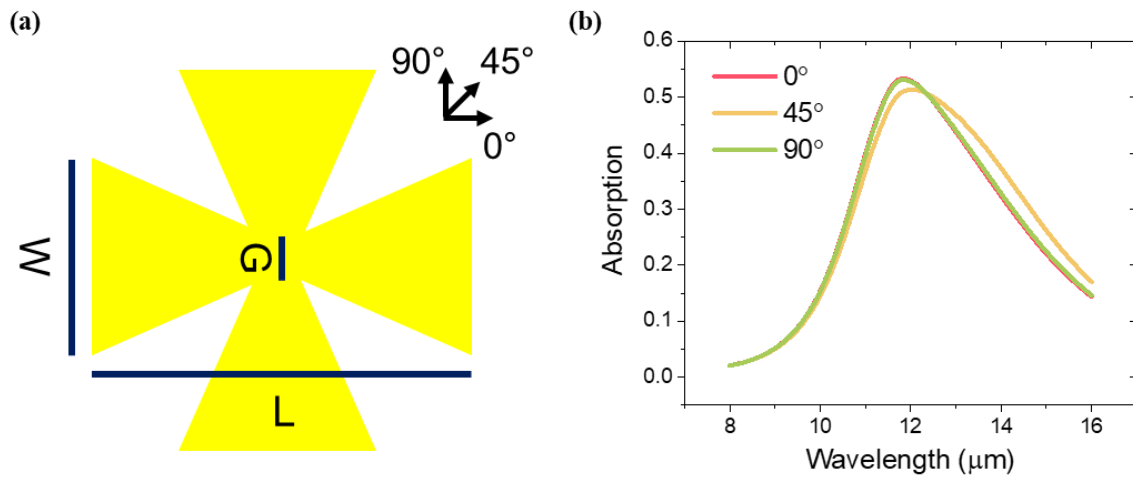
Fig 3.2.2 (a) The schematic of the cross-diabolo antenna. **(b)** The simulated absorption spectrum of the bolometer under different excitation polarizations. All panels: from ref. *(131)*.
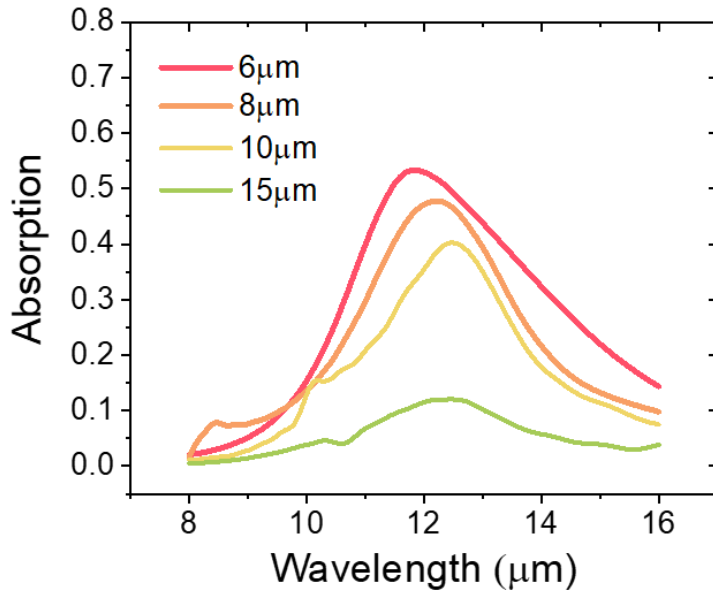
Fig 3.2.3 The simulated absorption spectrum of the bolometer under different simulation period.

Antenna crosstalk, namely the interaction of the antennas in neighboring pixels, is fundamental issue for antenna design (*302, 303*). The antenna crosstalk is desired to be minimized since it is destructive to optical absorption. In terms of simulation, the periodicity dependence of optical absorption is applied to probe antenna crosstalk (*304*). The simulation periodicity determines the distance between neighboring antennas. Therefore, the crosstalk issue is negligible if the resonance wavelength of optical absorption is independent on the simulation periodicity. **Fig 3.2.3** exhibits the simulated optical absorption spectra of the antenna under different periodicity. The resonance peak position remains almost unchanged with further increased periodicity in simulation, indicating that the crosstalk effect is very small with periodicity of 6.2 µm. Previously, we also designed a spiral antenna (*305*) which also exhibits strong and broadband absorption at 12.2 µm, as shown in **Fig 3.2.4a**. However, the absorption resonance shifts

120

prominently with increasing periodicity (**Fig 3.2.4b**), indicating a significant crosstalk issue. Therefore, the spiral antenna design is not appropriate for bolometers with pixel size of 6.2 µm.
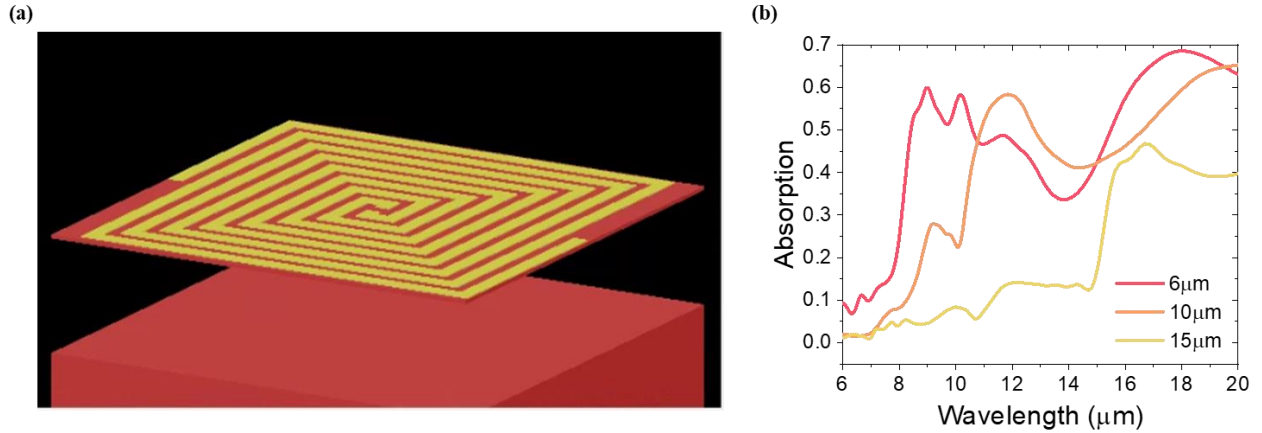
Fig 3.2.4 (a) The schematic of the spiral antenna. **(b)** The simulated absorption spectrum of the bolometer under different simulation period.
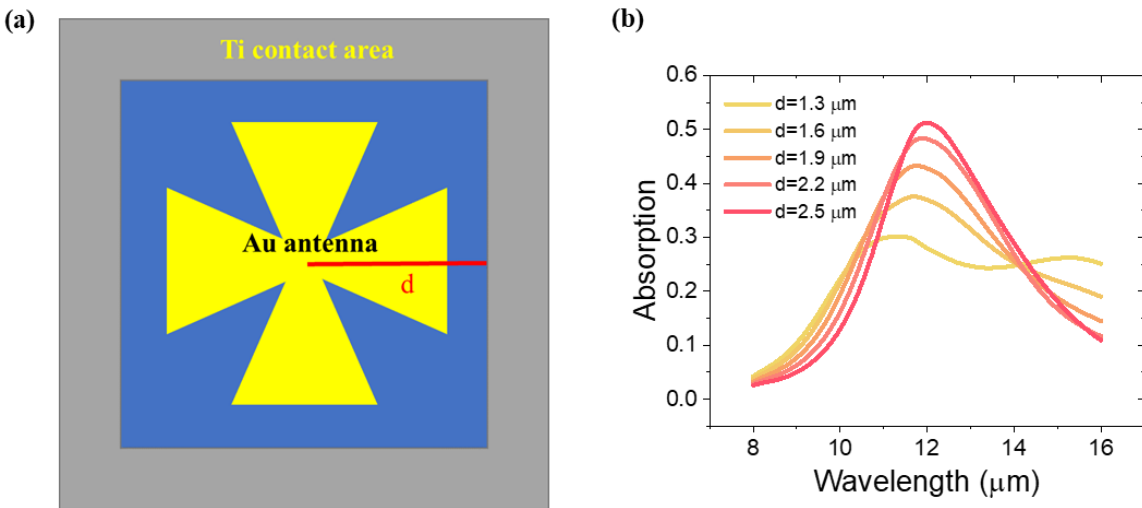
Fig 3.2.5 (a) Schematic illustration of the distance between the center of the antenna to the boundary of the Ti contact, represented by d. **(b)** The dependence of the simulated absorption spectrum on distance d. All panels: from ref. *(131)*.

Moreover, the Ti-Si-Ti resistor was constructed around the edge of the silicon nanomembrane square to minimize the impact of the metallic Ti on the performance of the gold antenna in the center. A proper distance between the center of antenna and the Ti metal lines (**Fig 3.2.5a**) needs to be maintained as the light absorption by the antenna can be quenched if the distance between the antennal and the Ti metal line becomes too short. According to the simulations results shown in **Fig 3.2.5b**, we chose 2.5 µm in our design to maximize light absorption. To realize a moderate resistance value suitable for bolometer applications (*306, 307*), the Ti metal wire was designed and optimized to form a square-shaped four narrow-strip structure surrounding the center antenna.

3.2.4 Microbolometer device fabrication
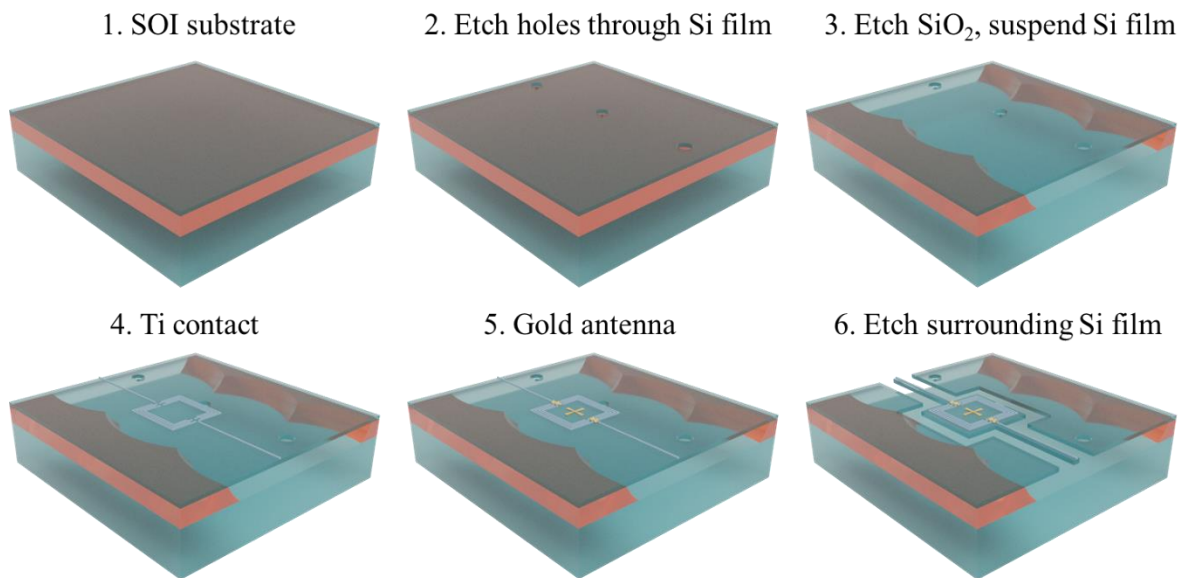
Fig 3.2.6 The schematic of process flow of the device fabrication. All panels: from ref. *(131)*.
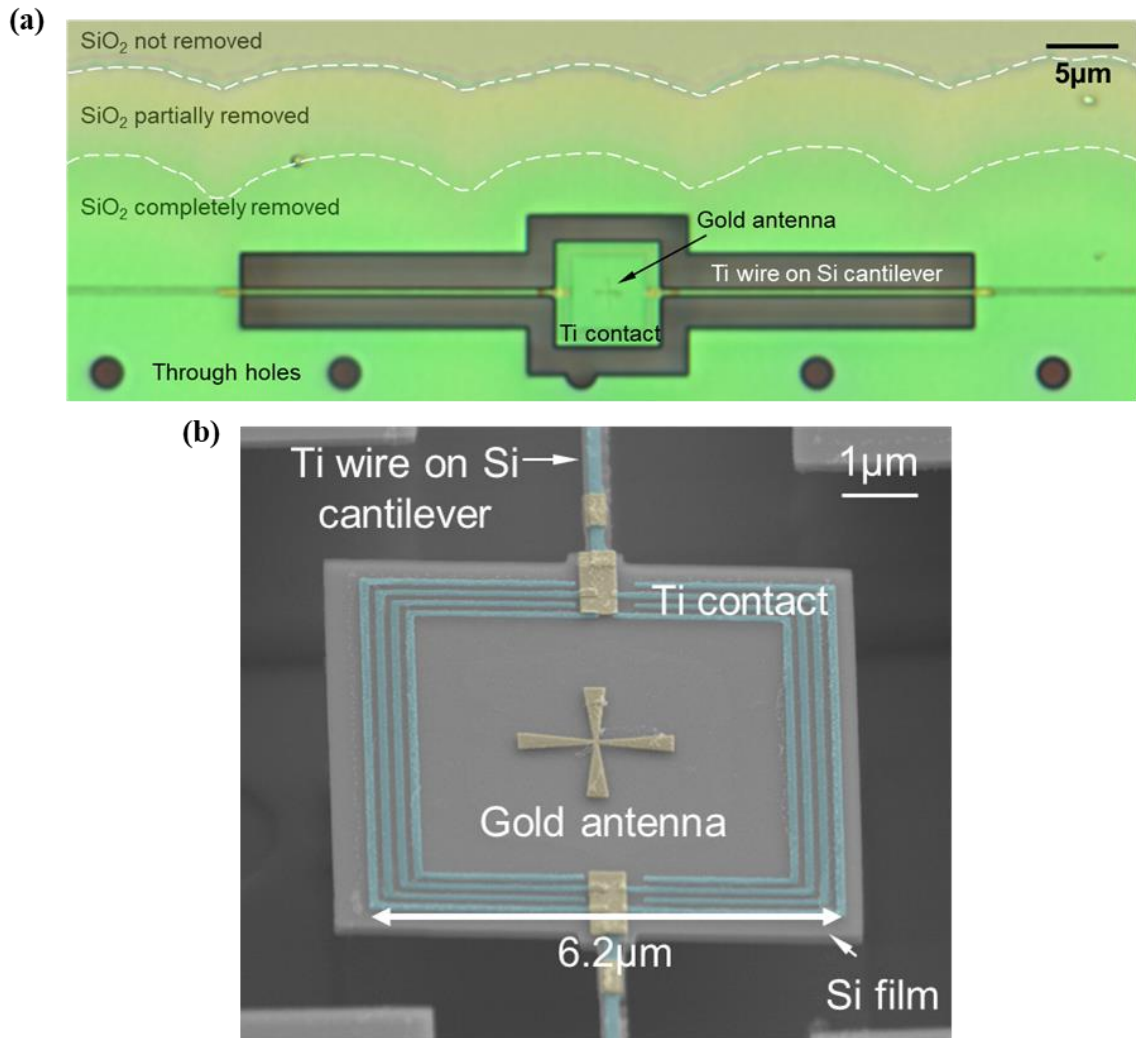
Fig 3.2.7 (a) An optical micrograph of a fabricated bolometer device. **(b)** Scanning electron micrograph (false color) of the device's central area. All panels: from ref. *(131)*.

A schematic of the device fabrication processes is illustrated in **Fig 3.2.6**. We started with a lightly p-type doped (Boron $< 1 \times 10^{15}$ cm^{-3}) SOI wafer that has a top silicon and buried oxide (BOX) thicknesses of 220 nm and 3000 nm, respectively. Using reactive ion etching, an array of holes of 2.4 μm in diameter for BOX removal were first formed on the top Si layer. A PMMA layer was used as an etching mask, which was patterned by a Raith EBPG 5000+ electron-beam

lithography system. The Si film was etched through by sulfur hexafluoride (SF_6) /octafluorocyclobutane (C_4F_8) plasma in an Oxford Plasmalab 180 inductively coupled plasma (ICP) system. Subsequently, the substrate was soaked in 5:1 buffered oxide etchant (BOE) for approximately 1 hour to remove the BOX in the vicinity of the holes, achieving a suspended silicon nanomembrane for the following fabrication steps. The Ti-Si-Ti resistor was fabricated by depositing a Ti layer (30 nm thick) to form the square shaped narrow strip metal lines on the suspended silicon nanomembrane. After that, the gold nanoantenna was fabricated in the center of the bolometer device. The surrounding Si nanomembrane outside of the Ti-Si-Ti spiral resistor was then removed by dry etch using the same ICP system to minimize heat capacity as well as thermal conductance. The PMMA layer used as the etching mask was removed with oxygen plasma. **Fig 3.2.7a** shows the optical microscope image of the device. The detailed structures of the fabricated microbolometer are shown in the false colored scanning electron micrograph (**Fig 3.2.7b**), showing an active device region of 6.2 µm by 6.2 µm. In this work, the pixel size refers to the active device region while the cantilevers are not included. The pixel size including the surrounding area of the bolometer is 7.2 µm by 7.2 µm.

3.2.5 Transport measurements and TCR

We characterized the electrical and thermal properties of the Ti-Si-Ti device at 300 K. The transport measurements were performed in the Lakeshore CPX cryogenic probe station. The source-drain bias voltage was applied by an Agilent B1500A semiconductor parameter analyzer. The device exhibits typical metal-semiconductor-metal I-V characteristics as illustrated in **Fig 3.2.8a**. The device current reaches $I_d = 6$ µA under a forward bias $V_b = 0.8$ V, corresponding to

an equivalent resistance of 0.133 MΩ. To obtain the TCR, the I-V characteristics of the device were measured at 300K and 305K, respectively. The TCR at 300K was calculated by

$$TCR = (\frac{R(300K) - R(305K)}{R(300K)})/5K \times 100\% \tag{30}$$

The typical TCR of the device is around 5% at 300 K, when the bias voltage is over 0.25 V (**Fig 3.2.8a**).
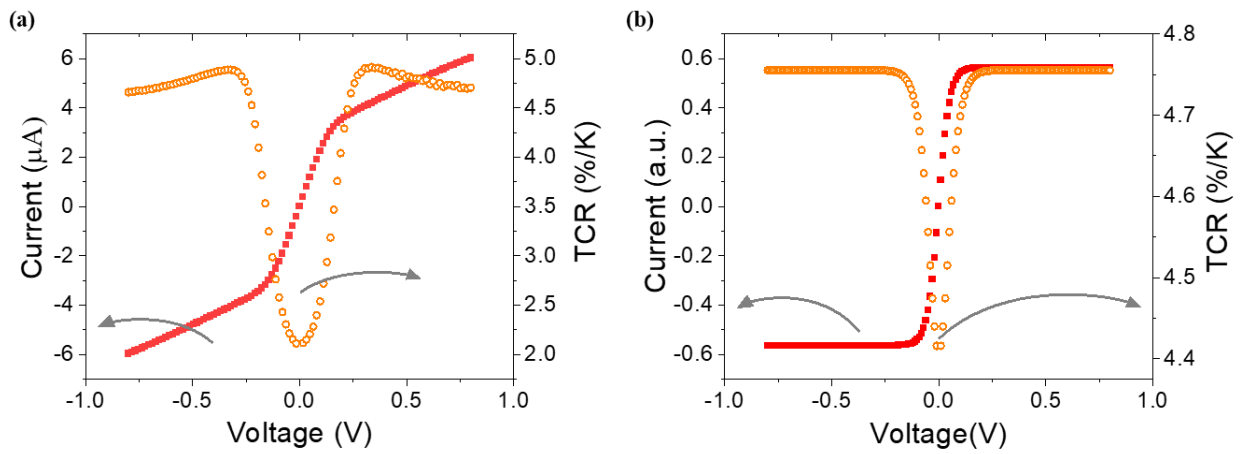
Fig 3.2.8 The **(a)** measured and **(b)** calculated I-V characteristics and TCR of the bolometer device as a function of the bias voltage. All panels: from ref. *(131)*.

A simplified device model can be used to understand the electrical characteristics of the device (*308*). In this electrical model, the Ti-Si-Ti is represented by two back-to-back connected Schottky diodes. Since the Si film was not intentionally doped, the metal and Si film forms a Schottky contact. A typical Schottky diode current versus applied voltage can be described by the following equation (*309*):

$$I = AA^*T^2 exp\left[-\frac{e\Phi_{B0}}{k_B T}\right]\left[1 - \exp\left(-\frac{eV_b}{k_B T}\right)\right] \tag{31}$$

Here, A is the cross-section area of the Schottky diode, A^* is the Richardson constant, T is temperature, Φ_{B0} is the Schottky barrier height, k_B is Boltzmann constant, e is elementary charge, and V_b is the applied voltage across the Schottky diode. In our bolometer, two Schottky diodes are connected in a back-to-back scheme. The bias voltage is distributed in these two Schottky diodes very differently and the current will be limited by the reservedly biased one. If we assume that the effective Schottky barrier height of our Ti-Si-Ti device is 0.31 eV, the calculated TCR is around 4.75% as shown in **Fig 3.2.8b**, which closely matches the measured TCR value. The effective Schottky barrier is smaller than the typical value, approximately 0.5-0.6 eV, reported in previous literatures (*310, 311*). This discrepancy can be attributed to the additional ultrathin silicon serial resistance and the nonideal Ti-Si interfaces. This additional resistance can be evidenced by the non-saturating current at bias voltage larger than 0.2 V, as shown in **Fig 3.2.8a**. Since the additional serial resistance is insensitive to the temperature, the overall TCR of the Ti-Si-Ti device is therefore suppressed, leading to the smaller effective Schottky barrier.

3.2.6 Photoresponse measurements and NETD

The photoresponse of the device under LWIR radiation was measured at the wavelength of 12.2 µm by a home-made infrared photocurrent measurement setup. The 12.2 µm infrared light from the Alpes Lasers sbcw7971 DN QCL was first collimated by a Thorlabs C028TME-F aspheric lens, and then modulated by a Thorlabs MC1F10 mechanical chopper. The infrared light was further guided into the FTIR and focused on the device by a Bruker Hyperion 2000 infrared microscope coupled to the FTIR. The total incident light power under the infrared microscope was measured to be 450 µW using a Thorlabs S401C thermal power sensor.

To calibrate the incident power intensity on the device, we applied a conventional knife-edge technique to determine the size of the Gaussian beam profile. From beam size and total power, the standard deviation of Gaussian distribution was determined to be 25 µm, corresponding to the peak power intensity of 0.115 µW/µm^2. The incident power on the device was then calculated assuming an antenna absorption cross section of $(\lambda/2)^2$, where λ is the resonance wavelength of 12.2 µm. Therefore, the LWIR incident power (P_{ex}) shined on the device was calculated as 4.4 µW.
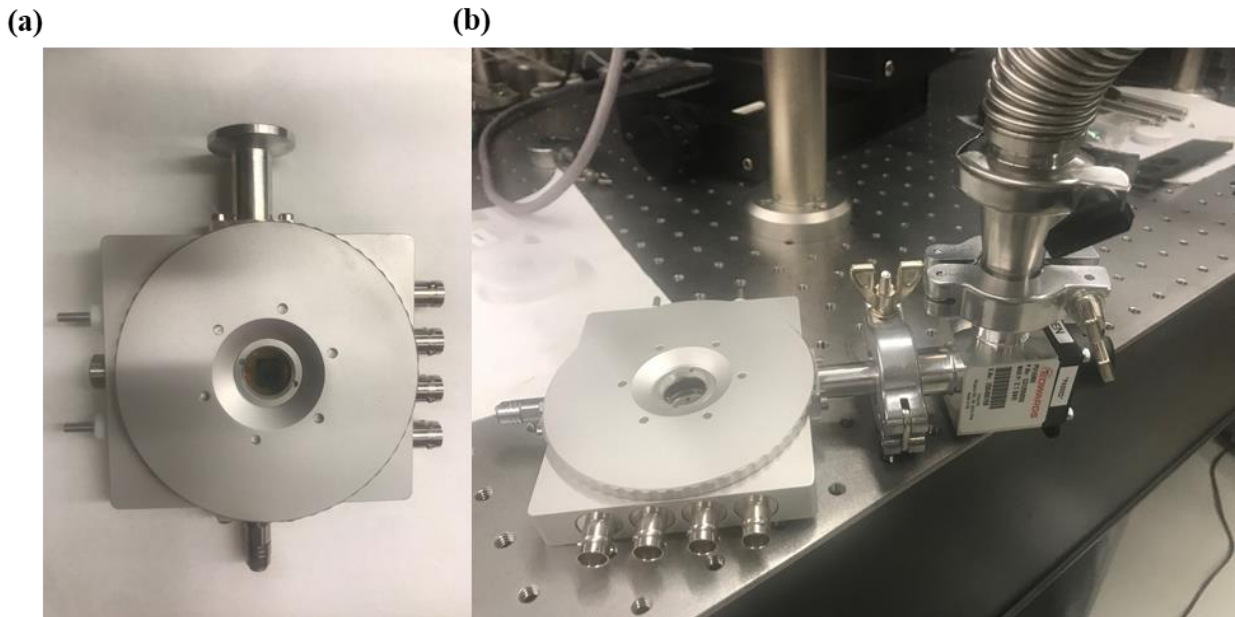
Fig 3.2.9 (a) A photo of vacuum chamber sample stage. **(b)** A photo of vacuum pumping system.

To minimize its thermal conductance, the device was placed in a HFS350VE-PB4 vacuum chamber from Linkam Scientific Instruments for optical measurements, as shown in **Fig 3.2.9a**. The vacuum chamber was connected to the pump by an Edwards PV16MK vacuum valve, which can be pumped down and maintained at a pressure of 10^{-4} Torr by an Edwards T-station, as shown in **Fig 3.2.9b**. The photoresponse was measured by a Stanford Research SR830 lock-in

amplifier in series with a Femto DLPCA-200 current amplifier with a gain G of 1000 V/A. The photocurrent I_{ph} was extracted from the lock-in signal V_L by $I_{ph} = 2\pi\sqrt{2}V_L/4G$, where the factor of $\sqrt{2}$ and 2 represent root-mean-square (RMS) amplitude and the peak-to-peak amplitude from the lock-in amplifier, respectively, and the factor of $\pi/4$ represents the amplitude of the fundamental sine-wave Fourier component of the square wave (*312, 313*). The integration time of the lock-in amplifier was set to be much longer than the laser modulation period to ensure the signal stability.
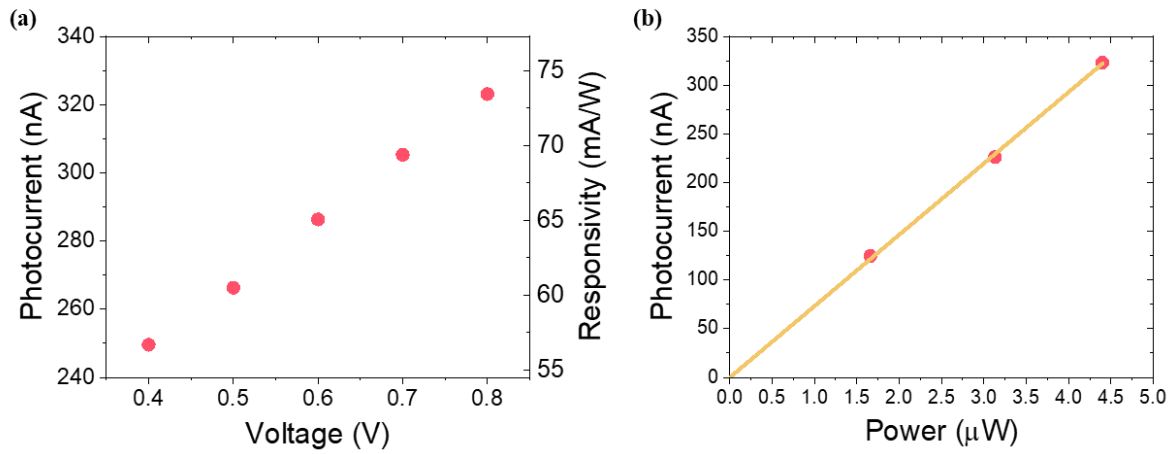
Fig 3.2.10 (a) The measured photocurrent and corresponding responsivity of the bolometer device against the bias voltage. **(b)** Incident power dependence of the photocurrent. All panels: from ref. *(131).*

Fig 3.2.10a plots the photocurrent (I_{ph}) of the device under different V_b ranging from 0.4 V to 0.8 V. In our device, the ratio of photocurrent over dark current (I_d) can be described as follows

$$\frac{I_{ph}}{I_d} = \frac{\Delta R}{R} = \Delta T \cdot TCR \tag{32}$$

128

Here, ΔT represents the temperature elevation across the device under LWIR excitation, ΔR represents the resistance change under ΔT, and R represents device resistance without infrared excitation. Since the TCR remains largely unchanged and the I_d increases linearly in this biasing voltage range, the I_{ph} also increases linearly. The I_{ph} was also measured under different incident power at V_b of 0.8V, as shown in **Fig 3.2.10b**. The I_{ph} increases linearly with incident power due to the linear relationship between the I_{ph} and the ΔT, as illustrated by the equation above.
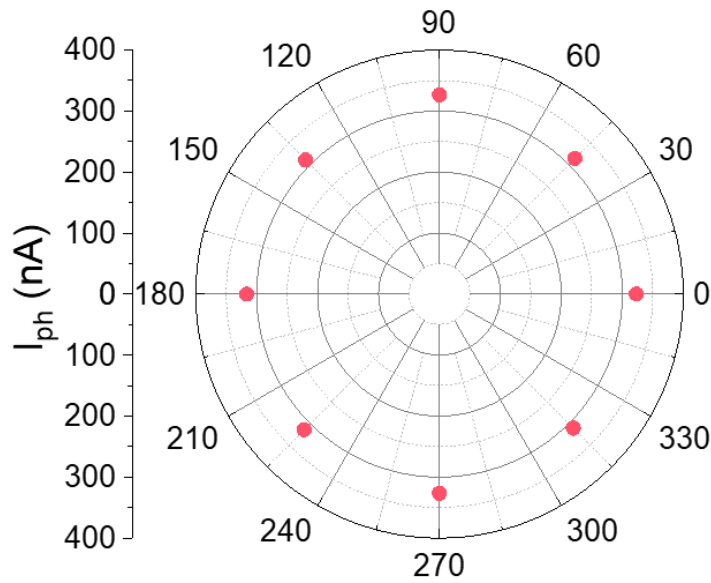
Fig 3.2.11 Polarization dependence of the photocurrent. All panels: from ref. *(131)*.

We further investigated the polarization dependence of the photocurrent. As illustrated in **Fig 3.2.11**, the photocurrent is insensitive to the incidence light polarization due to the four-fold rotational symmetry of the antenna. We calculated the extrinsic (R_{ex}) and the intrinsic responsivity (R_{in}) from the measured I_{ph}, respectively. Under the bias voltage of 0.8 V, the measured photocurrent is around 323 nA, corresponding to an extrinsic responsivity R_{ex} of 73.5 mA/W (I_{ph}/P_{ex}). With 50% of the incidence power being absorbed by the device, which is

estimated from our simulations, the R_{in} is 147 mA/W. We further calculated the noise equivalent power (NEP) and the NETD to quantify the device performance. The NEP can be calculated by (*314, 315*)

$$NEP = \frac{I_n}{R_{ex}} \tag{33}$$

Here I_n represents the current noise. The total current noise power spectral density of bolometer device is the combination of Johnson current noise and shot noise (*99*):

$$\delta I_n^2 = \frac{4k_B T}{R} + 2eI \tag{34}$$

Here k_B is Boltzmann constant, T, R and I are the operational temperature, device resistance and current, respectively. Therefore, $I_n = 1.45\ pA/\sqrt{Hz}$, and the NEP is determined to be $19.7\ pW/\sqrt{Hz}$. The NETD can be derived from the NEP, which can be expressed as (*314, 316, 317*)

$$NETD = \frac{4F^2}{\pi A_p \Phi_{\lambda_1 \to \lambda_2} (\frac{\Delta L}{\Delta T})_{300K_{\lambda_1 \to \lambda_2}}} \cdot NEP \tag{35}$$

Here, the *F* represents the optical aperture and typically *F*=1 in a LWIR device (*116, 318, 319*). A_p represents the area of the single pixel where A_p=37.2 μm^2 in our device. $\Phi_{\lambda_1 \to \lambda_2}$ represents the optical transmission rate, which is approximately $\Phi_{\lambda_1 \to \lambda_2}$=1 in LWIR due to the extraordinary atmospheric transmittance window of this wavelength band (*280, 281*). And $(\frac{\Delta L}{\Delta T})_{300K_{\lambda_1 \to \lambda_2}}$ is the luminance variation with the scene temperature around 300 K, which is evaluated to be 0.84 $W/(m^2 \cdot sr \cdot K)$ (*316*). Therefore, the NETD of our bolometer with an extrinsic responsivity of 73.5 mA/W is 803 mK.

We can further estimate the temperature evaluation ΔT based on the measured parameters using

$$\Delta T = \frac{I_{ph}}{I_d \cdot TCR} \tag{36}$$

The estimated temperature elevation from the measured TCR and I_{ph} is about 1.1 Kelvin. To cross-check the temperature elevation, we performed COMSOL® simulations based on the absorbed optical power. Considering an excitation power of 4.4 μW and an absorption efficiency of 50% from the antenna, the absorbed power by the bolometer is 2.2 μW, leading to a calculated temperature elevation of 1.8 Kelvin across the device (**Fig 3.2.12**). In this calculation, we assumed that heat only dissipates from the cantilevers. The temperature elevation estimated from measured TCR and I_{ph} is slightly lower than the calculated value. This discrepancy may be due to the following two reasons. First, the optical absorption can be lower than the optimized value of 50%. Second, the thermal conductivity of the bolometer is larger than the expected value due to the deviation of the cantilever dimensions from designed ones, and the nonideal vacuum conditions for thermal insulations.
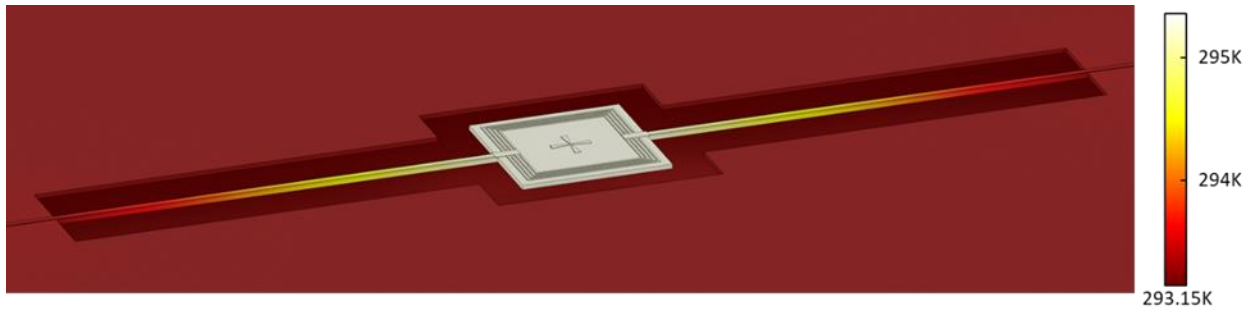
Fig 3.2.12 Simulated temperature elevation across the bolometer device. All panels: from ref. *(131)*.

3.2.7 TTC calculation and speed discussion

The frequency dependence of the bolometer photoresponse was characterized. The incident LWIR light was modulated at frequencies ranging from 50 Hz to 10 kHz using mechanical choppers. **Fig 3.2.13** plots the frequency-dependent I_{ph}, which shows negligible photoresponse degradation with the modulation frequency up to 10 kHz. The abrupt response change at around 900 Hz was caused by the switching of the choppers. The photoresponse up to 900 Hz (represented by solid red squares) was measured using a 10-blade chopper. In this case, the light beam spot is smaller than the width of each blade and the light modulation depth is 100%. However, to achieve a modulation frequency up to 10 kHz, a 100-blade chopper was needed and used. In this case, the light beam spot is larger than the width of the chopper blade and the modulation depth is therefore reduced, leading to the abrupt change in photoresponse at around 900 Hz (represented by orange rings). Such abrupt photoresponse change due to the switch of choppers has also been reported in our previous work (*102*).
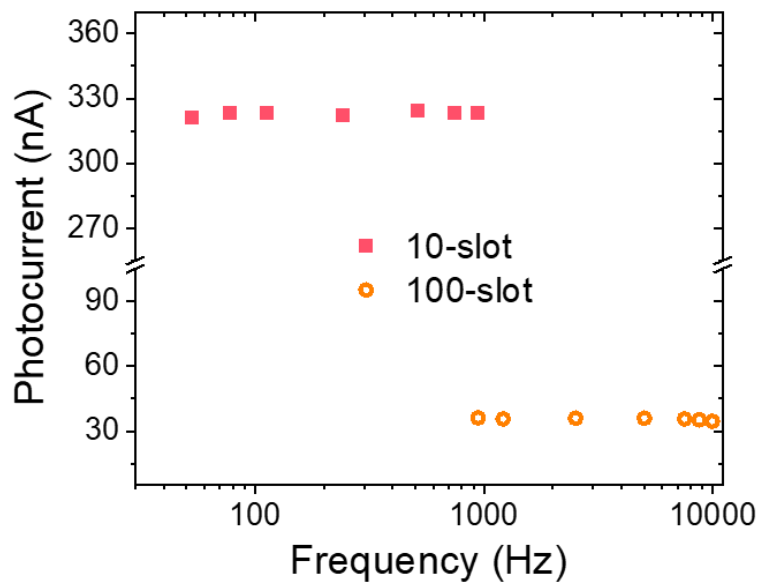
Fig 3.2.13 Modulation frequency dependence of the photocurrent from 50 Hz to 10 kHz. All panels: from ref. (*131*).

132
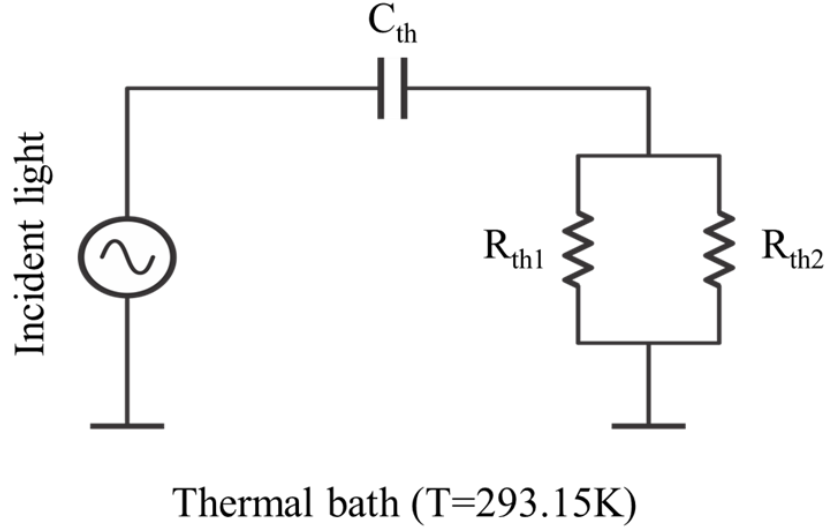
Fig 3.2.14 The schematic of thermal speed calculation. All panels: from ref. *(131)*.

We calculated the thermal speed of the microbolometer. **Fig 3.2.14** shows the schematic for the thermal speed calculation, in which the C_{th} *is* dominated by the silicon nanomembrane area and the R_{th} is mainly determined by the two Si cantilevers in parallel. The incident light absorbed by the devices functioned as the thermal power source and the whole device was soaked in a thermal bath. We calculated the heat capacity and thermal resistance based on the designed device structure, respectively.

The total device heat capacity is the combination of the heat capacity of the Si film, Ti contact, and the gold antenna. The heat capacity of each term can be calculated by the following equation:

$$C = c \times \rho \times V \tag{37}$$

Here, C is the heat capacity, c is specific heat, ρ is the density of the material, and V is the volume. The total heat capacity of the central device can be calculated by the following equation:

$$C_{total} = C_{Si} + C_{Ti} + C_{Au} \tag{38}$$

133

Here, C_{total} is the total bolometer heat capacity. C_{Si}, C_{Ti} and C_{Au} are the heat capacity of Si film, Ti contact and gold antenna, respectively. The calculated C_{total} is 1.92 J/K, in which the contribution of Si film dominates (1.86 J/K).

The thermal resistance of the cantilevers can be calculated by:

$$R_{th} = \frac{L}{\kappa \times A} \tag{39}$$

R_{th} is the thermal resistance, L is the length of the cantilever, κ is the thermal conductivity of the material, and A is the cross-section area of the cantilever. Since two cantilevers are connected to the device in parallel configuration, the total area is the cross-section area of one cantilever times two. Moreover, the heat dissipation pathway consists of Si cantilevers and Ti wires, which are in parallel. Therefore, the total thermal resistance can be calculated using the following equations:

$$R_{th,total} = \frac{R_{Si} \times R_{Ti}}{R_{Si} + R_{Ti}} \tag{40}$$

Here, $R_{th,total}$ is the total thermal resistance and R_{Si} and R_{Ti} are the thermal resistance of Si cantilevers, and Ti wires respectively. The calculated $R_{th,total}$ is $7.61 \times 10^5 (K/W)$. In fact, it is dominated by Si cantilevers and the impact of Ti wires is negligibly small.

The estimated τ_{th} of the microbolometer device is determined by $t_{th} = C_{total} \times R_{th,total} = 14.6 \ \mu S$, corresponding to a 3 dB cut-off frequency $f_{3dB} = 1/2\pi\tau_{th} \approx 11 \ kHz$. The calculated frequency dependent responsivity is shown in **Fig 3.2.15**. Although we have not been able to experimentally determine the cut-off frequency in our microbolometer due to the limitation of our measurement setup, the calculated cut-off frequency value may serve as a reasonable estimation for the fabricated device.
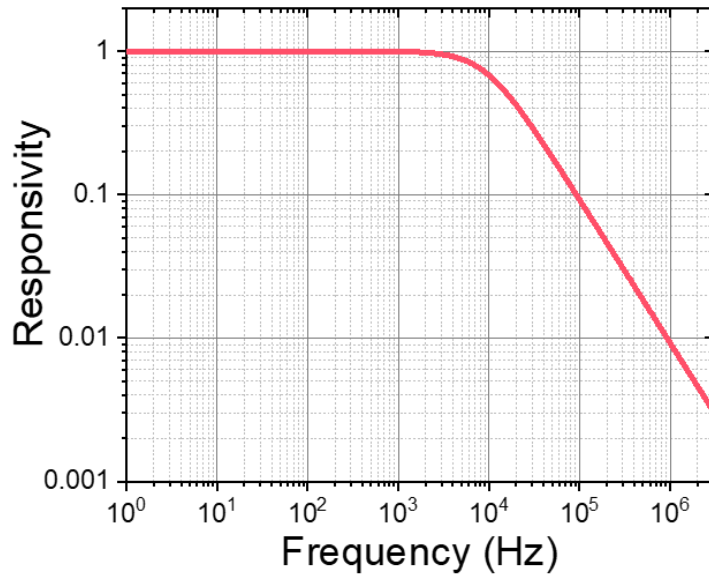
Fig 3.2.15 Calculated modulation frequency dependence of the responsivity. All panels: from ref. *(131).*
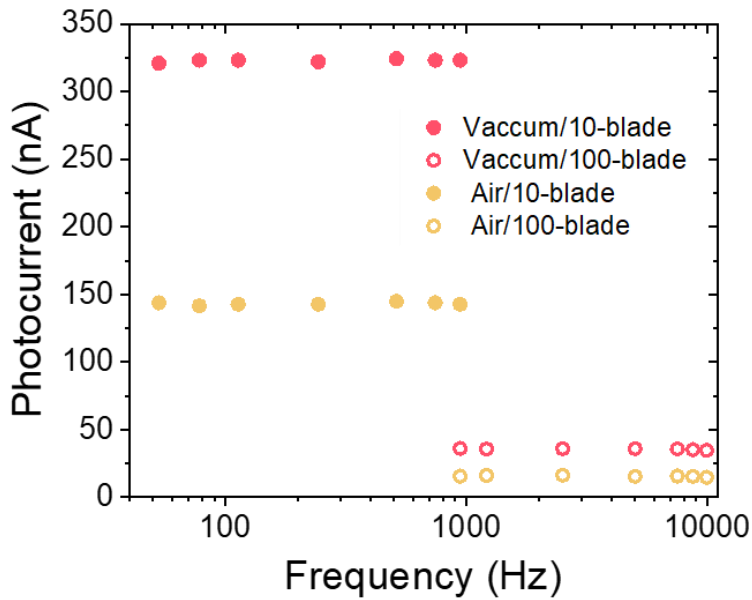
Fig 3.2.16 Modulation frequency dependence of the photocurrent of the same device measured in air compared with that measured in vacuum from 50 Hz to 10 kHz.

We further comment on the performance of microbolometer in the atmosphere. The frequency responses of the photocurrent of the same device measured in air and in vacuum from 50 Hz to 10 kHz were plotted in **Fig 3.2.16**. The photocurrent measured in air was 2.3 times lower than that measured in vacuum. Therefore, the responsivity and the NETD were also 2.3 times worse, which was 32.4 mA/W and 1694 mK, respectively in air. The degradation of the device performance can be attributed to the additional heat dissipation channel by air. On the other hand, the increasing thermal conductivity with further decrease the thermal time constant, leading to an even faster operational speed. Therefore, the device performance is still reasonable in the atmosphere.

3.2.8 Engineering the thermal resistance

To improve the thermal conductivity of the above described microbolometer, we implemented nanoholes in the Si cantilevers. These holes were designed to decrease the thermal conductivity of the cantilevers and hence to increase the temperature elevation under LWIR illumination and thus the responsivity. There are two factors contributing to the enhancement of the thermal resistance. First, the fabricated nano-scale holes will decrease the overall cross section of the Si cantilevers and correspondingly increase the thermal resistance. Meanwhile, the scale of nano-scale holes is in the order of 100 nm, which is comparable to the phonon mean free path in silicon. As a result, we expect a decrease in thermal resistivity itself induced by phonon scattering. **Fig 3.2.17** shows the scanning electron micrograph of such a device with nanoholes fabricated in its cantilevers. The central active device area remains to be 6.2 µm by 6.2 µm.

136
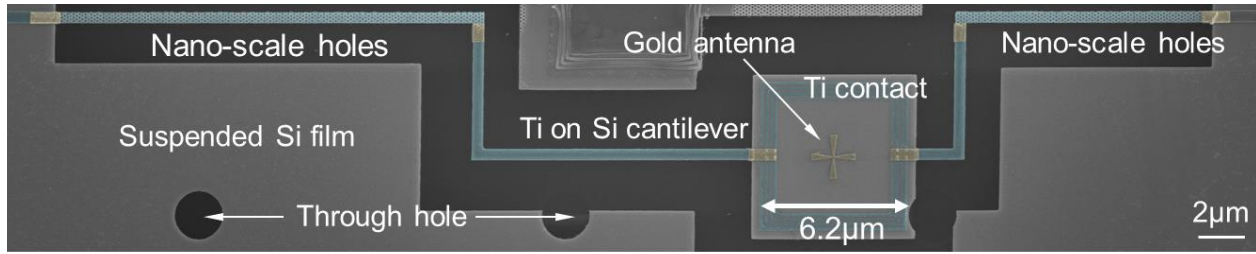
Fig 3.2.17 A SEM (false color) micrograph of the bolometer device with nano-scale holes fabricated on its cantilevers. All panels: from ref. *(131)*.
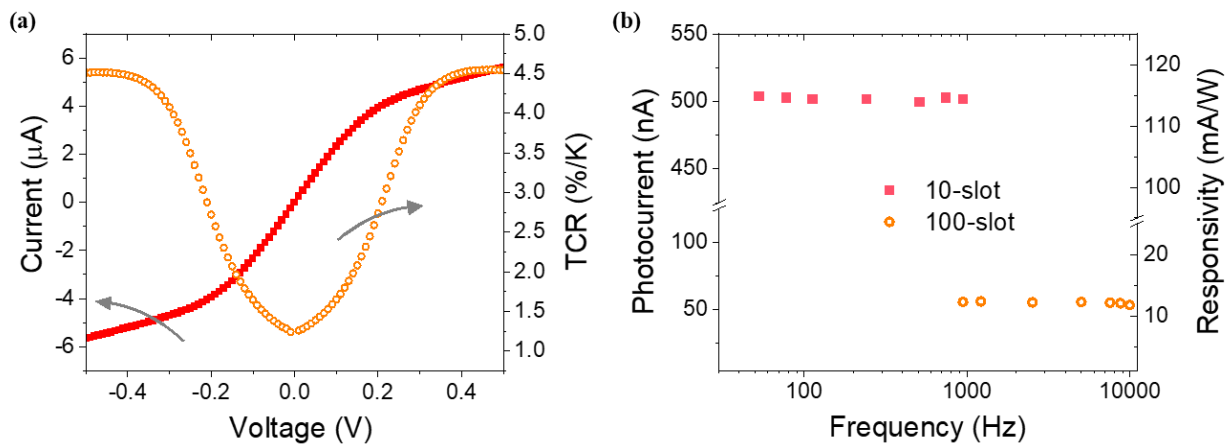
Fig 3.2.18 (a) The I-V characteristics and the TCR of the bolometer device as a function of the bias voltage. **(b)** The measured photocurrent and corresponding responsivity as a function of the modulation frequency. All panels: from ref. *(131)*.

The electrical and thermal properties of the device are shown in **Fig 3.2.18a**. The device exhibits a moderate resistance of ~90 kΩ and a TCR of 4.5% at bias voltage of 0.5 V. The photoresponse of the device was measured under the same condition as described above. A photocurrent of 501 nA was measured with the incident power of 4.4 μW, corresponding to an extrinsic responsivity of 114 mA/W. The NEP and NETD were calculated to be $NEP = 12.7\ pW/\sqrt{Hz}$ and $NETD = 518\ mK$, respectively. Moreover, as illustrated in **Fig 3.2.18b**, the photocurrent of the bolometer does not show noticeable degradation at modulation frequencies up to 10 kHz.

3.2.9 Discussion and summary

Compared with prior state-of-art bolometers, although the NETD of our bolometer is worse than that of commercialized ones, the τ_{th} is reduced by a factor of 500 (*116, 123, 124*). A figure of merit (FOM) has been introduced to compare the performance of different microbolometers by considering the NETD, the τ_{th}, and the pixel size (A_p) (*316, 320*). The FOM is defined as

$$FOM = NETD \times \tau_{th} \times A_p \tag{41}$$
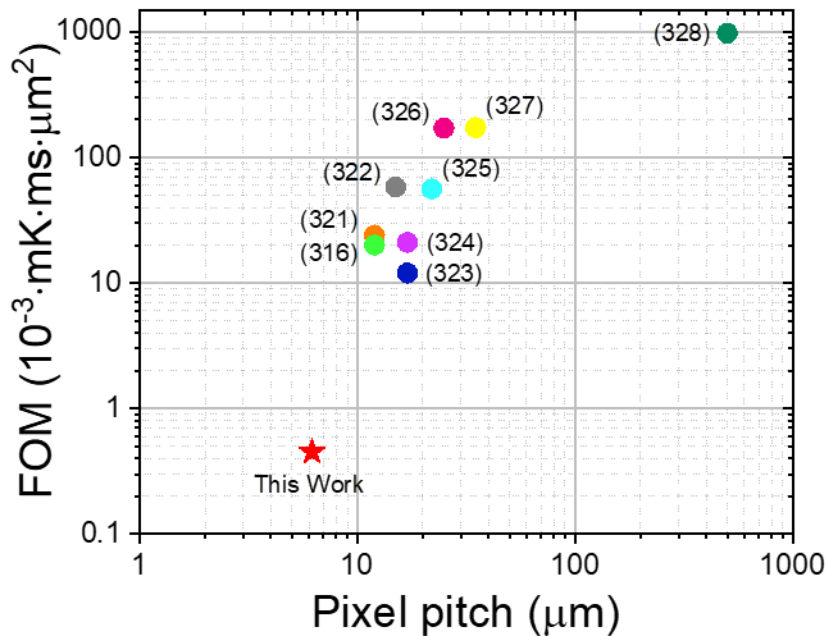
Fig 3.2.19 The FOM of our bolometer device in comparison with the values reported in previous literatures. Here, the NETD has been normalized with the noise bandwidth of 1 Hz. All panels: from ref. *(131)*.

Since it is desirable to have smaller NETD, τ_{th}, and A_p, their product quantifies the overall performance of the microbolometers. Therefore, the *FOM* value allows for the comparison among microbolometers based on different technical approaches. With this FOM, a comparison between the microbolometer described in this work and the reported ones (*316, 321-328*) is

138

shown in **Fig 3.2.19**, demonstrating the outstanding performance of this scheme. Despite the highest performance achieved, considering the trade-off between the NETD and the τ_{th}, it is feasible to simultaneously achieve even lower NETD and higher speed based on our demonstrated scheme (*116, 124, 125*).
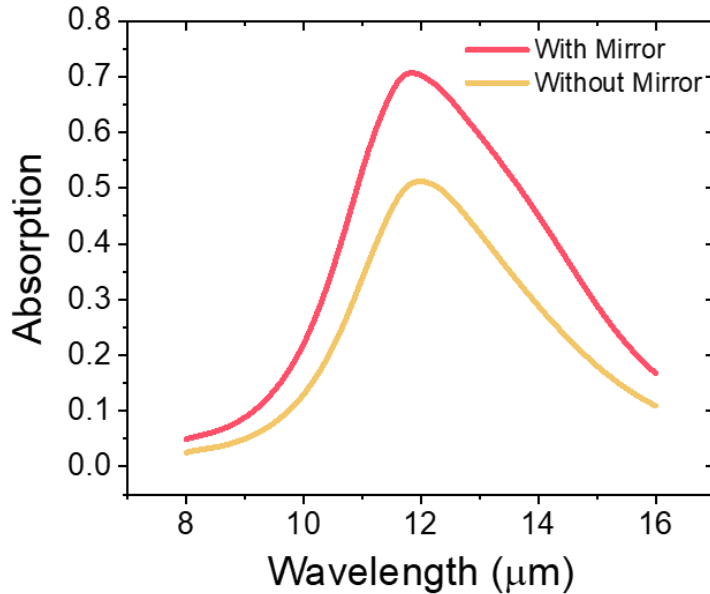
Fig 3.2.20 The simulated absorption spectrum of the bolometer with/without the gold back mirror.

Here, we discuss a few possible strategies to further improve the performance of our bolometers. First, a gold back mirror can be applied underneath the suspended silicon thin film to enhance the optical absorption, giving rise to an absorption efficiency of 70% at the detection wavelength of 12.2 μm, as shown in **Fig 3.2.20**. Second, the thermal resistance of the Si cantilever can be further increased. Larger and denser nano-scale holes can be fabricated into the Si cantilevers. A quick oxidization of such cantilevers with nanoholes can significantly enhance the thermal resistance since the thermal resistivity of SiO_2 is about two-orders of magnitude larger than that

of the Si (*329, 330*). Such quick oxidation will not affect the device area where the Si is relatively thick (200 nm). These two approaches will lead to reduced NETD.
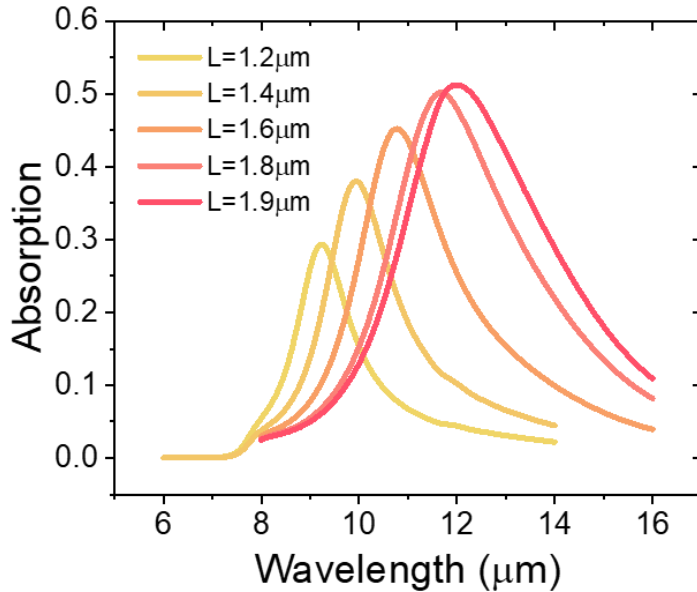
Fig 3.2.21 The simulated wavelength-tunable absorption spectrum of the bolometer with various antenna length.

Moreover, by changing the length of the antenna, the peak detection wavelength of the microbolometer can be tuned from 9 µm to 14 µm (**Fig 3.2.21**), covering a broad spectral region in LWIR. To further enhance the design space, it is also possible to etch trenches and embed the Schottky barrier resistor within the silicon thin film. The antennae can then be fabricated on top of the silicon thin film, thus separating the electrical and optical elements of the bolometer vertically. This design will likely allow us to include multiple antennae within a single pixel to broaden the absorption spectrum and enhance the absorption magnitude.

A few comments on the noise of the microbolometer are provided. Traditional bolometers made from amorphous silicon or VO_x usually have a low 1/f noise. The noise is dominated by thermal noise at a low frequency of 100 Hz. In the microbolometer described here, the high TCR is induced by the temperature dependent transport of carriers across the Schottky barrier. The 1/f noise in such a resistor with Schottky barriers is expected to be higher than that of traditional ones, as the 1/f noise is caused by the fluctuation in charge density at trap states modulating the Schottky barrier height (*331*). The 1/f noise is proportional to the square of device current and trap density. The metal-semiconductor interfaces formed during device processing can have a high density of trapped charges (*308*). Future work will need to address the noise issues, which may be overcome by using an electronic chopping scheme demonstrated previously (*332*) or employing a silicon p-n junction as the temperature sensitive resistor, as reported before (*333, 334*). In this former case, the bolometer is driven by an alternating electrical signal and the electronic chopping frequency can be much higher than the device thermal time constant, as it is only limited by the capacitance of circuits. In the latter case, the charge carrier transport energy barriers induces the TCR and the 1/f noise is expected to be much smaller (*335*).

In summary, we have demonstrated a LWIR microbolometer based on a suspended silicon nanomembrane and plasmonic antenna with an ultra-small heat capacity and high TCR. The negligibly small heat capacity of plasmonic antenna decouples the IR absorber and the thermistor. Therefore, the silicon nanomembrane and the plasmonic antenna can be separately designed to optimize the electrical, thermal and optical performance, respectively. The bolometer exhibits a peak extrinsic responsivity of 114 mA/W at a wavelength of 12.2 µm. Remarkably, the microbolometers exhibits an operational speed beyond 10 kHz. To best of our knowledge, this represents the record-high speed in LWIR microbolometers, which provides great opportunities

for many novel applications such as thermal video recording and high framerate thermal imaging unseen in conventional counterparts. The novel bolometer design scheme provides ample room for further reduction of thermal conductivity for responsivity enhancement. Moreover, the ultra-compact design scheme provides a new pathway towards the realization of sub-wavelength pixel sizes in the LWIR range. The demonstration of the sub-wavelength pixel will enable future thermal imaging at an unprecedented resolution. Finally, the fabrication process does not involve high temperature procedures thus it is feasible to directly integrate the bolometer with CMOS-compatible readout integrated circuits, making it promising for large array LWIR imaging applications.

4. Outlook and future works

4.1 Perspective on thin-film technology for infrared optoelectronic applications

In previous section, we provided a comprehensive overview on the development of mid-infrared optoelectronic technology from both the perspective of light generation and detection. The mid-infrared optoelectronic applications based on conventional bulk materials such as Si and MQW typically exhibit high responsivity and high quantum efficiency due to the strong light-matter interactions. Their extraordinary performance and large-scale fabrication make them highly appealed for commercialized applications. However, the considerable volume of conventional materials limits the operational speed due to the large thermal capacity. Moreover, their bulk nature is also inferior to optical or electrical modulation due to the insensitivity to external perturbation, making them lack of tunability over the wide spectrum region of mid-infrared. On the other hand, the emerging 2D materials have been extensively investigated for optoelectronic applications. The significantly reduced thickness of 2D materials gives rise to the ultra-small thermal capacity, extending operation bandwidth to above GHz. Meanwhile, the atomically thin nature makes them intrinsically sensitive to external electrical and mechanical perturbation, which provides great opportunities for achieving wide tunability over a broadband spectrum region. However, in monolayer and few-layer 2D materials, the light-matter interactions are extremely weak, which significantly degrades the performance of the 2D material-based devices. Therefore, the optoelectronic applications based on 2D materials are still at the stage of fundamental research, which is not competitive for commercialized applications.

Based on the discussions above, we provide a new perspective for the development of mid-infrared light generation, modulation and detection technology by utilizing thin-film materials,

i.e., ultrathin conventional materials or many-layer 2D materials with thickness ranging from tens to hundreds of nanometers. These materials provide a desired platform to combine the advantages of high efficiency, high speed and wide tunability due to significantly enhanced light-matter interactions compared with 2D monolayers and moderate thickness and volume compared with bulk materials. Our perspective has been successfully demonstrated by our works presented in previous section. For our work discussed in **Section 3.1**, the thin-film BP with moderate thickness exhibits strong brightness comparable with the InAs MQW sample, arising from the enhanced light-matter interactions and light absorption. Remarkably, the thin-film nature of BP still preserves its high sensitivity to external electrical field modulation, giving rise to the wide tunability of the light emissions over a broadband wavelength region from 3.7 µm to 7.7 µm in mid-infrared. For our work discussed in **Section 3.2**, the ultrathin conventional Si gives rise to the significantly improved operational speed of infrared microbolometers while maintaining reasonable responsivity and NETD. Therefore, thin-film technology provides great potential for future development of the mid-infrared optoelectronic applications, which is highly desired for more extensive explorations. In this section, we provide our insight into several possible future works.

4.2 Some possible future works

4.2.1 Mid-infrared light detection based on plasmons in layered graphite

The 2D materials based mid-infrared microbolometers have been demonstrated in monolayer and few-layer graphene and its plasmonic devices (*99-102*). Despite the high speed, the sensitivity of graphene based microbolometers is two orders of magnitude worse than that of commercialized ones. The compromised performance is mainly attributed to low mid-infrared optical absorption and low TCR (*99*). On the one hand, as the infrared absorber of the microbolometer, doped graphene exhibits minimal optical conductivity in mid-infrared regime (*103*). Due to Pauli blocking, the direct interband optical transition is forbidden for photons with energy lower than $2E_f$ (*104*). Here, E_f represents the Fermi level of the graphene. For example, for graphene with low doping level of 75 meV, the interband transition is forbidden for radiation wavelength longer than 8 µm. The residual optical absorption in mid-infrared mainly arises from disorders, which is suppressed to around 1% in monolayer graphene (*108*). The low mid-infrared optical absorption in graphene has been improved in its engineered nanostructures such as graphene nanoribbon arrays (*105-107*). Due to strong light-plasmon coupling, plasmonic resonances in engineered graphene nanostructures can be efficiently excited by electromagnetic radiation, leading to an enhanced mid-infrared optical absorption up to 10% (*99*). However, there is still ample room for further improvement of the optical absorption.

On the other hand, as the thermistor of the microbolometer, the graphene exhibits an extremely low TCR, especially for CVD graphene where the impurity scattering and defects dominate the electrical transport (*336, 337*). The TCR of unpatterned CVD graphene and graphene plasmonic device was reported as 0.01 and 0.06 %/K at room temperature, respectively (*99*). The TCR is significantly lower than that of Ti-Si-Ti Schottky barrier resistor (5%) demonstrated in **Section**

3.2 and amorphous Si or VO$_x$ (2-3%) for commercialized microbolometers (*288, 289*). In contrast, exfoliated graphene exhibits higher TCR (0.5%) compared with CVD graphene (*100*). However, large-scale exfoliated graphene is difficult to synthesize for patterning nanostructures. As illustrated in **Formula (36)**, the responsivity of the microbolometers scales linearly with TCR. Therefore, the low TCR further degrades the performance of current graphene-based microbolometers.

Recently, terahertz plasmonic absorption has been discovered in thin-film graphite (*338*), providing a new perspective for infrared light detection applications. Thin-film graphite takes advantages over monolayer or few-layer graphene from several aspects. First, thin-film graphite is quite intrinsic with low Fermi level. Therefore, the onset wavelength of interband optical transition dominated by Pauli blocking is prominently redshifted beyond the mid-infrared regime. The mid-infrared optical absorption by direct interband transition is allowed in thin-film graphite (*338*). In addition, the thin-film graphite nanoribbon array exhibits stronger plasmonic resonance than its monolayer or few-layer counterpart, giving rise to a plasmonic absorption over 40% in terahertz regime (*338*). By further tuning the ribbon width, the plasmonic resonant wavelength can be modulated. Therefore, it is highly attractive to investigate plasmonic properties of thin-film graphite in mid-infrared regime. It is expected that the overall optical absorption in thin-film graphite nanoribbon array is enhanced since it is contributed by both interband and plasmonic absorption. Meanwhile, the TCR of thin-film graphite and its plasmonic device has rarely been investigated. Therefore, it is also necessary to experimentally evaluate its potential as the thermistor of the microbolometer.

Graphite flakes were directly deposited onto 60-nm diamond-like carbon (DLC)/Si substrate using the mechanical exfoliation method. The DLC was used as the substrate due to its low

surface trap density and high phonon energy from its nonpolar nature (*339*). Therefore, the interaction between graphite plasmons and substrate surface polar phonons can be minimized compared with SiO_2 and other commonly used substrates (*105*). Meanwhile, DLC has a low thermal conductivity of 0.15-0.3 $W \cdot m^{-1} \cdot K^{-1}$ (*340*), which is highly desired for thermal isolation of a microbolometer. Large and homogeneous graphite flakes with size over 50 µm were required for patterning graphite nanoribbon arrays and infrared spectra measurements. The thickness of the graphite flakes was determined by AFM measurements and we focused on graphite flakes with thickness ranging from 15 nm to 40 nm. The PMMA was used as the e-beam resist and the dry etch mask, which was spin-coated onto graphite flakes at 3000 rpm for 90 seconds. The graphite nanoribbon arrays was defined by a Vistec 100 kV electron-beam lithography system and was then patterned in a SF_6 environment for 100 seconds by an Oxford Plasmalab 100 reactive ion etching system. The PMMA mask was removed in Acetone before infrared spectra measurements. **Fig 4.2.1** exhibits the optical image of the graphite nanoribbon array with width of 200 nm, thickness of 35 nm and period of 400 nm.
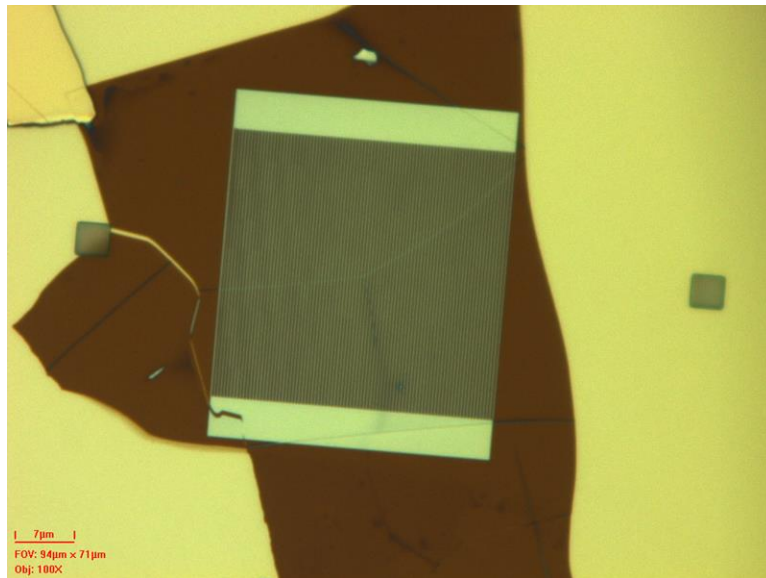
Fig 4.2.1 The optical image of the graphite nanoribbon array for infrared spectra measurements.

147
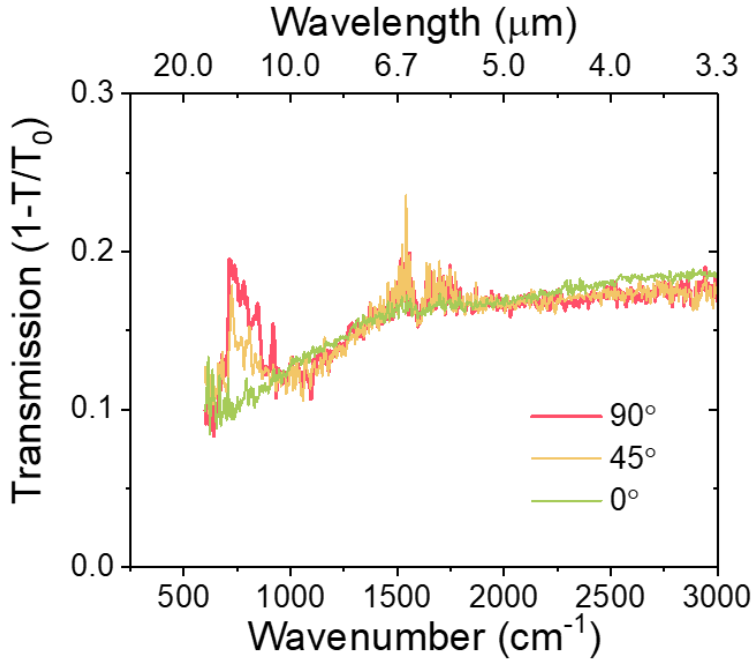
Fig 4.2.2 The linearly-polarized infrared extinction spectra of the graphite nanoribbon array. The red (green) curve shows the spectra for incident light polarization perpendicular (parallel) to graphite nanoribbon direction.

We performed infrared extinction spectra measurements on the graphite nanoribbon array to investigate its plasmonic resonance. The infrared spectra was measured by a Bruker Vertex 70 FTIR spectrometer coupled with a Hyperion 2000 infrared microscope. Both the transmission spectra through the graphite nanoribbon array (T) and the reference area nearby without graphite (T_0) were recorded, and the extinction spectra can be calculated by $1-T/T_0$. The optical window size was kept as 32 µm by 32 µm throughout the measurements, smaller than the area of the graphite nanoribbon array. We measured the extinction spectra under excitation polarizations either perpendicular or parallel to the graphite nanoribbon array at room temperature. The polarization of incident radiance was tuned by rotating a zinc selenide (ZnSe) wire-grid polarizer with respect to the graphite nanoribbon direction. The linearly-polarized extinction spectra were plotted in **Fig 4.2.2**. For light polarization perpendicular to the graphite nanoribbon direction, a

prominent plasmonic resonance was observed at 740 cm^{-1} with plasmonic absorption of 10%, corresponding to the absorption resonant wavelength of 13.5 µm. In contrast, the plasmonic resonance completely vanished for light polarization parallel to the graphite nanoribbon direction, verifying the nature of light-plasmon interaction. Notably, an isotropic background absorption of 10% was observed under both excitation polarizations, arising from interband optical transition in thin-film graphite (*338*). Due to the low Fermi level in intrinsic graphite, the onset of the interband absorption is significantly redshifted. Since both plasmonic absorption and interband absorption can contribute to the light detection in microbolometers, the graphite nanoribbon arrays exhibit a total absorption of 20% at resonant wavelength. This value takes significant advantages over the optical absorption achieved in graphene and engineered graphene nanostructures in mid-infrared reported in previous work. By further tuning the ribbon width of the graphite nanoribbon array, the resonant wavelength can be modulated, covering a wide spectrum region in mid-infrared.
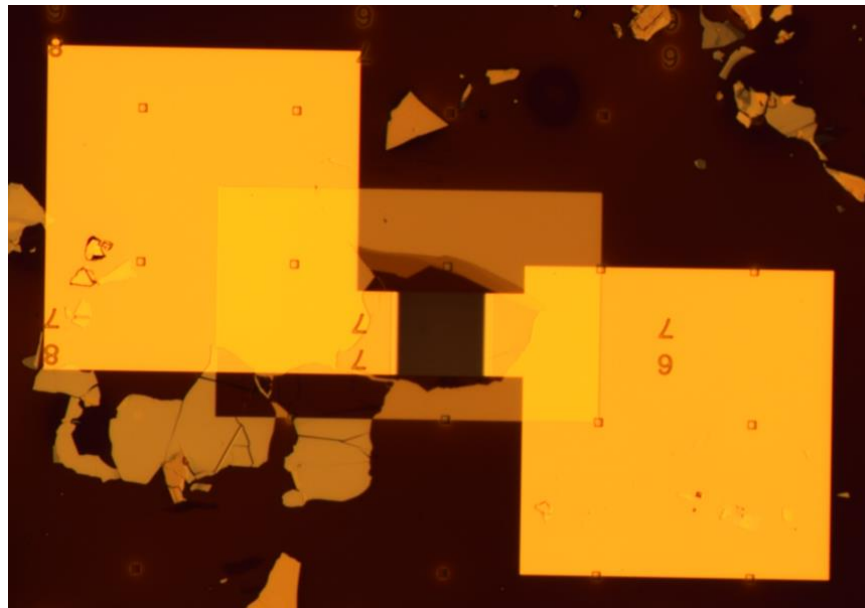
Fig 4.2.3 The optical image of the graphite nanoribbon array device for transport measurements.

The transport properties and TCR of the graphite nanoribbon array were further investigated to characterize its feasibility as the thermistor of microbolometer. The electrode pattern was defined by another electron-beam lithography process. 3 nm chromium and 37 nm gold were then evaporated by Kurt J. Lesker Nano 38 thermal evaporator, followed by a lift-off in acetone to form the metal contacts. The optical image of a fabricated graphite nanoribbon array device was shown in **Fig 4.2.3**. The temperature dependent transport measurements were performed in a Lakeshore CPX cryogenic probe station. The source-drain bias voltage was applied by an Agilent B1500A semiconductor parameter analyzer. **Fig 4.2.4** exhibits the I-V characteristics of the graphite nanoribbon array device. The device current reaches 74 μA under a forward bias of 10 mV, corresponding to an equivalent resistance of 135 Ω. Considering the geometry parameter of the graphite nanoribbon array, the resistivity can be calculated as 120 μOhm·cm, consistent with previously reported value. To explore the TCR, the I-V characteristics of the device were measured from 80K to 300K with an interval of 20K, as shown in **Fig 4.2.5a**. The insert of **Fig 4.2.5a** exhibits the detailed I-V characteristics at bias voltage near 0.01 V for clarity. The temperature dependence of the resistivity can be divided into two regimes, as illustrated in the insert of **Fig 4.2.5a** by the blue arrows. For temperature below 100K, the resistivity increases with increasing temperature, dominated by the enhanced electron-phonon scattering. In contrast, for temperature above 100K, the resistivity decreases with increasing temperature, arising from the activated thermal carrier excitation. The TCR at temperature T_0 was estimated by

$$TCR = (\frac{R(T_0 - 20K) - R(T_0)}{R(T_0)})/20K \times 100\% \qquad (41)$$

The calculated temperature dependence of TCR was plotted in **Fig 4.2.5b.** The graphite nanoribbon array device exhibits a maximum TCR of 0.34%/K at 160K and a moderate TCR of

0.09%/K at room temperature. The TCR of the graphite nanoribbon array as the thermistor is still significantly lower than that of Ti-Si-Ti Schottky barrier resistor (5%) and amorphous Si or VO_x (2-3%) (*288, 289*). However, it takes advantages over the CVD graphene plasmonic devices (0.06%/K) and unpatterned CVD graphene devices (<0.01%/K) for mid-infrared light detection (*99*).
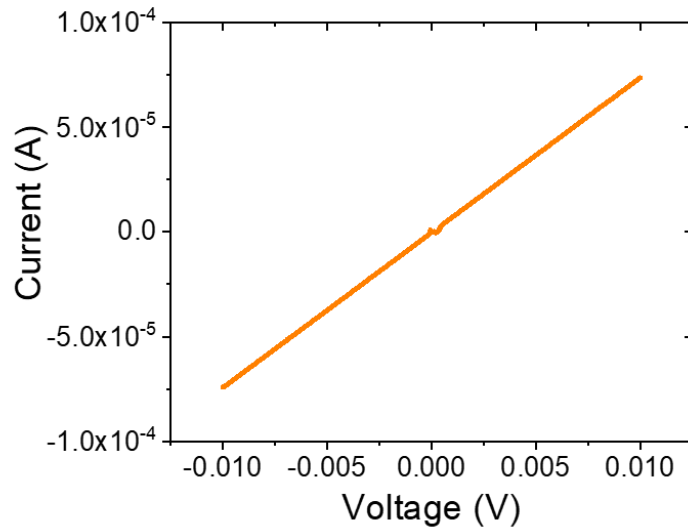
Fig 4.2.4 The I-V characteristics of the graphite nanoribbon array device at room temperature.
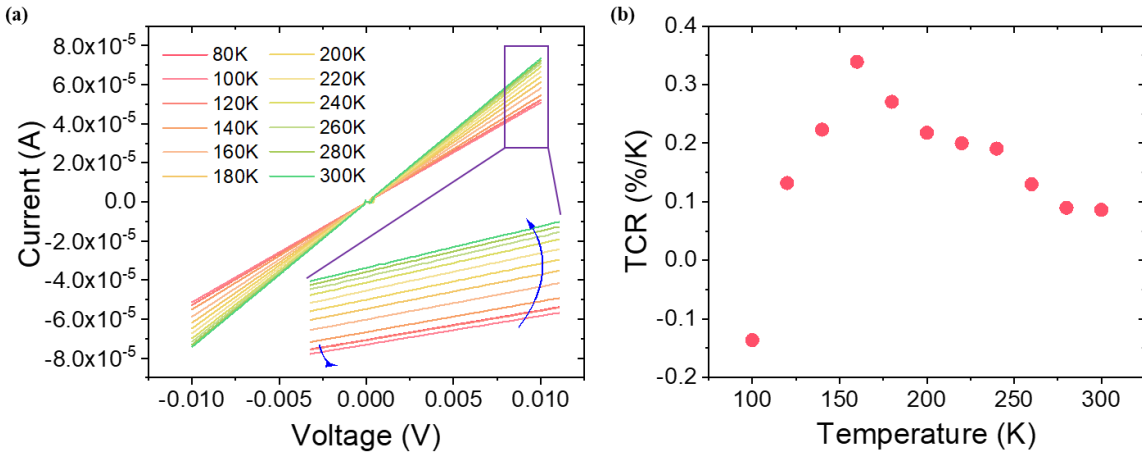
Fig 4.2.5 (a) The temperature dependent I-V characteristics of the graphite nanoribbon array device. The insert: detailed I-V characteristics at bias voltage near 0.01 V. **(b)** The calculated temperature dependence of TCR.

151

In summary, the thin-film graphite nanoribbon array exhibits significantly higher mid-infrared optical absorption compared to its monolayer or few-layer counterpart. The resonant absorption wavelength can be easily modulated over a broadband spectrum region in mid-infrared by tuning the ribbon width. These distinguished characteristics make thin-film graphite nanoribbon array an appropriate candidate as infrared absorber for microbolometers. Meanwhile, as the thermistor, the TCR of graphite nanoribbon array device is also slightly elevated compared to that of CVD graphene plasmonic devices. Therefore, the overall performance of the graphite nanoribbon array device will be superior to that of the graphene based mid-infrared microbolometers reported in previous work. Since its ultrathin nature preserves its ultrafast operational speed, the graphite nanoribbon array device exhibits a promising perspective for mid-infrared light detection applications.

However, we also point out that the performance of thin-film graphite nanoribbon array may vary from device to device. This is because the thin-film graphite is quite intrinsic with low Fermi level (*338*). Therefore, a slight variation in Fermi level among thin-film graphite flakes can prominently influence both the optical and transports properties of the fabricated graphite nanoribbon array devices. The investigations on engineered thin-film graphite nanostructure devices for mid-infrared light detection applications is still at its preliminary stage. Future work should focus on the synthesis of large and homogeneous graphite flakes, the optimization of the nanostructure fabrication techniques, and the fine tuning of Fermi level for controllable optical and transport properties.

4.2.2 Mid-infrared light emissions from thin-film Tellurene

The 2D Te has been recently discovered as a new member of the 2D material family (*341-343*). The bandgap of 2D Te evolves with its layer number, exhibiting an indirect to direct bandgap transition from bilayer Te to its bulk counterpart (*344, 345*). The thin-film Te exhibits a moderate bandgap of 0.3 eV, similar to that of thin-film BP. Since BP is highly reactive to moisture atmosphere, it suffers severely from oxidation issues (*95, 96*). The BP-based devices requires complicated passivation techniques, which limits its commercialized applications. On the contrary, thin-film Te exhibits an excellent air stability (*346, 347*), making it a promising substitute of BP for mid-infrared optoelectronic applications.
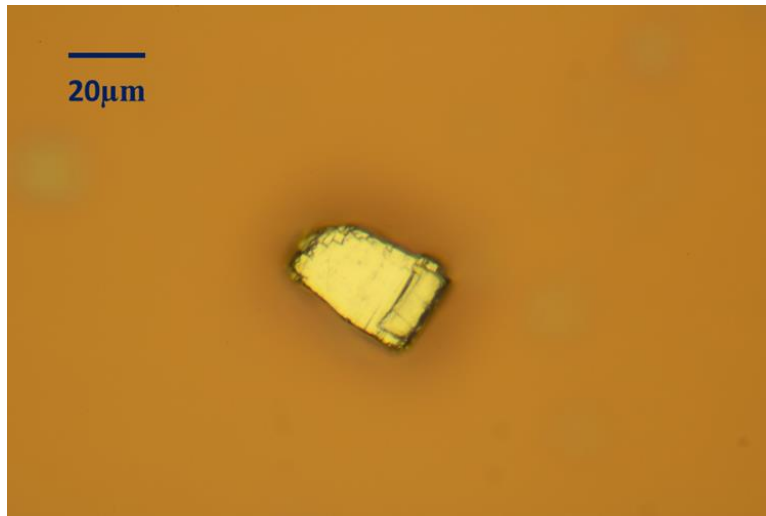
Fig 4.2.6 Optical image of a Te flake on a 285-nm SiO_2/Si substrate.

The Te crystals with purity over 99.99% was purchased from Smart Elements. Te flakes for optical characterizations were directly deposited onto the 285-nm SiO_2/Si substrate using the standard mechanical exfoliation method. **Fig 4.2.6** shows the optical microscope image of a typical Te flake used for optical characterization.
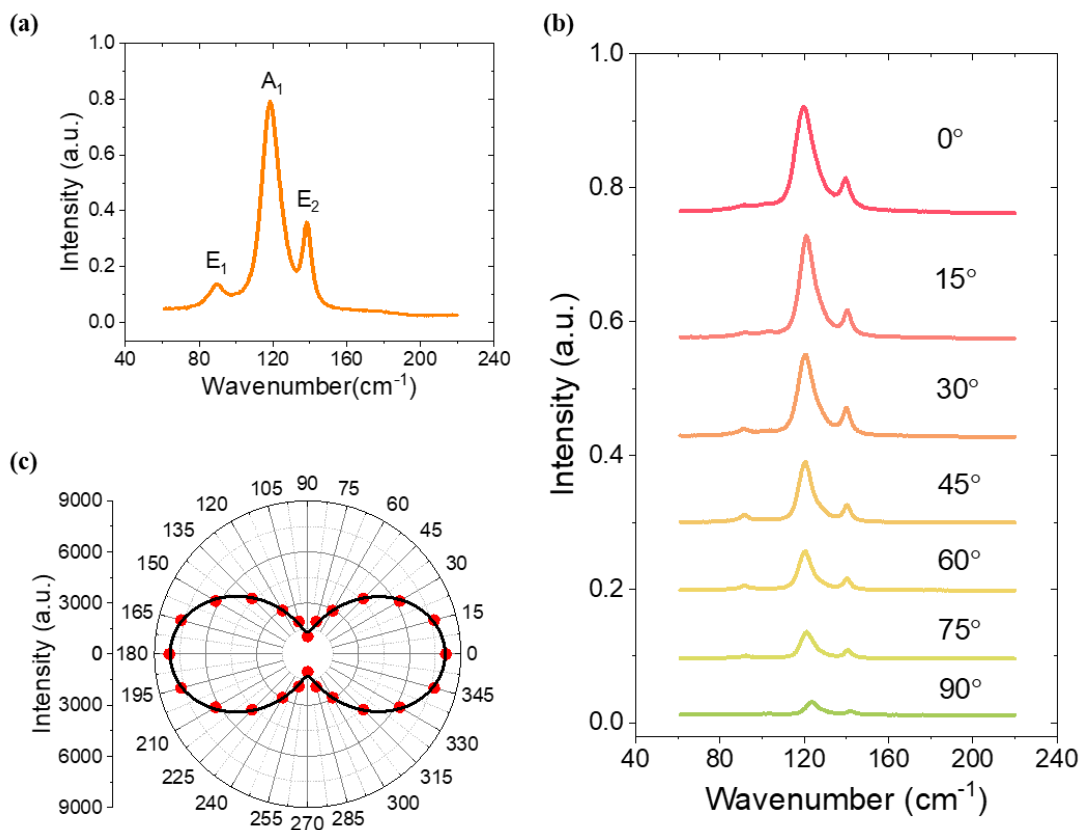
Fig 4.2.7 (a) Raman scattering spectra of the Te flake. **(b)** Polarization-resolved Raman spectrum of the Te flake. **(c)** The measured (dotes) and fitted (line) angular-resolved Raman intensity of A_1 mode.

The Te flake was first characterized by Raman spectroscopy. The Raman spectroscopy was performed with Horiba LabRAM HR Evolution Raman Microscope with excitation photon energy of 2.33eV. Three prominent Raman modes were resolved, corresponding to the E_1, A_1 and E_2 mode, as reported previously (*346*). All these Raman modes show the typical Lorentz shape and they are positioned at 90 cm^{-1}, 118 cm^{-1} and 138 cm^{-1}, respectively, as illustrated in **Fig 4.2.8a**. The angular-resolved Raman spectrum was then performed by rotating the sample with respect to the laser polarization to determine the crystal orientation, as exhibited in **Fig 4.2.8b**. The **Fig 4.2.8c** shows the angular-resolved Raman intensity of A_1 mode, where 0 degree

is determined as the x-direction of the Te crystal. We performed the PL measurements on the thin-film Te flake at 80K with excitation power of 10 µW/µm^2. As shown in **Fig 4.2.9**, the PL spectrum exhibits a peak position at 0.127 eV, which is significantly lower than the bandgap of thin-film Te estimated by theoretical calculation. This weak emission peak may arise from optical transition from the defect level due to the low quality of the Te flake. The light emission from intrinsic band transition in thin-film Te still remains an unexplored topic up to date.
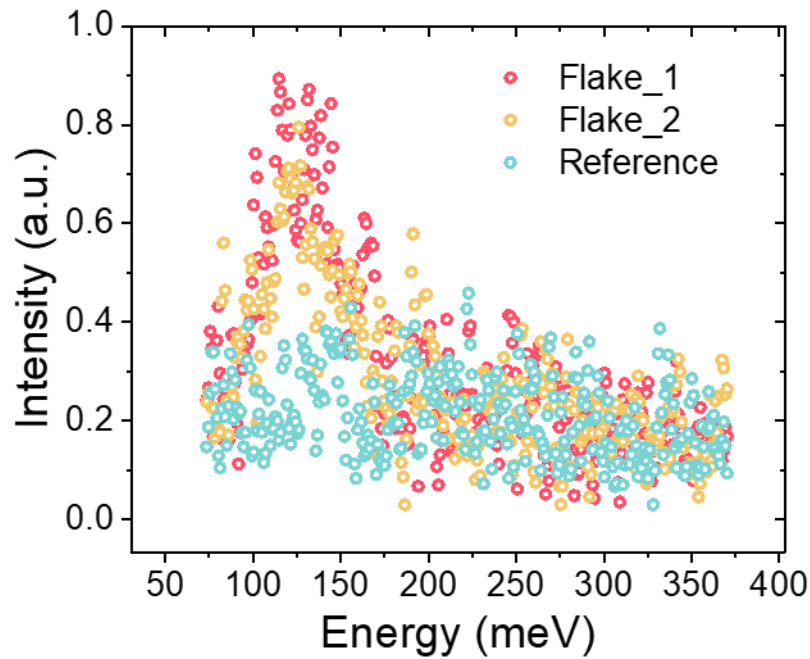
Fig 4.2.8 PL spectra from the Te flake and SiO$_2$/Si substrate .

Recently, the large-scale, high-quality monolayer and few-layer Te flakes have been successfully synthesized by a substrate-free solution process (*346*). Based on that, thin-film Te-based field effect transistors (FET) have been realized (*346*), exhibiting a high field effect mobility of 700 cm^2·V^{-1}·s^{-1} and a high on-off ratio of 10^5, comparable to that of thin-film BP transistors (*149*). Remarkably, the performance of Te-based FET exhibits insignificant degradation after 55 days' exposure in air, demonstrating its extraordinary air stability (*346*). The Te infrared photodetector

with high gain and wide bandwidth was then fabricated, indicating its great potential for infrared optoelectronic applications (*348, 349*). Therefore, with much improved sample quality and measurement scheme, it is appealed to investigate its possibility for mid-infrared light emitting applications. Meanwhile, the detection wavelength of Te photodetector was limited by 3.4 µm due to its intrinsic bandgap (*348*). It is also highly desired to explore the bandgap tunablity of thin-film Te to extend its mid-infrared optoelectronic applications beyond the cut-off wavelength.

5. Conclusion

In this thesis, we explore thin-film materials from both perspective of fundamental light-matter interaction properties and mid-infrared optoelectronic applications. On the one hand, the light-matter interaction in thin-film 2D materials provides new perspective and new materials system for probing the lattice symmetry and valley physics, giving rise to its great potential for next generation valleytronic and phononic applications. First, we discover the strong electron-phonon interactions in engineered 2D material/SiO$_2$ vdWs heterostructures where two optically silent phonon modes in amorphous SiO$_2$ are activated through coupling with the electronic transitions in 2D materials. We show that the chirality and anisotropy of the phonon modes in amorphous SiO$_2$ are dominated by the lattice symmetry and band properties of 2D materials. Our observation gives rise to a new perspective for probing the electronic band properties and optical selectivity in atomically thin materials. We then reveal that phonons in crystalline 2D materials can exhibit unique anisotropy and chirality as well, subjected to the crystal symmetry of 2D materials. We show that the phonon chirality in 2D honeycomb lattice can be influenced by vdWs interlayer interaction, evidenced by the decreasing circular polarization degree with increasing layer number. Our work provides a new method to probe the interlayer interaction in vdWs materials and heterostructures with honeycomb lattice symmetry. Finally, we demonstrate the valley-selective linear dichroism in SnS with orthorhombic lattice structure and reduced lattice symmetry. We show that the PL emissions, arising from the optical transitions from Γ-X and Γ-Y valley, are purely linearly polarized along x- and y-directions respectively. Our findings opens up new material system beyond 2D honeycomb lattice for exploring valley physics and valleytronic applications.

On the other hand, the thin-film technology provides a promising pathway for mid-infrared optoelectronics due to its high efficiency, high speed and wide tunability. First, we report a bright and widely tunable mid-infrared light emission from thin-film BP. We show that the brightness of PL emission from thin-film BP is comparable to that of InAs MQW, which has been applied for infrared room-temperature lasers. The PL emission can be further tuned from 3.7 µm to 7.7 µm under a moderate displacement filed of 0.48 V/nm, covering a wide spectrum region in mid-infrared. Our results demonstrate the high efficiency and wide tunablity of light emissions from thin-film BP, giving rise to its great potential for mid-infrared light generation applications. In addition, we demonstrate an ultrafast long-wavelength infrared microbolometer based on ultrathin silicon nanomembrane. The ultra-thinness of the silicon nanomembrane results in an ultra-small C_{th} of around $1.9 \times 10^{-11} J/K$, which allows for its operation at a speed of over 10 kHz. This represents the record-high speed in LWIR microbolometers, which has been improved by over 500 times compared to that of typical commercialized ones. Moreover, a compact diabolo antenna is leveraged for efficient LWIR light absorption, enabling the downscaling of the active area size to 6.2 µm by 6.2 µm. By establishing a FOM, our microbolometer significantly outperforms the commercialized ones, making it promising for future mid-infrared light detection applications. We further provide our outlooks on thin-film technology for mid-infrared optoelectronic applications and discuss some possible future works. We discuss the possibility of thin-film graphite plasmonic device for mid-infrared light detection applications since its optical absorption and TCR are superior to that of graphene-based microbolometers. We also discuss the potential of thin-film Te as an appropriate substitute of BP for mid-infrared light emitting applications.

Bibliography

1.   M. Xu, T. Liang, M. Shi, H. Chen, Graphene-Like Two-Dimensional Materials. *Chemical Reviews* **113**, 3766-3798 (2013).

2.   S. Z. Butler, S. M. Hollen, L. Cao, Y. Cui, J. A. Gupta, H. R. Gutiérrez, T. F. Heinz, S. S. Hong, J. Huang, A. F. Ismach, E. Johnston-Halperin, M. Kuno, V. V. Plashnitsa, R. D. Robinson, R. S. Ruoff, S. Salahuddin, J. Shan, L. Shi, M. G. Spencer, M. Terrones, W. Windl, J. E. Goldberger, Progress, Challenges, and Opportunities in Two-Dimensional Materials Beyond Graphene. *ACS Nano* **7**, 2898-2926 (2013).

3.   G. R. Bhimanapati, Z. Lin, V. Meunier, Y. Jung, J. Cha, S. Das, D. Xiao, Y. Son, M. S. Strano, V. R. Cooper, L. Liang, S. G. Louie, E. Ringe, W. Zhou, S. S. Kim, R. R. Naik, B. G. Sumpter, H. Terrones, F. Xia, Y. Wang, J. Zhu, D. Akinwande, N. Alem, J. A. Schuller, R. E. Schaak, M. Terrones, J. A. Robinson, Recent Advances in Two-Dimensional Materials beyond Graphene. *ACS Nano* **9**, 11509-11539 (2015).

4.   K. S. Novoselov, A. Mishchenko, A. Carvalho, A. H. Castro Neto, 2D materials and van der Waals heterostructures. *Science* **353**, aac9439 (2016).

5.   A. J. Mannix, B. Kiraly, M. C. Hersam, N. P. Guisinger, Synthesis and chemistry of elemental 2D materials. *Nature Reviews Chemistry* **1**, 0014 (2017).

6.   R. Mas-Balleste, C. Gomez-Navarro, J. Gomez-Herrero, F. Zamora, 2D materials: to graphene and beyond. *Nanoscale* **3**, 20-30 (2011).

7.   P. Miró, M. Audiffred, T. Heine, An atlas of two-dimensional materials. *Chemical Society Reviews* **43**, 6537-6554 (2014).

8.   P. Liu, J. R. Williams, J. J. Cha, Topological nanomaterials. *Nature Reviews Materials* **4**, 479-496 (2019).

9.   J. Wang, S. Deng, Z. Liu, Z. Liu, The rare two-dimensional materials with Dirac cones. *National Science Review* **2**, 22-39 (2015).

10.   N. Nagaosa, T. Morimoto, Y. Tokura, Transport, magnetic and optical properties of Weyl materials. *Nature Reviews Materials* **5**, 621-636 (2020).

11.   M. Gibertini, M. Koperski, A. F. Morpurgo, K. S. Novoselov, Magnetic 2D materials and heterostructures. *Nature Nanotechnology* **14**, 408-419 (2019).

12.   Y. Saito, T. Nojima, Y. Iwasa, Highly crystalline 2D superconductors. *Nature Reviews Materials* **2**, 16094 (2016).

13.   V. K. Sangwan, M. C. Hersam, Electronic Transport in Two-Dimensional Materials. *Annual Review of Physical Chemistry* **69**, 299-325 (2018).

14.   J. R. Schaibley, H. Yu, G. Clark, P. Rivera, J. S. Ross, K. L. Seyler, W. Yao, X. Xu, Valleytronics in 2D materials. *Nature Reviews Materials* **1**, 16055 (2016).

15.   A. Tartakovskii, Excitons in 2D heterostructures. *Nature Reviews Physics* **2**, 8-9 (2020).

16.   E. Y. Andrei, D. K. Efetov, P. Jarillo-Herrero, A. H. MacDonald, K. F. Mak, T. Senthil, E. Tutuc, A. Yazdani, A. F. Young, The marvels of moiré materials. *Nature Reviews Materials* **6**, 201-206 (2021).

17.   F. He, Y. Zhou, Z. Ye, S.-H. Cho, J. Jeong, X. Meng, Y. Wang, Moiré Patterns in 2D Materials: A Review. *ACS Nano* **15**, 5944-5958 (2021).

18.   G. Fiori, F. Bonaccorso, G. Iannaccone, T. Palacios, D. Neumaier, A. Seabaugh, S. K. Banerjee, L. Colombo, Electronics based on two-dimensional materials. *Nature Nanotechnology* **9**, 768-779 (2014).

19.   F. Xia, H. Wang, D. Xiao, M. Dubey, A. Ramasubramaniam, Two-dimensional material nanophotonics. *Nature Photonics* **8**, 899-907 (2014).

20.   X. Chia, M. Pumera, Characteristics and performance of two-dimensional materials for electrocatalysis. *Nature Catalysis* **1**, 909-921 (2018).

21.   X. Liu, M. C. Hersam, 2D materials for quantum information science. *Nature Reviews Materials* **4**, 669-684 (2019).

22.   X. Lin, W. Yang, K. L. Wang, W. Zhao, Two-dimensional spintronics for low-power electronics. *Nature Electronics* **2**, 274-283 (2019).

23.   S. Wang, D. W. Zhang, P. Zhou, Two-dimensional materials for synaptic electronics and neuromorphic systems. *Science Bulletin* **64**, 1056-1066 (2019).

24. S. J. Kim, K. Choi, B. Lee, Y. Kim, B. H. Hong, Materials for Flexible, Stretchable Electronics: Graphene and 2D Materials. *Annual Review of Materials Research* **45**, 63-84 (2015).

25. S. Zeng, Z. Tang, C. Liu, P. Zhou, Electronics based on two-dimensional materials: Status and outlook. *Nano Research* **14**, 1752-1767 (2021).

26. C. Anichini, W. Czepa, D. Pakulski, A. Aliprandi, A. Ciesielski, P. Samorì, Chemical sensing with 2D materials. *Chemical Society Reviews* **47**, 4860-4908 (2018).

27. M. Long, P. Wang, H. Fang, W. Hu, Progress, Challenges, and Opportunities for 2D Material Based Photodetectors. *Advanced Functional Materials* **29**, 1803807 (2019).

28. A. Jayakumar, A. Surendranath, M. Pv, 2D materials for next generation healthcare applications. *International Journal of Pharmaceutics* **551**, 309-321 (2018).

29. B. Dubertret, T. Heine, H. Terrones, The Rise of Two-Dimensional Materials. *Accounts of Chemical Research* **48**, 1-2 (2015).

30. A. H. Castro Neto, F. Guinea, N. M. R. Peres, K. S. Novoselov, A. K. Geim, The electronic properties of graphene. *Reviews of Modern Physics* **81**, 109-162 (2009).

31. V. Tran, R. Soklaski, Y. Liang, L. Yang, Layer-controlled band gap and anisotropic excitons in few-layer black phosphorus. *Physical Review B* **89**, 235319 (2014).

32. A. Splendiani, L. Sun, Y. Zhang, T. Li, J. Kim, C.-Y. Chim, G. Galli, F. Wang, Emerging Photoluminescence in Monolayer MoS_2. *Nano Letters* **10**, 1271-1275 (2010).

33. K. F. Mak, C. Lee, J. Hone, J. Shan, T. F. Heinz, Atomically Thin MoS_2: A New Direct-Gap Semiconductor. *Physical Review Letters* **105**, 136805 (2010).

34. K. Watanabe, T. Taniguchi, H. Kanda, Direct-bandgap properties and evidence for ultraviolet lasing of hexagonal boron nitride single crystal. *Nature Materials* **3**, 404-409 (2004).

35. G. Cassabois, P. Valvin, B. Gil, Hexagonal boron nitride is an indirect bandgap semiconductor. *Nature Photonics* **10**, 262-266 (2016).

36. C. R. Dean, A. F. Young, I. Meric, C. Lee, L. Wang, S. Sorgenfrei, K. Watanabe, T. Taniguchi, P. Kim, K. L. Shepard, J. Hone, Boron nitride substrates for high-quality graphene electronics. *Nature Nanotechnology* **5**, 722-726 (2010).

37. T. T. Tran, K. Bray, M. J. Ford, M. Toth, I. Aharonovich, Quantum emission from hexagonal boron nitride monolayers. *Nature Nanotechnology* **11**, 37-41 (2016).

38. N. Mendelson, D. Chugh, J. R. Reimers, T. S. Cheng, A. Gottscholl, H. Long, C. J. Mellor, A. Zettl, V. Dyakonov, P. H. Beton, S. V. Novikov, C. Jagadish, H. H. Tan, M. J. Ford, M. Toth, C. Bradac, I. Aharonovich, Identifying carbon as the source of visible single-photon emission from hexagonal boron nitride. *Nature Materials* **20**, 321-328 (2021).

39. G. Grosso, H. Moon, B. Lienhard, S. Ali, D. K. Efetov, M. M. Furchi, P. Jarillo-Herrero, M. J. Ford, I. Aharonovich, D. Englund, Tunable and high-purity room temperature single-photon emission from atomic defects in hexagonal boron nitride. *Nature Communications* **8**, 705 (2017).

40. A. Kumar, P. K. Ahluwalia, Electronic structure of transition metal dichalcogenides monolayers 1H-MX_2 (M = Mo, W; X = S, Se, Te) from ab-initio theory: new direct band gap semiconductors. *The European Physical Journal B* **85**, 186 (2012).

41. F. A. Rasmussen, K. S. Thygesen, Computational 2D Materials Database: Electronic Structure of Transition-Metal Dichalcogenides and Oxides. *The Journal of Physical Chemistry C* **119**, 13169-13183 (2015).

42. O. Lopez-Sanchez, D. Lembke, M. Kayci, A. Radenovic, A. Kis, Ultrasensitive photodetectors based on monolayer MoS_2. *Nature Nanotechnology* **8**, 497-501 (2013).

43. H. Wang, C. Zhang, W. Chan, S. Tiwari, F. Rana, Ultrafast response of monolayer molybdenum disulfide photodetectors. *Nature Communications* **6**, 8831 (2015).

44. J. S. Ross, P. Klement, A. M. Jones, N. J. Ghimire, J. Yan, D. G. Mandrus, T. Taniguchi, K. Watanabe, K. Kitamura, W. Yao, D. H. Cobden, X. Xu, Electrically tunable excitonic light-emitting diodes based on monolayer WSe_2 p–n junctions. *Nature Nanotechnology* **9**, 268-272 (2014).

45. F. Withers, O. Del Pozo-Zamudio, A. Mishchenko, A. P. Rooney, A. Gholinia, K. Watanabe, T. Taniguchi, S. J. Haigh, A. K. Geim, A. I. Tartakovskii, K. S. Novoselov, Light-emitting diodes by band-structure engineering in van der Waals heterostructures. *Nature Materials* **14**, 301-306 (2015).

46.   B. W. H. Baugher, H. O. H. Churchill, Y. Yang, P. Jarillo-Herrero, Optoelectronic devices based on electrically tunable p–n diodes in a monolayer dichalcogenide. *Nature Nanotechnology* **9**, 262-267 (2014).

47.   H. Tian, M. L. Chin, S. Najmaei, Q. Guo, F. Xia, H. Wang, M. Dubey, Optoelectronic devices based on two-dimensional transition metal dichalcogenides. *Nano Research* **9**, 1543-1560 (2016).

48.   A. Morita, Semiconducting black phosphorus. *Applied Physics A* **39**, 227-242 (1986).

49.   L. Li, J. Kim, C. Jin, G. J. Ye, D. Y. Qiu, F. H. da Jornada, Z. Shi, L. Chen, Z. Zhang, F. Yang, K. Watanabe, T. Taniguchi, W. Ren, S. G. Louie, X. H. Chen, Y. Zhang, F. Wang, Direct observation of the layer-dependent electronic structure in phosphorene. *Nature Nanotechnology* **12**, 21-25 (2017).

50.   G. Zhang, S. Huang, A. Chaves, C. Song, V. O. Özçelik, T. Low, H. Yan, Infrared fingerprints of few-layer black phosphorus. *Nature Communications* **8**, 14071 (2017).

51.   B. Deng, V. Tran, Y. Xie, H. Jiang, C. Li, Q. Guo, X. Wang, H. Tian, S. J. Koester, H. Wang, J. J. Cha, Q. Xia, L. Yang, F. Xia, Efficient electrical control of thin-film black phosphorus bandgap. *Nature Communications* **8**, 14474 (2017).

52.   T. Low, A. S. Rodin, A. Carvalho, Y. Jiang, H. Wang, F. Xia, A. H. Castro Neto, Tunable optical properties of multilayer black phosphorus thin films. *Physical Review B* **90**, 075434 (2014).

53.   Y. Liu, Z. Qiu, A. Carvalho, Y. Bao, H. Xu, S. J. R. Tan, W. Liu, A. H. Castro Neto, K. P. Loh, J. Lu, Gate-Tunable Giant Stark Effect in Few-Layer Black Phosphorus. *Nano Letters* **17**, 1970-1977 (2017).

54.   J. Bullock, M. Amani, J. Cho, Y.-Z. Chen, G. H. Ahn, V. Adinolfi, V. R. Shrestha, Y. Gao, K. B. Crozier, Y.-L. Chueh, A. Javey, Polarization-resolved black phosphorus/molybdenum disulfide mid-wave infrared photodiodes with high detectivity at room temperature. *Nature Photonics* **12**, 601-607 (2018).

55.   X. Chen, X. Lu, B. Deng, O. Sinai, Y. Shao, C. Li, S. Yuan, V. Tran, K. Watanabe, T. Taniguchi, D. Naveh, L. Yang, F. Xia, Widely tunable black phosphorus mid-infrared photodetector. *Nature Communications* **8**, 1672 (2017).

56.   R. Peng, K. Khaliji, N. Youngblood, R. Grassi, T. Low, M. Li, Midinfrared Electro-optic Modulation in Few-Layer Black Phosphorus. *Nano Letters* **17**, 6315-6320 (2017).

57.   K. F. Mak, L. Ju, F. Wang, T. F. Heinz, Optical spectroscopy of graphene: From the far infrared to the ultraviolet. *Solid State Communications* **152**, 1341-1349 (2012).

58.   F. Xia, H. Yan, P. Avouris, The Interaction of Light and Graphene: Basics, Devices, and Applications. *Proceedings of the IEEE* **101**, 1717-1731 (2013).

59.   S. Manzeli, D. Ovchinnikov, D. Pasquier, O. V. Yazyev, A. Kis, 2D transition metal dichalcogenides. *Nature Reviews Materials* **2**, 17033 (2017).

60.   J. D. Caldwell, I. Aharonovich, G. Cassabois, J. H. Edgar, B. Gil, D. N. Basov, Photonics with hexagonal boron nitride. *Nature Reviews Materials* **4**, 552-567 (2019).

61.   J. F. Cornwell, *Group theory in physics: An introduction* (Academic press, 1997).

62.   D. Xiao, G.-B. Liu, W. Feng, X. Xu, W. Yao, Coupled Spin and Valley Physics in Monolayers of MoS_2 and Other Group-VI Dichalcogenides. *Physical Review Letters* **108**, 196802 (2012).

63.   X. Xu, W. Yao, D. Xiao, T. F. Heinz, Spin and pseudospins in layered transition metal dichalcogenides. *Nature Physics* **10**, 343-350 (2014).

64.   K. F. Mak, K. He, J. Shan, T. F. Heinz, Control of valley polarization in monolayer MoS_2 by optical helicity. *Nature Nanotechnology* **7**, 494-498 (2012).

65.   A. M. Jones, H. Yu, N. J. Ghimire, S. Wu, G. Aivazian, J. S. Ross, B. Zhao, J. Yan, D. G. Mandrus, D. Xiao, W. Yao, X. Xu, Optical generation of excitonic valley coherence in monolayer WSe2. *Nature Nanotechnology* **8**, 634-638 (2013).

66.   B. Zhu, H. Zeng, J. Dai, Z. Gong, X. Cui, Anomalously robust valley polarization and valley coherence in bilayer WS_2. *Proceedings of the National Academy of Sciences* **111**, 11606 (2014).

67.   R. V. Gorbachev, J. C. W. Song, G. L. Yu, A. V. Kretinin, F. Withers, Y. Cao, A. Mishchenko, I. V. Grigorieva, K. S. Novoselov, L. S. Levitov, A. K. Geim, Detecting topological currents in graphene superlattices. *Science* **346**, 448-451 (2014).

68. M. Sui, G. Chen, L. Ma, W.-Y. Shan, D. Tian, K. Watanabe, T. Taniguchi, X. Jin, W. Yao, D. Xiao, Y. Zhang, Gate-tunable topological valley transport in bilayer graphene. *Nature Physics* **11**, 1027-1031 (2015).

69. Y. Shimazaki, M. Yamamoto, I. V. Borzenets, K. Watanabe, T. Taniguchi, S. Tarucha, Generation and detection of pure valley current by electrically induced Berry curvature in bilayer graphene. *Nature Physics* **11**, 1032-1036 (2015).

70. K. F. Mak, K. L. McGill, J. Park, P. L. McEuen, The valley Hall effect in MoS_2 transistors. *Science* **344**, 1489-1492 (2014).

71. J. Lee, K. F. Mak, J. Shan, Electrical control of the valley Hall effect in bilayer MoS_2 transistors. *Nature Nanotechnology* **11**, 421-425 (2016).

72. X. Ling, H. Wang, S. Huang, F. Xia, M. S. Dresselhaus, The renaissance of black phosphorus. *Proceedings of the National Academy of Sciences* **112**, 4523 (2015).

73. J. Kim, J.-U. Lee, J. Lee, H. J. Park, Z. Lee, C. Lee, H. Cheong, Anomalous polarization dependence of Raman scattering and crystallographic orientation of black phosphorus. *Nanoscale* **7**, 18708-18715 (2015).

74. X. Ling, S. Huang, E. H. Hasdeo, L. Liang, W. M. Parkin, Y. Tatsumi, A. R. T. Nugraha, A. A. Puretzky, P. M. Das, B. G. Sumpter, D. B. Geohegan, J. Kong, R. Saito, M. Drndic, V. Meunier, M. S. Dresselhaus, Anisotropic Electron-Photon and Electron-Phonon Interactions in Black Phosphorus. *Nano Letters* **16**, 2260-2267 (2016).

75. F. Xia, H. Wang, Y. Jia, Rediscovering black phosphorus as an anisotropic layered material for optoelectronics and electronics. *Nature Communications* **5**, 4458 (2014).

76. J. Qiao, X. Kong, Z.-X. Hu, F. Yang, W. Ji, High-mobility transport anisotropy and linear dichroism in few-layer black phosphorus. *Nature Communications* **5**, 4475 (2014).

77. X. Wang, A. M. Jones, K. L. Seyler, V. Tran, Y. Jia, H. Zhao, H. Wang, L. Yang, X. Xu, F. Xia, Highly anisotropic and robust excitons in monolayer black phosphorus. *Nature Nanotechnology* **10**, 517-521 (2015).

78. Q. Guo, A. Pospischil, M. Bhuiyan, H. Jiang, H. Tian, D. Farmer, B. Deng, C. Li, S.-J. Han, H. Wang, Q. Xia, T.-P. Ma, T. Mueller, F. Xia, Black Phosphorus Mid-Infrared Photodetectors with High Gain. *Nano Letters* **16**, 4648-4655 (2016).

79. N. Driza, S. Blanco-Canosa, M. Bakr, S. Soltan, M. Khalid, L. Mustafa, K. Kawashima, G. Christiani, H. U. Habermeier, G. Khaliullin, C. Ulrich, M. Le Tacon, B. Keimer, Long-range transfer of electron–phonon coupling in oxide superlattices. *Nature Materials* **11**, 675-681 (2012).

80. H. Wang, J. Bang, Y. Sun, L. Liang, D. West, V. Meunier, S. Zhang, The role of collective motion in the ultrafast charge transfer in van der Waals heterostructures. *Nature Communications* **7**, 11504 (2016).

81. C. M. Chow, H. Yu, A. M. Jones, J. Yan, D. G. Mandrus, T. Taniguchi, K. Watanabe, W. Yao, X. Xu, Unusual Exciton–Phonon Interactions at van der Waals Engineered Interfaces. *Nano Letters* **17**, 1194-1199 (2017).

82. C. Jin, J. Kim, J. Suh, Z. Shi, B. Chen, X. Fan, M. Kam, K. Watanabe, T. Taniguchi, S. Tongay, A. Zettl, J. Wu, F. Wang, Interlayer electron–phonon coupling in WSe_2/hBN heterostructures. *Nature Physics* **13**, 127-131 (2017).

83. M. Buscema, D. J. Groenendijk, G. A. Steele, H. S. J. van der Zant, A. Castellanos-Gomez, Photovoltaic effect in few-layer black phosphorus PN junctions defined by local electrostatic gating. *Nature Communications* **5**, 4651 (2014).

84. M. Buscema, D. J. Groenendijk, S. I. Blanter, G. A. Steele, H. S. J. van der Zant, A. Castellanos-Gomez, Fast and Broadband Photoresponse of Few-Layer Black Phosphorus Field-Effect Transistors. *Nano Letters* **14**, 3347-3352 (2014).

85. R. K. Ulaganathan, Y.-Y. Lu, C.-J. Kuo, S. R. Tamalampudi, R. Sankar, K. M. Boopathi, A. Anand, K. Yadav, R. J. Mathew, C.-R. Liu, High photosensitivity and broad spectral response of multi-layered germanium sulfide transistors. *Nanoscale* **8**, 2284-2292 (2016).

86. L. Hao, Y. Du, Z. Wang, Y. Wu, H. Xu, S. Dong, H. Liu, Y. Liu, Q. Xue, Z. Han, Wafer-size growth of 2D layered SnSe films for UV-Visible-NIR photodetector arrays with high responsivity. *Nanoscale* **12**, 7358-7365 (2020).

87. S. Wu, S. Buckley, J. R. Schaibley, L. Feng, J. Yan, D. G. Mandrus, F. Hatami, W. Yao, J. Vučković, A. Majumdar, X. Xu, Monolayer semiconductor nanocavity lasers with ultralow thresholds. *Nature* **520**, 69-72 (2015).

88. C. Husko, J. Kang, G. Moille, J. D. Wood, Z. Han, D. Gosztola, X. Ma, S. Combrié, A. De Rossi, M. C. Hersam, X. Checoury, J. R. Guest, Silicon-Phosphorene Nanocavity-Enhanced Optical Emission at Telecommunications Wavelengths. *Nano Letters* **18**, 6515-6520 (2018).

89.   T. Tsuji, H. Hattori, M. Watanabe, N. Nagaoka, Development of night-vision system. *IEEE Transactions on Intelligent Transportation Systems* **3**, 203-209 (2002).

90.   J. A. Ratches, Current and Future Trends in Military Night Vision Applications. *Ferroelectrics* **342**, 183-192 (2006).

91.   L. J. Jiang, E. Y. K. Ng, A. C. B. Yeo, S. Wu, F. Pan, W. Y. Yau, J. H. Chen, Y. Yang, A perspective on medical infrared imaging. *Journal of Medical Engineering & Technology* **29**, 257-267 (2005).

92.   E. F. J. Ring, K. Ammer, Infrared thermal imaging in medicine. *Physiological Measurement* **33**, R33-R46 (2012).

93.   Y. Ninomiya, B. Fu, Thermal infrared multispectral remote sensing of lithology and mineralogy based on spectral properties of materials. *Ore Geology Reviews* **108**, 54-72 (2019).

94.   J. D. Musgraves, J. Hu, L. Calvez, *Springer Handbook of Glass* (Springer Nature, 2019).

95.   A. Ziletti, A. Carvalho, D. K. Campbell, D. F. Coker, A. H. Castro Neto, Oxygen Defects in Phosphorene. *Physical Review Letters* **114**, 046801 (2015).

96.   A. Favron, E. Gaufrès, F. Fossard, A.-L. Phaneuf-L'Heureux, N. Y. W. Tang, P. L. Lévesque, A. Loiseau, R. Leonelli, S. Francoeur, R. Martel, Photooxidation and quantum confinement effects in exfoliated black phosphorus. *Nature Materials* **14**, 826-832 (2015).

97.   J. D. Wood, S. A. Wells, D. Jariwala, K.-S. Chen, E. Cho, V. K. Sangwan, X. Liu, L. J. Lauhon, T. J. Marks, M. C. Hersam, Effective Passivation of Exfoliated Black Phosphorus Transistors against Ambient Degradation. *Nano Letters* **14**, 6964-6970 (2014).

98.   Y. Cao, A. Mishchenko, G. L. Yu, E. Khestanova, A. P. Rooney, E. Prestat, A. V. Kretinin, P. Blake, M. B. Shalom, C. Woods, J. Chapman, G. Balakrishnan, I. V. Grigorieva, K. S. Novoselov, B. A. Piot, M. Potemski, K. Watanabe, T. Taniguchi, S. J. Haigh, A. K. Geim, R. V. Gorbachev, Quality Heterostructures from Two-Dimensional Crystals Unstable in Air by Their Assembly in Inert Atmosphere. *Nano Letters* **15**, 4914-4921 (2015).

99.   Q. Guo, R. Yu, C. Li, S. Yuan, B. Deng, F. J. García de Abajo, F. Xia, Efficient electrical detection of mid-infrared graphene plasmons at room temperature. *Nature Materials* **17**, 986-992 (2018).

100.   S. Yuan, R. Yu, C. Ma, B. Deng, Q. Guo, X. Chen, C. Li, C. Chen, K. Watanabe, T. Taniguchi, F. J. García de Abajo, F. Xia, Room Temperature Graphene Mid-Infrared Bolometer with a Broad Operational Wavelength Range. *ACS Photonics* **7**, 1206-1215 (2020).

101.   J. Yan, M. H. Kim, J. A. Elle, A. B. Sushkov, G. S. Jenkins, H. M. Milchberg, M. S. Fuhrer, H. D. Drew, Dual-gated bilayer graphene hot-electron bolometer. *Nature Nanotechnology* **7**, 472-478 (2012).

102.   B. Deng, C. Ma, Q. Wang, S. Yuan, K. Watanabe, T. Taniguchi, F. Zhang, F. Xia, Strong mid-infrared photoresponse in small-twist-angle bilayer graphene. *Nature Photonics* **14**, 549-553 (2020).

103.   T. Low, P. Avouris, Graphene Plasmonics for Terahertz to Mid-Infrared Applications. *ACS Nano* **8**, 1086-1101 (2014).

104.   Y.-C. Chang, C.-H. Liu, C.-H. Liu, S. Zhang, S. R. Marder, E. E. Narimanov, Z. Zhong, T. B. Norris, Realization of mid-infrared graphene hyperbolic metamaterials. *Nature Communications* **7**, 10568 (2016).

105.   H. Yan, T. Low, W. Zhu, Y. Wu, M. Freitag, X. Li, F. Guinea, P. Avouris, F. Xia, Damping pathways of mid-infrared plasmons in graphene nanostructures. *Nature Photonics* **7**, 394-399 (2013).

106.   V. W. Brar, M. S. Jang, M. Sherrott, J. J. Lopez, H. A. Atwater, Highly Confined Tunable Mid-Infrared Plasmonics in Graphene Nanoresonators. *Nano Letters* **13**, 2541-2547 (2013).

107.   B. Deng, Q. Guo, C. Li, H. Wang, X. Ling, D. B. Farmer, S.-j. Han, J. Kong, F. Xia, Coupling-Enhanced Broadband Mid-infrared Light Absorption in Graphene Plasmonic Nanostructures. *ACS Nano* **10**, 11172-11178 (2016).

108.   H. Yan, F. Xia, W. Zhu, M. Freitag, C. Dimitrakopoulos, A. A. Bol, G. Tulevski, P. Avouris, Infrared Spectroscopy of Wafer-Scale Graphene. *ACS Nano* **5**, 9854-9860 (2011).

168

109. H. C. Liu, B. F. Levine, J. Y. Andersson, *Quantum well intersubband transition physics and devices* (Springer Science & Business Media, 2012), vol. 270.

110. E. Rosencher, B. Vinter, B. F. Levine, *Intersubband transitions in quantum wells* (Springer Science & Business Media, 2012), vol. 288.

111. Y. Yao, A. J. Hoffman, C. F. Gmachl, Mid-infrared quantum cascade lasers. *Nature Photonics* **6**, 432-439 (2012).

112. J. Faist, *Quantum cascade lasers* (OUP Oxford, 2013).

113. J. Faist, F. Capasso, L. Sivco Deborah, C. Sirtori, L. Hutchinson Albert, Y. Cho Alfred, Quantum Cascade Laser. *Science* **264**, 553-556 (1994).

114. D. Ahn, S. L. Chuang, Intersubband optical absorption in a quantum well with an applied electric field. *Physical Review B* **35**, 4149-4151 (1987).

115. A. Harwit, J. S. Harris, Observation of Stark shifts in quantum well intersubband transitions. *Applied Physics Letters* **50**, 685-687 (1987).

116. A. Rogalski, P. Martyniuk, M. Kopytko, Challenges of small-pixel infrared detectors: a review. *Reports on Progress in Physics* **79**, 046501 (2016).

117. A. Rogalski, *Infrared detectors* (CRC press, 2000).

118. A. Rogalski, Infrared detectors: status and trends. *Progress in Quantum Electronics* **27**, 59-210 (2003).

119. A. Rogalski, HgCdTe infrared detector material: history, status and outlook. *Reports on Progress in Physics* **68**, 2267-2336 (2005).

120. S. L. Chuang, S. L. Chuang, Physics of optoelectronic devices. (1995).

121. J. Haas, B. Mizaikoff, Advances in Mid-Infrared Spectroscopy for Chemical Analysis. *Annual Review of Analytical Chemistry* **9**, 45-68 (2016).

122. M. Razeghi, B.-M. Nguyen, Advances in mid-infrared detection and imaging: a key issues review. *Reports on Progress in Physics* **77**, 082401 (2014).

123. M. Kimata, Uncooled infrared focal plane arrays. *IEEJ Transactions on Electrical and Electronic Engineering* **13**, 4-12 (2018).

124. L. Yu, Y. Guo, H. Zhu, M. Luo, P. Han, X. Ji, Low-Cost Microbolometer Type Infrared Detectors. *Micromachines* **11**, (2020).

125. J. Liu, L. Xiao, Y. Liu, L. Cao, Z. Shen, Development of long-wavelength infrared detector and its space-based application requirements. *Chinese Physics B* **28**, 028504 (2019).

126. C. Chen, X. Chen, H. Yu, Y. Shao, Q. Guo, B. Deng, S. Lee, C. Ma, K. Watanabe, T. Taniguchi, J.-G. Park, S. Huang, W. Yao, F. Xia, Symmetry-Controlled Electron–Phonon Interactions in van der Waals Heterostructures. *ACS Nano* **13**, 552-559 (2019).

127. C. Chen, X. Chen, B. Deng, K. Watanabe, T. Taniguchi, S. Huang, F. Xia, Probing interlayer interaction via chiral phonons in layered honeycomb materials. *Physical Review B* **103**, 035405 (2021).

128. C. Chen, X. Chen, Y. Shao, B. Deng, Q. Guo, C. Ma, F. Xia, Valley-Selective Linear Dichroism in Layered Tin Sulfide. *ACS Photonics* **5**, 3814-3819 (2018).

129. C. Chen, F. Chen, X. Chen, B. Deng, B. Eng, D. Jung, Q. Guo, S. Yuan, K. Watanabe, T. Taniguchi, M. L. Lee, F. Xia, Bright Mid-Infrared Photoluminescence from Thin-Film Black Phosphorus. *Nano Letters* **19**, 1488-1493 (2019).

130. C. Chen, X. Lu, B. Deng, X. Chen, Q. Guo, C. Li, C. Ma, S. Yuan, E. Sung, K. Watanabe, T. Taniguchi, L. Yang, F. Xia, Widely tunable mid-infrared light emission in thin-film black phosphorus. *Science Advances* **6**, eaay6134.

131. C. Chen, C. Li, S. Min, Q. Guo, Z. Xia, D. Liu, Z. Ma, F. Xia, Ultrafast Silicon Nanomembrane Microbolometer for Long-Wavelength Infrared Light Detection. *Nano Letters* **21**, 8385-8392 (2021).

132. C.-H. Ho, J.-X. Li, Polarized Band-Edge Emission and Dichroic Optical Behavior in Thin Multilayer GeS. *Advanced Optical Materials* **5**, 1600814 (2017).

133. Z. Song, Z. Li, H. Wang, X. Bai, W. Wang, H. Du, S. Liu, C. Wang, J. Han, Y. Yang, Z. Liu, J. Lu, Z. Fang, J. Yang, Valley Pseudospin with a Widely Tunable Bandgap in Doped Honeycomb BN Monolayer. *Nano Letters* **17**, 2079-2087 (2017).

134. P. A. M. Dirac, N. H. D. Bohr, The quantum theory of the emission and absorption of radiation. *Proceedings of the Royal Society of London. Series A, Containing Papers of a Mathematical and Physical Character* **114**, 243-265 (1927).

135. K.-z. Du, X.-z. Wang, Y. Liu, P. Hu, M. I. B. Utama, C. K. Gan, Q. Xiong, C. Kloc, Weak Van der Waals Stacking, Wide-Range Band Gap, and Raman Study on Ultrathin Layers of Metal Phosphorus Trichalcogenides. *ACS Nano* **10**, 1738-1743 (2016).

136. C.-T. Kuo, M. Neumann, K. Balamurugan, H. J. Park, S. Kang, H. W. Shiu, J. H. Kang, B. H. Hong, M. Han, T. W. Noh, J.-G. Park, Exfoliation and Raman Spectroscopic Fingerprint of Few-Layer NiPS$_3$ Van der Waals Crystals. *Scientific Reports* **6**, 20904 (2016).

137. C. Kamal, A. Chakrabarti, M. Ezawa, Direct band gaps in group IV-VI monolayer materials: Binary counterparts of phosphorene. *Physical Review B* **93**, 125428 (2016).

138. L. C. Gomes, A. Carvalho, Phosphorene analogues: Isoelectronic two-dimensional group-IV monochalcogenides with orthorhombic structure. *Physical Review B* **92**, 085406 (2015).

139. S. Tongay, W. Fan, J. Kang, J. Park, U. Koldemir, J. Suh, D. S. Narang, K. Liu, J. Ji, J. Li, R. Sinclair, J. Wu, Tuning Interlayer Coupling in Large-Area Heterostructures with CVD-Grown MoS$_2$ and WS$_2$ Monolayers. *Nano Letters* **14**, 3185-3190 (2014).

140. B. Miller, A. Steinhoff, B. Pano, J. Klein, F. Jahnke, A. Holleitner, U. Wurstbauer, Long-Lived Direct and Indirect Interlayer Excitons in van der Waals Heterostructures. *Nano Letters* **17**, 5229-5237 (2017).

141. W. Zhao, Z. Ghorannevis, L. Chu, M. Toh, C. Kloc, P.-H. Tan, G. Eda, Evolution of Electronic Structure in Atomically Thin Sheets of WS$_2$ and WSe$_2$. *ACS Nano* **7**, 791-797 (2013).

142. H. R. Gutiérrez, N. Perea-López, A. L. Elías, A. Berkdemir, B. Wang, R. Lv, F. López-Urías, V. H. Crespi, H. Terrones, M. Terrones, Extraordinary Room-Temperature Photoluminescence in Triangular WS$_2$ Monolayers. *Nano Letters* **13**, 3447-3454 (2013).

143. M. K. Gunde, Vibrational modes in amorphous silicon dioxide. *Physica B: Condensed Matter* **292**, 286-295 (2000).

144.   I. Montero, L. Galán, O. Najmi, J. M. Albella, Disorder-induced vibration-mode coupling in SiO_2 films observed under normal-incidence infrared radiation. *Physical Review B* **50**, 4881-4884 (1994).

145.   H. Zeng, J. Dai, W. Yao, D. Xiao, X. Cui, Valley polarization in MoS_2 monolayers by optical pumping. *Nature Nanotechnology* **7**, 490-493 (2012).

146.   T. Cao, G. Wang, W. Han, H. Ye, C. Zhu, J. Shi, Q. Niu, P. Tan, E. Wang, B. Liu, J. Feng, Valley-selective circular dichroism of monolayer molybdenum disulphide. *Nature Communications* **3**, 887 (2012).

147.   X. Li, T. Cao, Q. Niu, J. Shi, J. Feng, Coupling the valley degree of freedom to antiferromagnetic order. *Proceedings of the National Academy of Sciences* **110**, 3738 (2013).

148.   X. Xu, Q. Song, H. Wang, P. Li, K. Zhang, Y. Wang, K. Yuan, Z. Yang, Y. Ye, L. Dai, In-Plane Anisotropies of Polarized Raman Response and Electrical Conductivity in Layered Tin Selenide. *ACS Applied Materials & Interfaces* **9**, 12601-12607 (2017).

149.   L. Li, Y. Yu, G. J. Ye, Q. Ge, X. Ou, H. Wu, D. Feng, X. H. Chen, Y. Zhang, Black phosphorus field-effect transistors. *Nature Nanotechnology* **9**, 372-377 (2014).

150.   P. Z. Hanakata, A. Carvalho, D. K. Campbell, H. S. Park, Polarization and valley switching in monolayer group-IV monochalcogenides. *Physical Review B* **94**, 035304 (2016).

151.   S. Lin, A. Carvalho, S. Yan, R. Li, S. Kim, A. Rodin, L. Carvalho, E. M. Chan, X. Wang, A. H. Castro Neto, J. Yao, Accessing valley degree of freedom in bulk Tin(II) sulfide at room temperature. *Nature Communications* **9**, 1455 (2018).

152.   G.-B. Liu, D. Xiao, Y. Yao, X. Xu, W. Yao, Electronic structures and theoretical modelling of two-dimensional group-VIB transition metal dichalcogenides. *Chemical Society Reviews* **44**, 2643-2663 (2015).

153.   H. Yu, G.-B. Liu, P. Gong, X. Xu, W. Yao, Dirac cones and Dirac saddle points of bright excitons in monolayer transition metal dichalcogenides. *Nature Communications* **5**, 3876 (2014).

154.   M. M. Glazov, L. E. Golub, G. Wang, X. Marie, T. Amand, B. Urbaszek, Intrinsic exciton-state mixing and nonlinear optical properties in transition metal dichalcogenide monolayers. *Physical Review B* **95**, 035311 (2017).

155.   L. Zhang, Q. Niu, Chiral Phonons at High-Symmetry Points in Monolayer Hexagonal Lattices. *Physical Review Letters* **115**, 115502 (2015).

156.   M. Onga, Y. Zhang, T. Ideue, Y. Iwasa, Exciton Hall effect in monolayer MoS_2. *Nature Materials* **16**, 1193-1197 (2017).

157.   J. Wu, N. Mao, L. Xie, H. Xu, J. Zhang, Identifying the Crystalline Orientation of Black Phosphorus Using Angle-Resolved Polarized Raman Spectroscopy. *Angewandte Chemie International Edition* **54**, 2366-2369 (2015).

158.   H. B. Ribeiro, M. A. Pimenta, C. J. S. de Matos, R. L. Moreira, A. S. Rodin, J. D. Zapata, E. A. T. de Souza, A. H. Castro Neto, Unusual Angular Dependence of the Raman Response in Black Phosphorus. *ACS Nano* **9**, 4270-4276 (2015).

159.   D. Wolverson, S. Crampin, A. S. Kazemi, A. Ilie, S. J. Bending, Raman Spectra of Monolayer, Few-Layer, and Bulk $ReSe_2$: An Anisotropic Layered Semiconductor. *ACS Nano* **8**, 11154-11164 (2014).

160.   G. C. Resende, G. A. S. Ribeiro, O. J. Silveira, J. S. Lemos, J. C. Brant, D. Rhodes, L. Balicas, M. Terrones, M. S. C. Mazzoni, C. Fantini, B. R. Carvalho, M. A. Pimenta, Origin of the complex Raman tensor elements in single-layer triclinic $ReSe_2$. *2D Materials* **8**, 025002 (2020).

161.   G. Qiu, Y. Du, A. Charnas, H. Zhou, S. Jin, Z. Luo, D. Y. Zemlyanov, X. Xu, G. J. Cheng, P. D. Ye, Observation of Optical and Electrical In-Plane Anisotropy in High-Mobility Few-Layer $ZrTe_5$. *Nano Letters* **16**, 7364-7369 (2016).

162.   Z. Guo, H. Gu, M. Fang, B. Song, W. Wang, X. Chen, C. Zhang, H. Jiang, L. Wang, S. Liu, Complete Dielectric Tensor and Giant Optical Anisotropy in Quasi-One-Dimensional $ZrTe_5$. *ACS Materials Letters* **3**, 525-534 (2021).

163.   D. Tan, H. E. Lim, F. Wang, N. B. Mohamed, S. Mouri, W. Zhang, Y. Miyauchi, M. Ohfuchi, K. Matsuda, Anisotropic optical and electronic properties of two-dimensional layered germanium sulfide. *Nano Research* **10**, 546-555 (2017).

164.   X. Wang, Y. Li, L. Huang, X.-W. Jiang, L. Jiang, H. Dong, Z. Wei, J. Li, W. Hu, Short-Wave Near-Infrared Linear Dichroism of Two-Dimensional Germanium Selenide. *Journal of the American Chemical Society* **139**, 14976-14982 (2017).

165.   M. Li, Y. Wu, T. Li, Y. Chen, H. Ding, Y. Lin, N. Pan, X. Wang, Revealing anisotropy and thickness dependence of Raman spectra for SnS flakes. *Rsc Advances* **7**, 48759-48765 (2017).

166.   S.-Y. Chen, C. Zheng, M. S. Fuhrer, J. Yan, Helicity-Resolved Raman Scattering of MoS_2, $MoSe_2$, WS_2, and WSe_2 Atomic Layers. *Nano Letters* **15**, 2526-2532 (2015).

167.   S. G. Drapcho, J. Kim, X. Hong, C. Jin, S. Shi, S. Tongay, J. Wu, F. Wang, Apparent breakdown of Raman selection rule at valley exciton resonances in monolayer MoS_2. *Physical Review B* **95**, 165417 (2017).

168.   Y. Tatsumi, R. Saito, Interplay of valley selection and helicity exchange of light in Raman scattering for graphene and MoS_2. *Physical Review B* **97**, 115407 (2018).

169.   K. S. Burch, D. Mandrus, J.-G. Park, Magnetism in two-dimensional van der Waals materials. *Nature* **563**, 47-52 (2018).

170.   D. N. Basov, M. M. Fogler, F. J. García de Abajo, Polaritons in van der Waals materials. *Science* **354**, aag1992 (2016).

171.   T. Cheiwchanchamnangij, W. R. L. Lambrecht, Quasiparticle band structure calculation of monolayer, bilayer, and bulk MoS_2. *Physical Review B* **85**, 205302 (2012).

172.   T. Björkman, A. Gulans, A. V. Krasheninnikov, R. M. Nieminen, van der Waals Bonding in Layered Compounds from Advanced Density-Functional First-Principles Calculations. *Physical Review Letters* **108**, 235502 (2012).

173.   E. Mostaani, N. D. Drummond, V. I. Fal'ko, Quantum Monte Carlo Calculation of the Binding Energy of Bilayer Graphene. *Physical Review Letters* **115**, 115501 (2015).

174.   L. Spanu, S. Sorella, G. Galli, Nature and Strength of Interlayer Binding in Graphite. *Physical Review Letters* **103**, 196401 (2009).

175.   J. M. Gonzalez, I. I. Oleynik, Layer-dependent properties of SnS_2 and $SnSe_2$ two-dimensional materials. *Physical Review B* **94**, 125443 (2016).

176.   A. Klein, S. Tiefenbacher, V. Eyert, C. Pettenkofer, W. Jaegermann, Electronic band structure of single-crystal and single-layer WS_2: Influence of interlayer van der Waals interactions. *Physical Review B* **64**, 205416 (2001).

177. G. Constantinescu, A. Kuc, T. Heine, Stacking in Bulk and Bilayer Hexagonal Boron Nitride. *Physical Review Letters* **111**, 036104 (2013).

178. X. Luo, X. Lu, G. K. W. Koon, A. H. Castro Neto, B. Özyilmaz, Q. Xiong, S. Y. Quek, Large Frequency Change with Thickness in Interlayer Breathing Mode—Significant Interlayer Interactions in Few Layer Black Phosphorus. *Nano Letters* **15**, 3931-3938 (2015).

179. Y. Zhao, X. Luo, H. Li, J. Zhang, P. T. Araujo, C. K. Gan, J. Wu, H. Zhang, S. Y. Quek, M. S. Dresselhaus, Q. Xiong, Interlayer Breathing and Shear Modes in Few-Trilayer MoS_2 and WSe_2. *Nano Letters* **13**, 1007-1015 (2013).

180. Y. Zhao, J. Qiao, P. Yu, Z. Hu, Z. Lin, S. P. Lau, Z. Liu, W. Ji, Y. Chai, Extraordinarily Strong Interlayer Interaction in 2D Layered PtS_2. *Advanced Materials* **28**, 2399-2407 (2016).

181. Z. Wu, Y. Han, J. Lin, W. Zhu, M. He, S. Xu, X. Chen, H. Lu, W. Ye, T. Han, Y. Wu, G. Long, J. Shen, R. Huang, L. Wang, Y. He, Y. Cai, R. Lortz, D. Su, N. Wang, Detection of interlayer interaction in few-layer graphene. *Physical Review B* **92**, 075408 (2015).

182. F. Parhizgar, A. Qaiumzadeh, R. Asgari, Quantum capacitance of double-layer graphene. *Physical Review B* **96**, 075447 (2017).

183. M. Bayle, N. Reckinger, A. Felten, P. Landois, O. Lancry, B. Dutertre, J.-F. Colomer, A.-A. Zahab, L. Henrard, J.-L. Sauvajol, M. Paillet, Determining the number of layers in few-layer graphene by combining Raman spectroscopy and optical contrast. *Journal of Raman Spectroscopy* **49**, 36-45 (2018).

184. X.-L. Li, W.-P. Han, J.-B. Wu, X.-F. Qiao, J. Zhang, P.-H. Tan, Layer-Number Dependent Optical Properties of 2D Materials and Their Application for Thickness Determination. *Advanced Functional Materials* **27**, 1604468 (2017).

185. Y. Hao, Y. Wang, L. Wang, Z. Ni, Z. Wang, R. Wang, C. K. Koo, Z. Shen, J. T. L. Thong, Probing Layer Number and Stacking Order of Few-Layer Graphene by Raman Spectroscopy. *Small* **6**, 195-200 (2010).

186. Z. Ni, Y. Wang, T. Yu, Z. Shen, Raman spectroscopy and imaging of graphene. *Nano Research* **1**, 273-291 (2008).

187. A. Eckmann, A. Felten, A. Mishchenko, L. Britnell, R. Krupke, K. S. Novoselov, C. Casiraghi, Probing the Nature of Defects in Graphene by Raman Spectroscopy. *Nano Letters* **12**, 3925-3930 (2012).

188. E. H. Martins Ferreira, M. V. O. Moutinho, F. Stavale, M. M. Lucchese, R. B. Capaz, C. A. Achete, A. Jorio, Evolution of the Raman spectra from single-, few-, and many-layer graphene with increasing disorder. *Physical Review B* **82**, 125429 (2010).

189. R. V. Gorbachev, I. Riaz, R. R. Nair, R. Jalil, L. Britnell, B. D. Belle, E. W. Hill, K. S. Novoselov, K. Watanabe, T. Taniguchi, A. K. Geim, P. Blake, Hunting for Monolayer Boron Nitride: Optical and Raman Signatures. *Small* **7**, 465-468 (2011).

190. L. M. Malard, M. A. Pimenta, G. Dresselhaus, M. S. Dresselhaus, Raman spectroscopy in graphene. *Physics Reports* **473**, 51-87 (2009).

191. M. Koshino, Interlayer screening effect in graphene multilayers with ABA and ABC stacking. *Physical Review B* **81**, 125304 (2010).

192. F. Zhang, B. Sahu, H. Min, A. H. MacDonald, Band structure of ABC-stacked graphene trilayers. *Physical Review B* **82**, 035409 (2010).

193. N. W. Ashcroft, N. D. Mermin, *Solid state physics* (holt, rinehart and winston, new york London, 1976).

194. A. C. Ferrari, D. M. Basko, Raman spectroscopy as a versatile tool for studying the properties of graphene. *Nature Nanotechnology* **8**, 235-246 (2013).

195. L. Ju, Z. Shi, N. Nair, Y. Lv, C. Jin, J. Velasco, C. Ojeda-Aristizabal, H. A. Bechtel, M. C. Martin, A. Zettl, J. Analytis, F. Wang, Topological valley transport at bilayer graphene domain walls. *Nature* **520**, 650-655 (2015).

196. A. S. Rodin, A. Carvalho, A. H. Castro Neto, Excitons in anisotropic two-dimensional semiconducting crystals. *Physical Review B* **90**, 075429 (2014).

197. A. S. Rodin, L. C. Gomes, A. Carvalho, A. H. Castro Neto, Valley physics in tin (II) sulfide. *Physical Review B* **93**, 045431 (2016).

198. T. Zhang, S. Zhang, G. Xu, N. Wang, Z. Fang, Valley polarization generated in 3-dimensional group-IV monochalcogenids. *arXiv preprint arXiv:1708.01480*, (2017).

199. L. Li, P. Gong, W. Wang, B. Deng, L. Pi, J. Yu, X. Zhou, X. Shi, H. Li, T. Zhai, Strong In-Plane Anisotropies of Optical and Electrical Response in Layered Dimetal Chalcogenide. *ACS Nano* **11**, 10264-10272 (2017).

200. Z. Tian, C. Guo, M. Zhao, R. Li, J. Xue, Two-Dimensional SnS: A Phosphorene Analogue with Strong In-Plane Electronic Anisotropy. *ACS Nano* **11**, 2219-2226 (2017).

201. Z. Zhang, J. Yang, K. Zhang, S. Chen, F. Mei, G. Shen, Anisotropic photoresponse of layered 2D SnS-based near infrared photodetectors. *Journal of Materials Chemistry C* **5**, 11288-11293 (2017).

202. H. R. Chandrasekhar, R. G. Humphreys, U. Zwick, M. Cardona, Infrared and Raman spectra of the IV-VI compounds SnS and SnSe. *Physical Review B* **15**, 2177-2183 (1977).

203. J. Xia, X.-Z. Li, X. Huang, N. Mao, D.-D. Zhu, L. Wang, H. Xu, X.-M. Meng, Physical vapor deposition synthesis of two-dimensional orthorhombic SnS flakes with strong angle/temperature-dependent Raman responses. *Nanoscale* **8**, 2063-2070 (2016).

204. G. Plechinger, F. X. Schrettenbrunner, J. Eroms, D. Weiss, C. Schüller, T. Korn, Low-temperature photoluminescence of oxide-covered single-layer MoS_2. *physica status solidi (RRL) – Rapid Research Letters* **6**, 126-128 (2012).

205. V. Alex, S. Finkbeiner, J. Weber, Temperature dependence of the indirect energy gap in crystalline silicon. *Journal of Applied Physics* **79**, 6943-6946 (1996).

206. B. D. Malone, E. Kaxiras, Quasiparticle band structures and interface physics of SnS and GeS. *Physical Review B* **87**, 245312 (2013).

207. G. Kioseoglou, A. T. Hanbicki, M. Currie, A. L. Friedman, D. Gunlycke, B. T. Jonker, Valley polarization and intervalley scattering in monolayer MoS_2. *Applied Physics Letters* **101**, 221907 (2012).

208. A. P. Lambros, D. Geraleas, N. A. Economou, Optical absorption edge in SnS. *Journal of Physics and Chemistry of Solids* **35**, 537-541 (1974).

209. O. Loebich, The optical properties of gold. *Gold Bulletin* **5**, 2-10 (1972).

210. Y. P. Varshni, Temperature dependence of the energy gap in semiconductors. *Physica* **34**, 149-154 (1967).

211. E. B. Wilson, J. C. Decius, P. C. Cross, *Molecular vibrations: the theory of infrared and Raman vibrational spectra* (Courier Corporation, 1980).

212. A. Lambrecht, K. Schmitt, *16 - Mid-infrared gas-sensing systems and applications* in *Mid-infrared Optoelectronics* (Woodhead Publishing, 2020), pp. 661-715.

213. D. Popa, F. Udrea, Towards Integrated Mid-Infrared Gas Sensors. *Sensors* **19**, (2019).

214. P. L. Richards, C. R. McCreight, Infrared Detectors for Astrophysics. *Physics Today* **58**, 41-47 (2005).

215. G. H. Rieke, Infrared Detector Arrays for Astronomy. *Annual Review of Astronomy and Astrophysics* **45**, 77-115 (2007).

216. J. Liu, Z. Zhou, J. Zhang, W. Feng, J. Zuo, Advances and challenges in commercializing radiative cooling. *Materials Today Physics* **11**, 100161 (2019).

217. X. Chen, Z. Zhou, B. Deng, Z. Wu, F. Xia, Y. Cao, L. Zhang, W. Huang, N. Wang, L. Wang, Electrically tunable physical properties of two-dimensional materials. *Nano Today* **27**, 99-119 (2019).

218. Q. Ma, G. Ren, K. Xu, J. Z. Ou, Tunable Optical Properties of 2D Materials and Their Applications. *Advanced Optical Materials* **9**, 2001313 (2021).

219. H. Liu, A. T. Neal, Z. Zhu, Z. Luo, X. Xu, D. Tománek, P. D. Ye, Phosphorene: An Unexplored 2D Semiconductor with a High Hole Mobility. *ACS Nano* **8**, 4033-4041 (2014).

220. S. P. Koenig, R. A. Doganov, H. Schmidt, A. H. Castro Neto, B. Özyilmaz, Electric field effect in ultrathin black phosphorus. *Applied Physics Letters* **104**, 103106 (2014).

221. A. Castellanos-Gomez, L. Vicarelli, E. Prada, J. O. Island, K. L. Narasimha-Acharya, S. I. Blanter, D. J. Groenendijk, M. Buscema, G. A. Steele, J. V. Alvarez, H. W. Zandbergen, J. J. Palacios, H. S. J. van der Zant, Isolation and characterization of few-layer black phosphorus. *2D Materials* **1**, 025001 (2014).

222. F. Xia, H. Wang, J. C. M. Hwang, A. H. C. Neto, L. Yang, Black phosphorus and its isoelectronic materials. *Nature Reviews Physics* **1**, 306-317 (2019).

223. X. Chen, Y. Wu, Z. Wu, Y. Han, S. Xu, L. Wang, W. Ye, T. Han, Y. He, Y. Cai, N. Wang, High-quality sandwiched black phosphorus heterostructure and its quantum oscillations. *Nature Communications* **6**, 7315 (2015).

224. J. Yang, S. Tran, J. Wu, S. Che, P. Stepanov, T. Taniguchi, K. Watanabe, H. Baek, D. Smirnov, R. Chen, C. N. Lau, Integer and Fractional Quantum Hall effect in Ultrahigh Quality Few-layer Black Phosphorus Transistors. *Nano Letters* **18**, 229-234 (2018).

225. J. Kim, S. S. Baik, S. W. Jung, Y. Sohn, S. H. Ryu, H. J. Choi, B.-J. Yang, K. S. Kim, Two-Dimensional Dirac Fermions Protected by Space-Time Inversion Symmetry in Black Phosphorus. *Physical Review Letters* **119**, 226801 (2017).

226. R. Fei, V. Tran, L. Yang, Topologically protected Dirac cones in compressed bulk black phosphorus. *Physical Review B* **91**, 195319 (2015).

227. N. Gillgren, D. Wickramaratne, Y. Shi, T. Espiritu, J. Yang, J. Hu, J. Wei, X. Liu, Z. Mao, K. Watanabe, T. Taniguchi, M. Bockrath, Y. Barlas, R. K. Lake, C. Ning Lau, Gate tunable quantum oscillations in air-stable and high mobility few-layer phosphorene heterostructures. *2D Materials* **2**, 011001 (2014).

228. A. Mishchenko, Y. Cao, G. L. Yu, C. R. Woods, R. V. Gorbachev, K. S. Novoselov, A. K. Geim, L. S. Levitov, Nonlocal Response and Anamorphosis: The Case of Few-Layer Black Phosphorus. *Nano Letters* **15**, 6991-6995 (2015).

229. H. Yuan, X. Liu, F. Afshinmanesh, W. Li, G. Xu, J. Sun, B. Lian, A. G. Curto, G. Ye, Y. Hikita, Z. Shen, S.-C. Zhang, X. Chen, M. Brongersma, H. Y. Hwang, Y. Cui, Polarization-sensitive broadband photodetector using a black phosphorus vertical p–n junction. *Nature Nanotechnology* **10**, 707-713 (2015).

230. M. Engel, M. Steiner, P. Avouris, Black Phosphorus Photodetector for Multispectral, High-Resolution Imaging. *Nano Letters* **14**, 6414-6417 (2014).

231. S. Deckoff-Jones, H. Lin, D. Kita, H. Zheng, D. Li, W. Zhang, J. Hu, Chalcogenide glass waveguide-integrated black phosphorus mid-infrared photodetectors. *Journal of Optics* **20**, 044004 (2018).

232. R. J. Suess, E. Leong, J. L. Garrett, T. Zhou, R. Salem, J. N. Munday, T. E. Murphy, M. Mittendorff, Mid-infrared time-resolved photoconduction in black phosphorus. *2D Materials* **3**, 041006 (2016).

233. S. C. Dhanabalan, J. S. Ponraj, Z. Guo, S. Li, Q. Bao, H. Zhang, Emerging Trends in Phosphorene Fabrication towards Next Generation Devices. *Advanced Science* **4**, 1600305 (2017).

234. M. Qiu, W. X. Ren, T. Jeong, M. Won, G. Y. Park, D. K. Sang, L.-P. Liu, H. Zhang, J. S. Kim, Omnipotent phosphorene: a next-generation, two-dimensional nanoplatform for multidisciplinary biomedical applications. *Chemical Society Reviews* **47**, 5588-5601 (2018).

235. J. Kim, S. Baik Seung, H. Ryu Sae, Y. Sohn, S. Park, B.-G. Park, J. Denlinger, Y. Yi, J. Choi Hyoung, S. Kim Keun, Observation of tunable band gap and anisotropic Dirac semimetal state in black phosphorus. *Science* **349**, 723-726 (2015).

236. Y. Li, S. Yang, J. Li, Modulation of the Electronic Properties of Ultrathin Black Phosphorus by Strain and Electrical Field. *The Journal of Physical Chemistry C* **118**, 23970-23976 (2014).

237. M. C. Sherrott, W. S. Whitney, D. Jariwala, S. Biswas, C. M. Went, J. Wong, G. R. Rossman, H. A. Atwater, Anisotropic Quantum Well Electro-Optics in Few-Layer Black Phosphorus. *Nano Letters* **19**, 269-276 (2019).

238. L. Ye, P. Wang, W. Luo, F. Gong, L. Liao, T. Liu, L. Tong, J. Zang, J. Xu, W. Hu, Highly polarization sensitive infrared photodetector based on black phosphorus-on-WSe$_2$ photogate vertical heterostructure. *Nano Energy* **37**, 53-60 (2017).

239. P. Wang, S. Liu, W. Luo, H. Fang, F. Gong, N. Guo, Z.-G. Chen, J. Zou, Y. Huang, X. Zhou, J. Wang, X. Chen, W. Lu, F. Xiu, W. Hu, Arrayed Van Der Waals Broadband Detectors for Dual-Band Detection. *Advanced Materials* **29**, 1604439 (2017).

240. S. Zhang, J. Yang, R. Xu, F. Wang, W. Li, M. Ghufran, Y.-W. Zhang, Z. Yu, G. Zhang, Q. Qin, Y. Lu, Extraordinary Photoluminescence and Strong Temperature/Angle-Dependent Raman Responses in Few-Layer Phosphorene. *ACS Nano* **8**, 9590-9596 (2014).

241. J. Shao, W. Lu, X. Lü, F. Yue, Z. Li, S. Guo, J. Chu, Modulated photoluminescence spectroscopy with a step-scan Fourier transform infrared spectrometer. *Review of Scientific Instruments* **77**, 063104 (2006).

242. F. Fuchs, A. Lusson, J. Wagner, P. Koidl, *Double Modulation Techniques In Fourier Transform Infrared Photoluminescence* presented at the Proc.SPIE, 1989.

243. L. Wang, I. Meric, P. Y. Huang, Q. Gao, Y. Gao, H. Tran, T. Taniguchi, K. Watanabe, L. M. Campos, D. A. Muller, J. Guo, P. Kim, J. Hone, K. L. Shepard, C. R. Dean, One-Dimensional Electrical Contact to a Two-Dimensional Material. *Science* **342**, 614-617 (2013).

244. R. A. Doganov, E. C. T. O'Farrell, S. P. Koenig, Y. Yeo, A. Ziletti, A. Carvalho, D. K. Campbell, D. F. Coker, K. Watanabe, T. Taniguchi, A. H. C. Neto, B. Özyilmaz, Transport properties of pristine few-layer black phosphorus by van der Waals passivation in an inert atmosphere. *Nature Communications* **6**, 6647 (2015).

245. X. Li, W. Cai, J. An, S. Kim, J. Nah, D. Yang, R. Piner, A. Velamakanni, I. Jung, E. Tutuc, K. Banerjee Sanjay, L. Colombo, S. Ruoff Rodney, Large-Area Synthesis of High-Quality and Uniform Graphene Films on Copper Foils. *Science* **324**, 1312-1314 (2009).

246. K. S. Kim, Y. Zhao, H. Jang, S. Y. Lee, J. M. Kim, K. S. Kim, J.-H. Ahn, P. Kim, J.-Y. Choi, B. H. Hong, Large-scale pattern growth of graphene films for stretchable transparent electrodes. *Nature* **457**, 706-710 (2009).

247. B. R. Pamplin, *Molecular beam epitaxy* (Elsevier, 2017).

248. S. Liu, X. Yuan, P. Wang, Z.-G. Chen, L. Tang, E. Zhang, C. Zhang, Y. Liu, W. Wang, C. Liu, C. Chen, J. Zou, W. Hu, F. Xiu, Controllable Growth of Vertical Heterostructure GaTe$_x$Se$_{1-x}$/Si by Molecular Beam Epitaxy. *ACS Nano* **9**, 8592-8598 (2015).

249. Z. Wang, J. Wang, Y. Zang, Q. Zhang, J.-A. Shi, T. Jiang, Y. Gong, C.-L. Song, S.-H. Ji, L.-L. Wang, L. Gu, K. He, W. Duan, X. Ma, X. Chen, Q.-K. Xue, Molecular Beam Epitaxy-Grown SnSe in the Rock-Salt Structure: An Artificial Topological Crystalline Insulator Material. *Advanced Materials* **27**, 4150-4154 (2015).

250. X. Yuan, L. Tang, S. Liu, P. Wang, Z. Chen, C. Zhang, Y. Liu, W. Wang, Y. Zou, C. Liu, N. Guo, J. Zou, P. Zhou, W. Hu, F. Xiu, Arrayed van der Waals Vertical Heterostructures Based on 2D GaSe Grown by Molecular Beam Epitaxy. *Nano Letters* **15**, 3571-3577 (2015).

251. D. Jung, L. Yu, S. Dev, D. Wasserman, M. L. Lee, Room-temperature mid-infrared quantum well lasers on multi-functional metamorphic buffers. *Applied Physics Letters* **109**, 211101 (2016).

252. E. Yablonovitch, Inhibited Spontaneous Emission in Solid-State Physics and Electronics. *Physical Review Letters* **58**, 2059-2062 (1987).

253. A. Surrente, A. A. Mitioglu, K. Galkowski, W. Tabis, D. K. Maude, P. Plochocka, Excitons in atomically thin black phosphorus. *Physical Review B* **93**, 121405 (2016).

254. M. Leroux, N. Grandjean, B. Beaumont, G. Nataf, F. Semond, J. Massies, P. Gibart, Temperature quenching of photoluminescence intensities in undoped and doped GaN. *Journal of Applied Physics* **86**, 3721-3728 (1999).

255. J. S. Ross, S. Wu, H. Yu, N. J. Ghimire, A. M. Jones, G. Aivazian, J. Yan, D. G. Mandrus, D. Xiao, W. Yao, X. Xu, Electrical control of neutral and charged excitons in a monolayer semiconductor. *Nature Communications* **4**, 1474 (2013).

256. K. P. O'Donnell, X. Chen, Temperature dependence of semiconductor band gaps. *Applied Physics Letters* **58**, 2924-2926 (1991).

257. J. Wu, W. Walukiewicz, W. Shan, K. M. Yu, J. W. Ager, S. X. Li, E. E. Haller, H. Lu, W. J. Schaff, Temperature dependence of the fundamental band gap of InN. *Journal of Applied Physics* **94**, 4457-4460 (2003).

258. C. E. P. Villegas, A. R. Rocha, A. Marini, Anomalous Temperature Dependence of the Band Gap in Black Phosphorus. *Nano Letters* **16**, 5095-5101 (2016).

259. M. Baba, Y. Nakamura, K. Shibata, A. Morita, Photoconduction of Black Phosphorus in the Infrared Region. *Japanese Journal of Applied Physics* **30**, L1178-L1181 (1991).

260. A. S. Rodin, A. Carvalho, A. H. Castro Neto, Strain-Induced Gap Modification in Black Phosphorus. *Physical Review Letters* **112**, 176801 (2014).

261. J. Quereda, P. San-Jose, V. Parente, L. Vaquero-Garzon, A. J. Molina-Mendoza, N. Agraït, G. Rubio-Bollinger, F. Guinea, R. Roldán, A. Castellanos-Gomez, Strong Modulation of Optical Properties in Black Phosphorus through Strain-Engineered Rippling. *Nano Letters* **16**, 2931-2937 (2016).

262. Z. Zhang, L. Li, J. Horng, N. Z. Wang, F. Yang, Y. Yu, Y. Zhang, G. Chen, K. Watanabe, T. Taniguchi, X. H. Chen, F. Wang, Y. Zhang, Strain-Modulated Bandgap and Piezo-Resistive Effect in Black Phosphorus Field-Effect Transistors. *Nano Letters* **17**, 6097-6103 (2017).

263. R. Pässler, Temperature dependence of fundamental band gaps in group IV, III–V, and II–VI materials via a two-oscillator model. *Journal of Applied Physics* **89**, 6235-6240 (2001).

264. M. Cardona, M. L. W. Thewalt, Isotope effects on the optical spectra of semiconductors. *Reviews of Modern Physics* **77**, 1173-1224 (2005).

265. H. J. Lian, A. Yang, M. L. W. Thewalt, R. Lauck, M. Cardona, Effects of sulfur isotopic composition on the band gap of PbS. *Physical Review B* **73**, 233202 (2006).

266. P. Dey, J. Paul, J. Bylsma, D. Karaiskaj, J. M. Luther, M. C. Beard, A. H. Romero, Origin of the temperature dependence of the band gap of PbS and PbSe quantum dots. *Solid State Communications* **165**, 49-54 (2013).

267. Y. Aierken, D. Çakır, C. Sevik, F. M. Peeters, Thermal properties of black and blue phosphorenes from a first-principles quasiharmonic approach. *Physical Review B* **92**, 081408 (2015).

268. Z. Luo, J. Maassen, Y. Deng, Y. Du, R. P. Garrelts, M. S. Lundstrom, P. D. Ye, X. Xu, Anisotropic in-plane thermal conductivity observed in few-layer black phosphorus. *Nature Communications* **6**, 8572 (2015).

269. A. I. Kingon, J.-P. Maria, S. K. Streiffer, Alternative dielectrics to silicon dioxide for memory and logic devices. *Nature* **406**, 1032-1038 (2000).

270. K. K. Kim, A. Hsu, X. Jia, S. M. Kim, Y. Shi, M. Dresselhaus, T. Palacios, J. Kong, Synthesis and Characterization of Hexagonal Boron Nitride Film as a Dielectric Layer for Graphene Devices. *ACS Nano* **6**, 8583-8590 (2012).

271. T. Low, R. Roldán, H. Wang, F. Xia, P. Avouris, L. M. Moreno, F. Guinea, Plasmons and Screening in Monolayer and Multilayer Black Phosphorus. *Physical Review Letters* **113**, 106802 (2014).

272. J. W. Robinson, *Atomic spectroscopy* (CRC Press, 1996).

273. J. H. Davies, *The physics of low-dimensional semiconductors: an introduction* (Cambridge university press, 1998).

274. C. Mauser, T. Limmer, E. Da Como, K. Becker, A. L. Rogach, J. Feldmann, D. V. Talapin, Anisotropic optical emission of single CdSe/CdS tetrapod heterostructures: Evidence for a wavefunction symmetry breaking. *Physical Review B* **77**, 153303 (2008).

275. N. C. Greenham, I. D. W. Samuel, G. R. Hayes, R. T. Phillips, Y. A. R. R. Kessener, S. C. Moratti, A. B. Holmes, R. H. Friend, Measurement of absolute photoluminescence quantum efficiencies in conjugated polymers. *Chemical Physics Letters* **241**, 89-96 (1995).

276. G. Zhang, A. Chaves, S. Huang, F. Wang, Q. Xing, T. Low, H. Yan, Determination of layer-dependent exciton binding energies in few-layer black phosphorus. *Science Advances* **4**, eaap9977.

277. P. Koskinen, I. Fampiou, A. Ramasubramaniam, Density-Functional Tight-Binding Simulations of Curvature-Controlled Layer Decoupling and Band-Gap Tuning in Bilayer MoS_2. *Physical Review Letters* **112**, 186802 (2014).

278. A. Ramasubramaniam, D. Naveh, E. Towe, Tunable band gaps in bilayer transition-metal dichalcogenides. *Physical Review B* **84**, 205325 (2011).

279. T. Chu, H. Ilatikhameneh, G. Klimeck, R. Rahman, Z. Chen, Electrically Tunable Bandgaps in Bilayer MoS_2. *Nano Letters* **15**, 8000-8007 (2015).

280. J. Gribbin, Radiative Processes in Meteorology and Climatology. *Physics Bulletin* **27**, 554-554 (1976).

281. R. M. Goody, Y. L. Yung, *Atmospheric radiation: theoretical basis* (Oxford university press, 1995).

282. R. K. Bhan, V. Dhar, Recent infrared detector technologies, applications, trends and development of HgCdTe based cooled infrared focal plane arrays and their characterization. *Opto-Electronics Review* **27**, 174-193 (2019).

283. P. Martyniuk, A. Rogalski, Quantum-dot infrared photodetectors: Status and outlook. *Progress in Quantum Electronics* **32**, 89-120 (2008).

284. C. Arnaud, T. Jean-Luc, M. G. Yann, A. Pier Claudio, L. Joel, L. Hans-Joachim, P. Pierre, Y. Jean-Jacques, *Low cost uncooled IRFPA and molded IR lenses for enhanced driver vision* presented at the Proc.SPIE, 2004.

285. P. Pręgowski, Infrared detector arrays in the detection, automation and robotics-trends and development perspectives. *Measurement Automation Monitoring* **64**, (2018).

286. M. Kimata, *Trends in small-format infrared array sensors* presented at the SENSORS, 2013 IEEE, 3-6 Nov. 2013.

287. S. Horn, D. Lohrman, P. Norton, K. McCormack, A. Hutchinson, *Reaching for the sensitivity limits of uncooled and minimally cooled thermal and photon infrared detectors* presented at the Proc.SPIE, 2005.

288. T. Jean-Luc, R. Frederic, V. Corrinne, V. Michel, Y. Jean-Jacques, *LETI/LIR's amorphous silicon uncooled microbolometer development* presented at the Proc.SPIE, 1998.

289. E. M. Smith, D. Panjwani, J. Ginn, A. P. Warren, C. Long, P. Figuieredo, C. Smith, J. Nath, J. Perlstein, N. Walter, C. Hirschmugl, R. E. Peale, D. Shelton, Dual band sensitivity enhancements of a VOx microbolometer array using a patterned gold black absorber. *Appl. Opt.* **55**, 2071-2078 (2016).

290. A. Tanaka, S. Matsumoto, N. Tsukamoto, S. Itoh, K. Chiba, T. Endoh, A. Nakazato, K. Okuyama, Y. Kumazawa, M. Hijikawa, H. Gotoh, T. Tanaka, N. Teranishi, Infrared focal plane array incorporating silicon IC process compatible bolometer. *IEEE Transactions on Electron Devices* **43**, 1844-1850 (1996).

291. D. S. George, *Uncooled 10um FPA Development at DRS* presented at the Proc.SPIE, 2016.

292. C. H. Gerald, G. D. Ronald, Small detectors in infrared system design. *Optical Engineering* **51**, 1-10 (2012).

293. B. Rob, K. Kenneth, *Direct optimization of LWIR systems for maximized detection range and minimized size and weight* presented at the Proc.SPIE, 2014.

294. L. Hyung-Kew, Y. Jun-Bo, Y. Euisik, J. Sang-Baek, Y. Yoon-Joong, L. Wook, K. Sang-Gook, *A high fill-factor IR bolometer using multi-level electrothermal structures* presented at the International Electron Devices Meeting 1998. Technical Digest (Cat. No.98CH36217), 6-9 Dec. 1998.

295. O. Erturk, T. Akin, *Design and implementation of high fill-factor structures for low-cost CMOS microbolometers* presented at the 2018 IEEE Micro Electro Mechanical Systems (MEMS), 21-25 Jan. 2018.

296. A. Abdullah, A. Koppula, O. Alkorjia, T. Liu, E. Kinzel, M. Almasri, *Metasurface Integrated Microbolometers* presented at the 2019 IEEE Research and Applications of Photonics in Defense Conference (RAPID), 19-21 Aug. 2019.

297. T. Grosjean, M. Mivelle, F. I. Baida, G. W. Burr, U. C. Fischer, Diabolo Nanoantenna for Enhancing and Confining the Magnetic Optical Field. *Nano Letters* **11**, 1009-1013 (2011).

298. M. Yoo, S. Lim, Polarization-Independent and Ultrawideband Metamaterial Absorber Using a Hexagonal Artificial Impedance Surface and a Resistor-Capacitor Layer. *IEEE Transactions on Antennas and Propagation* **62**, 2652-2658 (2014).

299. F. S. Jafari, M. Naderi, A. Hatami, F. B. Zarrabi, Microwave Jerusalem cross absorber by metamaterial split ring resonator load to obtain polarization independence with triple band application. *AEU - International Journal of Electronics and Communications* **101**, 138-144 (2019).

300. K. A. Sameer, A. J. Syllaios, S. T. Greg, F. T. Michael, E. H. Russell, *Amorphous silicon thin-films for uncooled infrared microbolometer sensors* presented at the Proc.SPIE, 2010.

301. L. Kevin Charles, *The active microbolometer: a new concept in infrared detection* presented at the Proc.SPIE, 2004.

302. D. Rutledge, M. Muha, Imaging antenna arrays. *IEEE Transactions on Antennas and Propagation* **30**, 535-540 (1982).

303. G. D. Boreman, A. Dogariu, C. Christodoulou, D. Kotter, Modulation transfer function of antenna-coupled infrared detector arrays. *Appl. Opt.* **35**, 6110-6114 (1996).

304. T. Morf, B. Klein, M. Despont, U. Drechsler, L. Kull, D. Corcos, D. Elad, N. Kaminski, U. R. Pfeiffer, R. Al Hadi, H. M. Keller, M. Braendli, C. Menolfi, M. Kossel, P. A. Francese, T. Toifl, D. Plettemeier, Wide bandwidth room-temperature THz imaging array based on antenna-coupled MOSFET bolometer. *Sensors and Actuators A: Physical* **215**, 96-104 (2014).

305. W. Guo, L. Wang, X. Chen, C. Liu, W. Tang, C. Guo, J. Wang, W. Lu, Graphene-based broadband terahertz detector integrated with a square-spiral antenna. *Opt. Lett.* **43**, 1647-1650 (2018).

306.   A. Subrahmanyam, Y. Bharat Kumar Redd, C. L. Nagendra, Nano-vanadium oxide thin films in mixed phase for microbolometer applications. *Journal of Physics D: Applied Physics* **41**, 195108 (2008).

307.   A. D. y. Michael, I. F. Boris, N. O. Victor, V. M. Igor, O. P. Igor, L. V. i. Lyudmila, V. S. Valeri, *Uncooled 160x120 microbolometer IR FPA based on sol-gel VOx* presented at the Proc.SPIE, 2005.

308.   P. Zhang, E. Tevaarwerk, B.-N. Park, D. E. Savage, G. K. Celler, I. Knezevic, P. G. Evans, M. A. Eriksson, M. G. Lagally, Electronic transport in nanometre-scale silicon-on-insulator membranes. *Nature* **439**, 703-706 (2006).

309.   A. Allain, J. Kang, K. Banerjee, A. Kis, Electrical contacts to two-dimensional semiconductors. *Nature Materials* **14**, 1195-1205 (2015).

310.   M. O. Aboelfotoh, Influence of thin interfacial silicon oxide layers on the Schottky-barrier behavior of Ti on Si(100). *Physical Review B* **39**, 5070-5078 (1989).

311.   M. O. Aboelfotoh, K. N. Tu, Schottky-barrier heights of Ti and $TiSi_2$ on n-type and p-type Si(100). *Physical Review B* **34**, 2311-2318 (1986).

312.   L. Vicarelli, M. S. Vitiello, D. Coquillat, A. Lombardo, A. C. Ferrari, W. Knap, M. Polini, V. Pellegrini, A. Tredicucci, Graphene field-effect transistors as room-temperature terahertz detectors. *Nature Materials* **11**, 865-871 (2012).

313.   R. Tauk, F. Teppe, S. Boubanga, D. Coquillat, W. Knap, Y. M. Meziani, C. Gallon, F. Boeuf, T. Skotnicki, C. Fenouillet-Beranger, D. K. Maude, S. Rumyantsev, M. S. Shur, Plasma wave detection of terahertz radiation by silicon field effects transistors: Responsivity and noise equivalent power. *Applied Physics Letters* **89**, 253511 (2006).

314.   R. K. Willardson, E. R. Weber, D. D. Skatrud, P. W. Kruse, *Uncooled infrared imaging arrays and systems* (Academic press, 1997).

315.   P. W. Kruse, *Uncooled thermal imaging: arrays, systems, and applications* (SPIE press, 2001), vol. 51.

316.   L. Laurent, J.-J. Yon, J.-S. Moulet, M. Roukes, L. Duraffourg, 12 µm-Pitch Electromechanical Resonator for Thermal Sensing. *Physical Review Applied* **9**, 024016 (2018).

317.   N. Frank, V. Christian, J. Henrik, *MEMS-based uncooled infrared bolometer arrays: a review* presented at the Proc.SPIE, 2008.

318.   A. M. Filachev, V. P. Ponomarenko, I. I. Taubkin, M. B. Ushakova, *Infrared focal plane arrays: state of the art and development trends* presented at the Proc.SPIE, 2003.

319.   K. Margaret, R. B. Neal, *Performance limits of uncooled VOx microbolometer focal plane arrays* presented at the Proc.SPIE, 2004.

320.   D. S. George, C. J. Han, L. Chuan, *Uncooled microbolometers at DRS and elsewhere through 2013* presented at the Proc.SPIE, 2014.

321.   E. Tsutomu, T. Shigeru, Y. Takao, T. Yutaka, O. Kuniyuki, K. Seiji, M. Masaru, K. Kouji, Y. Takashi, O. Yuuhi, S. Tokuhito, I. Haruo, N. Tomohiko, S. Kentaro, T. Tetsuo, *Uncooled infrared detector with 12um pixel pitch video graphics array* presented at the Proc.SPIE, 2013.

322.   F. Daisuke, M. Tomohiro, O. Yasuaki, K. Yasuhiro, O. Takahiro, H. Hisatoshi, U. Masashi, O. Hiroshi, S. Ryota, K. Haruyoshi, I. Tadashi, U. Munetaka, *Two-million-pixel SOI diode uncooled IRFPA with 15µm pixel pitch* presented at the Proc.SPIE, 2012.

323.   U. Mizrahi, N. Argaman, S. Elkind, A. Giladi, Y. Hirsh, M. Labilov, I. Pivnik, N. Shiloah, M. Singer, A. Tuito, M. Ben-Ezra, I. Shtrichman, *Large-format 17µm high-end VOx µ-bolometer infrared detector* presented at the Proc.SPIE, 2013.

324.   J. L. Tissot, A. Durand, G. Th, C. Minassian, P. Robert, S. Tinnes, M. Vilain, *High performance uncooled amorphous silicon VGA IRFPA with 17-µm pixel-pitch* presented at the Proc.SPIE, 2010.

325.   I. Koichi, H. Hiroto, F. Ikuo, S. Keita, Y. Hitoshi, S. Kazuhiro, K. Honam, A. Masaki, F. Hideyuki, *Temperature stability improvement of a QVGA uncooled infrared radiation FPA* presented at the Proc.SPIE, 2013.

326.   W. Dirk, R. Marco, W. Daniel, L. Renee, Y. Pin, B. Jochen, V. Holger, *A digital 25 µm pixel-pitch uncooled amorphous silicon TEC-less VGA IRFPA with massive parallel Sigma-Delta-ADC readout* presented at the Proc.SPIE, 2010.

327.   J. Lv, H. Zhong, Y. Zhou, B. Liao, J. Wang, Y. Jiang, Model-Based Low-Noise Readout Integrated Circuit Design for Uncooled Microbolometers. *IEEE Sensors Journal* **13**, 1207-1215 (2013).

328. M. B. Pisani, K. Ren, P. Kao, S. Tadigadapa, Application of Micromachined *Y*-Cut-Quartz Bulk Acoustic Wave Resonator for Infrared Sensing. *Journal of Microelectromechanical Systems* **20**, 288-296 (2011).

329. M. G. Burzo, P. L. Komarov, P. E. Raad, Thermal transport properties of gold-covered thin-film silicon dioxide. *IEEE Transactions on Components and Packaging Technologies* **26**, 80-88 (2003).

330. C. J. Glassbrenner, G. A. Slack, Thermal Conductivity of Silicon and Germanium from 3 K to the Melting Point. *Physical Review* **134**, A1058-A1069 (1964).

331. C. Meva'a, X. Letartre, P. Rojo-Romeo, P. Viktorovitch, Low temperature MBE grown AlInAs: Investigation of current voltage and low frequency noise behaviour of schottky diodes. *Solid-State Electronics* **41**, 857-864 (1997).

332. M. J. Bevan, W. L. McCardel, M. V. Wadsworth, G. H. Westphal, Bolometer autocalibration. US6064066A (1996).

333. V. T. Dau, D. V. Dao, T. Shiozawa, S. Sugiyama, *Convective Gas Gyroscope Based on Thermo-Resistive Effect in Si P-N Junction* presented at the TRANSDUCERS 2007 - 2007 International Solid-State Sensors, Actuators and Microsystems Conference, 10-14 June 2007.

334. T. Yamada, N. Inomata, T. Ono, Sensitive thermal microsensor with pn junction for heat measurement of a single cell. *Japanese Journal of Applied Physics* **55**, 027001 (2016).

335. O. Mueller, Temperature fluctuations and flicker noise in p-n junction diodes. *IEEE Transactions on Electron Devices* **21**, 539-540 (1974).

336. P. Y. Huang, C. S. Ruiz-Vargas, A. M. van der Zande, W. S. Whitney, M. P. Levendorf, J. W. Kevek, S. Garg, J. S. Alden, C. J. Hustedt, Y. Zhu, J. Park, P. L. McEuen, D. A. Muller, Grains and grain boundaries in single-layer graphene atomic patchwork quilts. *Nature* **469**, 389-392 (2011).

337. J. Heo, H. J. Chung, S.-H. Lee, H. Yang, D. H. Seo, J. K. Shin, U. I. Chung, S. Seo, E. H. Hwang, S. Das Sarma, Nonmonotonic temperature dependent transport in graphene grown by chemical vapor deposition. *Physical Review B* **84**, 035421 (2011).

338. Q. Xing, C. Song, C. Wang, Y. Xie, S. Huang, F. Wang, Y. Lei, X. Yuan, C. Zhang, L. Mu, Y. Huang, F. Xiu, H. Yan, Tunable Terahertz Plasmons in Graphite Thin Films. *Physical Review Letters* **126**, 147401 (2021).

339. J. Robertson, Diamond-like amorphous carbon. *Materials Science and Engineering: R: Reports* **37**, 129-281 (2002).

340. M. Shamsa, W. L. Liu, A. A. Balandin, C. Casiraghi, W. I. Milne, A. C. Ferrari, Thermal conductivity of diamond-like carbon films. *Applied Physics Letters* **89**, 161921 (2006).

341. W. Wu, G. Qiu, Y. Wang, R. Wang, P. Ye, Tellurene: its physical properties, scalable nanomanufacturing, and device applications. *Chemical Society Reviews* **47**, 7203-7212 (2018).

342. X. Cai, X. Han, C. Zhao, C. Niu, Y. Jia, Tellurene: An elemental 2D monolayer material beyond its bulk phases without van der Waals layered structures. *Journal of Semiconductors* **41**, 081002 (2020).

343. Z. Shi, R. Cao, K. Khan, A. K. Tareen, X. Liu, W. Liang, Y. Zhang, C. Ma, Z. Guo, X. Luo, H. Zhang, Two-Dimensional Tellurium: Progress, Challenges, and Prospects. *Nano-Micro Letters* **12**, 99 (2020).

344. J. Qiao, Y. Pan, F. Yang, C. Wang, Y. Chai, W. Ji, Few-layer Tellurium: one-dimensional-like layered elementary semiconductor with striking physical properties. *Science Bulletin* **63**, 159-168 (2018).

345. B. Wu, X. Liu, J. Yin, H. Lee, Bulk β-Te to few layered β-tellurenes: indirect to direct band-Gap transitions showing semiconducting property. *Materials Research Express* **4**, 095902 (2017).

346. Y. Wang, G. Qiu, R. Wang, S. Huang, Q. Wang, Y. Liu, Y. Du, W. A. Goddard, M. J. Kim, X. Xu, P. D. Ye, W. Wu, Field-effect transistors made from solution-grown two-dimensional tellurene. *Nature Electronics* **1**, 228-236 (2018).

347. X. Huang, J. Guan, Z. Lin, B. Liu, S. Xing, W. Wang, J. Guo, Epitaxial Growth and Band Structure of Te Film on Graphene. *Nano Letters* **17**, 4619-4623 (2017).

348. C. Shen, Y. Liu, J. Wu, C. Xu, D. Cui, Z. Li, Q. Liu, Y. Li, Y. Wang, X. Cao, H. Kumazoe, F. Shimojo, A. Krishnamoorthy, R. K. Kalia, A. Nakano, P. D. Vashishta, M. R. Amer, A. N. Abbas, H. Wang, W. Wu, C. Zhou, Tellurene Photodetector with High Gain and Wide Bandwidth. *ACS Nano* **14**, 303-310 (2020).

349. L. Tong, X. Huang, P. Wang, L. Ye, M. Peng, L. An, Q. Sun, Y. Zhang, G. Yang, Z. Li, F. Zhong, F. Wang, Y. Wang, M. Motlag, W. Wu, G. J. Cheng, W. Hu, Stable mid-infrared polarization imaging based on quasi-2D tellurium at room temperature. *Nature Communications* **11**, 2308 (2020).